UNIVERSITÀ DEGLI STUDI DI VERONA

DIPARTIMENTO DI BIOTECNOLOGIE

SCUOLA DI DOTTORATO IN SCIENZE NATURALI ED INGEGNERISTICHE

DOTTORATO DI RICERCA IN BIOTECNOLOGIE

CICLO XXXIII

STUDY ON THE MOLECULAR MECHANISMS AT THE BASIS OF PHOTOSYNTHESIS TOWARD MICROALGAE DOMESTICATION

COORDINATORE E TUTOR: PROF. MATTEO BALLOTTARI

DOTTORANDO: LUCA ZULIANI

INDEX

SUMMARY

Oxygenic photosynthesis sustains life on Earth, being the process through which sunlight is used to drive carbon fixation into biomass releasing oxygen as by-product. Photosynthetic organisms convert light energy into chemical energy thanks to the activity of pigment-binding multiproteic complexes known as photosystems and their relative light-harvesting antenna complexes. Included in a dedicated electron transport chain located in the thylakoid membranes of the chloroplast, photosystems use light energy to initiate electrons transport from their reaction center to a number of different transporters. While electrons are ultimately used to produce reducing power (NADPH), the coupled buildup of an electrochemical gradient drives ATP synthesis. Reducing power and ATP are thus used by the CO_2-fixing reactions to produce triose phosphates. More than often, light availability is non-optimal, either too scarce or in excess compared to the photosynthetic capacity of the organism operating photosynthesis, to the point it may result dangerous. Among the most sensitive complexes of the photosynthetic chain, photosystem II is the main site of Reactive Oxygen Species (ROS) formation. These detrimental compounds may lead to a compromised growth and losses in biomass productivity. For this reason, photosynthetic organisms evolved different photoprotection mechanisms, among which Non-Photochemical Quenching (NPQ) is one of the most important and investigated. NPQ has an important role in the quenching of chlorophyll's singlet excited state, safely dissipating the excess excitation energy in the form of heat. Microalgae dissipate most of the absorbed energy through this safe-valve mechanism, even when conditions are not dangerous, determining a consequent reduction of biomass accumulation. Moving towards an optimized photosynthetic yield is one of the main objectives in microalgae domestication, which itself is an ever-growing interest, because sustainable microalgal industrial applications have the potential to satisfy many global demands. Among the most important, is the use of algal biomass as food and feed, bio-fuels production, extraction of high-value nutraceuticals and pharmaceuticals, recovery of wastewaters, and carbon capture. However, realization of this potential requires a decrease of the current production costs. To achieve profitability, identification of limiting factors is fundamental. Particularly, light-to-biomass conversion efficiency is a key

bottleneck that needs to be addressed to achieve domestication. With this focus, the aim of this thesis was to study microalgal photosynthetic behavior upon different growth conditions and the relative activated energy dissipation processes as a possible target to improve productivity, thus enabling the use of microalgae as green cell factories. All the studies herein presented were conducted on the model organism for green algae, *Chlamydomonas reinhardtii*, for which extensive literature, mutants' libraries, and genetic tools are available.

In chapter two we investigated the physiologic and metabolic responses of *C. reinhardtii* to an increased CO_2 availability. Elucidation of the adaptation mechanisms to such condition poses the base to develop strategies to improve the carbon assimilation efficiency, thus achieving sustainability of microalgal industrial applications. We evidenced how an increased carbon assimilation in high CO_2 concentration redirected the metabolism toward biosynthesis of lipids (TAGs). Also, in the same condition, we registered a lowered NADPH accumulation rate compared to the control condition, suggesting that the increased NADPH requirement of carbon fixation caused the chloroplast to act as a sink for reducing power. Because of this we investigated how mitochondrial respiration adapted to the reducing power scarcity, evidencing a preference towards alternative respiratory pathways.

In chapter three of this thesis, we present our study on the role of the LPA2 protein of *Chlamydomonas reinhardtii*. Previous work, although retracted, suggested that the homolog protein of *A. thaliana* had a role in PSII assembly. We evidenced that in *C. reinhardtii*, the LPA2 protein has indeed a role in PSII assembly and functioning. Knockout lpa2 mutants were generated by using the CRISPR-Cas9 target-specific genome-editing system. Through biochemical analysis we were able to determine a drastic reduction of D1, D2, CP43, and CP47 proteins, the main constituents of the PSII complex. As a consequence of such severe protein reorganization, the physiological behavior of the mutant lines was altered. Chlorophyll content per cell, PSII quantum yield, and light-dependent oxygen evolution were diminished with the result of an impaired photoautotrophic growth. Moreover, through a pulse and chase experiment we were able to evidence that the absence of the LPA2 protein caused a reduced PSII assembly and turnover.

The fourth chapter is focused on the molecular mechanisms responsible for NPQ activation in *C. reinhardtii*. Higher plants rely on both lumen acidification and zeaxanthin accumulation to induce activation of excess energy thermal dissipation. While it is well established that *C. reinhardtii* triggers quenching mechanisms activation upon luminal pH drops in high light condition, zeaxanthin's role remained rather elusive so far. With a double approach, *in vivo* and *in vitro*, we contributed to characterize the unclear impact of zeaxanthin in the induction of NPQ in *C. reinhardtii*. LHCSR3 protein, the main responsible for light energy dissipation in *C. reinhardtii*, was engineered to be unable to sense pH changes in the luminal space by removing the protein region believed to confer such capability, namely the C-terminal region. Moreover, the engineered protein was *in vitro* refolded in the presence of two pigment mixes that resemble normal and high light condition of the cell. While the normal-light pigment mix is characterized by a high violaxanthin content, the high-light-resembling one has an increased zeaxanthin content, which in physiological conditions derives from the epoxidation of violaxanthin in the so-called xanthophyll cycle, activated upon high light exposure. With a single-molecule spectroscopic approach we were able to determine that pH and zeaxanthin activate distinct quenching processes within LHCSR3 and that both parameters are able to induce LHCSR3 in a quenched state able to provide photoprotection. The parallel *in vivo* study was conducted making use of different mutants and their relative level of LHCSRs accumulation. This enabled us to separate the contributions of the different components of NPQ partially or fully. We concluded that quenching could occur without zeaxanthin accumulation (as already presented in the literature), solely depending on the pH drop in the luminal space. However, we also evidenced the ability of a mutant strain which constitutively accumulates zeaxanthin to be able to onset a quenching mechanism unrelated to the pH drop and LHCSRs activity.

Chapter five deepens the focus on the role of the C-terminal acidic residues of the LHCSR3 protein through which it supposedly gains part of its pH-sensing capability. We produced a chimeric LHCSR3 protein which C-terminal region was substituted by the terminal region of another LHC protein that naturally lacks acidic residues. Since the chimeric protein could not be accumulated by the alga *in vivo*, we proceeded with an *in vitro* characterization through TRPL and TA spectroscopies. We determined that the pH-

dependent protein activation as a quencher was reduced, consistently with previous results in the literature, albeit not fully impaired. Specifically, the *Chl-Car* interactions that concur in the NPQ phenomenon within LHCSR were unaltered in the chimeric protein and could be ascribed to the remaining protonatable residues. Thus, we hypothesized that the registered reduced quenching capability could be assigned to *Chl-Chl* interactions.

1 INTRODUCTION

1.1 OXYGENIC PHOTOSYNTHESIS

1.1.1 Evolution of oxygenic photosynthesis

Earth is bountiful with life that thrives directly or indirectly by drawing energy from the Sun through the process of photosynthesis. Photosynthetic organisms can harness photons energy to drive chemical reactions against their equilibrium. Most photosynthetic organisms split water into protons and molecular oxygen, generating electrons that are used to reduce inorganic carbon and build their cellular components. Oxygen-dependent forms of life rely on these compounds to survive, re-oxidizing them and releasing water as byproduct, eventually closing this redox cycle (Falkowski, Fenchel and Delong, 2008). Before evolution allowed adoption of water as main electron source, early photosynthetic life made use of other compounds, such as hydrogen, ferrous iron, and hydrogen sulfide. Utilization of these substrates together with inorganic carbon left geological signatures that allow tracing of the evolution of metabolic strategies and life on Earth. Virtually all oxygen in our atmosphere has been produced by the photosynthetic activity of organisms over the history of our planet, dating its appearance around 2.4 billion years ago during what is called the great oxidation event (Buick, 2008). Cyanobacteria are considered responsible of such planet-changing event, given the mineralized imprints similar to modern stromatolites they left behind around 2.7 billion years ago (Lepot *et al.*, 2008; Soo *et al.*, 2017). After that, life had to adapt to oxygen or become extinct. Those who were able to tolerate oxygen and harness the amount of energy released when used as terminal oxidant, won the lottery of evolution, and grew new metabolisms and strategies to survive and thrive. Nevertheless, still today some components of the oxygenic photosynthesis remain oxygen-sensible and susceptible to its reactive species as will be described in the following chapters (e.g., RuBisCO and photosystem II), confirming the anaerobic origin of such complexes. Chlorophylls are themselves the product of evolution and could be used to trace back the evolution aspects of photosynthesis in general. The first part of their pathway is common to heme biosynthesis with later steps dedicated to the insertion of magnesium and other ring substituents. While in the earliest version of this pathway

oxygen presence was not tolerate, modern oxygenic organisms require oxygen to catalyze certain steps, again highlighting the adaptation that the oxygen presence forced onto ancestral life (Raymond and Blankenship, 2004). Current evidence indicate that all photosynthetic reaction centers have a common ancestor while the light-harvesting antenna complexes have been invented multiple times during the evolutionary path (Blankenship, 2010). However, the evolutionary origin of oxygenic photosynthesis remains unknown, but it certainly is a complex non-linear process.

1.1.2 The photosynthetic reactions

Photosynthesis is the process that makes use of light energy to drive conversion of CO_2 in organic matter, utilizing water as reducing substrate, thus ultimately producing oxygen as byproduct. The reaction is summarized as:

$$6H_2O + 6CO_2 \rightarrow C_6H_{12}O_6 + 6O_2$$

The whole photosynthetic process can be divided into two phases, commonly referred to as "light" and "dark". The light phase, in which water is split into molecular oxygen, protons and electrons using light energy, fuels the dark reactions, so called because do not directly depend on sunlight energy but rather hinge on NADPH and ATP accumulated during the light phase. These reactions reduce CO_2 into carbohydrates through the Calvin-Benson cycle. These powerful reactions require a plethora of sophisticate protein complexes embedded in specific functional membrane compartments. Oxygenic photoautotrophs like plants and algae embody this machinery in the chloroplast, a complex organelle characterized by two outer membranes, an aqueous space known as stroma, a third interconnected vesicular membrane structure, the thylakoid, that encloses a second aqueous solution, the lumen. Chloroplasts made their appearance circa 1 to 1.5 billion years ago, originated by endocytosis of a cyanobacterium by an ancestral pre-eukaryotic cell. From that single evolutionary event, almost all the organisms that nowadays perform oxygenic photosynthesis were originated.

1.1.2.1 Light phase

The light phase of photosynthesis takes place in the thylakoid membrane. Four major protein complexes are involved: Photosystem II (PSII), Photosystem I (PSI), cytochrome b6f and ATP synthase. These complexes, together with other intermediate transporters,

represent the electron transport chain, that catalyzes the process of light harvesting and photophosphorylation. The general reaction can be described as:

$$2NADP^+ + 2H_2O + LIGHT \rightarrow 2NADPH + O_2 + 2H^+$$

$$ADP + Pi + 3H_{in}^+ \rightarrow ATP + H_2O + 3H_{out}^+$$

PSII and PSI are responsible for light harvesting and consequent energy conversion to electric potential through charge separation. Cytochrome b6f mediates electron transport from PSII to PSI while operating proton translocation in the lumen. ATPase catalyzes ATP synthesis making use of the proton-motive force (pmf) built during electron transport. The overall process is better described taking into account the redox potential of the involved partners, herein showed by the so called Z-scheme (Hill and Bendall, 1960).

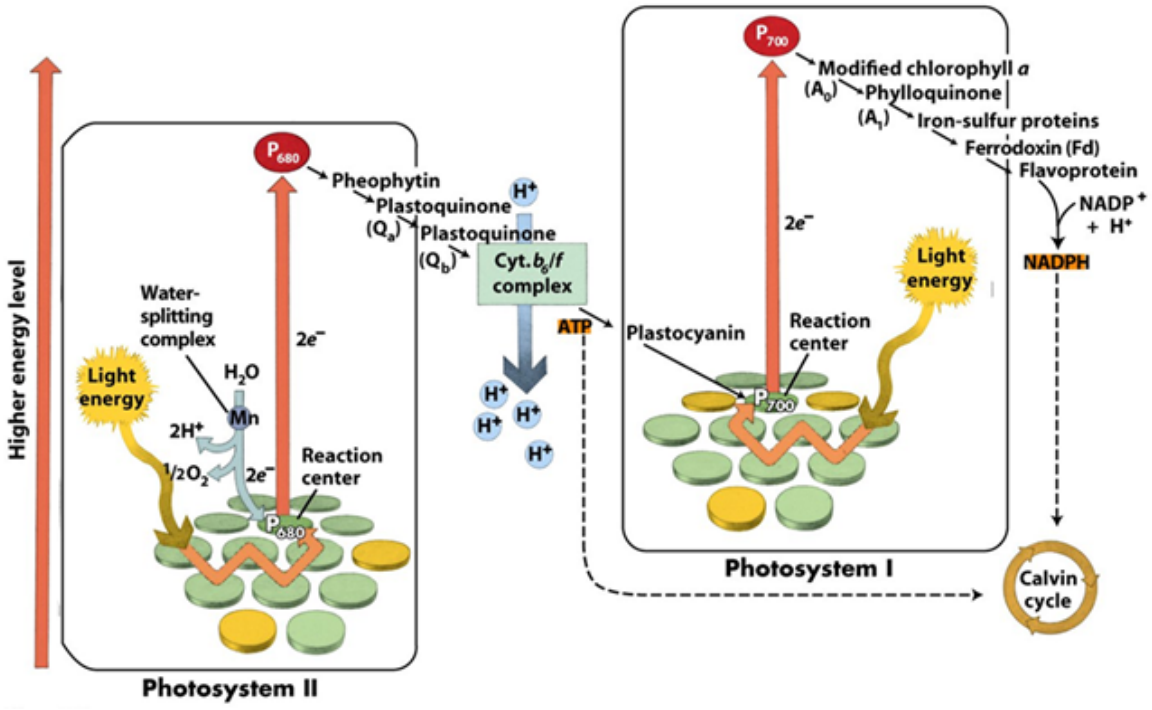

Figure 1 Z-scheme developed by Wilbert Veit and Govindjee, 2000. The electron transport from H2O to nicotinamide adenine dinucleotide (NADP+) is traced from left to right on the diagram. This process is initiated by the simultaneous absorption of light by two antenna complexes.

As described in figure, the electron transport flows from lower to higher values of redox potential. A photon absorbed by the PSII reaction center, known also as P680 (because of its absorption maximum at 680 nm), leads to an excited energy state able to drive the transfer of an electron to an acceptor molecule, pheophytin. P680 redox state is restored oxidizing water through the Mn-Cluster of the oxygen evolving complex (OEC), enabling P680 to be excited again. The electron bound to pheophytin enters the electron transport

chain via plastoquinones A (QA) and B (QB). While QA is attached to PSII, QB can freely move across the thylakoid membrane once two electrons, and subsequently two protons from the stroma, are bound to it (QH2B). Cytochrome B6f binds QH2B which releases its electrons to the plastocyanin and its two protons to the lumen, contributing the building of pmf. PSI works similarly to PSII with the exception that whenever its reaction center, P700 (again, because of its absorption maximum at 700 nm), is oxidized, plastocyanin readily yields one electron. From P700 to NADP+ the electrons flow runs through A0 (a chlorophyll molecule), A1 (a phylloquinone) and three different Fe-S protein complexes (FX, FB, and FA in sequence). These proteins coordinate iron atoms with the aid of cysteine residues, so that they can run into redox reactions and lead the electron flow to ferredoxin (Fd). Fd can drive NADPH production by the ferredoxin-NADP reductase (FNR) enzyme. During the electron transfer reactions, an electrochemical potential is built across the thylakoid membrane, constituting a pH difference between the stromal and lumenal side. Water oxidation of OEC produces four protons for each oxygen molecule produced. Moreover, the so-called Q-cycle of quinones around CytB6f moves three protons for each couple of electrons transported towards PSI. The proton gradient produced is then exploited by ATPsynthase to produce ATP from ADP and Pi. In case of additional ATP requirement, a cyclic electron transport may take place around PSI: Fd is oxidized by cytb6f causing protons translocation to the lumen enabling PSI to absorb photon independently by PSII (Harbinson and Foyer, 1991).

1.1.2.2 The dark phase

Via the Calvin-Benson cycle carbon dioxide is fixed to carbohydrates, consuming the ATP and NADPH produced by the light reactions of photosynthesis and fueling them back with ADP and $NADP^+$. The phase is summarized in the following reaction:

$$CO_2 + H^+ + 4e^- + NADPH_2 + ATP \rightarrow CH_2O + H_2O + NADP^+ + ADP + Pi$$

The conversion of CO_2 to sugar happens in four phases. The first one, the carboxylation phase involves RuBisCO, the enzyme responsible for carbon fixation. It adds two CO_2 molecules to ribulose bisphosphate and produces two phosphoglycerate molecules. In the reduction phase, phosphoglycerate is converted to triose phosphates drawing energy from ATP and $NADPH_2$. The next phase, the regeneration step, sees ribulose phosphate

synthesis from a series of reaction involving 6-carbon and 3-carbon sugars catalyzed by transketolase and aldolase enzymes. The last phase of the cycle is the so-called production phase, in which not only sugars are produced, in fact during these steps, fatty acids, amminoacids, and organic acids are accumulated. Oxygen acts as competitor in the carboxylation phase, determining accumulation of phosphoglycolate from the oxygenation of RubP performed by RuBisCO. Phospglycolate is then converted into CO_2 without metabolic gain. This competitive cycle is called photorespiration and it is stimulated by the relative ratio of oxygen and CO_2 concentrations.

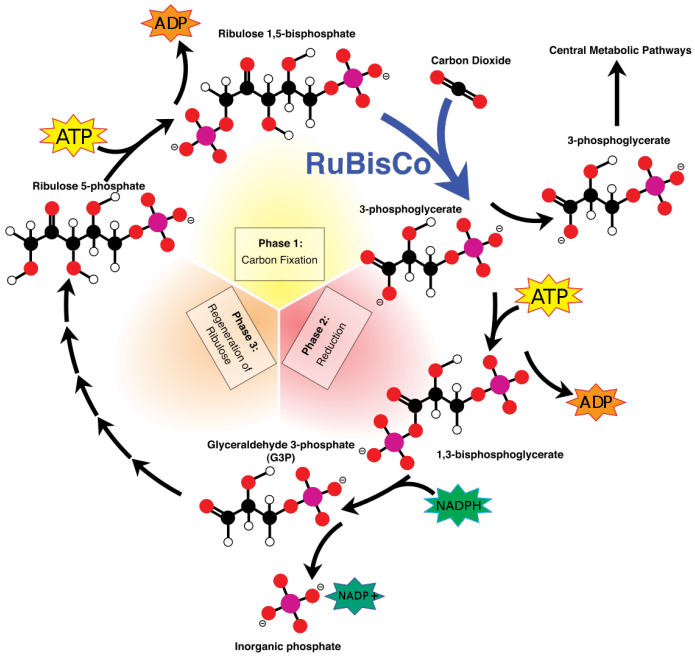

Figure 2 Calvin-Benson Cycle schematization showing the three different phases

1.1.3 The photosynthetic pigments

Only few pigments take part in the photosynthetic process among which are chlorophylls (Chls) and carotenoids (Cars). Photosynthetic complexes make use of pigments for their light harvesting properties enabled by the chemical structure they share, the key to handle photons energy: an alternating series of single and double carbon bonds that form a conjugated π-electron system (Johnson, 2016).

1.1.3.1 Chlorophyll

Chlorophylls are constituted of a tetrapyrrole ring structure (also known as porphyrin) that coordinates a magnesium atom by means of four nitrogen atoms (Von Wettstein, Gough and Kannangara, 1995). Chlorophylls are classified in 6 different types (a to f),

based on their side-group substituents. As mentioned before, double conjugated carbon bonds are responsible for the light-dependent behavior of the molecule, alongside its side-group substitution, each combination determining a different spectroscopic property. The biosynthesis of these molecules takes place in the chloroplast, starting from the building block ALA (5-aminolevulonic acid), a non-protein amino acid formed from glutamate. ALA-dehydratase catalyzes the condensation of two ALA molecules to produce porphobilinogen. Four porphobilinogen molecules are converted into hydroxymethylbilane forming a ring. From this point the ring is submitted to a series of reactions involving its side-groups leading to the addition of the coordinated Mg group and the esterification of the molecule with phytol, generating ultimately the *Chl* molecule (Buchanan BB and (eds.), 2015). *Chl* a and b are the most distributed among vascular plants and green algae and differs from one another as *Chl* b contains an aldehyde in the second pyrrole ring, derived from oxygenation of *Chl* a. Chlorophyll's absorption spectrum is characterized by two bands: one in the Soret region (450-475 nm) and the other in the Qy region (630-675 nm). The latter indicates the transition of an electron from S0 to S1 state. *Chl a* exclusively populates the core and the reaction center of photosystems, while, alongside *Chl* b, occupies the light-harvesting antennae proteins. Not only the presence of these pigments in the apoprotein confers the needed light-handling capability but it is also fundamental to reach the correct protein folding (PAULSEN, FINKENZELLER and KÜHLEIN, 1993).

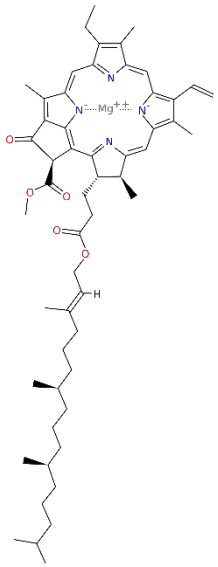

Figure 3 Chl a structure

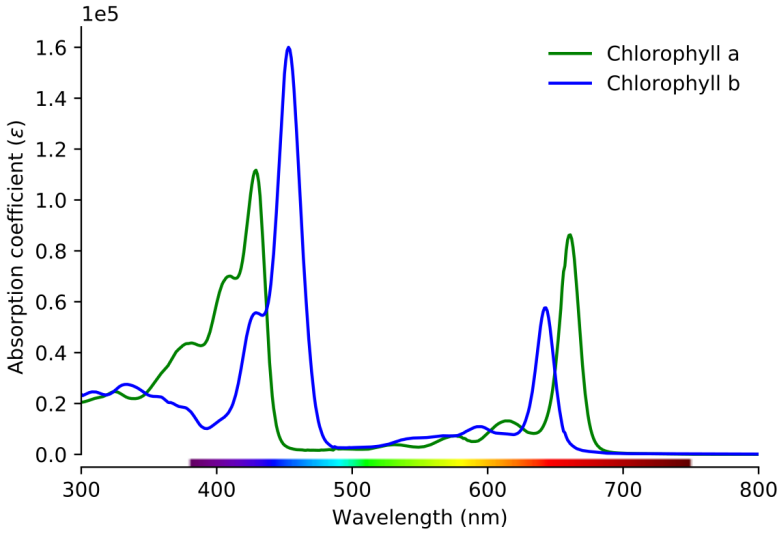

Figure 4 Chl a and b absorption spectrum

1.1.3.2 Carotenoids

Carotenoids are polyisoprenoid composed of 40 carbon atoms and are synthetized by bacteria, algae, fungi, and plants. The general structure is characterized by a long carbon chain rich in conjugated double bonds and cyclic groups at the extremities. The hydrogenation degree together with the wide variety of side-groups composes a large family of compounds with diverse properties and colors (Cazzonelli, 2011). In photosynthetic organisms like plants and green algae two different classes of carotenoids are found: carotenes and their oxygenated derivatives, xanthophylls (Bhosale and Bernstein, 2005). The most abundant carotenoids associated with the functionality of thylakoids are α and β -carotenes and the xanthophylls lutein, violaxanthin, neoxanthin and zeaxanthin. While carotenes are mainly found connected to the core complex of both photosystems, xanthophylls are found into the antenna complexes (BASSI *et al.*, 1993; Ruban *et al.*, 1999; Caffarri *et al.*, 2001). Another important xanthophyll worth of mention is astaxanthin, known for its strong effect on preventing photodamage adducible to ROS formation, which industrial relevance has increasingly risen to date given the high interest in pharmaceutical implementation, other than the current application in aquaculture.

Carotenoids have many crucial functions in a photosynthetic organism:

- Structure stabilization and assembly of protein complexes of the thylakoid membrane (Plumley and Schmidt, 1987; PAULSEN, FINKENZELLER and KÜHLEIN, 1993).
- Ligh absorption and excited energy transfer to chlorophylls (Mimuro and Katoh, 1991; Gradinaru *et al.*, 2000).
- Photoprotection via dissipation of excited states of chlorophylls and/or ROS scavenging (Moore *et al.*, 1982; Havaux and Niyogi, 1999).

Carotenoids' synthesis starts from the formation of the main C40 compound, phytoene, from head-to-head condensation of two molecules of GGDP (geranylgeranyl diphosphate). Sequential desaturation reactions yield lycopene which is the cyclized to β-carotene by two β-cyclizations or to α-carotene by one β-cyclization and one ε-cyclization. Hydroxylation of α-carotene yield lutein, the most abundant carotenoid. On the other side of the metabolic pathway, β-carotene is converted to zeaxanthin, antheraxanthin, violaxanthin and neoxanthin through consequent hydroxylation and epoxidation reactions.

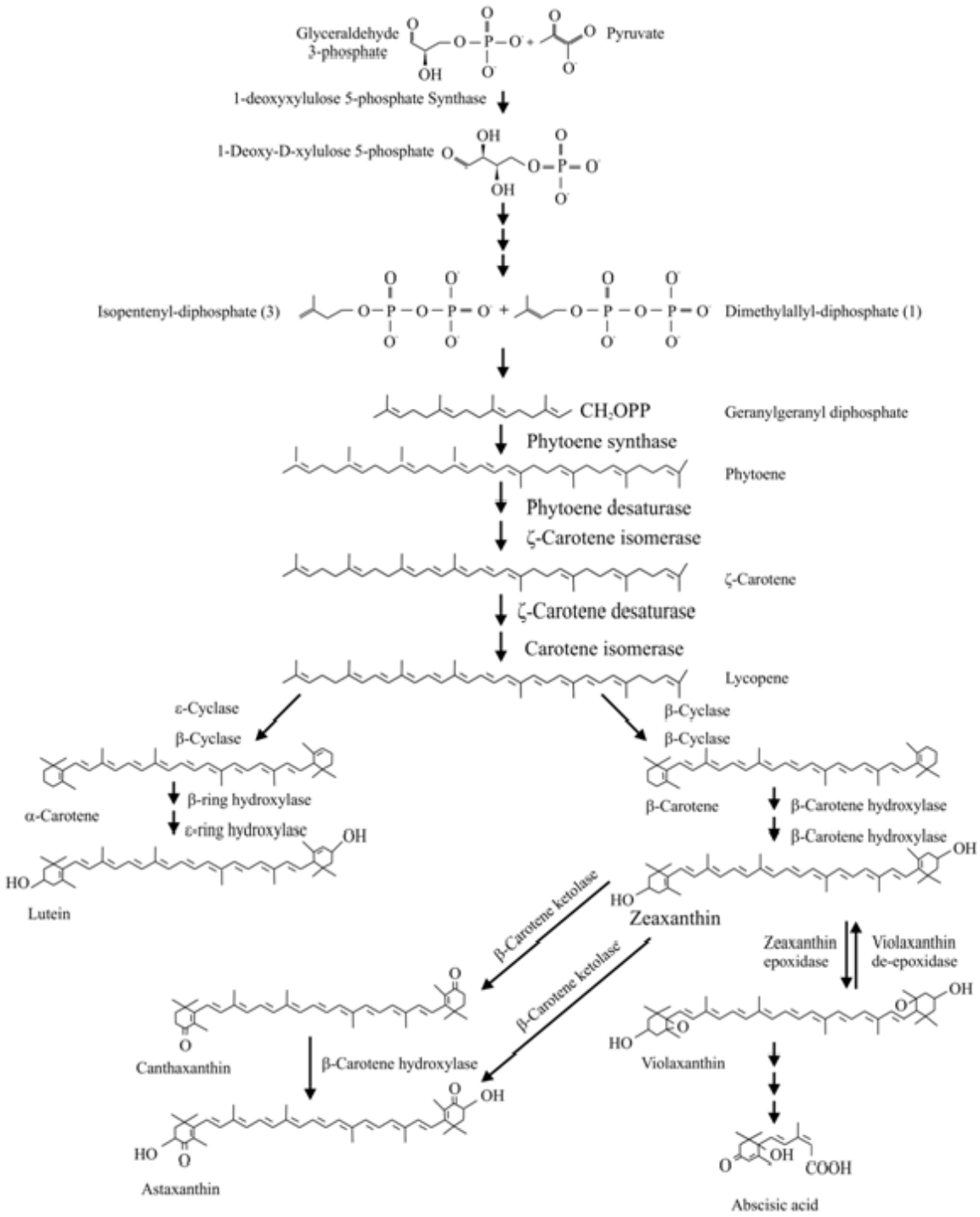

Figure 5 Carotenoid biosynthesis and xanthophyll cycle

1.1.3.2.1 Xanthophyll Cycle

The carotenoid composition of the photosynthetic apparatus is subject to variations given the everchanging light conditions. This adaptation represents one of the diverse photoprotection measures a photosynthetic organism can enact and determines the activation of several other photoprotective mechanisms such as the thermal dissipation of excess absorbed energy (Niyogi, 1999; Holt, Fleming and Niyogi, 2004). The xanthophyll cycle involves violaxanthin (vio), antheraxanthin and zeaxanthin (zea) and consists in a light-dependent reversible de-epoxidation of vio to *Zea* though the intermediate antheraxanthin, catalyzed by the enzyme violaxanthin de-epoxidase (VDE). The reverse reaction Is catalyzed by the enzyme zeaxanthin epoxidase (ZE) (Yamamoto and Kamite, 1972). VDE is activated upon luminal acidification, a condition that results after high light exposure with the consequence of a stressed electron transport chain. The xanthophylls cycle is present in higher plants, green and brown algae (Yamamoto, Nakayama and Chichester, 1962). In plants, *Zea* lowers the light use efficiency to the point of decreasing plant growth if accumulated constitutively (Havaux, Dall'Osto and Bassi, 2007). The role of the xanthophyll cycle in microalgae is less clear. In the model green alga *C. reinhardtii* *Zea* accumulation is not required for the ΔpH-dependent thermal dissipation (Niyogi, Björkman and Grossman, 1997a), oppositely to *Chlorella vulgaris* and *Chlorella saccharophila* that show a *Zea*-dependent NPQ (Quaas *et al.*, 2015).

1.1.4 Photosystems

Photosystems catalyze the light-driven electron transfer to form ATP and reducing power. Oxygenic photosynthesis requires two photosystems, namely photosystem I (PSI) and photosystem II (PSII) to work cooperatively linked by common intermediates. These two systems were discovered because of slight differences in the wavelengths of light to which they respond. The PSI absorbs far-red light with a quantum efficiency of charge separation around 1, while PSII absorbs red light and its quantum efficiency is more variable also depending on the antenna system (Wientjes, Van Amerongen and Croce, 2013). Even though these two complexes are structurally different, they share some proprieties: both bind exclusively *Chl* a and carotenes to form the so-called core complex or reaction center, where charge separation occurs. Also, they feature a peripheral antennae system composed by the chlorophyll (a and b) and xanthophylls -binding light-harvesting

proteins, which function is to catch the light energy and transfer it to the core complex. While the genetic information encoding for the two photosystems is well conserved, the antennae system can widely vary in the different organisms. Genes encoding core proteins are called Psa and Psb for the PSI and the PSII, respectively. These genes are located both in the plastidial and nuclear genome. The antenna complexes belonging to the LHC (Light Harvesting Complex) family, are called LHCI or LHCII, depending on the main association with PSI or PSII and are encoded by the nuclear Lhca or Lhcb genes respectively (Jansson, 1999; Dekker and Boekema, 2005). LHCs proteins are translated into the cytoplasm and targeted to the translocons system of the chloroplast (Tic-Toc), which realizes proteins import into the stroma. There, the transit peptide is removed, and the proteins can finally find their proper conformation with the aid of chlorophylls and carotenoids (Oreb, Tews and Schleiff, 2008).

1.1.4.1 PSII

PSII is a homodimeric multiproteic complex composed by 20-30 subunits with a relative molecular mass of about 350 kDa. It is located in the thylakoid membranes of higher plants, cyanobacteria and green algae and functions as a water-plastoquinone oxidoreductase, transferring electrons from water to PQ producing oxygen (Linke and Ho, 2014). The precise number of subunits that this complex is composed by is still unknown as well as species-specific. From a functional point of view, PSII is composed by a quinone type reaction center (6Q-type/type II), an Oxygen Evolving Complex (OEC) and by an inner light-harvesting complex. The PSII core complex of *C. reinhardtii* is predicted to have a dimeric structure, consisting of the two protein D1 and D2, as in plants and cyanobacteria. These two proteins bind all the prosthetic groups needed for charge separation to occur, including the special *Chl* pair P680, pheophytin, plastoquinone Qa and Qb (Nelson and Yocum, 2006). After two charge separation events, QB is being reduced and protonated twice yielding plastoquinol QBH2. Once this reduced state is reached, plastoquinol leaves the acceptor side of PSII, replaced by another plastoquinone molecule from the thylakoid membrane. On the other hand, an oxidized P680 is reduced by a nearby tyrosine residue (Tyr 161 of D1, Yz) determining oxidation of a Mn cluster, the catalytic center of the oxygen evolving complex (OEC). After four events of oxidation, the OEC is oxidized enough to drive the split of two water molecules obtaining four

protons and one oxygen molecule (Shen, 2015). Surrounding the D1 and D2 subunits are the CP47 and CP43 subunits together forming the inner antenna of the PSII. In addition to these 4 large subunits, there are 13 low-molecular-weight transmembrane subunits. Furthermore, there are 3 peripheral, extrinsic proteins associated with the lumenal side of PSII, necessary to maintain the OEC (Nield and Barber, 2006).

1.1.4.1.1 PSII assembly

In accordance with the high complexity of PSII, its assembly is an elaborate and highly coordinated process. Even if studied for more than 30 years, only recently, with the advent of new and detailed structural information, the necessary framework to understand the process has been established. Characterization of a collection of PSII *Synechocystis* 6803 mutants, lacking specific sub-units of the PSII complex plus radioactive pulse–chase experiments have provided support for the stepwise assembly of the complex herein described. Cytocrome b-559 seems to act as a nucleation factor in initialization of PSII assembly. The first sub-complex thought to form is D2-Cyt b-559 (Komenda *et al.*, 2008). Together with a newly formed D1-PsbI subcomplex, a PSII RC-like complex is shaped (Dobáková, Tichý and Komenda, 2007; Komenda *et al.*, 2008). To allow a proper Mn cluster assembly, D1 protein must be processed. In *Synechocystis*, D1 C-terminal is cleaved of 8 amino acids by the protein CtpA (Komenda *et al.*, 2007). CP43 is unable to attach to the RC if CP47 is not already complexed. In fact, different PSII RC complexes, each one brought together with different assembly factors, have been found in the thylakoid membranes, like RC–CP47 (Komenda *et al.*, 2008). This complex, although unable to oxidize water, can drive oxidation of Yz after performing charge separation (Metz *et al.*, 1989). When CP43 is attached in place, the monomeric PSII core complex is ready to form, together with PsbO, U and V (the protein subunits that stabilize the OEC), the so called RCC1 complex. At this point the complex is functional and ready to dimerize. Notably, in *Synechocystis* mutants lacking PsbO, the dimeric form of the complex is missing (Komenda and Barber, 1995; Nixon *et al.*, 2010).

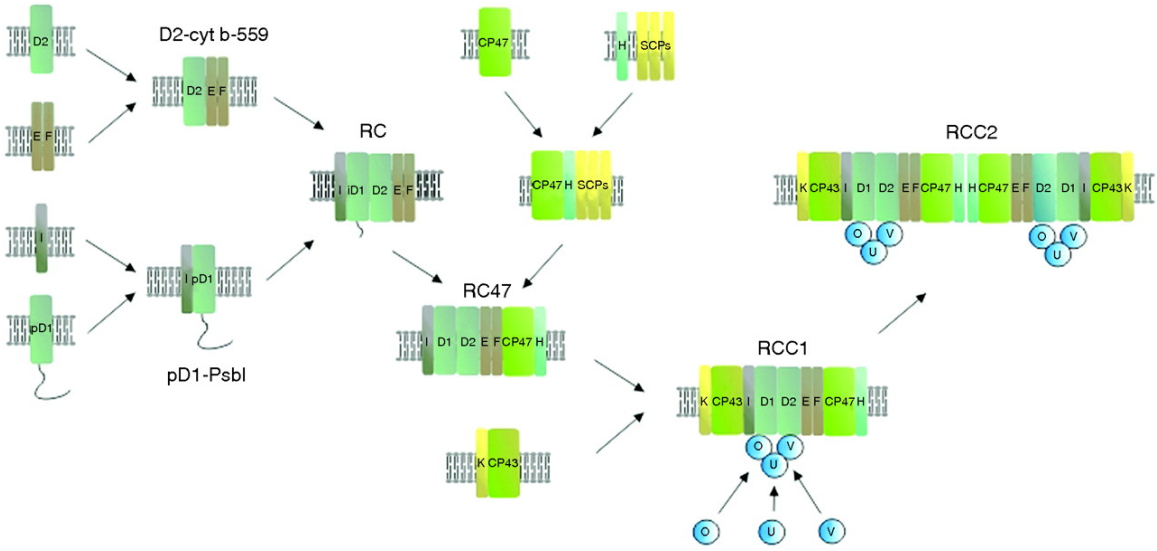

Figure 6 Schematic representation of the PSII assembly process

Several assembly components are common to cyanobacterial and chloroplast processes (Nickelsen and Rengstl, 2013). One of the first conserved factors to be characterized was Hcf136, identified in a mutant of A. thaliana with a high *Chl* fluorescence (typical phenotype of PSII mutants) (Meurer *et al.*, 1998). PSII was found only in traces in this mutant. How this factor and its homologous in *Synechocistys* (Ycf48) interact and operate towards PSII assembly remains unclear, however, it is likely that that they may interact with the C-terminal region of D1 and D2, also considering its luminal localization bound to the membrane. However, algae and higher plants have extended their catalogue of tools during evolution, giving rise to new, specific factors.

1.1.4.2 PSI

PSI is a multi-subunit protein complex with an iron-sulphur reaction center capable of generating redox potential with extreme efficiency, using light to transport electrons from plastocyanin on the luminal side to ferredoxin on the stromal side of the thylakoid membrane to produce NADPH2 (Jensen *et al.*, 2007). High resolution structures were resolved both for cyanobacteria and higher plants (Jordan *et al.*, 2001; Amunts *et al.*, 2010). Being one of the most elaborated membrane complexes to date, PSI operates with an unprecedented photochemical quantum yield close to 1.0 (Amunts and Nelson, 2009). The core complex is composed by 17 polypeptides, among which PsaB and PsaA are the larger (80 kDa). These proteins bind the cofactors needed for light harvesting (80 *Chl* a and 20 β-carotenes) and those involved in electron transfer (6 *Chl* a, 2 phylloquinones and a Fe-S

cluster). Among the smaller subunits (4-18 kDa), PsaF is involved in plastocyanin docking, PsaC binds the terminal electron acceptor, the Fe-S cluster. PsaC, PsaD, and PsaE are involved in ferredoxin docking on the stromal side. PsaK and PsaG are involved in LHCI stabilization, while PsaH and PsaO are important for LHCII interaction during state transitions. PSI binds at least 173 *Chls* (100 *Chls* bound to the core) with a *Chl* a/b ratio of about 8,2/9,7 and 33-34 carotenoids (12 bound to LHCA and 22 β-carotenes bound to the core) (Amunts *et al.*, 2010; Galka *et al.*, 2012). PSI of higher plants also binds from 8 to 10 low energy *Chls* referred to as red forms, which function can be adducible to light harvesting in shaded light conditions (Morosinotto *et al.*, 2003; Caffarri *et al.*, 2014).

Nine lhca genes encoding for LHCI proteins were identified in *C. reinhardtii*. Being bound to the reaction center's subunits PsaJ/F/G, these proteins are arranged as a double layer (Drop *et al.*, 2011). LHCA can be divided in three subgroups, based on their content of so-called red forms (high wavelength absorbing chlorophylls). The first group is represented by the "Blue LHCAs" and includes LHCA1, 3 and 7 with emission maxima at 682,5-683,5 nm. The second group is called "intermediate LHCA" and it is composed LHCA5, 6 and 8 with peaks between 694,5 and 697,5 nm. The third class of LHCAs is called "Red LHCAs" and comprehend LHCA2, 4 and 9, showcasing maxima emission between 707 and 715 nm (Mozzo *et al.*, 2010).

1.1.5 Alternative electron pathways

ATP/NADPH ratio can significantly vary based on the metabolic status of the cell: nitrate assimilation, lipid, and amino acids metabolic pathways, as well as trophic conditions can interfere in the balance of such ratio, therefore alternative electron flow pathways have evolved. The photosynthetic apparatus can operate to produce exclusively the electrochemical potential used by ATPase to produce ATP, without determining accumulation of NADPH nor oxygen, bypassing the activity of PSII. Cyclic electron flow involves the transfer of electrons from ferredoxin to the cytochrome b6f complex which produces a proton gradient while transferring the electrons to plastocyanin to regenerate the P700 reaction center (Harbinson and Foyer, 1991). Two pathways of PSI cyclic electron transport are known: the first involves ferredoxin (fd), the proteins PGR5 (proton gradient regulation 5) and PGRL1 (proton gradient regulation like 1) while the second one requires

the activity of a multi-subunit plastidial NADPH dehydrogenase complex (NDA2) (Dang *et al.*, 2014).

Another electron transport flow is represented by the pseudo-cyclic electron transport (pseudoCET). It is referred to two pathways: the water-water cycle and the flavodiiron pathway. The first of the two depends on the reduction of molecular oxygen around PSI in ROS which is then scavenged by the superoxide dismutase (SOD) and ascorbate peroxidase (APX). The flavodiiron pathway, on the other hand, mediates direct reduction of O_2 to H_2O using either NADPH or Fd as electron donor (Shikanai and Yamamoto, 2017).

Also, electron flow from PSII can be redirected through a protein called PTOX (plastoquinone terminal oxidase) that oxidizes PQH2 and reduces O_2 to H_2O, only determining accumulation of ATP. PTOX is also involved in chlororespiration, a light-independent electron transport pathway. It involves a non-photochemical reduction of PQ by a chloroplast NADPH dehydrogenase and the oxidation of PQH2 by means of PTOX (Bennoun, 1982; Jans *et al.*, 2008). This pathway provides a mechanism to prevent total oxidation of the plastoquinone pool in the dark while averting its complete reduction as well in excess light.

1.1.6 Photoinibition

Photosynthetic organisms thrive on sunlight but at the same time they must be very careful in harnessing such energy since it can be extremely harmful. Also, light quality and intensity fluctuates during the year, the single day or even within the hour. In a matter of minutes, or even seconds – considering sun flecks, light can become limiting or a stressor. As a second level of complication, the photosynthetic process is strongly influenced by environmental and trophic conditions such as temperature and nutrient availability. In certain conditions, light energy absorbed may exceed the capacity for its chemical conversion and utilization, leading to the generation of reactive species, among which the oxygen ones (ROS) can severely damage the photosynthetic apparatus. This detrimental process is called photoinhibition. LHCs, PSII and acceptor side of PSI are the major sites of ROS production. Upon absorption of a photon in an LHC antenna (for example), an electron is raised from the ground state to a higher energy state. From there, excitation energy can be relaxed back to the ground state via different competitive

pathways: being re-emitted in the form of fluorescence, transferred to a lower-energy-chlorophyll, non-radiatively dissipated under the form of heat through non photochemical quenching, or being converted through the process known as intersystem crossing (ISC) to a triplet excited state. The latter pathway is rather slow, and its rate becomes relevant when the population of singlet chlorophylls is high, which in turn depends on the saturation of photochemical reactions. Usually, photochemistry becomes saturated in excess light condition when downstream chemical reaction and NPQ are not able to process the ever-accumulating excitation energy in the antennae. Triplet chlorophylls are not harmful *per se* but are very dangerous since long-lived (in the ms range). During their lifetime, triplet chlorophylls can react with triplet oxygen to form singlet oxygen, able to determine oxidation of nucleic acids, proteins, pigments and lipids (Tardy and Havaux, 1996). In the PSII, after the primary charge transfer P680+ and pheophytin- specie are produced. Once the electron is transferred to Qa, the redox state of pheophytin is re-established, however, in light excess condition the PQ pool is greatly reduced therefore impairing or delaying the electron flow. P680+ and pheophytin- are free to recombine and produce triplet P680*, which in turn can generate singlet oxygen and damage D1 protein (Aro *et al.*, 2005). Oppositely, P700 is a more stable quencher of excitation energy (Dau, 1994). On the other side of PSI, the acceptor side, however, ferredoxin can reduce O_2 to O_2* that is then metabolized in H_2O_2 or OH*, strong ROS.

1.1.7 Photoprotection

Photosynthetic organisms have evolved different strategies to contrast over-excitation acting on different timescales, being this attribute the main trait used to classify them into short- or long-term responses. The first response induced by high light stress in *C. reinhardtii* is avoidance, realized by negative phototaxis. In the case that light evasion may not be enough, excess absorbed light can be dissipated in the form of heat through NPQ. At the same timescale, the antenna complexes are rearranged between the two photosystems and in a matter of minutes the xanthophyll cycle is activated. As the exposure to stressing light continues, antioxidant compounds are being accumulated and transcriptional changes are put in place, determining adjustment of the antenna size of photosystems and of the electron transport (Erickson, Wakao and Niyogi, 2015).

1.1.7.1 NPQ

Non-photochemical quenching is a set of mechanisms that dissipate excess energy absorbed under the harmless form of heat. Up to 75% of absorbed photons can be diverted to this fate (Frank *et al.*, 2000). NPQ can be monitored as a quenching of chlorophyll fluorescence (Genty, Briantais and Baker, 1989). According to the kinetics of NPQ response, at least three components can be identified (Horton and Hague, 1988): an energy quenching (qE) component, a state transition-related quenching component, and a photoinhibitory quenching (qI) component that can be also related to zeaxanthin accumulation (Dall'Osto, Caffarri and Bassi, 2005).

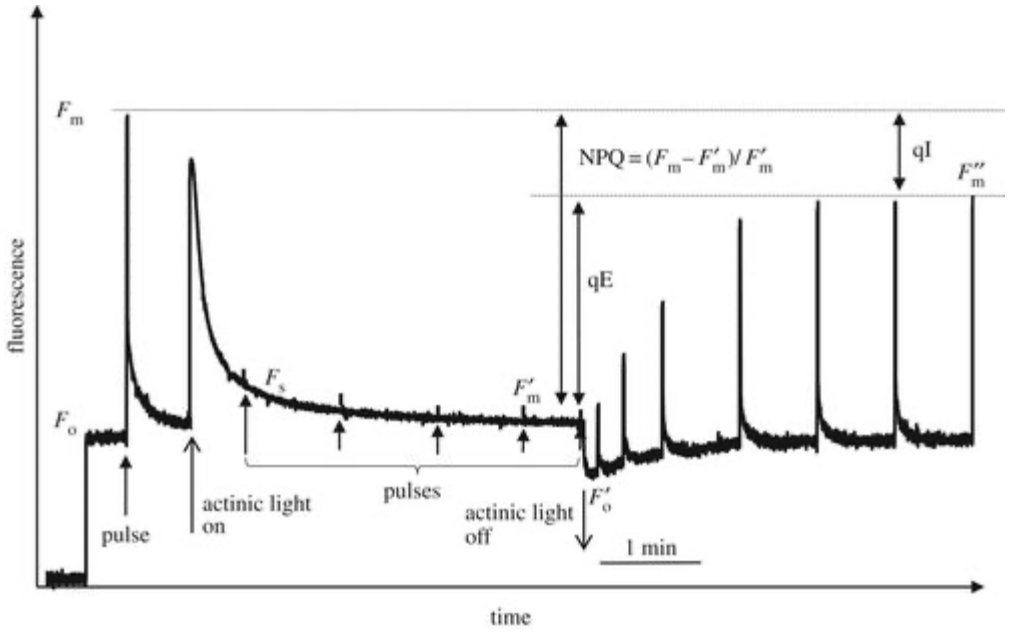

Figure 7 Typical PAM fluorescence measurement of an Arabidopsis leaf showing induction and relaxation of NPQ. Fm and F0 are the maximum and minimum fluorescence levels in the dark before actinic light illumination (1000 μmol m−2 s−1, on/off indicated by open arrows). Fs and F′m are the steady-state fluorescence and maximum fluorescence levels during actinic light illumination, respectively. F′0 is the minimum fluorescence level after actinic light is switched off. F′′m is the maximum fluorescence level following the recovery of the rapidly reversible components of NPQ. Pulses of light (indicated by vertical arrows, 10 000 μmol m−2 s−1, normally of 0.5–1.0 s duration) are applied to close all RCIIs and estimate Fm and F′m. qE and qI are the quickly and slowly reversible components of NPQ, respectively.

As previously mentioned, when absorbed sunlight exceeds the capacity of the photosynthetic organism to fix CO_2, a proton gradient builds across the thylakoid membrane as a product of the linear electron flow. Because of this, the lumenal space is rapidly acidified, immediately triggering qE activation. This was experimentally confirmed using uncoupler agents like nigericin, able to prevent the buildup of the pH gradient across the thylakoid membrane, therefore inhibiting NPQ activation. Also, mutant showcasing a lower qE induction, allowed to uncover an underlying defection in

the generation of a ΔpH (Shikanai *et al.*, 1999). qE is widespread across photosynthetic organisms, however, the proteins responsible for it differs between taxa. Cyanobacteria depend on the presence of a soluble carotenoid-binding protein called OCP (Wilson *et al.*, 2006). It is worth mentioning that the quenching mechanisms of cyanobacteria is not ΔpH-dependent (Magdaong and Blankenship, 2018). In eukaryotic organisms qE is triggered by two different members of the LHC family: LHCSR (light harvesting complex stress related) for green algae (Peers *et al.*, 2009) and PsbS for higher plants (Li *et al.*, 2000). Mosses (e.g. *Physcomitrella patens*) can rely on the activity of both LHCSR and PsbS proteins to onset NPQ (Alboresia *et al.*, 2010). PsbS is able to sense pH through two glutamate residues facing the lumenal side (Li *et al.*, 2004). Apart from a theorized chl-binding site in a dimerization pocket of the protein (Fan *et al.*, 2015), PsbS is considered a non-pigment-binding protein (Bonente *et al.*, 2008). The molecular mechanisms through this protein acts are still unclear and under debate. Given the absence of pigments it is thought that it cannot represent itself the main site of quenching. Models are based on the interaction of PsbS with antenna proteins such to cause a shift to a dissipative conformation. Conversely, recent findings show that *C. reinhardtii* features a transient expression of PsbS in high light even though its role is still not clear (Tibiletti *et al.*, 2016), considering its observed quenching behavior relies on the accumulation of the LHCSR protein (Peers *et al.*, 2009). *C. reinhardtii* features three genes (Lhcsr3.1, Lhcsr3.2 and Lhcsr1) encoding for LHCSR isoforms on chromosome 8. Lhcsr3.1 and Lhcsr3.2 encode for the same polypeptide and are overexpressed in high light conditions. Lhcsr1 shares 87% identity with Lhcsr3.1/Lhcsr3.2. It is constitutively present even a low light and it is overexpressed in high CO_2 regimes and (Merchant *et al.*, 2007; Maruyama, Tokutsu and Minagawa, 2014). *C. reinhardtii* shows a linear correlation between light intensity, LHCSR3 protein level and NPQ, being this isoform the main contributor to the quenching mechanism (Peers *et al.*, 2009). LHCSRs are composed by three trans-membrane helices and bind six to seven chlorophylls with a *Chl* a/b ratio around 6,3, and two carotenoids: lutein and violaxanthin. An additional xanthophyll can be bound to a third peripheral site (Bonente, Ballottari, *et al.*, 2011). Being a pigment-binding protein, LHCSR can be theorized to be direct site of quenching. In fact, this can be verified by its short-lived excited state, given the energetic conformation of its pigments such to determine a dissipative form. Sequence analysis

revealed multiple conserved lumen-exposed protonatable residues in the C-terminal region, suggesting a pH-sensing function of this protein portion. Mutation analysis of these residues confirmed their importance in triggering NPQ (Liguori *et al.*, 2013; Ballottari *et al.*, 2016). LHCSR3 is thought to establish a reversible interaction induced by low luminal pH with LHCB antenna proteins, especially LHCBM1, 4, 6 and 8 (Elrad, Niyogi and Grossman, 2002; Bonente, Ballottari, *et al.*, 2011; Tokutsu and Minagawa, 2013).

The differences between the quenching mechanisms (and the relative actor proteins) of vascular plants and algae can be adduced to evolutionary reasons: land colonization forced photosynthetic organisms to adapt to faster and more pronounced light fluctuations, to a totally different water availability and to a sessile lifestyle. Comparison of A. thaliana and *C. reinhardtii* NPQ induction at different light intensities shows that the alga activates and saturates NPQ at a relative low light intensity, while A. thaliana responds proportionally to the light (Ballottari *et al.*, 2007; Bonente *et al.*, 2012).

1.1.7.1.1 qZ

Zeaxanthin is accumulated in high light conditions by the activity of the VDE enzyme, determining qE triggering in higher plants. qZ is the zeaxanthin dependent NPQ component and it is characterized by a slow initial rise in means of minutes as well as a slow relaxation time in tens of minutes. It is thought that zeaxanthin is directly involved in quenching singlet chlorophylls as well as determining structural changes in determined antenna complexes into a dissipative state (Dall'Osto, Caffarri and Bassi, 2005; Nilkens *et al.*, 2010).

1.1.7.1.2 qT

Considering the everlasting quest of balancing between light harvesting and its dissipation on behalf of the photosynthetic organisms, they evolved an apparatus capable of collecting energy when in limiting conditions and distributing it between the two photosystems. In fact, PSII and PSI have different light absorption properties and distinct light harvesting systems characterizing their relative performance. PSII absorbs in the blue and red regions, while PSI has a broad absorption peak in the far-red region. When in "State 1" LHCII are bound to PSII and LHCI to PSI. Whenever the light quality changes to blue, in favor of PSII, PQ pool becomes rapidly reduced. This triggers the STT7 kinase that

operates phosphorylation of LHCII. Once phosphorylated, LHCII are induced to dissociate from PSII and interact with PSI in the so-called "State 2", increasing PSI antenna size and re-equilibrating the energy distribution between the two photosystems (Lemeille *et al.*, 2009). The process is reversed by a phosphatase (Depège, Bellafiore and Rochaix, 2003). Up to 80% of LHCII antennae are known to dissociate from PSII when state transition is triggered in *C. reinhardtii*, whereas in plants only 20% antennae are involved (Allen, 1992; Finazzi, 2005).

1.1.7.1.3 qI

When stressing conditions are protracted, the PSII repair cycle could be outpaced by the rapid stacking up of damages (Aro, Virgin and Andersson, 1993). When this happens, the qI component of NPQ, also known as photoinhibition, rises determining a decrease in the emitted fluorescence from PSII supercomplexes.

1.1.7.2 Long-term photoprotective responses

Upon long-term stress, other mechanisms besides NPQ are activated. Generally, changes in the architecture of the plant (or the cell's) and stoichiometry of the photosynthetic apparatus require prolonged exposition to stressing conditions for protein expression to adjust. For example, Calvin cycle enzymes or ATPase and electron transport components can be upregulated in previously mentioned conditions. Also, acclimation to high light involves changes in composition of the plant or the alga from a molecular point of view. First, chlorophyll content can be halved, while carotenoid content can be more than doubled (Niyogi, Björkman and Grossman, 1997a; Shapira *et al.*, 1997). Carotenoids can indeed act as scavenger of accumulated reactive oxygen species and excited state chlorophylls. Also, tocopherols, ascorbate and glutathione play a key role in detoxifying such reactive species (FOYER, DESCOURVIÈRES and KUNERT, 1994; Müller-Moulé, Havaux and Niyogi, 2003).

Among the numerous strategies that can be activated towards high light acclimation, light harvesting antenna size adjustment is one of the most important and characterized (Escoubas *et al.*, 1995). A. thaliana was observed to strongly downregulate antenna protein upon high light shifting, shaping a reduced antenna size. On the other hand, *C. reinhardtii* acclimation to high light responds by reducing chlorophyll content per cell reducing the

photosystems number, rather than downregulating antennae proteins as plants (Bonente *et al.*, 2012).

1.2 AEROBIC CELLULAR RESPIRATION

Photosynthetic organisms harbor in their cells both chloroplasts and mitochondria. The two processes of photosynthesis and mitochondrial respiration coexist and are in close communication between each other. While chloroplasts convert light energy into chemical energy (NADPH and ATP) by means of light energy through photosynthesis, mitochondria convert sugars into ATP while releasing CO_2 through respiration as in:

$$(CH_2O)_n + nO_2 \rightarrow nCO_2 + nH_2O + ATP$$

Cellular respiration can be divided into three stages: glycolysis, Krebs cycle, and electron transport chain. While glycolysis operates glucose oxidation into pyruvate, Krebs cycle completes pyruvate oxidation producing reducing power and CO_2. Products of these steps are used to fuel the electron transport chain that through oxidative phosphorylation produces ATP.

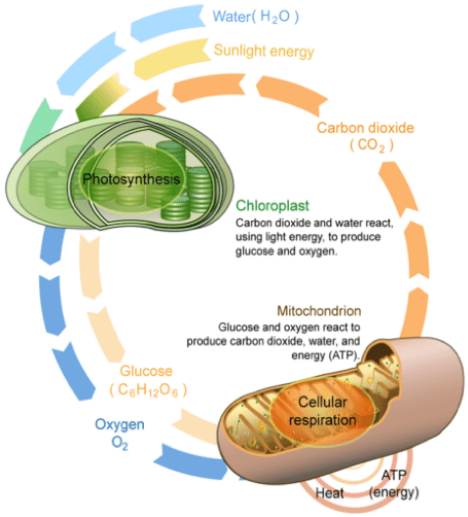

Figure 8 Representation of the relationship between chloroplast and mitochondrion

1.2.1 Mitochondrion

The mitochondrion is the organelle in which cellular respiration takes place. It features a double membrane: an outer one and an inner one. The latter is considerably folded on itself, forming layered structures called cristae. This very membrane hosts the multi-protein complex forming the respiratory chain. The innermost compartment of the mitochondrion is called matrix and harbors several soluble enzymes, mitochondrial DNA and ribosomes. On the other hand, the compartment between the two membranes, called intermembrane space, has a composition similar to the one of cytosol, since exchange across the outer membrane is facilitated by porins protein. In *C. reinhardtii* the majority of

the mitochondrial proteins are nucleus-encoded and imported into the organelle by the TIM-TOM translocation system (Yang *et al.*, 2015).

1.2.2 Mitochondrial electron transport chain (mETC)

Oxidative phosphorylation takes place in the mETC: reducing power from glycolysis and Krebs cycle is used to generate a proton gradient between the intermembrane space and the matrix, which is subsequently used to drive ATP synthesis. The mETC resides within the inner membrane of the mitochondrion and it is composed of five complexes: ATP synthase (complex V), NADH dehydrogenase (complex I), succinate dehydrogenase (complex II), cytochrome c reductase (complex III), and cytochrome c oxidase (complex IV). Electrons are transferred to a ubiquinone, a membrane-soluble electron carrier, from NADH or $FADH_2$ by complexes I and II. Complex III transfers electron from ubiquinol to cytochrome c. Complex IV transfer electrons from cytochrome c to molecular oxygen producing water. Complexes I, III, and IV couple electron transport to proton translocation from the mitochondrial matrix to the intermembrane space, generating the proton gradient needed by complex V (ATPase) to drive ADP phosphorylation (Boekema and Braun, 2007). A branching pathway is realized by the so-called alternative oxidase (AOX). AOX couples ubiquinol oxidation to O_2 reduction to water, drastically reducing the ATP output of the respiratory chain. Under certain physiological conditions, such as high light, the alternative pathway is thought to represent an overflow protection mechanism as described by (Vanlerberghe, 2013).

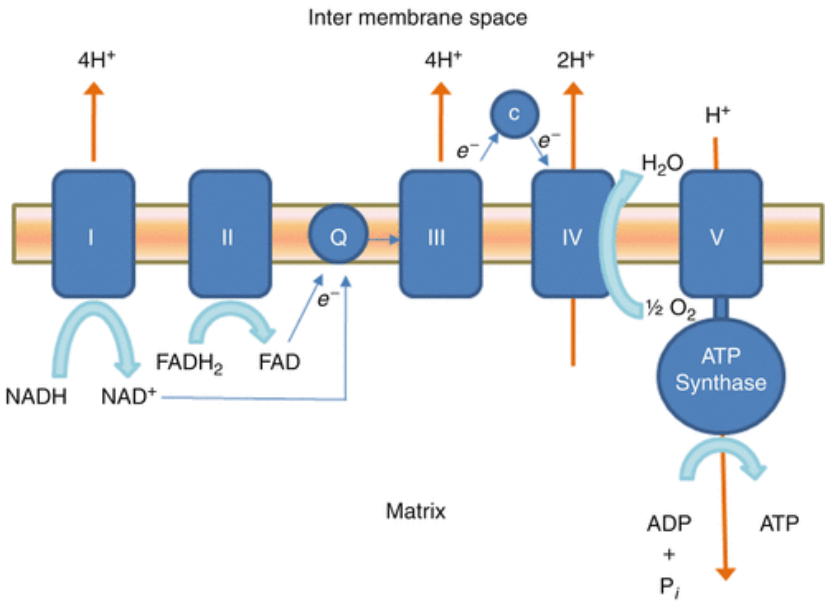

Figure 9 Schematic representation of the mETC

1.2.3 Carbon flux regulation into the cell

The global output of photosynthesis comprehends triose phosphates, reducing power and ATP, supporting all cell activities. Coordination, management e partition of these products is vital. Since membranes are not passively permeable by these molecules, complex trafficking mechanisms evolved to coordinate NAD(P)H and ATP repartition between subcellular compartments (Burlacot, Peltier and Li-Beisson, 2019). Chloroplast and mitochondrion share a metabolite pool that can act as sink for excess reducing equivalents or ATP to sustain carbon fixation or to chloroplast electron transport (Erickson, Wakao and Niyogi, 2015). It is also important to mention peroxisomes activity, since NADH can be produced by β-oxidation of fatty acids. *C. reinhardtii* evolved a series of shuttles system to maintain this vital balance between different subcellular compartments. Malate dehydrogenase, for example, catalyzes the reversible oxidation of NAD(P)H to $NAD(P)^+$ oxidizing malate to oxalacetate. Malate and oxalacetate are shuttled between compartments. Another molecular shuttle is realized by the oxidation of dihydroxyacetone 3-phosphate (DHAP) to 3-phosphoglycerate (3PGA) coupled with NAD(P)H generation, while being exported (Hoefnagel, Atkin and Wiskich, 1998).

1.3 MICROALGAE AS CELL BIO FACTORIES

The idea of exploiting microalgal biomass dates to the 50s, when it was considered as a potential candidate to combat food shortage all over the world. Combined with the necessity for an alternative fuel source studies followed in the 60s and the 70s culminating because of the oil crisis, giving the right incentive to start production (Oswald and Golueke, 1960). However, since then, profitability of such oil alternative has never been reached. Nevertheless, microalgae showcase several features that will be presented in the following paragraphs, such to pose a possible solution for many challenges that our kind is facing and will have to address soon.

Microalgae are eukaryotic single-celled photosynthetic organisms able to grow in almost every aquatic habitat, being widely tolerant towards temperature, salinity, pH and light intensities. Their minimal nutritional requirements are limited to inorganic compounds, but they can also thrive on carbon sources, switching to a mixotrophic growth. Industrial waste gasses enriched in CO_2 (Lum, Kim and Lei, 2013), as well as wastewaters (Zuliani *et al.*, 2016), can be used as growth supplements for algal growth while being treated to be released afterwards, also providing the benefit of bioremediation. Counterintuitively, microalgal cultivation requires less water than the average crop since it can also be recycled. Microalgae present a rapid life cycle and their biomass, oppositely to land plants, is totally productive from a photosynthetic point of view. Light and nutrients are converted into biomass, which can be rich in protein and/or lipids, on a specie-basis. One more microalgal pro fact represents the real game-changer: microalgal cultivation does not compete for arable land, posing an end in the case of biofuel production to the feed vs. fuel struggle. Microalgae can in fact be cultured in open ponds or photobioreactor, which installation can be limited to marginal rural areas or even integrated in city buildings or roads. The potential of their application extends far from the sole fuel production, in fact, given the availability of modern genetic tools and techniques, microalgae can be turned into cell factories to produce superfoods, dietary supplements, pharmaceuticals, feed, fertilizers, and raw materials (e.g., polymers).

1.3.1 Food and feed

Microalgae such as A. platensis (commercially known as Spirulina) or C. vulgaris have been historically used as food ingredients while nowadays are commercialized as supplements, given the complete nutritional composition of their biomass: proteins, vitamins, polyunsaturated fatty acids (PUFA) and antioxidant compounds (Li *et al.*, 2015; Al-Dhabi and Valan Arasu, 2016; Wu *et al.*, 2016; García, de Vicente and Galán, 2017; Lupatini *et al.*, 2017; Hynstova *et al.*, 2018). Research evidenced so far that microalgae-derived feed could successfully replace feed in aquaculture and improve growth and meat quality in various land animal. Moreover, in ruminants, dietary inclusion of marine microalgae has improved the milk and meat fatty acid profile. Such feeds have several bioactive compounds that have been shown to enhance defense activity and health status in several animal species while conferring tissue protection and antioxidant effects, also affecting pigmentation in fish for example (Valente *et al.*, 2021).

1.3.2 Pharmaceuticals

Pigments like carotenoids represent the commercial microalgae product with the highest market being used as coloring agent or components for cosmetics (Vílchez *et al.*, 2011). Given the antioxidant ability of these molecules and the power to detoxify from free radical species, the biomedical interest towards microalgal products have significantly increased lately (Young and Lowe, 2018). β-carotene, astaxanthin, lutein, zeaxanthin and canthaxanthin are the main carotenoids commercialized for such application produced by microalgae. Prevention of toxin build-up in the liver, maintenance of the well-being of the eye macula (Dufossé *et al.*, 2005; Manayi *et al.*, 2016), treatment of blood disorders (Zhang *et al.*, 2014), prevention of diabetes, treatment of neurological disorders, and cancer prevention (Naguib, 2000) are some of the benefits that these molecules can provide to the human organism among all.

Fatty acids deriving from algal biomass occupy a relevant market share of diet supplements as well. PUFAs are important elements for human nutrition starting from the fetal stage. In fact, a balanced maternal nutrition is known to positively modulate the neonatal incidence of obesity and obesity-induced metabolic syndrome later in life. Also, fatty acids can control health and adipose tissue development in early post-natal years, as

well as improving health outcomes and decrease obesity risk in adults (Akerele and Cheema, 2016; Huang *et al.*, 2016).

Eukaryotic microalgae are also capable of performing complex post-translational modifications and folding intricate proteins. These features enable them, for example, to be used as cell factories to produce low costs human antibodies for therapeutic purposes, representing an attractive alternative to traditional mammalian-based expression system which are difficult to transform and maintain (Mayfield and Franklin, 2005).

1.3.3 Biofuel

Third generation biofuels are considered promising over previous biofuel generations since algal culture does not compete for arable land (Shuba and Kifle, 2018). The carbohydrate rich microalgal biomass can be fermented into bioethanol or biogas while the oil fraction can be used to produce biodiesel through trans-esterification of TAGs (Montingelli, Tedesco and Olabi, 2015; Venkata Mohan *et al.*, 2015; Shokrkar, Ebrahimi and Zamani, 2017). As aforementioned, profitability of such fuels remains unmet compared to the current carbon fossil market (Benvenuti *et al.*, 2017). Another promising fuel alternative that microalgae could enable is biohydrogen, although current production capability is extremely low and its usage is considered expensive, given the high technological and engineering associated costs (Dubini and Ghirardi, 2015).

1.3.4 Genetic engineering of microalgae

Similarly to what happened to land crops over the past 50 years, microalgal strain must undergo a process of domestication (Khush, 2001). Unlike half a century ago, modern DNA technologies and genetic engineering tools enable us to achieve chosen results in less time, since the scientific effort can be precisely directed towards desirable traits without the compromises that traditional breeding technologies impose. Moreover, microalgae have a short life cycle and do not present cell differentiation. Together with the fact that some of them are haploid, manipulation in general and phenotypic selection are way faster compared to higher plants. Genetic manipulation of algal genome can lead to the generation of required traits by up- or down-regulation of specific genes as well as inserting new exogenous genes carrying qualities from different species. Several algal species are now being domesticated through consolidated transformation methods or via

CRISPR technologies resulting in an increased biomass or bioproducts accumulation. Among the strategies to achieve such objective is the optimization of light penetration into high density cultures via selection of mutants containing less chlorophyll per cell (Beckmann *et al.*, 2009; Bonente, Formighieri, *et al.*, 2011; Perin *et al.*, 2015). Photoprotection mechanisms activation was recently shown to be an interesting target for genetic manipulation in plants, considering that a faster recovery from a dissipative behavior could prevent up to a 70% loss of productivity (Kromdijk *et al.*, 2016). In cyanobacteria, a mutant lacking the OCP protein, responsible for triggering quenching, was shown to be 30% more productive in lab-controlled conditions (Peers, 2011). Loera-Quezada et al. transferred to microalgae the gene PTXD from *P. stutzeri* that confers the ability to use phosphite as phosphorous source. This give algae a growth advantage over undesirable microorganisms which cannot use phosphite when cultivation is carried on in open ponds (Loera-Quezada *et al.*, 2016).

2 PHYSIOLOGICAL EFFECTS OF A HIGH-CO_2 AERATION REGIME ON *CHLAMYDOMONAS REINHARDTII*

2.1 INTRODUCTION

Atmospheric levels of carbon dioxide, one of the major green-house gases responsible for global warming, have significantly and uncontrollably increased since pre-industrial revolution to 409.8 +- 0.1 ppm in 2019, with an annual rate of increase about 100 times faster than previous natural increases, i.e., the end of the last ice age between 11,000 and 17,000 years ago. If no countermeasures are put into place, its atmospheric concentration is projected to exceed 900 ppm by the end of the century (Lindsey, 2020). One possibility to overcome this urgent situation and to slow the inevitable consequences on planet's climate, is to exploit microalgae as agents of sequestration. In fact, microalgae contribute for half of total photosynthetic activity and carbon fixation worldwide, representing fundamental players in the carbon flux happening in the biosphere (Field *et al.*, 1998; Salomé and Merchant, 2019). Microalgae possess high photosynthetic efficiency, 10 to 50 times greater than land plants. Also, it is reported that to produce 1 kg of algae biomass 1.8 kg of CO_2 are being fixed (Chisti, 2007; Khan *et al.*, 2009; Rosenberg *et al.*, 2011; Brown and Blackburn, 2014). Moreover, algal biomass can be exploited for several applications ranging from food and feed, supplements, high-value pharmaceuticals, to biofuels. On top of this, during their growth, microalgae can make use of wastewaters as well as CO_2-enriched industrial flue gasses (Lum, Kim and Lei, 2013), making them the ideal industrial actors for carbon assimilation and transformation.

Microalgae are oxygenic photosynthetic microorganisms able to harvest light by means of their pigment-binding protein complexes composed of Photosystem I (PSI), Photosystem II (PSII), and the light-harvesting antenna system. PSI and PSII work in series with other several partners in the chloroplast's thylakoid membrane to generate an electron flow from water to $NADP^+$ producing NADPH and oxygen. The electron transport is coupled with proton pumping in the luminal space, which in turn establishes an electrochemical gradient exploited by ATPase to synthetize ATP. ATP and NADPH are used by the Calvin-Benson cycle to fix CO_2 into triose phosphates sugars. Parallelly, respiratory

processes occur in the mitochondria by dedicated electron transport chains, transferring electrons from reduced cofactors as NADH and FADH2 to oxygen. This electron transport is coupled with proton transport from the matrix to the endomembrane space, by which a proton electrochemical gradient is formed and used by ATP synthase to produce ATP. Alternatively, reduced cofactors can be oxidized by a mitochondrial alternative oxidase (AOX) by which the reducing potential is dissipated as heat without leading to ATP production. A refined crosstalk between organelles ensures energy balance and thriving of the organisms in an everchanging environment.

CO_2 levels and its relative sensing are of great importance for organisms thriving on carbon fixation, therefore their metabolic activity as their photosynthetic efficiency must respond accordingly to CO_2 availability. To do so, different adaption pathways and mechanisms were evolved to guarantee their survival. Of primary importance is the activity of the RNA-binding protein NAB1, triggered by the transcription factor LCRF (Low Carbon dioxide Response Factor), that consist in repressing the translation of transcripts encoding light-harvesting antenna proteins (Mussgnug *et al.*, 2005; Berger *et al.*, 2014; Blifernez-Klassen *et al.*, 2021). In fact, Calvin-Benson cycle limitation caused by low CO_2 levels is known to lead to oxidative stress: in the occurrence of a reduced consumption of ATP and NADPH by the light-independent reactions, the photosynthetic transport chain results over-reduced (Wang, Stessman and Spalding, 2015). The truncation of the PSII antenna by the NAB1 cascade, reduces the excitation pressure on the photosynthetic apparatus as a response to diminished CO_2 availability (Berger *et al.*, 2014). The use of excitation energy absorbed by photosystems is thus strongly influenced by the availability of CO_2 as it represents the final electron acceptor of reducing power formed by the light phase of photosynthesis. NPQ and state transitions are among the major mechanisms evolved to regulate the distribution of excitation energy in photosynthetic organisms. NPQ is the mechanism by which excess energy absorbed is dissipated as heat. It is triggered in microalgae by the activity of LHCSR3 and 1 (Peers *et al.*, 2009; Dinc *et al.*, 2016). LHCSR3 is the most studied among the two as it is the main actor of quenching and it is readily expressed upon high-light exposure (Allorent *et al.*, 2013). LHCSR1 accumulation, beyond responding to high-light, is also triggered by CO_2 availability, being increased in high concentrations of it (Maruyama, Tokutsu and Minagawa, 2014; Polukhina *et al.*, 2016).

State transitions, on the other hand, are a mechanism triggered by changes in the redox state of electron transporters between PSII and PSI when illumination conditions determine excessive or low excitation of either one of the photosystems. Light-harvesting antenna are transitioned from a photosystem to the other to facilitate optimization of the energy distribution (Lemeille *et al.*, 2009). Another response to limited CO_2 availability is the expression of a carbon-concentrating mechanism (CCM). It is noteworthy that CO_2 diffusion coefficient in water is strongly reduced compared to the one in air. Because of these reasons, several microalgal species evolved a CCM by which inorganic carbon is actively transported in close proximity to its fixation site, the RuBisCO enzyme (Wang, Stessman and Spalding, 2015). In this chapter we studied how an increased CO_2 level influences growth and light utilization in *Chlamydomonas reinhardtii*, the green algae model organism, to gain a better insight on the possibility to exploit microalgal activity in the matter of carbon sequestration.

2.2 RESULTS

C. reinhardtii productivity was assessed by following its growth in lab-scale (80 ml) airlift photobioreactors at different light intensities (100, 200, 500 and 1000 μmol photons m^{-2} s^{-1} (μE)). Photobioreactors were insufflated with air with an atmospheric level of CO_2 (~0.04% CO_2, defined as AIR) or enriched with 3% CO_2 (defined as CO_2). Growth kinetics were followed measuring cell scattering at 720 nm. Growth curves were fitted with sigmoidal functions (showed in Figure 1A, B, C, and D). CO_2 condition presents a faster growth rate compared to the AIR condition, as showed by the first derivative of the growth curves (Figures 1E, F) and by the calculated average daily productivity (Figure 1H). Biomass accumulation was in general higher in CO_2 compared to AIR. In AIR condition, the biomass productivity, in terms of dry weight, ranges from ~0,4 to ~0,5 g/l with similar values at light intensities above 200 μE. Differently, in the CO_2 condition biomass productivity ranged from ~0,4 to ~0,9 g/l with an increasing biomass accumulation at higher irradiances (Figure 1G), hinting that CO_2 may represent a limiting factor in AIR.

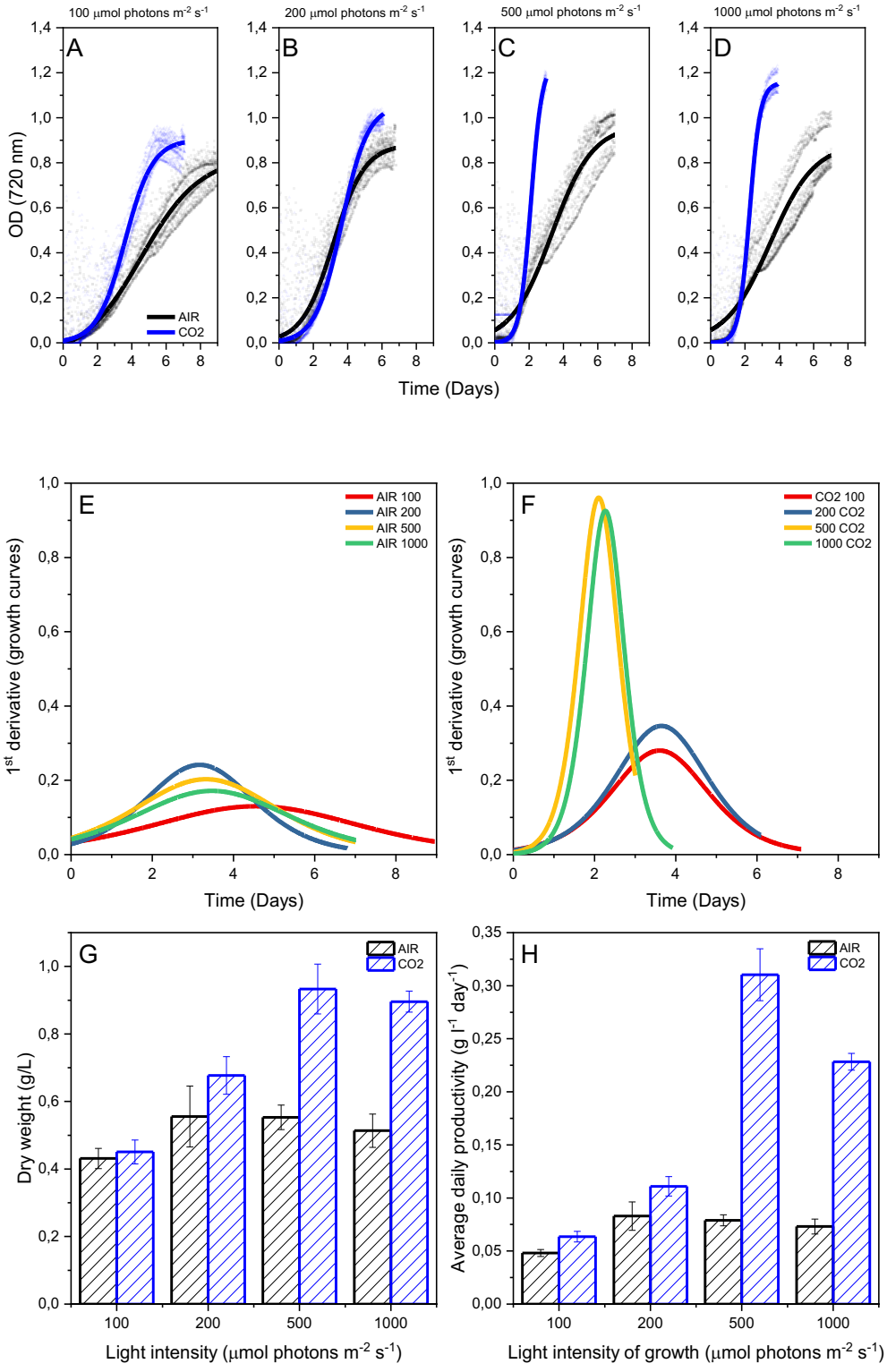

Figure 1. Growth curve and biomass productivity in AIR vs. CO2*. Growth curve are reported in panel A-D in AIR condition (~0.04% CO2) compared to CO2 condition (3% CO2) at increasing light conditions. Growth curve were obtained measuring OD at 720nm fitted with sigmoidal function. (E, F): first derivate of growth curves reported in panels A-D. (G) Dry weight (g/L), (H) average and maximum daily productivity (g L-1 day-1) obtained harvesting the biomass at the end of the growth curve.*

2.2.1 LHCSRs response to high-CO_2 content

We assessed the qE levels at the end of the growth phase (Figure 2B). In the AIR condition, qE was increased at higher irradiances of growth, while in a CO_2-enriched regime the NPQ amplitude (Figure 2A) is reduced compared to AIR conditions, with a strong reduction of its qE component. qE in *C. reinhardtii* has been previously reported to be strongly related to LHCSR accumulation (Peers *et al.*, 2009). As evidenced by the blot analysis, accumulation of LHCSR1 in CO_2 is increased (Figure 2C), while LHCSR3 is decreased (Figure 2B), as previously reported (Yamano, Miura and Fukuzawa, 2008; Maruyama, Tokutsu and Minagawa, 2014; Polukhina *et al.*, 2016). Different levels of NPQ in AIR vs. CO_2 conditions determines a different fraction of excitation energy absorbed by PSII available to fuel the thylakoidal electron transport chain.

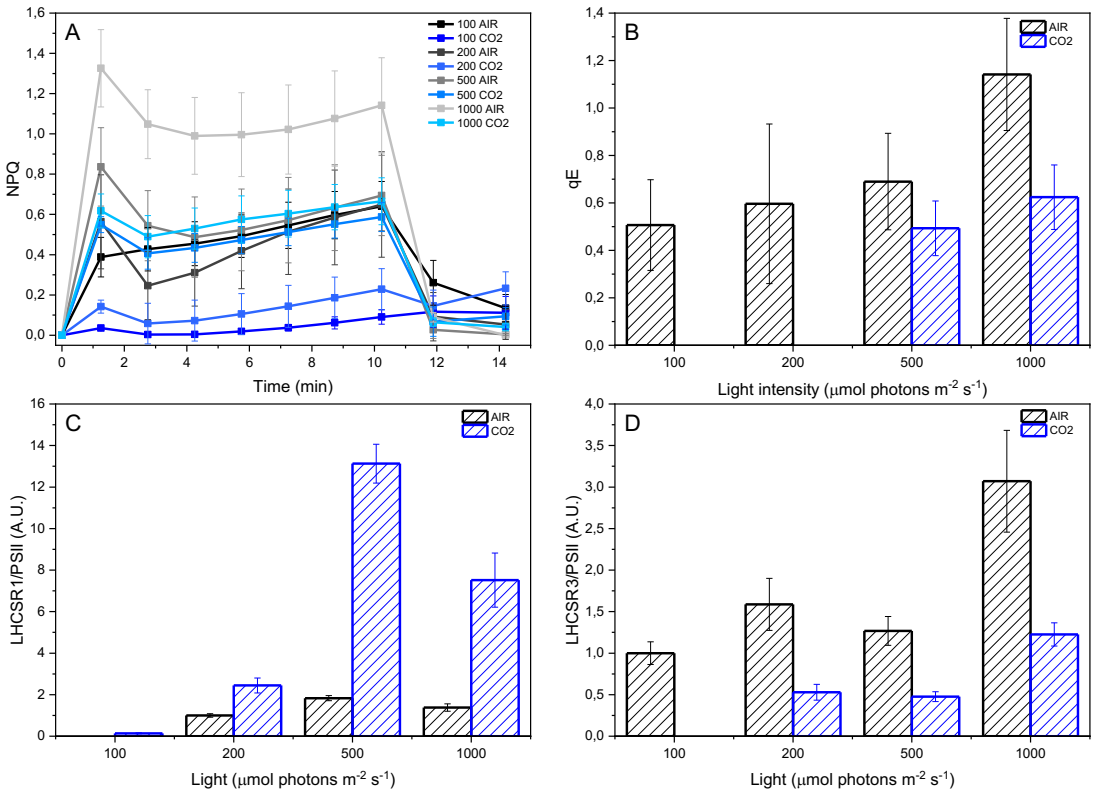

Figure 2. NPQ and qE measurements and relative LHCSR3/1 protein content. *(A) NPQ traces measured upon 1500 µmol photons m^{-2} s^{-1} illumination of samples grown at various light intensities expressed in µmol photons m^{-2} s^{-1} indicated as 100, 200, 500, and 1000 AIR (greyscale) vs. CO2 (blue gradation). (B) qE values calculated as in NPQ (last measured point in light) – NPQ (last measured point during recovery). (C and D) LHCSR1-3/PSII (CP43) protein content normalized at 200 µmol photons m^{-2} s^{-1} AIR (LHCSR1) or normalized at 100 µmol photons m^{-2} s^{-1} AIR (LHCSR3)*

2.2.2 PSI activity and PSI/PSII ratio are influenced by CO_2 concentration

PSI photochemical activity was measured by transient absorption of the oxidized PSI reaction center at 830 nm upon exposure to an actinic light. In the presence of DCMU, which inhibits electron transport from PSII to PSI, ascorbate (AS) as electron donor, and methyl viologen (MV) as electron acceptor, we can determine the maximum P700 activity when whole cells are submitted to a saturating light pulse (Bonente *et al.*, 2012). Figure 3.2 depicts two examples of P700 oxidation kinetics (on a *Chl* basis) of dark-adapted whole cells of *C. reinhardtii* grown at 500 μE in the two studied aeration regimes. In general (Figure 3A), Maximal P700 oxidation on a *Chl* basis was similar in the two conditions at the different light irradiances except for cells grown at 500 μE, where we registered a significative increase in the P700 maximal activity in CO_2, compared to the control condition (Figure 3A and 3.2). These results are consistent with the results obtained by western blot analysis on subunits of PSI (PsaA) and PSII (CP43) core subunits. The PSI/PSII (PsaA/CP43) ratios determined by western blot demonstrate an increased PSI/PSII ratio in CO_2 compared to AIR condition (Figure 3B).

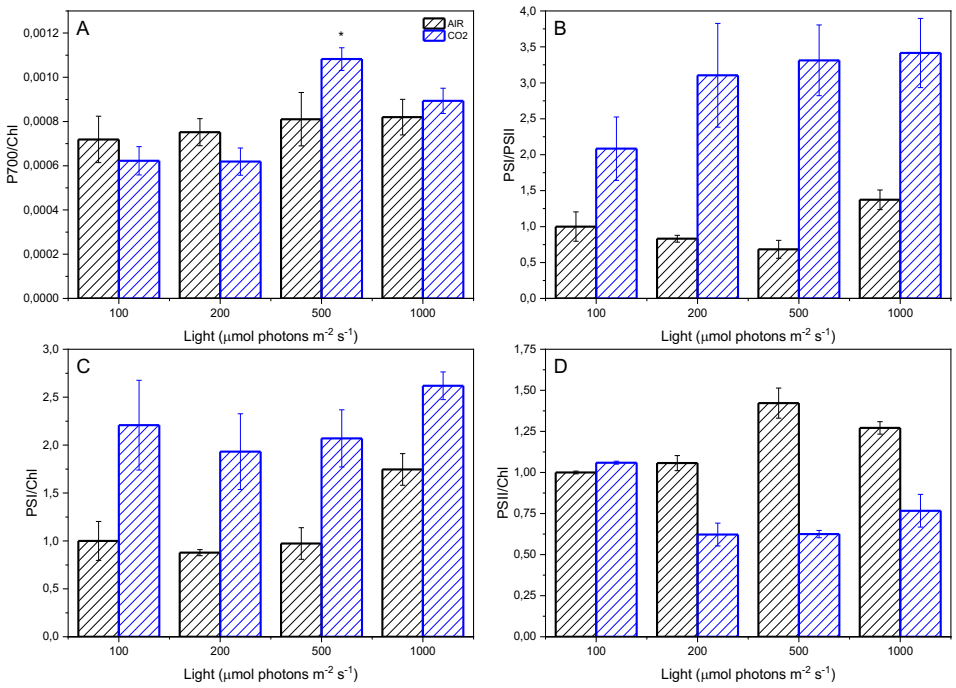

Figure 3. Analysis of PSI and PSII content by immunoblots, P700 activity. *(A) Maximal P700 oxidation on a chlorophyll basis (B, C and D) Immunoblot analysis of PSI (α-PsaA antibody), PSII (α-CP43 antibody). Loading was performed on a chlorophyll basis. Ratios calculated by densitometry of immunoblot signals.*

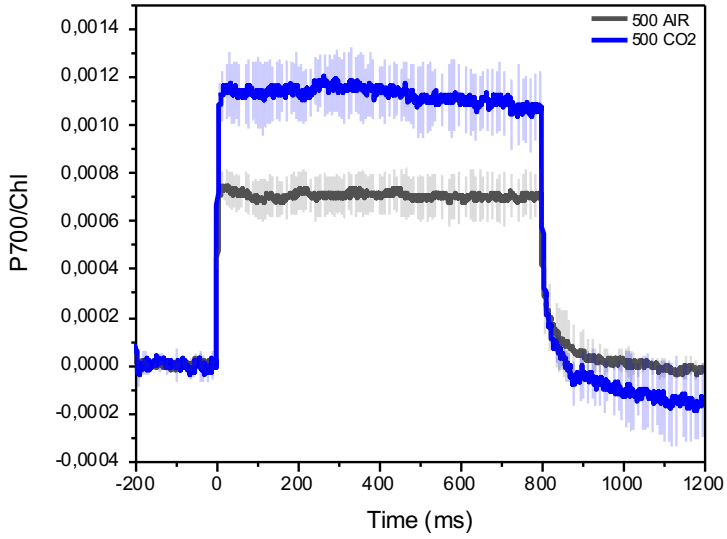

Figure 3.2 P700 oxidation kinetic. *Detail of P700 oxidation kinetic upon actinic light illumination (from 0 to 800 ms) of dark-adapted C. reinhardtii whole cell grown at 500 µE.*

2.2.3 PSII-related oxygen evolution and antenna size are increased by high CO_2

We focused onto analyzing the 500 μE grown cultures' photosynthetic behavior. We do not report significant changes in the PSII maximum quantum yield (data not shown), being comprise between 0,6 and 0,7 in both conditions demonstrating a similar PSII quantum yield in AIR and CO_2 conditions. We also assessed the light-dependent oxygen evolution and we do not report significative differences between the two tested conditions in terms of net oxygen evolution on a *Chl* basis (Figure 4). These results suggest that photochemical activity of samples in AIR or CO_2 conditions is similar, with increased biomass accumulation observed in CO_2 conditions related to increased carbon availability rather than different light phase induction.

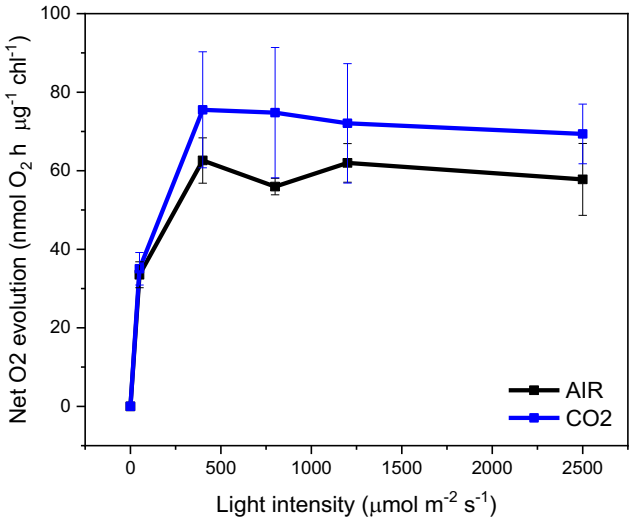

Figure 4. Light-dependent O_2 evolution. *Oxygen evolution rates in response to different light intensities were measured to determine the rate of oxygen consumption in the dark. Cells were grown in photoautotrophic conditions for this measurement. The net oxygen evolution rates were measured on samples at the same Chl content.*

Chlorophyll content is reduced in the CO_2 condition (Figure 5A), while the *Chl* a/b ratio resulted significantly increased (Figure 5B). Considering that *Chl* b is bound exclusively to LHCs while *Chl* a is bound to both LHCs and core complexes, different *Chl* a/b suggests possible reorganization of antennae and core complexes relative stoichiometries.

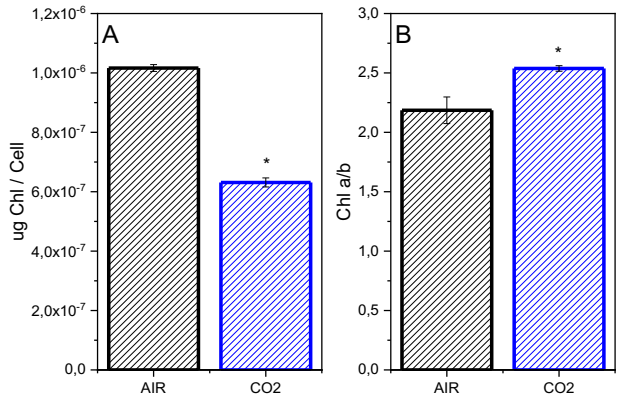

Figure 5. Chl content analysis. *(A) Chl/Cell content and (B) Chl a/b ratio.*

To investigate this, we assessed the functional antenna size on dark-adapted cells incubated with 50 μM DCMU as described by (Malkin *et al.*, 1981). Fast fluorescence *Chl* induction kinetics were obtained with a red light of 11 μmol photons m^{-2} s^{-1} using a Dual-PAM 100 instrument (WALZ). PSII antennae size was calculated as the reciprocal of time corresponding to two-thirds of the fluorescence rise ($\tau_{2/3}$) (Malkin *et al.*, 1981). We determined that high CO_2 levels affected this parameter by increasing it by ~60%, compared to the control condition (Figure 6A and B). Such outcome is reportedly being ascribed to the effects of NAB1 protein, accumulated in CO_2-limiting conditions in *C. reinhardtii* (Berger *et al.*, 2014). NAB1 acts as regulatory hub, controlling PSII excitation pressure in function of the carbon availability by repressing the translation of specific transcripts, LHC subunits included. In agreement with this observation, a decreased LHCII/PSII ratio was measured in the AIR condition (Figure 6C).

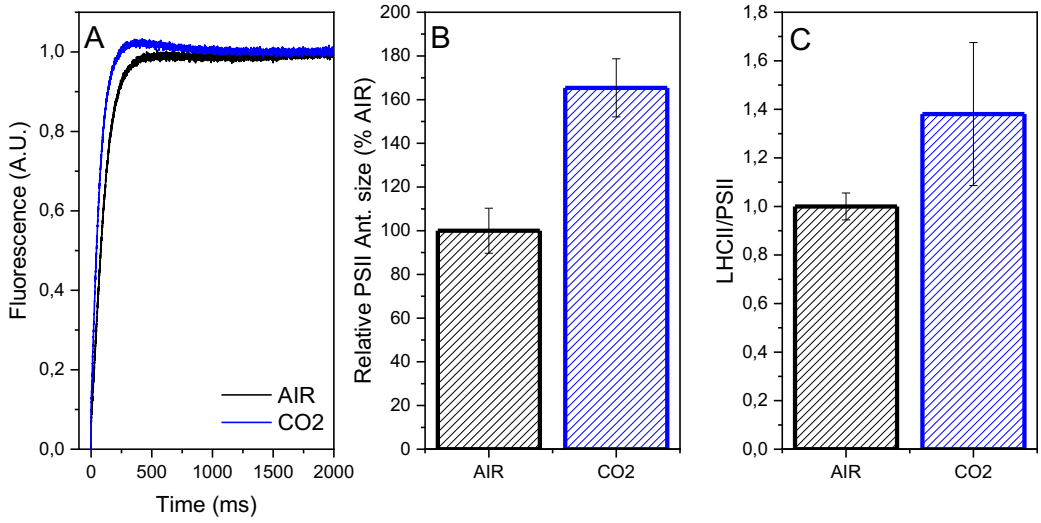

Figure 6. (A) Functional antenna size of the photosystem II. (B) Functional antenna size expressed as $1/\tau_{2/3}$ relative to WT. (C) Immunoblot analysis of LHCII (α-LHCII antibody). Loading was performed on a chlorophyll basis.

2.2.4 Increased requirement for excitation pressure on PSII in CO_2

We then verified the capability of cells grown in CO_2 or AIR conditions to perform state transitions. LHCs are partly bound to PSI or PSII and to ensure the excitation balance of the two photosystems, LHC complexes are subjected to a process defined to as state transitions. In *C. reinhardtii* phosphorylation of the LHC complexes by means of STT7 kinase induces LHC to move from PSII to PSI in the so-called state 2 (S2). State 1 (S1), in which LHCs move from PSII to PSI, is achieved by means of a phosphatase (Depège, Bellafiore and Rochaix, 2003; Lemeille *et al.*, 2009). S1 and S2 can be induced and measured exploiting *Chl* fluorescence emission at 77K, a situation in which both PSI and PSII fluorescence contribution are detectable. Maximum capacities for state transitions were then quantified from the maximum fluorescence emission at 720 nm as $(F_{S2}-F_{S1})/F_{S2}$. As shown in Figure 7, a high CO_2 regime decreased the capacity of *C. reinhardtii* to realize state transitions. In fact, as shown in Figure 7A, induced S2 in CO_2 has a decreased PSI contribution compared to S2 of AIR, suggesting that a smaller fraction of LHCs moiety being available to migrate from PSII to PSI. This could be related to a general increased requirement of excitation pressure on PSII to maintain a steady flow of electrons given the increased need for the photosynthetic machinery of electrons to operate CO_2 fixation. This observation agrees with an increased PSII antenna size (Figure 6A) and a slightly increased O_2 evolution (Figure 4) in this aeration regime.

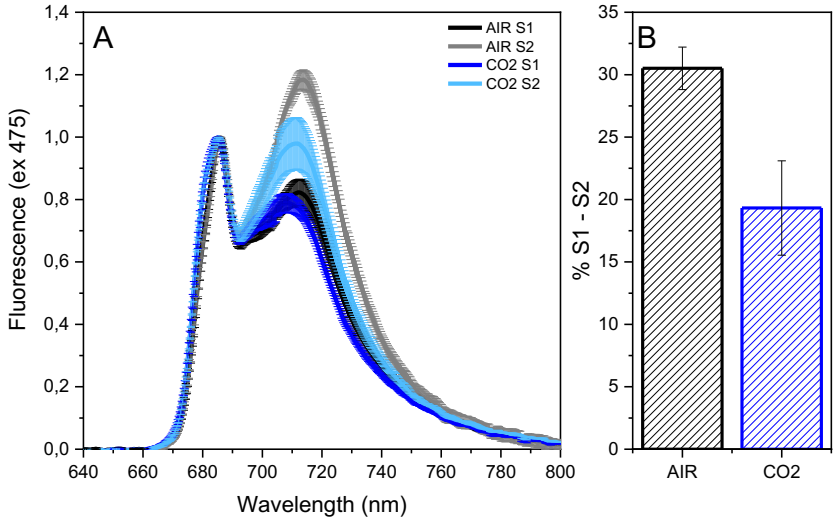

Figure 8. State transitions in AIR vs. CO2. *(A) State transition analysis by 77K fluorescence emission spectra in state 1 (S1) or state 2 (S2) conditions. S1 was induced by shaking vigorously cells in a low light (~5µmol m2 s-1) with 10µm of DCMU for at least 15 min to oxidize the plastoquinone pool while S2 was induced by adding 250 µm sodium azide to inhibit mitochondrial respiration and to reduce the plastoquinone pool as described in Fleischmann et al. 1999 (B) Maximum capacities for state transitions were then quantified from the maximum fluorescence emission at 720 nm as (FS2-FS1)/FS2.*

Electrochromic shift of carotenoid absorption was measured to estimate the proton-motive force (pmf) generated by the photosynthetic electron transport. Pmf of samples grown either in AIR or CO_2 conditions was measured upon exposition to different increasing light intensities. The behavior in the two aeration regimes was similar (Figure 9A and B). When DCMU is supplied to the sample, linear electron flow is hampered, enabling us to investigate the cyclic electron flow while measuring ECS of carotenoid absorption. No differences were evidenced among the two conditions (Figure 9B). We then measured by immunoblotting the ATPase content per cell which was significantly increased in the samples grown in CO_2 condition (Figure 9C).

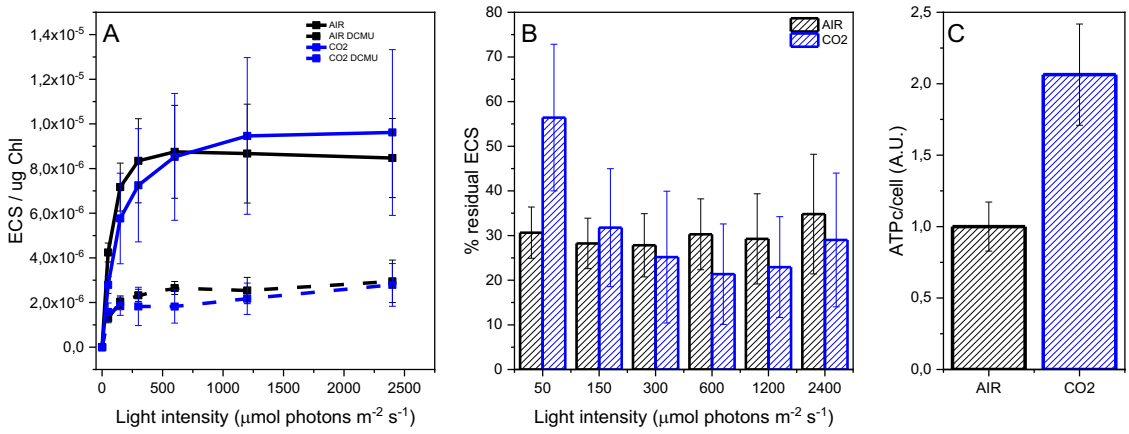

Figure 9. ATPase content and electrochromic shift in AIR vs. CO2*. (A) ECS measurements. ECS results in presence of DCMU are reported with dashed lines or in graph (B). (C) Immunoblot analysis of ATPase content (atpC subunit antibodies).*

We verified accumulation of some of the components relative to the carbon concentrating mechanism (CCM), a complex set of regulatory elements and enzymes involved in actively concentrating inorganic forms of carbon inside of the cell, precisely close to the site of fixation, the RuBisCO enzyme (Wang, Stessman and Spalding, 2015). It is important to note that assimilation of inorganic carbon is a crucial and limiting step for photosynthetic organisms. Moreover, CO_2 diffusion in watery environments is strongly reduced compared to CO_2 diffusion in the atmosphere. We observed that on a cell basis, in CO_2-limiting conditions the RuBisCO content was increased, similarly to carbonic anhydrase, which resulted upregulated in the same condition (Figure 10), as described in (Fang *et al.*, 2012).

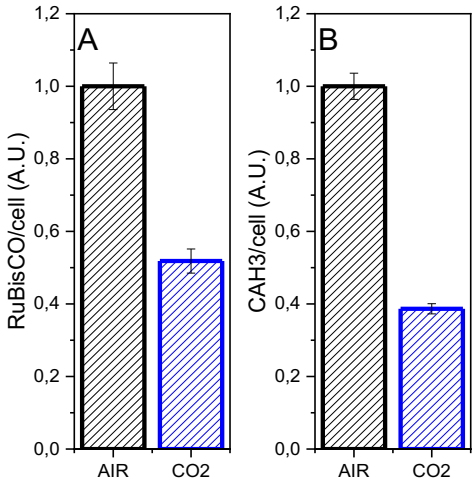

Figure 10. RuBisCO and Carbonic anhydrase (CAH3) content*. Immunoblot analysis of RuBisCO (A) and carbonic anhydrase 3 (CAH3) (B) in AIR vs. CO_2.*

2.2.5 Response to CO_2 availability of the mitochondrial respiratory pathways

We then investigated NAD(P)H formation and the respiratory metabolism. Specifically, light-dependent NADPH formation was evaluated by following NAD(P)H fluorescence changes upon exposure to a 500 μE light for 120 seconds (Figure 11A). In the AIR condition the NAD(P)H rate of accumulation is positive, meaning that NAD(P)H production exceeds the consumption rate. On the other hand, in the CO_2 condition, the formation's slope is almost zero, which means that the rate of NAD(P)H accumulation equals the consumption one (Figure 11B). These results are consistent with the increased requirement

of NADPH in the case of cells grown in CO_2 condition to provide reducing power required for CO_2 assimilation. Because fluorescence-based evaluation of NAD(P)H production cannot distinguish between NADH and NADPH, we measured NADH consummation by mitochondrial respiration in the dark by using a Clark-type electrode. Mitochondrial respiration produces ATP while releasing NAD+ via the respiratory electron transport which includes an ATP synthase complex and four oxidoreductase complexes. The electron transport produces an electrochemical gradient across the mitochondrial membranes which drives oxidative phosphorylation. An alternative oxidase (AOX) operates ubiquinol oxidation coupled to O_2 reduction to H_2O, generating an alternative branch for the electron flow of the mitochondrial transport chain. AOX action determines a dramatic decrease in ATP yields per NADH, acting as an overflow protection mechanism of the respiratory chain (Boekema and Braun, 2007; Vanlerberghe, 2013). Dark respiration rates were essentially unaffected by different CO_2 availabilities (Figure 10). Individual contribution of the cytochrome and alternative pathways were explored by measuring dark respiration upon inhibition of AOX with SHAM (salicylhydroxamic acid) or complex III with myxothiazol, blocking respectively the alternative and the cytochrome pathway. The relative contribution of cytochrome and alternate pathways to the total respiration rate were indeed different in the two growth conditions, being the cytochrome pathway disadvantaged in favor of the alternative one in CO_2 conditions (Figure 11C).

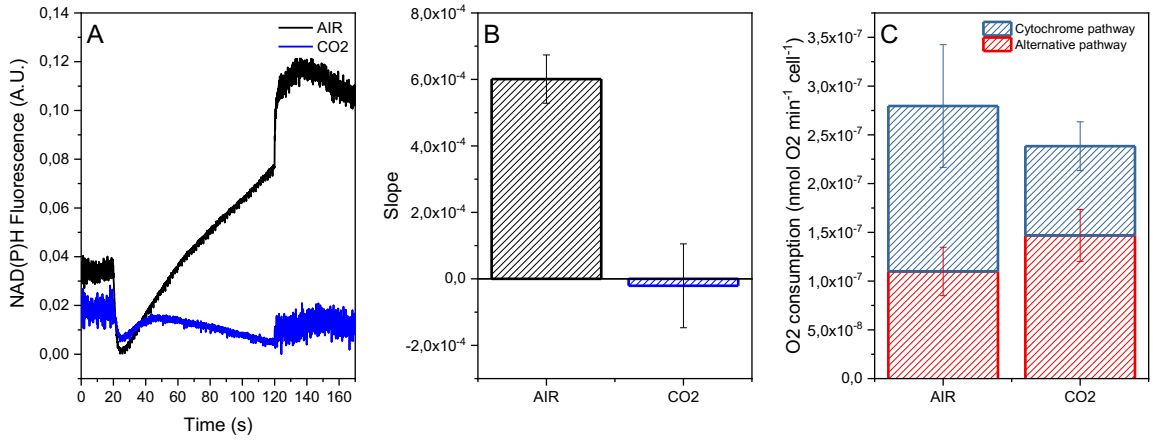

Figure 11. NAD(P)H formation rate and dark respiration in AIR vs. CO2*. (A) Light dependent rate of NAD(P)H formation upon exposure to light (300 µmol photons m−2 s−1) for 120s. (B) Data were calculated from the slope of the NAD(P)H fluorescence emission curve upon exposure to actinic light. (C) The relative contribution of cytochrome and alternative respiration was reported normalized to cell content.*

At the end of the growth experiment, the 500 μE test condition was selected for a biomass composition analysis (Figure 12). Specifically, the fractions of starch and protein on dry weight were lowered in a CO_2-enriched regime compared to AIR (Figure 12A and B). In the case of lipids, fatty acids compositional levels showed that triacylglycerol (TAG) levels were more than doubled at high CO_2 at the expense of galactolipids (Figure 12C), the major constituents of the thylakoid membranes, while phospholipids remained unchanged. In fact, the polar lipids' compositional analysis evidenced a decreased amount of MGDG galactolipids fraction in the CO_2 condition, while no substantial alteration of the overall fatty acid composition was evidenced, compared to the control condition (Figure 12C and D). The TAGs surplus registered in CO_2 may derive both from de novo lipid biosynthesis and recycling of pre-existent membrane lipids (Simionato *et al.*, 2013), which in our case could probably originate from the thylakoids' MGDG galactolipids followed by a photosynthetic re-arrangement.

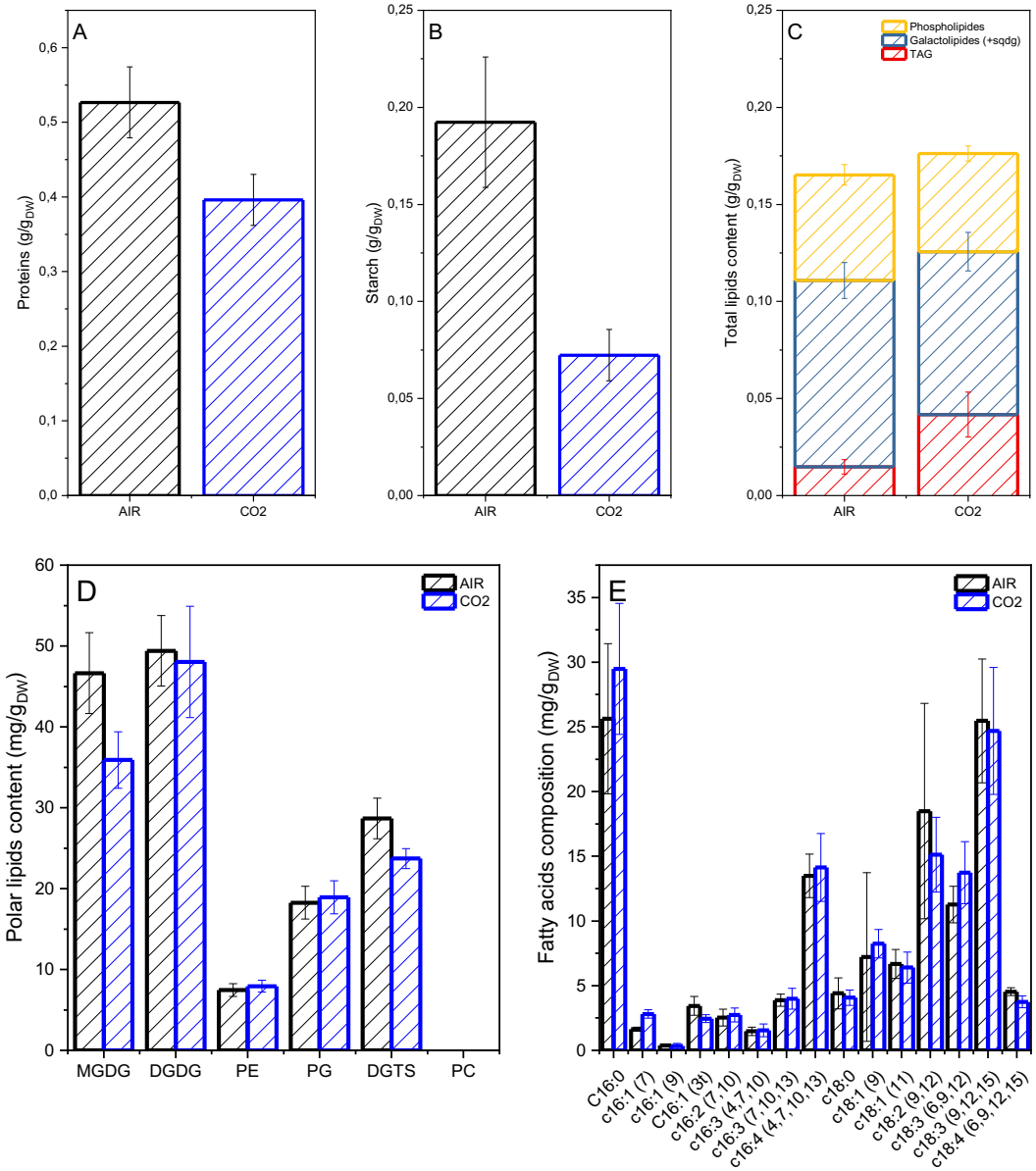

Figure 12. Biomass composition. *Protein (A), starch (B) and lipids (C) content in AIR vs. CO_2. (D) Polar lipid profile obtained by thin layer chromatography. (E) Fatty acids profile obtained by gas chromatography.*

2.3 DISCUSSION

The continuous rise of the atmospheric CO_2 level is leading to a severe environmental crisis caused by global warming. Microalgal-based CO_2 sequestration is considered a promising platform to sequester carbon back into the biosphere with the aim of reducing greenhouse effects. Microalgal potential to use CO_2-rich industrial flue gasses as carbon source is reviewed in (Cheah *et al.*, 2015). Understanding the process that leads to high CO_2 growth regimes acclimation is crucial to develop new strategies to expand and consolidate the microalgal-based CO_2 sequestration platform. In this study we analyzed the model green alga *C. reinhardtii* adaptation process to high CO_2 regime (3% CO_2). *C. reinhardtii* was grown in lab scale photobioreactors under atmospheric CO_2 level (0.04% CO_2, defined as AIR) or 3% CO_2 (CO_2). The metabolic adaptation in terms of photosynthetic and respiratory processes was investigated and herein discussed.

2.3.1 CO_2 availability and photoprotection limit biomass accumulation

C. reinhardtii biomass accumulation increased when cultured in a high-CO_2 regime, specifically we registered an increase in the harvested dry weight of ~68% at 500 μE and ~50% at 1000 μE. Moreover, such yields were obtained in almost half of the growth time, compared to the AIR condition, as indicated by the distinctly higher average daily productivity values registered in these conditions. Specifically, ~0.075 vs. ~0.3 g l^{-1} day^{-1} at 500 μE for AIR and CO_2 respectively (Figure 1H). Considering that the harvested dry biomass in AIR plateaued at 200 μE, while in a CO_2-enriched regime kept growing along with the light increase, we can confirm that CO_2 concentration is a limiting factor for algal biomass accumulation. It is also important to note that the decreased qE levels of the CO_2 condition, caused by the differential expression patterns of LHCSRs isoform in response to the CO_2 concentration (Merchant *et al.*, 2007; Maruyama, Tokutsu and Minagawa, 2014; Polukhina *et al.*, 2016), may play a role in the increased biomass yield registered. In fact, a smaller photoprotection amplitude or a faster recovery from it may result in an increased biomass accumulation as reported by (Kromdijk *et al.*, 2016). Specifically, culture's qE amplitudes when grown in high CO_2 and at 100 or 200 μE was null. At 500 μE, CO_2's qE level reached AIR's and plateaued, remaining practically unchanged at 1000 μE. In this latter light, AIR's qE level almost reached 1,1.

2.3.2 Increased carbon availability remodels the photosynthetic machinery

Among the physiological remodeling strategies we observed in the CO_2 condition, was the downregulation of RuBisCO and carbonic anhydrase accumulation. In fact, CO_2-limiting conditions are known to increase CCM components expression (Xiang, Zhang and Weeks, 2001; Yamano, Miura and Fukuzawa, 2008; Renberg *et al.*, 2010). Moreover, we observed a reduction of the *Chl* content per cell compared to AIR as well as a reduction of LHCII/PSII content in agreement with (Polukhina *et al.*, 2016). The reduced LHCII content did not affect the functional antenna size, on the contrary it was augmented in the CO_2 condition. This observation fits with the regulatory effects of NAB1 as translational repressor for LHCII encoding mRNAs described by (Berger *et al.*, 2014). PSI maximal activity was registered to be increased in CO_2, as supported by the blot analysis in which the reported PSI/PSII ratio resulted augmented in the very same condition. We also investigated the buildup of the pmf across the thylakoid membrane trough measurement of the ECS of carotenoids. No differences were evidenced between the two conditions, also indicating a similar contribution of cyclic electron transport. The increased PSI/PSII ratio in CO_2 and the similar contribution of cyclic electron flow to total electron transport suggest an increased activity of PSI at high CO_2 availability to reduce NADP+ to produce NADPH, which is required to assimilate the extra carbons available in CO_2 conditions. Carbon affixation process requires both NADPH and ATP: a doubled level of atpC was registered in CO_2 on a cell basis. Considering the equal pmf measured in the two conditions, we can theorize that an increased ATPase content may be the result of a regulatory response of a more electron-yielding electron transport chain, as the one we witness in high CO_2, and of an increased carbon fixation rate by the Calvin-Benson cycle that readily consumes ATP and reducing power.

2.3.3 ATP production in the mitochondrion is unfavored

We then investigated NAD(P)H formation/usage and mitochondrial respiration to gain a global insight of the energy flow in the cell. NAD(P)H formation in the CO_2 condition equals its consuming rate, oppositely to the positive rate of accumulation of NAD(P)H in the control condition. We hypothesized that an increased CO_2 availability translates into an increased activity of the Calvin-Benson cycle such to determine a higher NAD(P)H and ATP consumption in the CO_2 condition, making the chloroplast act as sink of reducing

power at the expense of the mitochondrion. Even though the total dark respiration rate seems to be unaffected by high CO_2 levels, its portion adducible to the cytochrome pathway is specifically diminished in CO_2, in favor of the alternative one. It is possible that in such condition we witness a diminished demand for ATP accumulation on behalf of the mitochondrion, therefore alternative pathways, through AOX activity, are preferred.

2.3.4 Biomass composition shifts to energy-dense metabolites

Biomass composition in terms of starch, protein and lipids was altered in the CO_2 condition. A decrease in starch accumulation and an increase in TAGs were detected, suggesting a shift of energy storing molecules towards more energy-dense compounds, TAGs in our case. However, the overall lipids content was unaffected between the two conditions. What we registered was rather a change in the relative composition of lipids in the CO_2 condition, with a decrease in the content of galactolipids (specifically MGDG), the main lipids of photosynthetic membranes (Li-Beisson *et al.*, 2019), in favor of TAGs. TAGs could both derive from recycling of other lipids and *de novo* biosynthesis (Simionato *et al.*, 2013). Given the reduced starch accumulation, we also theorize a reroute of photosynthates (triose phosphates) towards the glycolytic pathway to produce acetyl-CoA and ultimately TAGs, as observed in the diatom *Phaeodactylum tricornutum* (Li-Beisson *et al.*, 2019). Also, an elevated CO_2 level could directly impact on the cellular C/N ratio resulting in the dilution of the amount of protein within the organism as a response. Plants, for example, degrade RuBisCO as it is the major storage protein and source of nitrogen during leaf senescence (Hakeem, 2015). Considering the observed diminished total protein content in the CO_2 condition together with the diminished RuBisCO level, we could theorize that *C. reinhardtii* may dilute its protein levels in response to the augmented carbon content. Increased RuBisCO and carbon anhydrase in AIR conditions compared to CO_2 is also a clear mark of increased CCM in *C. reinhardtii* due to reduced carbon availability.

2.4 CONCLUSIONS

High CO_2 availability has a positive role on the productivity of the culture, enabling faster replication cycles, thus achieving higher biomass yields, despite a reduced photoprotection level. The photosynthetic machinery can adapt to the increased carbon availability and the augmented carbon fixation's energy demand: PSII antenna size, PSI activity and the chloroplast ATPase content are increased. The chloroplast acts as energy sink, in fact NAD(P)H accumulation equals its consumption rate. These rearrangements are reflected on the mitochondrion activity. Specifically, the cytochrome component of dark respiration, the main responsible for ATP production in the mitochondria, is decreased. Possibly, ATP synthesis spatially shifts towards chloroplast and cytoplasm. Given the increased availability of photosynthates, glycolysis may represent a key source for the energetic needs of the cell in CO_2 condition, but the possible increased reduced cofactors generated are translocated back to the plastids, rather than being used for mitochondrial respiration, to support carbon assimilation and energy-rich lipids accumulation. In fact, we also assist to a decreased starch accumulation, coupled with an increase of the more energy-dense TAGs.

2.5 MATERIAL AND METHODS

2.5.1 Microalgae cultivation

C. reinhardtii 4A+ was grown in the Multi-Cultivator MC 1000 tubes aerated with air or with 3% CO_2-enriched air obtained by a gas mixing system. Cells were grown in HS medium (Sueoka, 1960) starting from $1*10^6$ cell/ml at 300 μmol photons $m^{-2}\,s^{-1}$ (Allen and Stanier, 1968). Cell number was determined Countless®II FL automated cell counter (Thermo Fisher). The cell density was automatically monitored every ten minutes by measuring the absorption at 720 nm. For physiological measurements, cultures were harvested during the exponential growth phase. At the end of the growth curve the dry weight determination was performed: cell culture was harvested by centrifugation at 4500g for 5 min at 20°C then drying in a lyophilizer for 48h and then net dry weight was calculated.

2.5.2 Biomass composition analysis

Lipid, starch and protein content of the biomass harvested at the end of the exponential phase were analyzed as previously reported in Cecchin *et al*., 2019.

2.5.3 Photosynthetic parameters and pigments extraction

Pigments were extracted with 80% acetone at 4°C in dark conditions and measured with Jasco V-550 UV/VIS spectrophotometer. Proton motive force upon exposure to different light intensities was measured by Electrochromic shift (ECS) with MultispeQ v2.0 (PhotosynQ) according to Kuhlgert et al. 2016 and normalized to the *Chl* content of the sample. PSII activity and NPQ were analyzed by fluorescence measurements on whole cells using a Dual-PAM 100 instrument (WALZ). NPQ was measured with an actinic light of 1500 μmol photons m^{-2} s^{-1}. 77K fluorescence emission spectra were acquired with a charge-coupled device spectrophotometer (JBeamBio) as previously described (Allorent *et al*., 2013). State transitions were measured on whole cells induced to state 1 or state 2 as described in Fleischmann et al. 1999. PSII functional antenna size was measured from fast *Chl* induction kinetics induced with a red light of 11 μmol photons m^{-2} s^{-1} on dark-adapted cells incubated with 50 μM DCMU (Malkin *et al*., 1981). The reciprocal of time corresponding to two-thirds of the fluorescence rise ($\tau_{2/3}$) was taken as a measure of the PSII functional antenna size (Malkin *et al*., 1981). P700 activity was measured with the DUAL-PAM-100 (Heinz-Walz) following the transient absorption at 830 nm upon exposure to actinic light. Maximum P700 activity was measured after a pulse of saturating light in whole cells treated with DCMU (3-(3,4-dichlorophenyl)-1,1-dimethylurea), ascorbate, and methyl-viologen, as described in Bonente et al. 2012. The formation rate of NADPH was determined with the NADPH/9-AA module of the Dual-PAM 101 (Schreiber and Klughammer, 2009). Measurement was performed as described in Schreiber and Klughammer 2009 at the same light intensity of growth (500 μmol photons m^{-2} s^{-1}). The slope during the light phase, between 60-120s, was used to determine the rate of NADPH formation. Light-dependent O_2 evolution curves were measured using Clark electrode, as reported in (Perozeni, Cazzaniga and Ballottari, 2019).

2.5.4 SDS-PAGE and immunoblotting

SDS-PAGE and immunoblotting were performed as described in Bonente et al. 2011. The following antibodies obtained from Agrisera company (https://www.agrisera.com/) were

used: RbcL AS03 037, CAH3 AS05 073, PsaA AS06 172, CP43 AS11 1787, LHCSR3 AS14 2766, LHCSR1 AS14 2819.

2.5.5 Mitochondrial respiration

Samples in the exponential phase were subjected to respiratory rate measurements in the dark using a Clark-type O2 electrode (Oxygraph Plus; Hansatech Instruments; Clark, 1956). Respiratory rates were normalized to cells number obtained by Countless®II FL automated cell counter (Thermo Fisher). To discriminate between the individual contributions of the alternative and the cytochrome pathway dark respiration measurements were conducted as follows: cell samples ($5*10^7$ cell/ml) were transferred to the measurement chamber of the Clark electrode, respiration rates were recorded for 3 min prior to the addition of the first inhibitor, then respiration rates were recorded for 3 additional min finally the second inhibitor was added and measurements were continued for another 3 min. Alternative respiration was inhibited by adding 2 mM SHAM (salicylhydroxamic acid), while the cytochrome pathway (complex III) was inhibited by adding 5µM myxothiazol. To assess the relative contribution of the cytochrome pathway, respiration was first measured in the absence of inhibitors (total dark respiration) before alternative respiration was inhibited by adding SHAM. Cytochrome dependent respiration was then inhibited using myxothiazol and the residual respiration determined in relation to the uninhibited state. The contribution of alternative respiration was determined by reversing the order of inhibitor addition (myxothiazol followed by SHAM) (Bailleul *et al.*, 2015).

3 LPA2 PROTEIN IS INVOLVED IN PHOTOSYSTEM II ASSEMBLY IN *CHLAMYDOMONAS REINHARDTII*

Michela Cecchin[1], Jooyeon Jeong[2], Woojae Son[3], Minaje Kim[2], Seunghye Park[2], Luca Zuliani[1], Stefano Cazzaniga[1], Andrea Pompa[4,5], Chan Young Kang[3], Sangsu Bae[3], Matteo Ballottari[1], EonSeon Jin[2]

1 Dipartimento di Biotecnologie, Università di Verona, Verona, Italy; 2 Department of Life Science, Hanyang University, Seoul, Korea; 3 Department of Chemistry, Hanyang University, Seoul, Korea; 4 Dipartimento di Scienze Biomolecolari, Università degli studi di Urbino; 5 Istituto di Bioscienze e Biorisorse, Consiglio Nazionale delle Ricerche, Perugia, Italy.

Published on The Plant Journal, 2021 (https://doi.org/10.1111/tpj.15405)

3.1 ABSTRACT

Photosynthetic eukaryotes require the proper assembly of photosystem II (PSII) to strip electrons from water and fuel the carbon fixation reactions. In *Arabidopsis thaliana*, one of the PSII subunits (CP43/PsbC) was suggested to be assembled into the PSII complex via its interaction with an auxiliary protein called Low PSII Accumulation 2 (LPA2). However, the original articles describing the role of LPA2 in PSII assembly have been retracted. To investigate the function of LPA2, here we generated in the model organism for green algae, *Chlamydomonas reinhardtii,* knockout *lpa2* mutants by using the CRISPR-Cas9 target-specific genome-editing system. Biochemical analyses revealed the thylakoidal localization of LPA2 protein in the WT while *lpa2* mutants were characterized by a drastic reduction in the level of D1, D2, CP47 and CP43 proteins. Consequently, reduced PSII supercomplex accumulation, chlorophyll content per cell, PSII quantum yield and photosynthetic oxygen evolution were measured in the *lpa2* mutants, leading to an almost complete impairment of photoautotrophic growth. Pulse-chase experiments demonstrated that the absence of LPA2 protein caused a reduced PSII assembly and reduced PSII turnover. Taken together, our data indicate that, in *C. reinhardtii*, LPA2 is required for PSII assembly and its proper function.

3.2 INTRODUCTION

Photosystem II (PSII) is the initial complex in the linear electron transport of photosynthesis in chloroplasts (Nelson and Junge, 2015). It comprises the light-harvesting antenna complex that absorbs sunlight and the core complex that converts light into photochemical energy (Croce and Van Amerongen, 2013; Shen *et al.*, 2019). The PSII core complex contains at least 20 subunits with various cofactors, including electron donors and acceptors (Gokhale and Sayre, 2009). Because of the structural complexity of PSII, the proper assembly of its subunits is important for its function (Nickelsen and Rengstl, 2013; Lu, 2016).

Although photosynthetic eukaryotes have, through endosymbiosis, acquired chloroplasts that perform oxygenic photosynthesis, the chloroplast genome does not encode all the proteins necessary for the photosynthetic machinery (Shinozaki *et al.*, 1986). Numerous nuclear genes encode components of the photosynthetic apparatus. Moreover, multiple proteins required for the biogenesis and assembly of protein complexes in the chloroplast, e.g., the CpSRP54, CpSRP43, CpFTSY, and LTD proteins from the chloroplast signal recognition particle pathway, are encoded by nuclear genes (Kirst and Melis, 2014; Jeong *et al.*, 2017, 2018; Ziehe, Dünschede and Schünemann, 2017).

The biogenesis of PSII is a stepwise assembly process (Nickelsen and Rengstl, 2013; Lu, 2016). The first step is the formation of the D1 and D2 heterodimer, where the chlorophyll special pair involved in PSII photochemistry is bound (Rokka *et al.*, 2005). Next, the inner antenna proteins CP47 and CP43 are sequentially bound (Boehm *et al.*, 2011). Subsequently, the oxygen-evolving complex assembles on the luminal side of the PSII pre-complex, which is converted into an active monomeric PSII (Rokka *et al.*, 2005; Bricker *et al.*, 2012). Finally, the active PSII forms dimers and is surrounded by the peripheral light-harvesting antenna complex, which completes the *de novo* biogenesis of PSII (Nickelsen and Rengstl, 2013; Shen *et al.*, 2019).

Many regulatory factors are involved in the appropriate organization of the PSII subunits. Of these, Psb27 in cyanobacteria interacts with CP43 and PSII during both *de novo* biogenesis and repair of PSII (Komenda *et al.*, 2012). Because two Psb27 homologs have been identified in the green lineage, the role of cyanobacterial Psb27 was proposed to be

divided between two genes in eukaryotes (Nickelsen and Rengstl, 2013). One of them, Psb27-H2 (LPA19), participates in *de novo* PSII assembly by interacting with D1 and CP43 (Wei *et al.*, 2010).

In cyanobacteria, CP43 incorporation into PSII requires another assembly factor, Sll0606, whose absence results in a drastic reduction in the level of PSII (Zhang, Frankel and Bricker, 2010). A homolog of Sll0606 is found in the microalga *Chlamydomonas reinhardtii*, but not in the land plant *Arabidopsis thaliana*, suggesting that Sll0606 might be functionally replaced by other proteins in embryophytes (Chi, Ma and Zhang, 2012). One possible replacement is low PSII accumulation 2 (LPA2), which has been suggested to interact with CP43 during PSII assembly in *A. thaliana*, although based on reports that have been retracted (Ma *et al.*, 2007; Cai *et al.*, 2010). A reduced PSII activity and reduced growth was also reported in *A. thaliana lpa2* mutants in a following work, where LPA2 was shown to interact with TerC (Tellurite resistance C) protein, involved in insertion of thylakoid membrane proteins (Schneider *et al.*, 2014). LPA2 homologs have been found in other embryophytes, but not in *C. reinhardtii* or cyanobacteria (Chi, Ma and Zhang, 2012; Nickelsen and Rengstl, 2013). Therefore, CP43 assembly was not expected to require an LPA2 homolog in *C. reinhardtii*, but no detailed study of the assembly factors for CP43 in this microalga has been performed. In this study, we identified an LPA2 homolog in the *C. reinhardtii* genome. To investigate the function of this protein *in vivo*, we used the ribonucleoprotein (RNP)-mediated CRISPR-Cas9 system to generate target-specific knockout mutants (*lpa2*) of *C. reinhardtii*. In the absence of the LPA2 protein, *lpa2* mutants had reduced amount of PSII core subunits and dysfunctional PSII supercomplexes. These results indicate that LPA2 is required for efficient PSII assembly in *C. reinhardtii*. In addition, *lpa2* mutants had enhanced electron transport around PSI, suggesting that PSI can be used to dissipate excitation energy in PSII-deficient conditions.

3.3 RESULTS

3.3.1 LPA2 gene in *C. reinhardtii*

The putative *LPA2* gene (Cre02.g105650) was identified in the *C. reinhardtii* genome based on the amino acid sequence similarity between its product and LPA2 in *A. thaliana* (Figure 1). Homologs were also identified in the green lineage, including chlorophytes, but not in

cyanobacteria. Moreover, no LPA2 homologs could be found in *Glaucophytes, Rhodophyta* or in species derived from secondary endosymbiosis as *Cryptophyta, Haptophyta*, or *Heterokonta* suggesting that the LPA2 protein is of eukaryotic origin, being evolved in particular in *Viridiplantae* (Table S1, Figure 1A). *LPA2* gene could be identified also in bryophytes, lycophytes and tracheophytes but not in hornwort, where no homolog could be found. The absence of LPA2 gene in hornwort could be related to some specific evolutive events that require a dedicated and in-depth analysis. The *C. reinhardtii LPA2* gene (*CrLPA2*) encodes a protein of 175 amino acids, including a 24 amino-acid-long chloroplast transit peptide predicted by Predalgo software (https://giavap-genomes.ibpc.fr/predalgo/) and two transmembrane domains (amino acids 109–131 and 146–163) determined by TMHMM software (http://www.cbs.dtu.dk/services/TMHMM/). The CrLPA2 protein shares 23.2% identity and 43.2% similarity with its *Arabidopsis* homolog (Figure 1B).

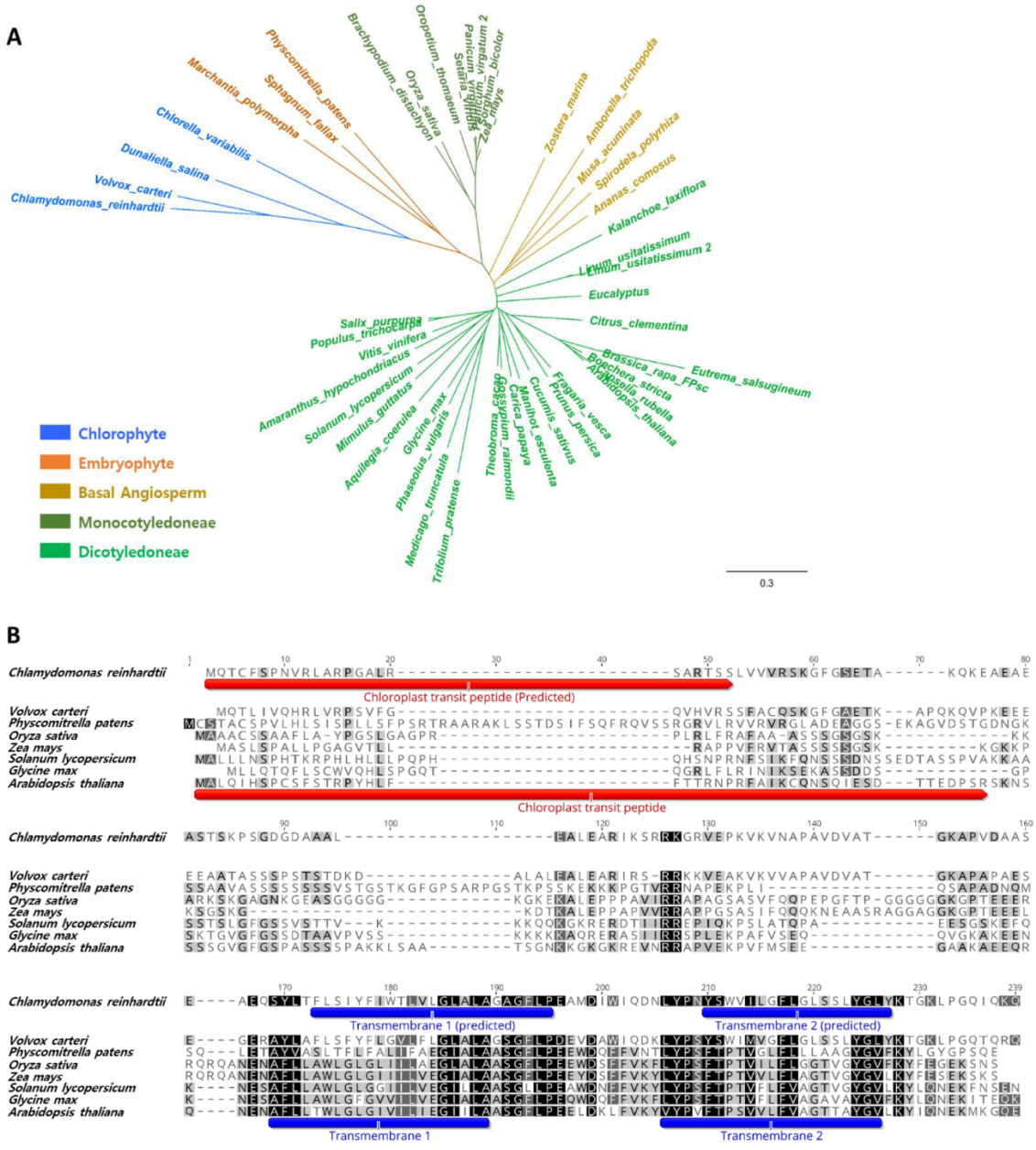

Figure 1. *Maximum-likelihood tree (**A**) and amino acid sequence alignment (**B**) of LPA2 homologs in the green lineage. The sequences were aligned using MUSCLE alignment, and selected species representing each clade are shown in **B**. Node labels are bootstrap support values from 100 replicates. The species names and accession number of individual sequences are labeled in the tip of the branch. Green closed triangle represents the Cas9 driven mutation site of LPA2 gene in lpa2.*

To investigate the function of *C. reinhardtii* LPA2, we analyzed the light-inducible expression of *LPA2*. We exposed *C. reinhardtii* strain CC503 to high light (500 μmol photons m^{-2} s^{-1}) for 0, 30, and 60 min and used qRT-PCR to analyze the transcript levels of *ELIP2* and *LPA2* (Supporting Information Figure S1A). While in the case of *ELIP2* high light treatment caused a statistically significant increased transcription, *LPA2* expression was only moderately enhanced after exposure to high light. Western blotting revealed the

presence of LPA2 in purified chloroplasts, specifically in the thylakoid membranes, but not in the stromal fraction (Supporting Information Figure S1B).

3.3.2 Generation of knock-out mutants without the lpa2 gene in C. *reinhardtii*

To further characterize *C. reinhardtii* LPA2, we generated target-specific knockout mutants by using preassembled Cas9 protein–small guide RNA (sgRNA) RNP complex–mediated CRISPR-Cas9. Different sgRNA were tested for the generation of *lpa2* mutants with positive results obtained only in the case of sgRNA2 containing the 5′-CAAGGGCTTTGGTTCAGAGACGG-3′ sequence (Table S2). Considering a possible phenotype on the assembly of the pigment binding complexes (Ma *et al.*, 2007), *lpa2* mutant strains were screened on the basis of Chl fluorescence. Transformants with lower F_v/F_m fluorescence signals than the background cells (Figure 2A) were selected for Sanger sequencing analysis of the target locus. All such transformants had small indels in the *LPA2* gene (Figure 2B). The knock-out efficiency, calculated as the ratio of the mutant number (3) to the total colony number (606), was 0.495%, which was similar to the targeted mutation frequency obtained from the total gDNA of CRISPR-Cas9–transfected cells (0.4%; Table S3). Transcription of *LPA2* gene was investigated in the *lpa2* mutants compared to the WT case revealing a reduced transcription in the mutants (Figure 2C). Cas9 driven mutations occurred at the first exon of *LPA2* gene, where *lpa2#1* and *lpa2#2* mutants were deleted by 2bp and 5bp, respectively (Figure 2B): we can speculate that these deletions may cause non-functional transcripts that could be unstable in mutants, as previously reported for other genes edited by Cas9 (Tang *et al.*, 2018; Tuladhar *et al.*, 2019), even if further work is required to support this hypothesis. LPA2 protein accumulation was then investigated by immunoblotting analysis showing no detectable results in the case of *lpa2* mutant strains (Figure 2D). Analysis of the *lpa2* mutants for potential off-target effects by targeted deep sequencing revealed no indels (Table S4).

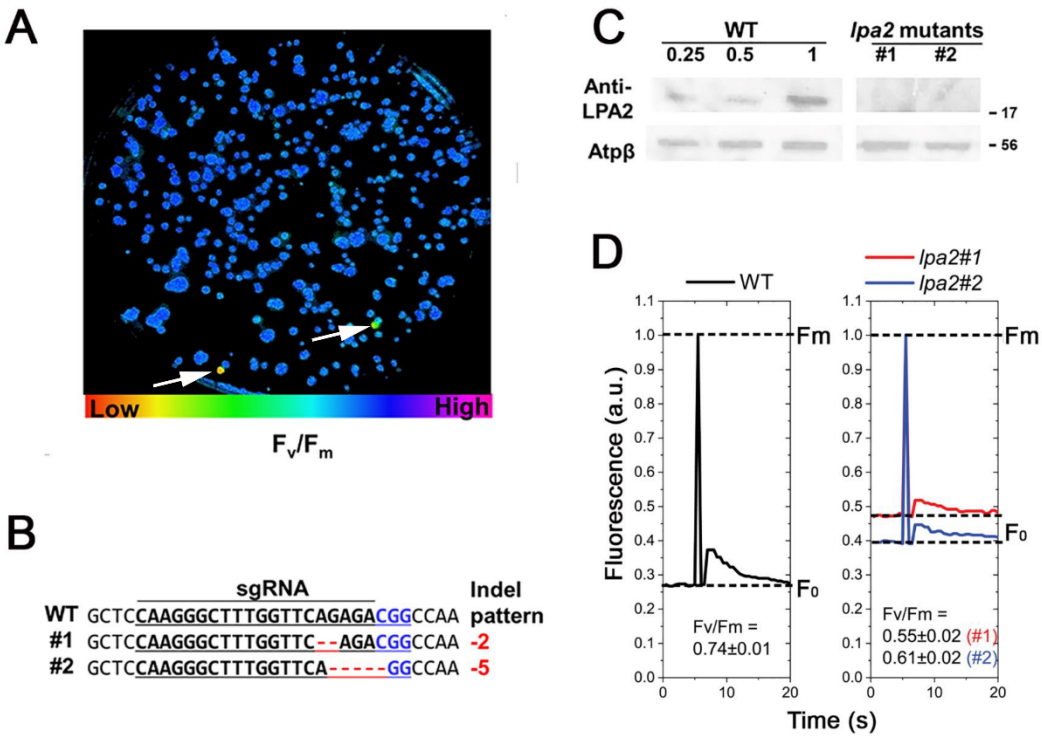

***Figure 2**. CRISPR-Cas9-mediated lpa2 mutants' generation in C. reinhardtii. **A**. The measurement of F_v/F_m to select putative LPA2 gene knockout mutants grown on TAP agar medium under 50 µmol photons m^{-2} s^{-1}. The cells (marked with white arrows) presenting lower F_v/F_m than the background cells were picked and confirmed by Sanger sequencing. **B**. DNA sequence alignment of the wild-type (WT) and lpa2 mutants obtained from Figure 2A at the LPA2 locus. The 20-bp target sequence of sgRNA2 is underlined, and the PAM sequence is shown in blue. The column on the right indicates the number of inserted (+) or deleted (−) bases. C. Relative mRNA expression of the LPA2 gene in lpa2 mutants compared to the WT case. mRNA expression level was calculated based on the WT upon normalization with the expression level of the RACK1 gene, used as internal standard. Error bars are reported as standard deviation (n=3). D. **D**. Immunoblot with LPA2 and AtpB (loading control) antibodies in the WT and lpa2 1# and lpa2 #2, which were used for all further experiments. Proteins were loaded on the basis of equal cell numbers, and the WT samples were loaded at three different concentrations (25%, 50%, and 100%). **E**. The measurement of Chl fluorescence kinetics in the WT and lpa2 mutants grown in liquid TAP medium under 50 µmol photons m^{-2} s^{-1}. The measuring light (ML) and saturating light (SL) were 5 and 1,250 µmol photons m^{-2} s^{-1}, respectively. The F_v/F_m differed significantly between the WT and lpa2 mutants, as determined by Student t-test (n = 4; the values shown are means ± SD; $p < 0.05$).*

3.3.3 Decreased chlorophyll (Chl) content in the lpa2 mutants

As As revealed during mutant screening, *lpa2* mutants had an aberrant F_v/F_m fluorescence signal (Figure 2E). Interestingly, although the F_m/Chl ratios of the mutants were similar to that of the wild type, the F_0/Chl ratios of the mutants were increased, resulting in a low F_v/F_m fluorescence signal. The increased F_0/Chl ratio suggests the partial disconnection of antenna complexes from PSII. The organization of the photosynthetic apparatus was thus investigated on the basis of 77K fluorescence emission spectra. In the case of *lpa2* mutants, the spectra were characterized by an increased fluorescence emission at 680 nm which can be ascribed to the presence of a disconnected LHC protein, confirming the partial

destabilization of the PSII complexes (Supporting Information Figure S2). Interestingly, *lpa2* mutants were characterized by an increased 715/686 nm and 715/690 fluorescence emission ratios. 686 and 690 nm fluorescence emission are related to PSII contributions, while 715 nm is due to PSI emission(Snellenburg *et al.*, 2017; Girolomoni *et al.*, 2019): increased 715/686 nm or 715/690 nm fluorescence emission ratios in *lpa2* mutants compared to the WT case suggests an increased PSI/PSII ratio and/or increased antenna proteins bound to PSI in the mutant strains.

To understand the change in Chl fluorescence caused by the mutation, we analyzed the Chl content of the *lpa2* mutants (Table 1). In photoautotrophic cultures, *lpa2* mutants exhibited approximately 50% reduction in total Chl content per cell compared with that in the wild type, whereas the Chl *a/b* ratio were not significantly affected. The reduction in Chl content per cell was not related to a change in cell size, which was similar in the different strains analyzed (Table 1).

	Chl/cell (pg/cell)	**Chl a/b ratio**	**Chl/car**	**Cell dimension (μm)**
WT	2.50 ± 0.11	2.61 ± 0.01	3.20 ± 0.03	8.92 ± 0.81
***lpa2* #1**	1.35 ± 0.11*	2.58 ± 0.02	2.70 ± 0.07*	8.57 ± 0.96
***lpa2* #2**	1.17 ± 0.05*	2.47 ± 0.07	2.82 ± 0.08*	8.39 ± 0.75

Table1. *Chlorophyll (Chl) content and cell diameter of the wild type (WT) and lpa2 mutants. The statistical significance of differences between WT and lpa2 mutants ($p < 0.05$, n=4) is indicated as *, as determined by Student t-test.*

3.3.4 lpa2 mutants had strongly reduced photoautotrophic growth and reduced photosynthetic activity

To To investigate how the reduced Fv/Fm and reduced chlorophyll content found in the *lpa2* mutants affected their growth, we cultivated wild-type (WT) and mutant strains under photoautotrophic, mixotrophic, and heterotrophic conditions. Under heterotrophic conditions (with acetate as a source of organic carbon), the growth of *lpa2* mutants was similar to that of WT, indicating that the mutations introduced did not affect the light-independent cell functions. In mixotrophy, *lpa2* mutants showed slower growth than the WT in both solid and liquid media. Under photoautotrophic conditions, the growth of *lpa2* mutants was severely impaired (Figure 3), presumably because the lower photosynthetic activity of the mutants could not maintain whole-cell metabolism under these conditions.

Interestingly, in the case of lpa2 mutants the doubling time at exponential phase were similar in mixotrophy and heterotrophic conditions, suggesting that the growth rate in TAP medium was essentially driven by acetate consumption in this mutant strains (Table 2). Consistently, *lpa2* mutants were essentially not replicating in the time range analyzed in photoautotrophic growth conditions. Differently, WT cells grown in mixotrophy were characterized by a reduced doubling time compared to both heterotrophic and photoautotrophic conditions. The photosynthetic activity of *lpa2* mutants was then analyzed using pulse-amplitude-modulated (PAM) fluorescence (Supporting Information Figure S3). The operating efficiency of PSII electron transport (ΦPSII) was lower in the mutants than in the WT at light intensities below 400 μmol $m^{-2}s^{-1}$, but similar at higher irradiances (Supporting Information Figure S3). The fraction of excitation energy not used for the photochemical reaction could be lost through safe non-photochemical reactions leading to controlled energy conversion into heat (ΦNPQ) or through uncontrolled dissipation (ΦNO), which is usually related to oxidative stress and photoinhibition. Controlled thermal dissipation of the absorbed excitation energy (ΦNPQ) was also lower in the *lpa2* mutants than in the WT, whereas the fraction of absorbed energy lost by uncontrolled dissipation (ΦNO) was higher in *lpa2* (Supporting Information Figure S3A,B and C). Accordingly, the NPQ values, calculated as (Fm-Fm')/Fm', were lower in the *lpa2* mutants than in the WT, implying a lower photoprotective capacity in the mutants (Supporting Information Figure S3E and F). The fraction of closed PSII centers, calculated from the 1 - q_L value, was similar in the *lpa2* mutants compared to that in WT (Supporting Information Figure S3E). This result indicates that, despite the reduced efficiency of PSII, the redox state of Q_A was maintained similar to that in the WT at the different light intensities owing to an acclimation of the overall photosynthetic apparatus. We further investigated PSII activity by measuring the light-dependent oxygen evolution curves and found reduced oxygen evolution on a per-cell basis in the *lpa2* mutants, confirming its reduced photosynthetic activity (Figure 4A). In order to investigate specifically the PSII activity, oxygen evolution was measured in presence of electron acceptor for plastoquinones as 2,6-Dichloro-1,4-benzoquinone (DCBQ) and its the secondary acceptor potassium ferricyanide (III), in presence of inhibitor DBMIB, preventing possible influence of PSI on plastoquinone redox state (Böhme, 1976; Brinkert *et al.*, 2016). As reported in

Figure 4C reduced PSII activity was measured in presence of DCBQ, potassium ferricyanide (III) and DBMIB in *lpa2* mutants. Interestingly, in presence of electron acceptor for plastoquinones, light dependent net oxygen evolution was linearly correlated with the level of D1 or D2 (Figure 4D). This result suggests that the lower oxygen evolution was due to decreased PSII accumulation in the mutants.

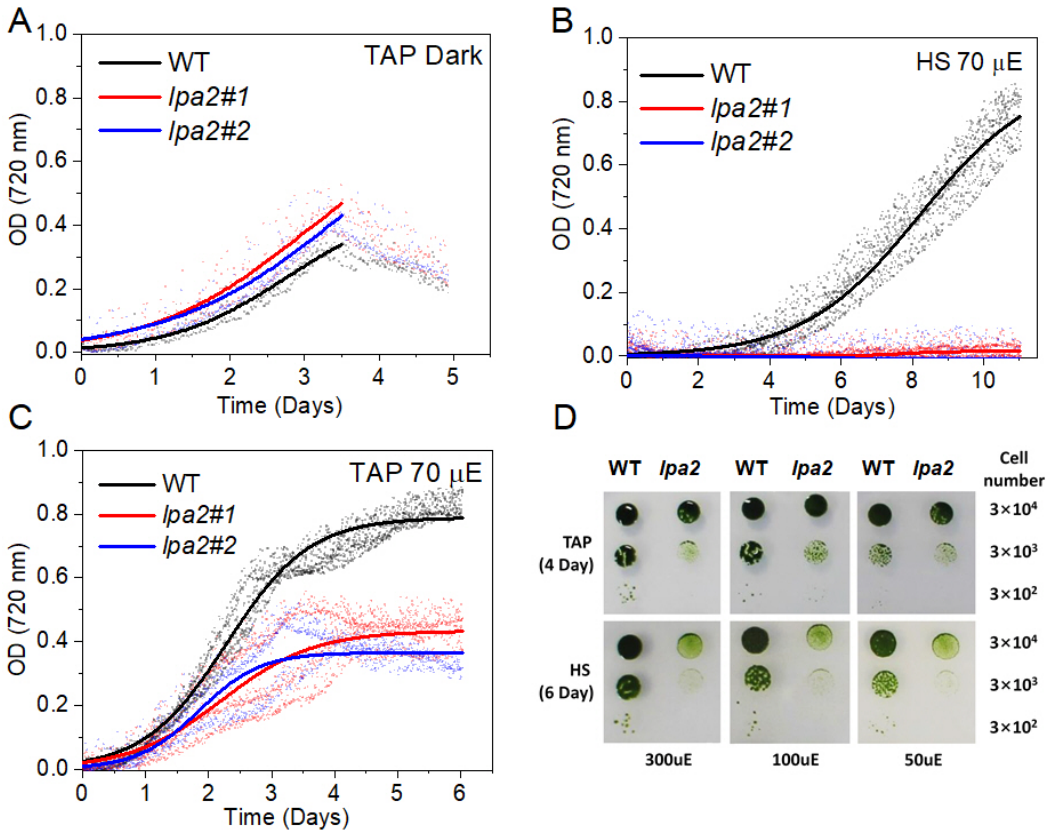

Figure 3. *Growth curves of WT and lpa2 mutants. Heterotrophic (**A**), photoautotrophic (**B**), and mixotrophic (**C**) growth of the lpa2 mutants measured in liquid medium and compared to the wild type (WT). Heterotrophic conditions were induced growing microalgae strains in the dark in TAP medium, while photoautotrophic and mixotrophic conditions were obtained growing the cells in continuous light respectively in HS or TAP media. Growth curves are reported as optical density (OD) measured at 720 nm every 30 minutes. The growth curves obtained were fitted using sigmoidal function (n = 4). Doubling time of cells in the different growth conditions are reported in Table 2. Photoautrophic and mixotrophic growth was also evaluated by spot test in solid HS or TAP media at 50, 100 and 300 µmol photons m^{-2} s^{-1} (**D**). The number of cells spotted for each drop are reported on the right of the Panel D.*

.

	mixotrophy	**autotrophy**	**heterotrophy**
	TAP + LIGHT	**HS + LIGHT**	**TAP + DARK**
WT	7.8 ± 0.4	19.4 ± 0.3	18.3 ± 1.0
lpa2#1	14.6 ± 0.7*	388.3 ± 8.7*	15.4 ± 1.5
lpa2#2	11.8 ± 1.1*	406.5 ± 9.1*	18.3 ± 1.5

Table 2. *Doubling times of WT and lpa2 mutant strains. Doubling times (h) for WT and lpa2 mutant were calculated for cells in exponential phase in mixotrophic, photoautotrophic and heterotrophic growth conditions as reported in Figure 3. The statistical significance of differences between WT and lpa2 mutants ($p < 0.05$, n=3) is indicated as *, as determined by Student t-test.*

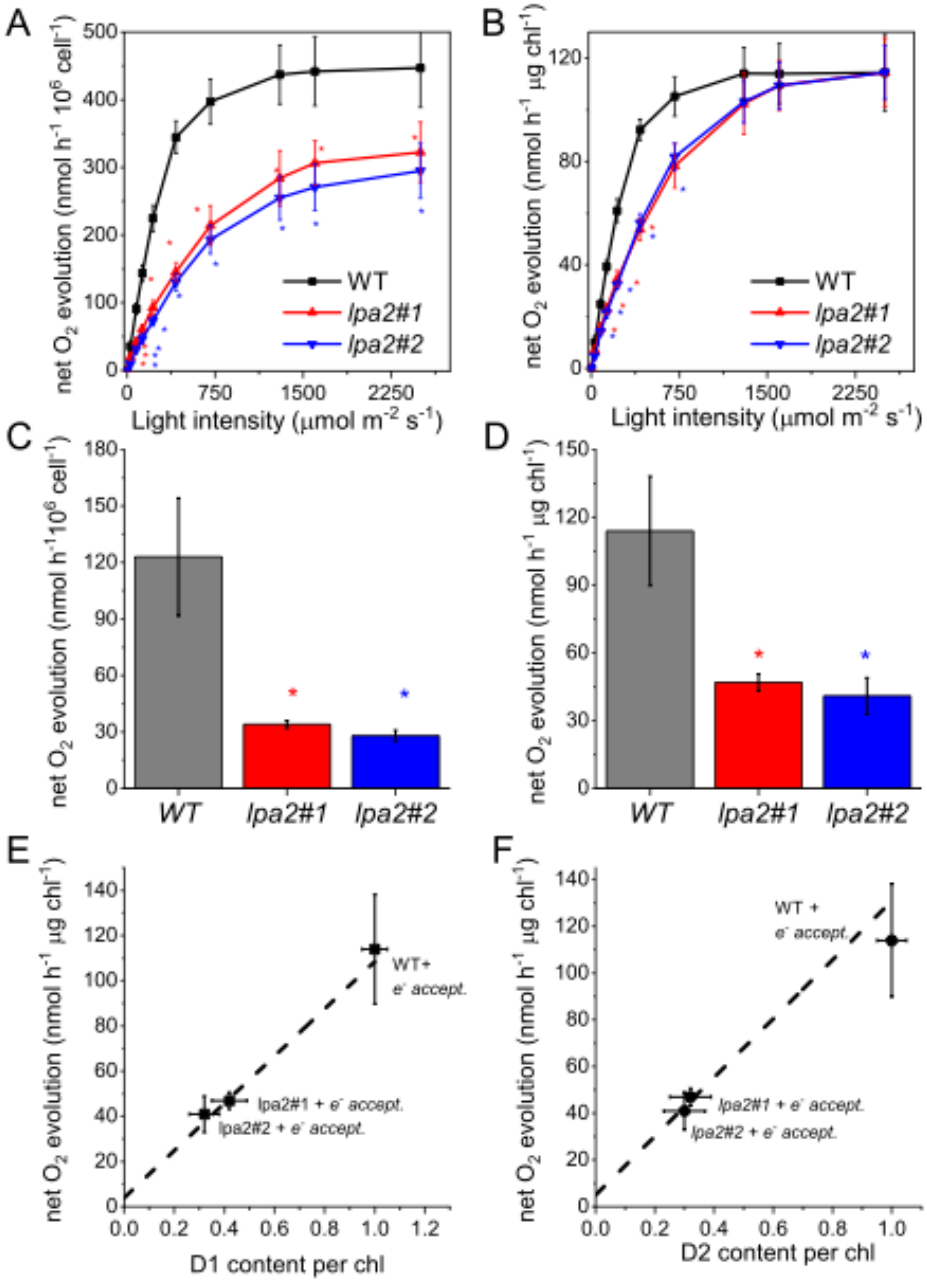

Figure 4*. Oxygen evolution curves of WT and lpa2 mutants. Oxygen evolution rates of both the WT and lpa2 mutants in response to different light intensities were measured to determine the rate of oxygen consumption in the dark. Cells were grown in TAP medium, washed with HS medium, and cultivated in photoautotrophy for 12 h prior to measurement. The net oxygen evolution rates were measured on samples at the same cell concentration (**A**)). Oxygen evolution was also measured at 600 µmol photons m^{-2} s^{-1} in presence of PSII electron acceptors DCBQ and Potassium ferrocyanide and DMBIB as inhibitor of plastoquinone reduction by cyclic electron flow: the net oxygen evolution rates were normalized to total cell contents (**B**). Oxygen evolution rates produced by WT and lpa2 mutants in presence of DCBQ, Potassium ferrocyanide and DBMIB were then plotted as a function of D1 or D2 content per Chl (**C, D**). Error bars indicate standard deviation (n = 3). The statistical significance of differences between WT and lpa2 is indicated as * $p < 0.05$, as determined by Student t-test. Results of linear fit of data reported in Panel C and D are reported as dashed line (R^2=0.926 and R^2= 0.99545 respectively for linear fits in Panel C and D).*

3.3.5 The lpa2 mutants have enhanced electron transport flow around PSI

PSI activity was measured as maximum P700 oxidation, which was higher on a Chl basis in the *lpa2* mutants than in the wild type (Figure 5A), but similar on a per cell basis because of the reduced Chl content per cell in the mutants (Figure 5B). These results suggest that the defect in PSII activity increased PSI activity on a chlorophyll basis in the *lpa2* mutants.

Next, we measured the electrochromic shift (ECS) to estimate the proton-motive force (*pmf*) across the thylakoid membranes generated by the light-driven electron flux. The *pmf* in the *lpa2* was similar to that in the WT (Figure 5C). Considering the reduced PSII activity in the *lpa2* mutants, we investigated the possible influence on cyclic electron flow (CEF) around PSI on *pmf* by measuring the ECS in the presence of DCMU to inhibit linear electron flow. The *lpa2* mutants had an increased fraction of *pmf* related to CEF (Figure 5C), causing a similar total *pmf* despite decreased PSII activity.

We reasoned that the altered amounts PSII activity in the *lpa2* mutants might affect the state transitions that balance the energy between PSI and PSII by using LHCII migration from PSII to PSI. We examined the capacity of the *lpa2* mutants to perform state transitions by measuring the 77K fluorescence emission spectra of cells under state 1 or state 2 conditions (Figure 5D, E and F). The *lpa2* mutants showed increased migration of light-harvesting antenna proteins to PSI under state 2 conditions, suggesting an increased pool of mobile LHCII subunits, likely because of the reduced PSII assembly.

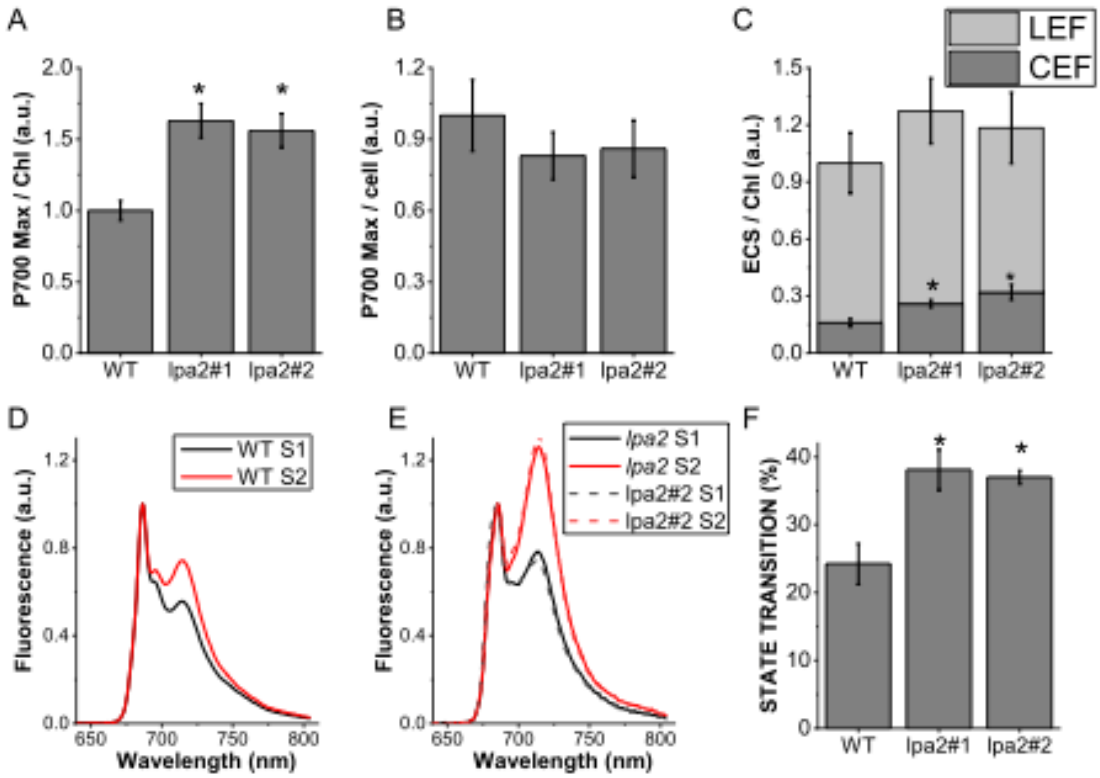

***Figure 5**. PSI activity, ECS and state transitions. (A, B) Maximal P700 oxidation on a Chl (A) or cell (B) basis in the WT and lpa2 mutants. (C). Linear electron flow (LEF) and cyclic electron flow (CEF) of the WT and lpa2#1 and lpa2#2 estimated from the electrochromic shift (ECS) on a Chl basis. (D, E) State transitions analysis by using 77K fluorescence emission spectra of the wild type (WT; D) and lpa2 #1 and lpa2#2 mutants (E) in state 1 (S1) or state 2 (S2) conditions. (F) Maximum level of state transition measured as percentage variation of PSII fluorescence in S2 compared to S1. Error bars are indicated as standard deviation (n = 3). The statistical significance of differences between WT and lpa2 mutants ($p < 0.01$) is indicated as *, as determined by Student t-test.*

3.3.6 The lpa2 mutants accumulate low amount of PSII core subunits

We investigated the effect of the *LPA2* gene mutation on the organization of photosynthetic complexes in isolated thylakoid membranes (Figure 6). In the 2D-Deriphat/SDS-PAGE analysis, the intensity of the bands representing the PSII core and PSII supercomplexes was markedly reduced in the *lpa2* mutant, with a particularly strong decrease in the CP43/CP47 band and, even if to lower extent, D1/D2 band. Interestingly, LPA2 protein was detected in the WT as a monomer and at higher oligomerization state, likely interacting with other proteins involved in PSII assembly, as previously reported in the case of *A. thaliana* (Ma *et al.*, 2007; Schneider *et al.*, 2014).

Western blot analyses of specific photosystem subunits (Figure 7), revealing, on a chlorophyll basis, the strongest decrease in CP43, with ~20% residual CP43 in the *lpa2* mutants, followed by CP47, D1 and D2 which were reduced to ~30-40% compared to the WT case. Significant reduced accumulation of other PSII core subunits as PsbO and PsbP

was also detected in the case of *lpa2* mutants (Figure 7). The accumulation of LHCII complexes in the *lpa2* mutants was similar to that in the WT on a chlorophyll basis, indicating that the LHCII/PSII ratio in the mutants was increased. Considering the low NPQ measured in the case of *lpa2* mutants, the accumulation of LHCSR3, the main chlorophyll binding protein involved in this photoprotective mechanism was also investigated (Peers *et al.*, 2009). As reported in Figure 7, a ~50% reduction of LHCSR3 was measured on chlorophyll basis in the absence of LPA2. LHCSR proteins have been reported to be involved in quenching mechanisms occurring both at the level of PSII, disconnected LHCII and PSI-LHCI (Dinc *et al.*, 2016; Girolomoni *et al.*, 2019; Cazzaniga *et al.*, 2020): while in the ratio LHCSR3/PSII was similar in WT and *lpa2* mutants, a reduced LHCSR3/LHCII and LHCSR3/PSI was evident in the latter.

PSI accumulation on a chlorophyll basis was not affected by the *LPA2* mutation (Figure 7), with a consequent increase in the PSI/PSII ratio in the *lpa2* mutants compared with that in the WT. Interestingly, in the case of LHCI a possible reorganization of different Lhca subunit likely occurred in *lpa2* mutants, as evinced by the different content of subunits recognized by α-Lhca3 and α-Lhca4 antibodies in the *lpa2* mutants, which were respectively decreased and increased on a chlorophyll basis compared to the WT case. It has already been reported that the quality of the Lhca complexes bound by PSI can be modulated according to the different growth conditions (Bonente *et al.*, 2012): the destabilization of PSII observed in *lpa2* is thus likely inducing acclimation mechanisms at the level of PSI.

The accumulation of the cytochrome b_6f complex and ATP synthase was investigated using western blotting by using antibodies specific to cytochrome *f* and the ATPase β-subunit, respectively (Figure 7). The levels of both subunits were significantly increased on a chlorophyll basis in the *lpa2* mutant. The large Rubisco subunit, a representative enzyme of the Calvin–Benson cycle, was clearly increased in the mutants on a chlorophyll basis. As reported in Figure 7D the reduced PSII content on a chlorophyll basis was accompanied in *lpa2* mutants by a strong increase of cytochrome b_6f complex, PSI, Rubisco, and ATP synthase content per PSII. On a cell basis, due to the reduce chlorophyll content observed in the case of *lpa2* mutants, the strong decrease in PSII subunits in these strains was accompanied by a reduction of PSI and cytochrome b_6f complex, and a similar content

of Rubisco and ATP synthase compared to the WT case (Supporting Information Figure S4).

In order to evaluate if the absence of LPA2 protein specifically affected PSII assembly or its turnover rate, we performed pulse-chase experiments, followed by thylakoid solubilization and PSII core immunoprecipitation by using D2 antibodies. As reported in Figure 7E, upon SDS-PAGE separation of proteins co-immunoprecipitated by D2 antibody, two main bands respectively at ~45 kDa and ~35 kDa were appearing: the former can be attributed to CP43 and/or CP47, while the latter to D2, likely with the comigration of the subunit D1 (Figure 7F). The *lpa2* mutants were characterized by similar incorporation of D1/D2 and in PSII complex compared to WT in time range herein analyzed. Differently, a strongly reduced CP43/CP47 assembly was evident after a 60- or 120-minutes pulse F, suggesting the key role of LPA2 in PSII assembly. After 1 hour of chase in low light, the D1/D2 and CP47 contents were strongly reduced in the case of WT because of its high turnover rate and assembly of new label-free complexes, but not in the *lpa2* mutants, indicating a slower PSII turnover, likely as a consequence of the partially impaired assembly.

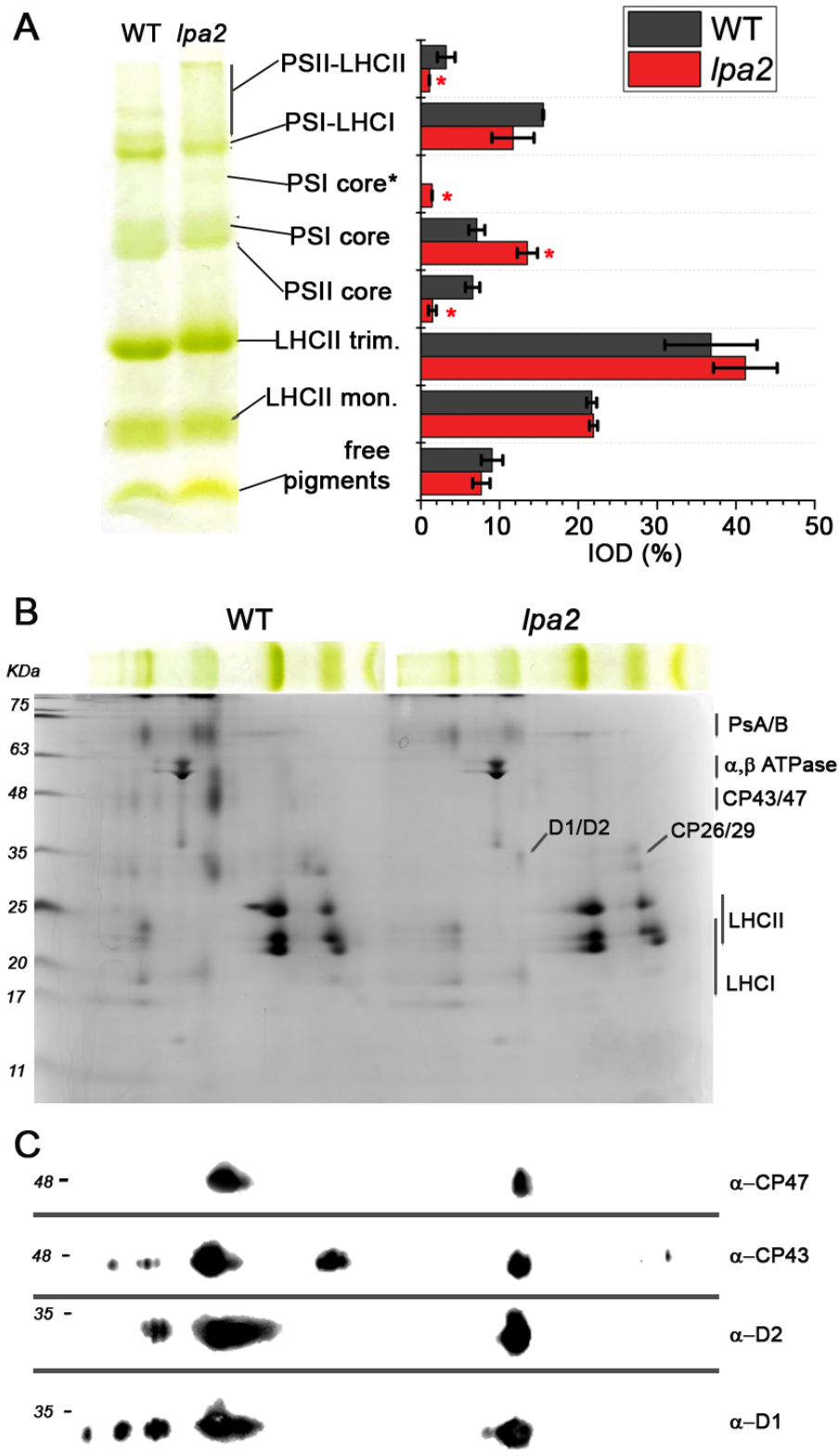

Figure 6. *The 2D-Deriphat/SDS-PAGE of purified thylakoid membranes. Deriphat-PAGE of WT and lpa2 mutants (**A**): density of each band was quantified by densitometric analysis of the green channel of the picture. Band marked with PSI core* is related to PSI-core with residual Lhca antenna bound. Second dimension of the 2D-Deriphat/SDS-PAGE was performed by running the Deriphat-PAGE lanes in Tris-Tricine poly-acrylamide gel. The statistical significance of differences between WT and lpa2 is indicated as * $p < 0.05$, as determined by Student t-test ($n=3$). (**B**): Western blot analysis on 2D-Deriphat/SDS-PAGE by using specific antibodies recognizing D1, D2, CP43 or CP47 subunits is reported in (**C**).*

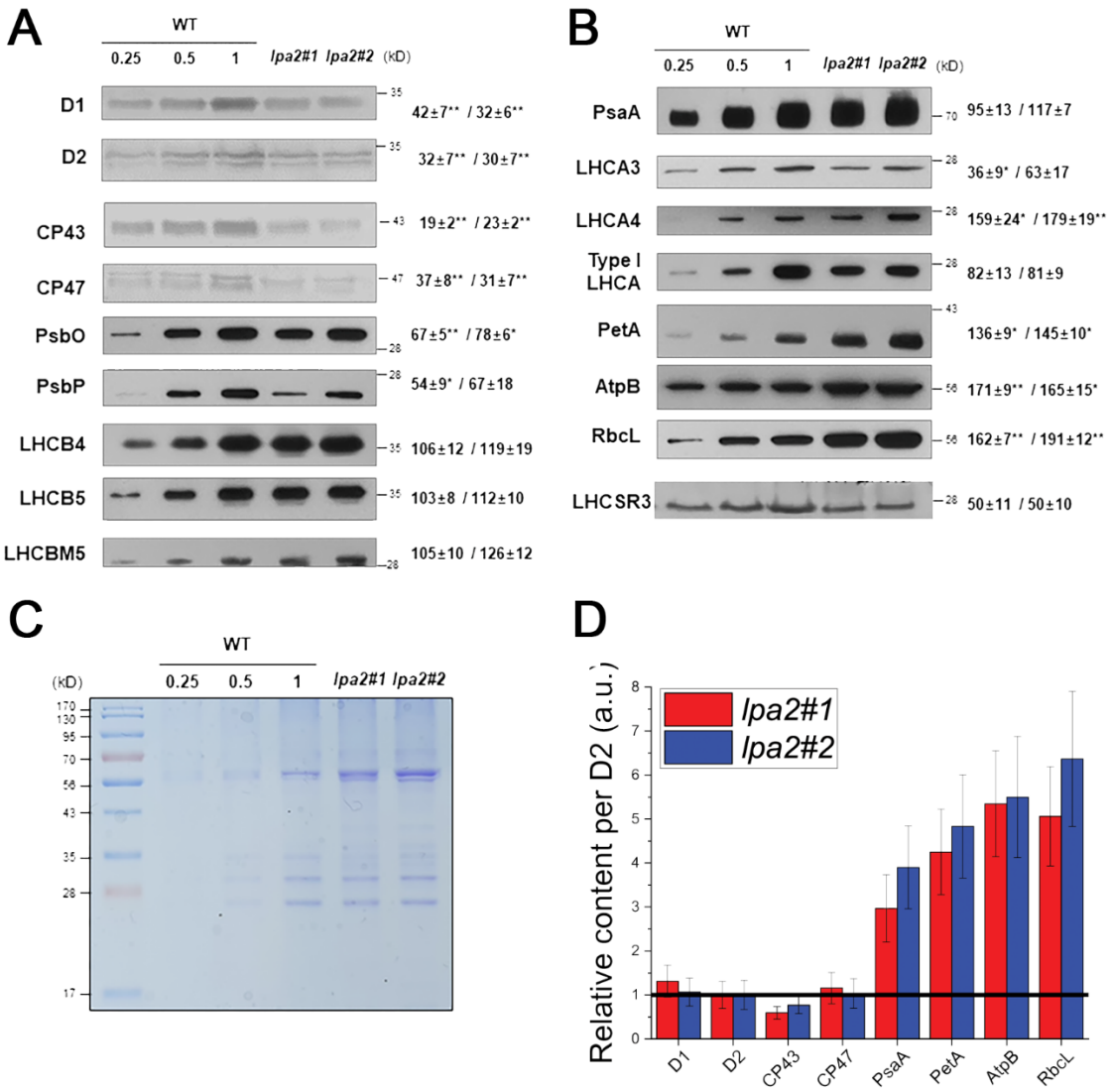

Figure 7. *Immunoblot analysis (**A, B**,) and Coomassie blue-stained SDS-PAGE gel (**C**) and of chloroplast proteins from the wild type (WT) and lpa2 mutants. Results from immunoblotting with antibodies against PSII-LHCII are shown in **A** where specific antibodies recognizing the PSII core subunits D1, D2, CP4, CP47, PsbO and PsbP and the LHCII antenna complexes LHCB4 (CP29), LHCB5 (CP26) and LHCBM were used. For the latter in particular, the antibody LHCBM5 was adopted which was reported to recognize all the different LHCBM subunits. Results from immunoblotting with antibodies against PSI core (α-PsaA), LHCI antenna (α-LHCA3, α-LHCA4), Cyt f (α-PetA), chloroplast ATPase β-subunit (α-AtpB), Large subunit of RUBISCO (α-RbcL) and LHCSR3 are shown in **B**. Each lane was loaded on a per Chl basis (1 μg), and the WT samples were loaded at three different concentrations (0.25, 0.5, and 1 μg). The amounts of proteins in the lpa2#1 and lpa2#2 mutants compared to the WT are presented next to the protein bands expressed as percentage of WT level (n ≥ 3; the values shown are means ± SD). The statistical significance of differences between WT and lpa2 is indicated as * $p < 0.05$ and ** $p < 0.01$, as determined by Student t-test. In Panel **D** the protein content of D1, D2, CP43 CP47, PsaA, PetA, AtpB and RUBISCO were also reported normalized to D2 content, with the different ratios set as 1 in the case of WT (black line). (**E**) autoradiography of immunoprecipitated PSII complexes. C. reinhardtii WT and lpa2 mutants' cells were grown in TAP medium at low light (70μmol $m^{-2}s^{-1}$) in presence of [^{35}S] methionine and [^{35}S] cysteine at different timing (pulses) indicated on top of the figure in minutes. PSII core complexes were extracted from thylakoid membranes by membrane solubilization and immunoprecipitation using D2 antibody. Chase experiments were performed after 60 minutes of pulse removing the labelled amino acids from the growth medium. The bands corresponding to D1/D2 and CP43/CP47 were identified according to their migration pattern, as reported in Panel **F** where immunoblotting results obtained on thylakoids membranes isolated from WT and loaded on the same SDS-PAGE gel system as in the case of **E**.*

3.3.7 PSII photosensitivity and D1 repair in lpa2 mutants

PSII complexes which are not fully assembled are highly unstable and more sensitive to high light treatment, which causes photooxidation (Fu *et al.*, 2007). We monitored the level of D1 protein during high light (500 μmol m^{-2} s^{-1}), exposure in the presence or absence of lincomycin, a chloroplast protein biosynthesis inhibitor (Supporting Information Figure S5). In the *lpa2* mutant, the relative level of D1 protein decreased faster than in the WT when they were shifted from low light to high light, suggesting an increased photosensitivity of PSII complexes in the mutants. To explore the photosensitivity of PSII in *lpa2* mutants and the potential role of the LPA2 protein in repairing D1 subunit, we performed light shift experiments and monitored the rate of photoinhibition and recovery. After exposure to strong light (1800 μmol m^{-2} s^{-1}), the Fv/Fm values were remarkably reduced in *lpa2* mutants (Figure 8A), with a considerably faster rate than that of the WT, suggesting a strong photosensitivity in the absence of the LPA2 protein. Upon shift to low light (15 μmol m^{-2} s^{-1}), PSII repair mechanisms were activated: the PSII repair occurred faster in the *lpa2* mutants (Figure 8B). On a longer time, PSII repair in the WT was more effective, leading to the restoration of higher Fv/Fm values than those in *lpa2* mutants. These results are consistent with the reduced CP43/CP47 incorporation in PSII complexes resulting in pulse experiments at longer time scale (60- or 120-minutes pulses).

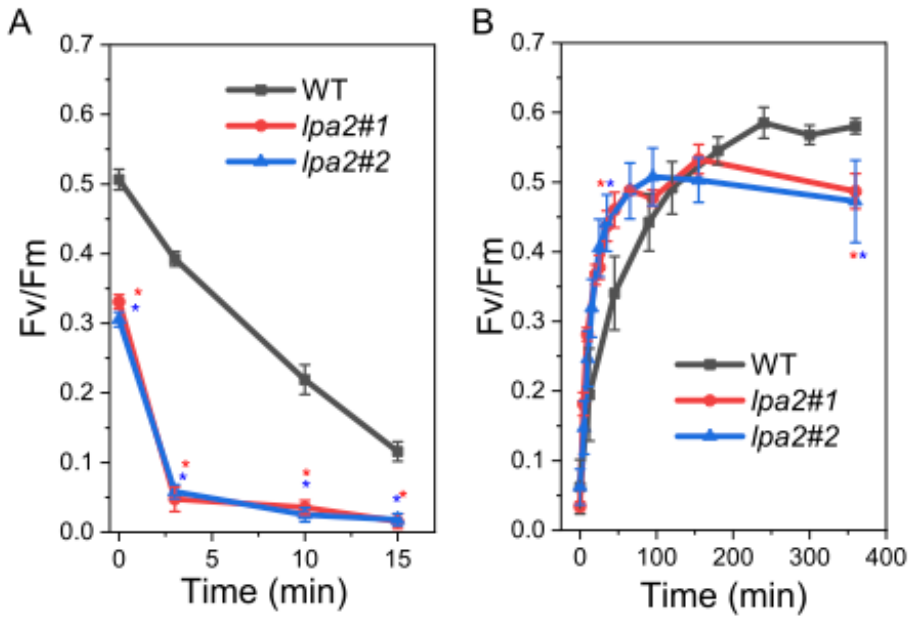

Figure 8. *Kinetics of PSII activity photoinhibition and repair. Kinetics of PSII photoinhibition (A) and repair (B) was measured following the changes in maximum quantum yield (Fv/Fm) after exposure to strong light (1800 μmol m^{-2} s^{-}*

*[1]). Panel A: kinetics of PSII activity (Fv/Fm) photoinhibition. Panel B: kinetics of Fv/Fm recovery in low light (15 µmol m^{-2} s^{-1}) after exposure to strong light (1800 µmol m^{-2} s^{-1}) for 15 minutes in the case of lpa2 mutants and 25 minutes in the case of WT. Error bars are indicated as standard deviation (n = 3). The statistical significance of differences between WT and lpa2 mutants ($p < 0.05$) is indicated as *, as determined by Student t-test.*

3.4 DISCUSSION

Here, we demonstrate that differently from previous report (Ma *et al.*, 2007), a LPA2 homolog is present in the model organism for green algae *C. reinhardtii*. Moreover, we found LPA2 homologs in different *Chlorophytes*, but not in cyanobacteria, or in other eukaryotic algae species, suggesting that LPA2 evolved specifically in eukaryotes belonging to the green lineage. Therefore, to expand our understanding of PSII biogenesis and assembly in green algae, we used the CRISPR-Cas9 methodology to investigate this nuclear-encoded protein, LPA2, and elucidate its role in PSII biogenesis via photochemical and biochemical analysis of two independent *lpa2* mutants.

3.4.1 Lack of LPA2 affects PSII assembly in *Chlamydomonas reinhardtii*

The lack of the LPA2 protein, which is localized in the thylakoid membranes, resulted in a strong reduction of the growth of *lpa2* mutants in mixotrophy condition and an almost complete impairment of growth in photoautotrophy (Figure 3). Similar results were previously obtained in *C. reinhardtii* mutants depleted of CP43 (Zerges, Auchincloss and Rochaix, 2003; Marín-Navarro *et al.*, 2007): in the case of *lpa2* mutants CP43 subunit was observed reduced to ~20% of the WT level. In the absence of LPA2 protein, other PSII core subunits were also decreased, with ~60-70% reduced accumulation of CP47, D1 and D2 being lost on a chlorophyll basis in *lpa2* mutants (Figure 7). Pulse-chase experiments showed that, in the absence of LPA2, the assembly of D1/D2 complexes into PSII occurs to similar rate compared to WT. Differently, in the case of CP43/CP47, their assembly into PSII was essentially saturated in *lpa2* mutants in the first 30 minutes while further increased in the WT even after 120 minutes pulse (Figure 7E). The thylakoidal LPA2 protein is thus involved in the assembly of CP43/CP47 to PSII, which also contributes to the stabilization of the overall PSII core complex. It is worth to mention that PSII assembly proceed through the formation of D1/D2/CP47 complex with a following incorporation of CP43: LPA2 could be specifically involved in the assembly of CP43 to PSII, as previously suggested in *A. thaliana* by the retracted work of Ma and coworker (Ma *et al.*, 2007).

Alternatively, LPA2 could be involved in both CP43 and CP47 assembly to PSII: additional research efforts are required to discriminate between these two different hypotheses.

PSII in t3Dhe *lpa2* mutants showed increased photosensitivity (Figure 8 and Supporting Information Figure S5) at high light intensity. D1 is the PSII component that is the most sensitive to excess light energy (Mellis, 1999; Nickelsen and Rengstl, 2013); photodamaged D1 is rapidly replaced with newly synthesized D1 (Nickelsen and Rengstl, 2013; Järvi, Suorsa and Aro, 2015). For D1 replacement, PSII is partially disassembled by the detachment and reassembly of CP43 (Nickelsen and Rengstl, 2013; Järvi, Suorsa and Aro, 2015). Previous works demonstrated that in *C. reinhardtii* de novo PSII assembly and D1 repair are distinct mechanisms occurring in different regions of the chloroplast (Uniacke and Zerges, 2007). Indeed, despite a slower PSII turnover rate observed in the case of *lpa2* mutants during chase experiments, D1 repair was enhanced in the shorter time scale in the mutants upon strong light exposure (Figure 8). Faster recovery of PSII activity in *lpa2* mutants (Figure 8B) could be related to increased activation of D1 repair mechanism as an acclimation response due to increased photosensitivity of the partially assembled PSII complexes occurring in the absence of LPA2 protein. In *A. thaliana*, LPA3 is a major factor required for CP43 detachment during D1 repair; no evidence suggests that LPA2 is involved in PSII repair (Chi, Ma and Zhang, 2012; Järvi, Suorsa and Aro, 2015). Our D1 regeneration results in *C. reinhardtii lpa2* mutants indicate that indeed the involvement of LPA2 in PSII repair is limited and related to longer time scale, while the main role of this protein is occurring in *de novo* biogenesis of PSII.

3.4.2 Lack of LPA2 affects the accumulation of the photosynthetic machinery

The absence of the LPA2 protein increased the F_0/Chl ratio and caused an increased contribution of the 77 K fluorescence emission spectra at 680 nm in the *lpa2* mutant, indicating that the efficiency of excitation energy transfer from the antenna complex to the reaction center is reduced because of the partial disconnection of the PSII-LHCII supercomplex (Figure 2E, Supporting Information Figure S2). Likewise, native Deriphat-PAGE showed a lower level of the PSII-LHCII supercomplex in the mutant, if any, but the unconnected LHCII remained as a free antenna (Figure 6). A large decrease in CP43 and CP47 in the mutants implies that *C. reinhardtii* LPA2 participates in their accumulation, as these subunits are an important link between the PSII reaction center and the antenna

complex. The reduced PSII assembly in *lpa2* mutants caused a reduction of PSII activity (Figure 4), which contributed to the reduced growth phenotype observed in the *lpa2* mutants (Figure 3), which became even more severe under photoautotrophic conditions causing the whole-cell metabolism to rely on photosynthesis. The increase in the ΦNO of the mutants also indicated insufficient photoprotective regulation of energy dissipation (Supporting Information Figure S3), in agreement with the increased photosensitivity of PSII in these mutants and posing a serious problem for *lpa2* mutants' survival without a carbon source (Figure 3). One of the main photoprotective mechanism in green algae, NPQ was reduced in *lpa2* mutants, despite the trigger for this mechanism, protons accumulation in the lumen (Peers *et al.*, 2009), was similar compared to WT, as resulting from ECS measurements (Figure 5C). Accordingly, LHCSR3 content was reduced in the absence of LPA2 protein (Figure 7), but the ratio between LHCSR3 and PSII was similar in WT and *lpa2* mutants. However, it is worth to note that LHCSR proteins has been reported to functions as a quencher also at the level of disconnected LHCII (Dinc *et al.*, 2016) and PSI-LHCI antenna (Kosuge *et al.*, 2018; Girolomoni *et al.*, 2019), with LHCSR3/LHCII and LHCS3/PSI ratios being reduced in the *lpa2* mutants (Figure 7). Moreover, LHCSR3 expression and maximum NPQ activity should be investigated in high light, while *lpa2* mutants presented a reduced growth phenotype even at low light (Peers *et al.*, 2009): further work is required to investigate more deeply the reason for the low NPQ phenotype of *lpa2* mutants. Another mechanism previously reported to be involved in photoprotection of *C. reinhardtii* is the migration of balance of excitation pressure among PSI and PSII by state transitions (Allorent *et al.*, 2013). The increase state transition capacity of *lpa2* mutants could be a consequence of the reduced PSII activity, inducing a migration of antenna proteins toward PSI. Alternatively, the reduced PSII-LHCII supercomplex formation might cause and increased fraction of mobile LHCII, resulting in increased state transitions capacity.

Unlike PSII, the abundance of PSI core subunits and PSI activity were not reduced by the lack of LPA2 protein (Figure 7, Figure 5) with a consequent increase of the PSI/PSII ratio in the mutant. These findings differ from those of previous studies showing lower PSI activity in mutants defective in PSII biogenesis (Zhang *et al.*, 2011; Wang *et al.*, 2013), including the case of *lpa2* mutants in *A. thaliana* (Ma *et al.*, 2007). These features suggest

that in *C. reinhardtii* the *lpa2* mutants might preferentially operate PSI-mediated electron transport flow to release excitation pressure and generate trans-thylakoid proton transport to compensate for the inactive PSII. Indeed, the fraction of CEF, which is critical in maintaining the *pmf*, was higher in the *lpa2* mutants than in the WT (Figure 5).

The imbalance between PSII and PSI in the *lpa2* mutants resulted in another interesting phenotype: over accumulation on a chlorophyll basis of the cytochrome b_6f complex and Rubisco, which are involved in down-stream photosynthetic reactions (Figure 7D). Similarly, ATP synthase content was increased in *lpa2* mutants, suggesting a possible faster relaxation of lumen acidification. However, the observed reorganization of the photosynthetic apparatus in the *lpa2* mutants is not sufficient to sustain photoautotrophic growth, likely because of the reduced PSII dependent linear electron flow, causing a consequent reduced NADPH formation and increased photosensitivity.

3.4.3 Comparison between LPA2 functions in *Chlamydomonas reinhardtii* and Arabidopsis thaliana

Comparing the effect of *lpa2* mutation in *C. reinhardtii* with the previous retracted results reported in the *A. thaliana* (Ma *et al.*, 2007), several features were shared, as severely reduced growth, reduced PSII assembly, strong reduction in PSII core subunits accumulation, reduced PSII activity and photochemical efficiency, and increase in Cyt *f* content and ATPase (Ma *et al.*, 2007). However, in the case of *C. reinhardtii* an increase PSI/PSII ratio and increased P700 activity on a chlorophyll basis were evident in the *lpa2* mutant, while in *A. thaliana* both PSI accumulation and P700 activity were lower compared to the WT case. In the absence of LPA2 protein causing reduced PSII assembly, the cell acclimation mechanisms were thus partially different in *C. reinhardtii* compared to *A. thaliana*, with a specific increase in PSI activity in the former. Moreover, here we report increased RUBISCO content, increased state transitions, increased CEF, increased D1 repair but reduced NPQ capacity in *C. reinhardtii* in *lpa2* mutants, while similar acclimation events in the case of *A. thaliana lpa2* mutants were not investigated up to now, to our knowledge.

In conclusion, the knockout mutation of *LPA2* in *C. reinhardtii* resulted in a drastic reduction in the level of PSII, with a concomitant decrease in its efficiency. In the absence

of the thylakoidal LPA2 protein, not only the accumulation of CP43/CP47/D1/D2 were strongly reduced, but residual PSII was more prone to photoinhibition leading to increased D1 repair on a short time scale. However, further studies are required to understand the detailed mechanism by which LPA2 plays that role. The process of PSII protein assembly is complicated, and the functions of various assembly factors are almost certainly coordinated. Some of these factors such as LPA1/rep27, PAM68, and Alb3, which function in the same step, could form a protein complex (Armbruster *et al.*, 2010); thus, building a protein interaction network that can provide a comprehensive view of the interplay among different assembly factors, repair complexes, and PSII subunits is necessary. PSII assembly factors such as Alb3 and PAM68 emerged early in the evolution of photosynthetic organisms because they are present in all cyanobacterial groups, green algae, and embryophytes (Chi, Ma and Zhang, 2012). Conversely, LPA2 is present in the green lineage (Figure 1), but no homolog of LPA2 has been identified in the cyanobacterium *Synechocystis* PCC6803, red algae, glaucophytes, and algae that contain a red algal plastid, suggesting that LPA2 appeared in the green plant lineage (Chi, Ma and Zhang, 2012). It is worth to note that during the revision process of this work, a preprint was released reporting a role of LPA2 in PSII assembly in *C. reinhardtii*, essentially confirming the results herein described (Spaniol *et al.*, 2021).

3.5 EXPERIMENTAL PROCEDURES

3.5.1 Sequence alignments and phylogenetic analysis

LPA2 homologs were identified in the NCBI non-redundant protein sequences database using BlastP. The obtained sequences showed a Blast query coverage more than 50 % of the alignment and at least 40 % amino acid identity to LPA2 of *A. thaliana* or *C. reinhardtii*. Additionally, we searched more homolog sequences in the DOE-JGI Phytozome proteome database using Blast and selected sequences that matched the HMM profile with an e value < 10^{-3} (Potter *et al.*, 2018). The species and accession numbers of LPA2 homologs were summarized in Table S1. LPA2 homolog was not found in *Glaucocystophyceae*, *Rhodophyta*, *Cryptophyceae*, *Haptista*, *Rhizaria*, *Stramenopiles* and *Alveolata*. The amino acid sequences were aligned using MUSCLE with the default settings of Geneious R10 software and the non-conserved regions of the alignment were trimmed manually using Mesquite software

Version 3.61 (http://www.mesquiteproject.org). Maximum likelihood tree was constructed using PhyML3 with 100 bootstrap analysis (Guindon *et al.*, 2010). The WAG substitution model was selected assuming an estimated proportion of invariant sites and four gamma-distributed rate categories by SMS (Whelan and Goldman, 2001; Lefort, Longueville and Gascuel, 2017). The obtained tree was visualized and edited using Archaeopteryx ((Whelan and Goldman, 2001; Lefort, Longueville and Gascuel, 2017). The obtained tree was visualized and edited using Archaeopteryx (http://www.phylosoft.org/archaeopteryx).

3.5.2 CRISPR-Cas9-driven mutagenesis

All procedures were performed according to (Baek *et al.*, 2016) by using 100 μg of Cas9 protein and 70 μg of gRNA. After CRISPR-Cas9 transformation, cells were incubated in TAP liquid medium supplemented with 40 mM sucrose for 12 h and harvested for genotype characterization or immediately diluted (to 2 × 103 cells) and plated on TAP medium containing 1.5% agar to obtain single colonies. The colonies were screened on the basis of the Fv/Fm fluorescence signal by using a Walz Imaging PAM System (M-series; Heinz Walz GmbH). To confirm the mutation of the target site, we further analyzed the putative mutants by using Sanger sequencing.

3.5.3 Genotype characterization

Genomic DNA was extracted as described in (Jeong *et al.*, 2018). For Sanger sequencing, the target regions were PCR-amplified by using specific primers (5′-GTAGTGTGCTTACATTTGCTGATT-3′ and 5′-CTACTGCTTCTGGATCTGTCC-3′ for the lpa2 gene locus). The PCR products were separated by agarose gel electrophoresis, eluted from the gel, and sequenced (Macrogen). For targeted deep sequencing, genomic DNA segments that encompassed the nuclease target sites were amplified using Phusion polymerase (New England Biolabs). Equal amounts of PCR amplicons were subjected to paired-end read sequencing by using the Illumina MiSeq platform. The obtained next-generation sequencing data were analyzed using Cas-Analyzer (Park *et al.*, 2017). Reads that occurred only once were excluded to remove errors associated with amplification and sequencing. Insertions and deletions (indels) located around the Cas9 cleavage site (3 bp upstream of the protospacer–adjacent motif sequence) were considered to be induced

mutations by Cas9. The targeted mutation efficiency was calculated from the mutation counts and the total counts of the reads. To examine the occurrence of potential off-target mutation sites, we used Cas-OFFinder (Bae, Park and Kim, 2014), which lists potential off-target sites with a DNA or RNA bulge in length that differ from the on-target sites by up to 4 nucleotides.

3.5.4 Pigment and cell size analysis

Pigment analyses were performed on cells grown in TAP medium at 70 μmol photons m^{-2} s^{-1} by HPLC, as described in (Lagarde, Beuf and Vermaas, 2000). Cell size was investigated using Countless® II FL automated cell counter (Themo Fisher).

3.5.5 Growth conditions

The *C. reinhardtii* strains were grown in minimal (HS) medium or in the presence of acetate (Tap medium; Kropat et al. 2011). Photoautotrophic and mixotrophic growth were evaluated in 80 mL photobioreactors in a Multi-cultivator system (Photon System Instruments, Cech Republic) by growing different strains in either HS or TAP medium in continuous light at 70 μmol photons m^{-2} s^{-1}. Heterotrophic growth was evaluated in cells grown in TAP medium in the dark. Doubling times were calculated from the exponential phase of the growth curve as described in (Gokhale and Sayre, 2009). Spot test was performed spotting cells grown in TAP medium at 70 μmol m−2s−1 at exponential phase. In particular, 3x102, 3x103 and 3x104 cells were spotted in TAP or HS medium with 1% agar added; plates were then exposed to 50, 100 or 300 μmol m−2s−1 for four or six days respectively for cells in TAP or HS media.

3.5.6 2D-Deriphat/SDS-PAGE electrophoresis and western blots

The 2D-Deriphat/SDS-PAGE analysis was performed as described in. Thylakoid membranes isolated according to (Ferrante *et al.*, 2012) from cells in exponential phase grown in TAP medium in continuous light at 70 μmol photons m^{-2} s^{-1}. Isolated thylakoids were solubilized at a *Chl* concentration of 0.5 mg/mL with n-dodecyl-α-d-maltoside (final concentration, 0.75% for both wild type and lpa2), incubated on ice for 10 min, and centrifuged at 20,000 ×g for 10 min to remove unsolubilized material. Thylakoid membrane proteins (25 μg Chl) were loaded in each lane. After separation, one-dimensional native Deriphat–PAGE strips were cut and soaked in SDS-PAGE stacking

buffer containing 5 M urea twice for 25 min each. The proteins were then separated using SDS-PAGE (12% gel containing 2 M urea). The acrylamide gels were stained with Coomassie blue. Immunoblot analysis for profiling chloroplast proteins was performed cells in exponential phase grown in TAP medium in continuous light at 70 μmol photons m^{-2} s^{-1}, as described by (Jeong *et al.*, 2018). Antibodies were purchased from Agrisera (α-D1: AS05084; α-D2: AS06146, α-CP43: AS111787, α-CP47: AS04038, α-PsbO: AS06142-33, α-PsbP: AS06142-23, α-LHCB4: AS06117, α-LHCB5: AS09407, α-LHCBM5: AS09408, α-LHCSR3: AS142766, α-PsaA: AS09408, α-Type I Lhca: AS01005, α-PetA: AS01005, α-AtpB: AS05085-10, α-RbcL: AS03037) except for Lhca3 and Lhca4 antibodies which were provided by Prof. Hippler (Petroutsos *et al.*, 2011; Jeong *et al.*, 2018) and the LPA2 antibody. Polyclonal antibodies for LPA2 protein were raised against two peptides—CGFGSETAKQKEAEAEASTSKP and EALEARIKSRRKGRVEPKVKVC (Abrfontier). In the case of α-LHCBM5 it is important to note that the antibody recognize not only LHCBM5, but all the different LHCBM subunits in *C. reinhardtii*, as previously described (Girolomoni *et al.*, 2017).

3.5.7 Photosynthetic activity analysis

Photosynthetic activity of WT and mutant strains was measured in cells at exponential growth phase grown in TAP medium in continuous light at 70 μmol photons m^{-2} s^{-1}. Before the measurements, cells were washed with HS medium and cultivated in photoautotrophy for 12 hours. The PSII activity was analyzed by conducting fluorescence measurements on whole cells by using a Dual-PAM 100 instrument (WALZ). In particular, φPSII, φNO, φNPQ, and NPQ were measured in dark adapted samples (1 hour) using different actinic lights from 0 to 1700 μmol photons m^{-2} s^{-1}. The 77K fluorescence emission spectra were acquired using a charge-coupled device spectrophotometer (JBeamBio), as previously described (Allorent *et al.*, 2013). State transitions were measured on whole cells induced to state 1 or 2, as described in (Fleischmann *et al.*, 1999): in brief, State 1 (S1) was induced by shaking vigorously cells in a low light (~5μmol m-2 s-1) with 10μm of DCMU for at least 15 min to oxidize the plastoquinone pool while State 2 (S2) was induced by adding 250 μm sodium azide to inhibit mitochondrial respiration and to reduce the plastoquinone pool. The P700 activity was measured using the Dual-PAM 101 following the kinetics of transient absorption at 830 nm after exposure to actinic light. The maximum

P700 activity was measured after a pulse of saturating light. Electrochromic shift measurements were performed using a Photosynq that set the actinic light at 500 μmol photons m^{-2} s^{-1}. Light-dependent O_2 evolution curves were measured using Clark electrode, as reported in (Perozeni, Cazzaniga and Ballottari, 2019). Light dependent O_2 evolution was also measured at 600 μmol photons m^{-2} s^{-1} in presence of artificial PSII electron acceptor 2,6-Dichloro-1,4-benzoquinone (DCBQ) 0.25 mM, 1mM Potassium ferricyanide(III) and 1mM Dibromothymoquinone (DBMIB) (Brinkert *et al.*, 2016). PSII repair kinetics were measured after exposure to strong light (1800 μmol photons m^{-2} s^{-1}) until the Fv/Fm values were reduced to 0.05. PSII regeneration was then induced in low light (15 μmol photons m^{-2} s^{-1}) by measuring the Fv/Fm. The Fv/Fm values were measured after 3 min dark adaptation of whole cells.

3.5.8 Pulse-chase and immunoprecipitation

Immunoprecipitation experiments were performed in cells in exponential phase grown in TAP medium in continuous light at 70 μmol photons m^{-2} s^{-1} as described by (De Marchis *et al.*, 2018) for tobacco protoplasts, with minor modifications. In brief, approximately three million algae cells as sample were subjected to pulse-labelling up to 2 h by using Pro-Mix (a mixture of [^{35}S]Met and [^{35}S]Cys; GE Healthcare Little Chalfont, Buckinghamshire, United Kingdom). After the pulse, chase was performed by adding unlabeled Met and Cys to final concentrations of 10 and 5 mM, respectively. Cells were sampled at different pulse and chase time points. The cells were homogenized by adding homogenization buffer (150 mm Tris–Cl, pH 7.5; 150 mm NaCl; 1.5 mm EDTA; 2% Triton X-100; and Complete protease inhibitor cocktail [Roche]) to frozen samples. Proteins were immunoselected using rabbit polyclonal antisera against D2. The immunoprecipitates were analyzed using SDS-PAGE. After electrophoresis, gels were treated with AmplifyTM fluorography reagent (GE Healthcare), dried, and exposed for fluorography.

3.5.9 The de novo biosynthesis of D1 protein

To block the translation of the chloroplast-encoded D1 protein, we added lincomycin, an inhibitor of plastid protein biosynthesis, to the cultures, as described in (Jin *et al.*, 2003), and the cells were incubated in TAP medium under either normal growth light (50 μmol photons m^{-2} s^{-1}) or high light (500 μmol photons m^{-2} s^{-1}). Cells were harvested at 0, 30, 60,

and 90 min after the light treatment, and the cell pellets were resuspended in Laemmli sample buffer (Laemmli, 1970) without bromophenol blue. After vigorous vortexing, the protein content of the crude extracts was measured using Bradford reagent (Bio-Rad).

3.5.10 RNA expression analysis

Total RNA was isolated from high light–treated cells in TAP medium by using an RNeasy Plant Mini Kit (Qiagen). Total RNA (1 μg) was used as a template for cDNA synthesis by using SuperScript III reverse transcriptase (ThermoFisher Scientific). Next, the cDNA was used as a template to amplify PsbC with real-time PCR by using SYBR Premix Ex Taq II (TaKaRa) and a Thermal Cycler Dice Real Time System (TaKaRa). The relative quantities of the transcript were normalized to those of the constitutively expressed RACK1 gene. The following primer sequences used for the amplification: 5′-CAAGAACGTCGTGCTGCTGAA-3′ and 5′-CCTGCGTGCCATAAGTGACC-3′for ELIP2, (Cre09.g393173),5′-CAACTACAGCTGGGTGATCCT-3′ and 5′-AGTGTCCAGCTCCCTTTCAG-3′ for LPA2, and 5′-GGCTGGGACAAGATGGTCAA-3′ and 5′-GAGAAGCACAGGCAGTGGAT-3′ for RACK1(Cre06.g278222).

3.6 Supporting Figures

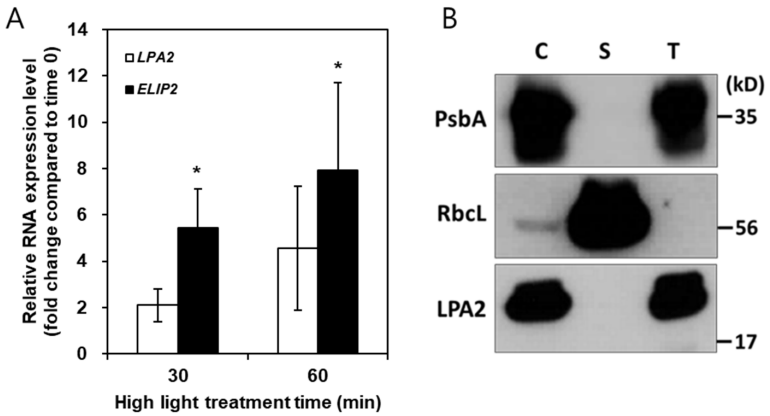

***Figure S1**: Gene expression and localization of LPA2 in C. reinhardtii. A. RNA expression analysis of LPA2 gene with ELIP2 (Cre09.g393173) in Chlamydomonas reinhardtii. qRT PCR was performed with the RNAs extracted from wild type cells exposed to high light (500 µmol photons m−2 s−1) for 0, 30, and 60 minutes. The relative RNA expression level was calculated based on the level obtained at 0 min (value =1) and the values shown are the fold change compared to time 0 upon normalization to the internal control RACK 1. Error bars are reported as standard deviation (n=3). The statistical significance of differences between 0 time to 30 min and 60min are indicated as *, as determined by the Student t-test (*p < 0.05). B. Immunoblot analysis of wild type C. reinhardtii fractions. C, chloroplast fraction; S, stroma fraction; T, thylakoids fraction. Proteins were loaded on an equal protein basis (30 µg).*

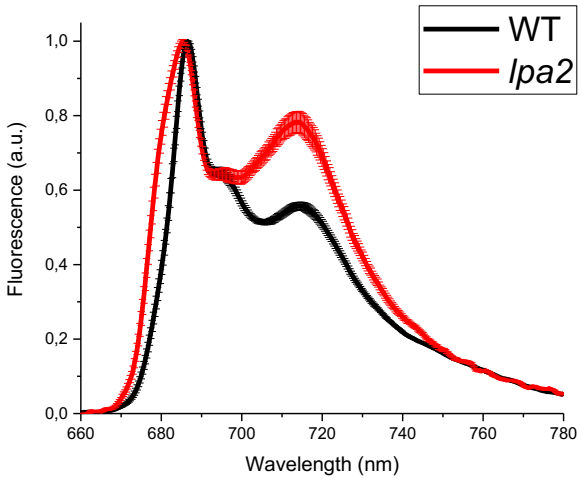

***Figure S2**. 77K fluorescence emission spectra of wild type (WT) and lpa2 mutant. Fluorescence emission spectra are reported in the case of lpa2#1 mutant. Similar results were obtained in the case of lpa2#2 mutant, as reported in Figure S4. Cells grown in TAP medium were washed with HS medium and grown in photoautotrophy for 12 hours. Before the measurements cells were incubated in the dark on a shaker for one hour. Fluorescence emission spectra were normalized to the maximum peak (at 686.5 nm in the case of WT and 685.5 nm in the case of lpa2 mutant). Error bars are reported*

as standard deviation (n=3). The statistical significance of differences at 680 nm and 715 nm between WT and lpa2 were verified by Student t-test obtaining p-values respectively of 0.001 and 0.003.

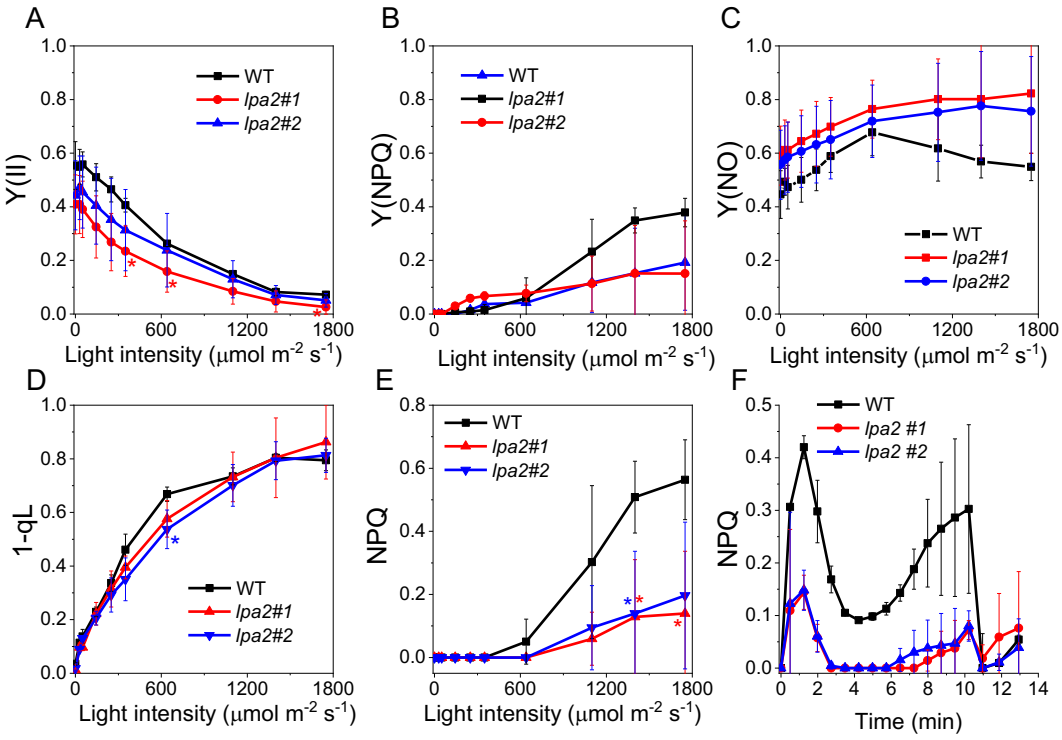

***Figure S3**. Light intensity response curves of fluorescent photosynthetic parameters. Intensity response curves for φPSII, φNPQ, and φNO in the wild-type (WT), lpa2#1, and lpa2#2 mutants are shown in A, B, and C, respectively. NPQ and 1-qL are reported in D and E. Kinetics of NPQ induction and recovery are reported in Panel F: NPQ induction were measured with an actinic light of at 1200 µmol m-2 s-1 for 10 minutes followed by dark recovery for 3 minutes. Error bars indicate standard deviation (n = 3). The statistical significance of differences between WT and lpa2 mutants ($p < 0.05$) is indicated as *, as determined by Student t-test.*

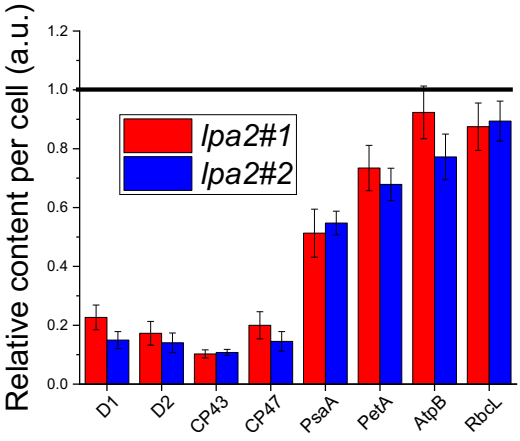

***Figure S4**. Accumulation of photosynthetic proteins per cell in lpa2 mutants. Immunoblotting results reported in Figure 7 were obtained loading the same chlorophyll content on SDS-PAGE gel. Here, on the base of the Chl/cell ratio*

of WT and lpa2 mutants, the protein content on a cell of D1, D2, CP43 CP47, PsaA, PetA, AtpB and RUBISCO are reported in the case of lpa2 mutants. Black line indicates the protein content on a cell basis in the case of WT, set to 1 for the different proteins herein investigated.

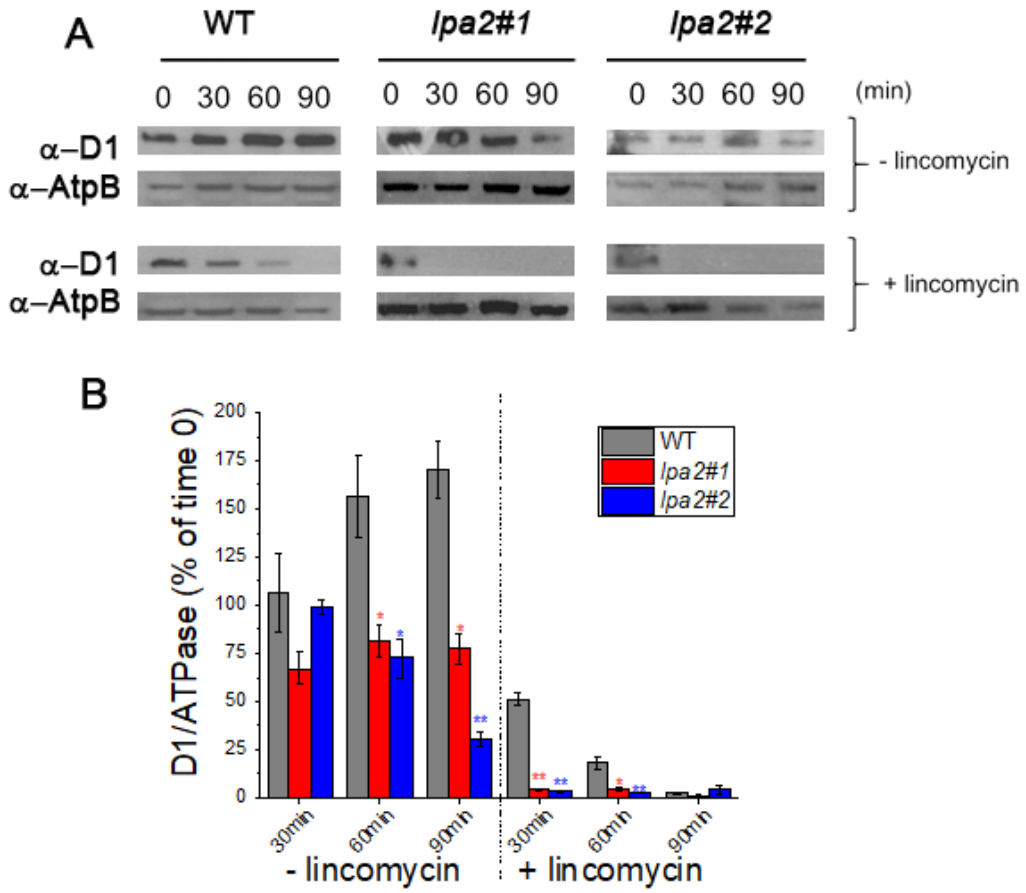

***Figure S5**. Time course analysis for the loss of the D1 protein after a low light to high light shift. Cells grown in TAP medium in low light (70 µmol photons m–2 s–1) were transferred to high light (500 µmol photons m–2 s–1) in presence (+) or absence (-) of 5 mM lincomycin. Immunoblots (A) were probed with anti-D1 proteins and anti-AtpB proteins. The results obtained were quantified by densitometry and the data obtained: D1/AtpB ratios were calculated for each time point as expressed as percentage of D1/ATP measured at time 0 in presence or absence of lincomycin (B). Error bars indicate standard deviation (n = 2). The statistical significance of differences between WT and lpa2 mutants at the different time points is indicated as ** for p < 0.01 or * for p < 0.05, as determined by Student t-test.*

3.7 SUPPORTING TABLES

Table S1*. Accession numbers of LPA2 homologs used in phylogenetic analysis.*

Species	Group	Gene bank/Phytozome accession number
Chlamydomonas reinhardtii	Chlorophyte	Cre02.g105650
Volvox carteri	Chlorophyte	Vocar.0083s0005.1
Micromonas sp. RCC299	Chlorophyte	XP_002504630.1
Ostreococcus tauri	Chlorophyte	XP_003084445.1
Chlorella variabilis	Chlorophyte	XP_005849843.1
Physcomitrium patens	Bryophyte	XP_024366975.1
Ceratodon purpureus 1	Bryophyte	KAG0578248.1
Ceratodon purpureus 2	Bryophyte	KAG0617694.1
Selaginella moellendorffii 1	Lycophyte	XP_024545296.1
Selaginella moellendorffii 2	Lycophyte	XP_024533501.1
Picea sitchensis	Tracheophyta	ABK23742.1
Brachypodium distachyon	Monocotyledoneae	Bradi3g02420.1
Musa acuminata	Monocotyledoneae	GSMUA_Achr1T08220_001
Oryza sativa	Monocotyledoneae	Os02g03250
Panicum hallii	Monocotyledoneae	Pahal.1G020400.1
Setaria viridis	Monocotyledoneae	Sevir.1G102700
Sorghum bicolor	Monocotyledoneae	Sobic.004G023400
Zea mays	Monocotyledoneae	GRMZM2G043500_T01
Arabidopsis thaliana	Dicotyledoneae	AT5G51545
Brassica rapa FPsc	Dicotyledoneae	Brara.C01471
Capsella rubella	Dicotyledoneae	Carubv10027154m
Eutrema salsugineum	Dicotyledoneae	Thhalv10015015m
Glycine max	Dicotyledoneae	Glyma.09G232600
Medicago truncatula	Dicotyledoneae	Medtr4g035825
Nicotiana tabacum 1	Dicotyledoneae	XP_016496621.1
Nicotiana tabacum 2	Dicotyledoneae	XP_016492480.1
Phaseolus vulgaris	Dicotyledoneae	Phvul.011G004500
Solanum lycopersicum	Dicotyledoneae	Solyc03g083570.2.1
Trifolium pratense	Dicotyledoneae	Tp57577_TGAC_v2_mRNA15623

Table S2*. Target sequences of sgRNA used to recognize the lpa2 gene.*

	RGEN target (5' to 3')	Position	Direction	GC content (%, w/o PAM)	Out-of-frame score	Mismatches				
						0	1	2	3	4
sgRNA1	GTTGTCCGCTCCAAGGGCTTTGG	79	+	60	59.4	1	0	0	0	8
sgRNA2	CAAGGGCTTTGGTTCAGAGACGG	90	+	50	74.4	1	0	0	0	5
sgRNA3	GCAAGCACCTCCAAGCCGTCGGG	139	+	65	50.2	1	0	0	2	17
sgRNA4	CAAGGGGCGTGTTGAGCCCAAGG	216	+	65	62.7	1	0	0	0	11

Table S3. *Mutation (insertion and deletion; indel) frequency of wild type and RGEN-transfected cells for each sgRNA*

Target sites	Cells	Total counts	Mutation counts	Mutation ratio (%)
lpa2	Wild type	53898	21	0.00%
	gRNA1	52609	71	0.10%
	Wild type	42061	3	0.00%
	gRNA2	41760	172	0.40%
	Wild type	32156	2	0.00%
	gRNA3	34532	492	1.40%
	Wild type	334	0	0.00%
	gRNA4	316	0	0.00%

***Table S4**. Analysis of off-target effects in the wild type and lpa2 mutant. Mutation frequencies at potential off-target sites of the lpa2 gene-specific sgRNA2 were measured by targeted deep sequencing in the wild type and lpa2 #1 and #2. Potential off-target sites that differed from the on-target sites by up to 4 nucleotides were selected. Different nucleotides between the on-target and off-target are highlighted in red.*

Target (5′ to 3′)	Cells	Total counts	Mutation counts	Mutation ratio (%)
	Wild type	31640	0	0.00%
CAAGtGCTTTGGcTtcGAGACGG	*lpa2* #1	23022	0	0.00%
	lpa2 #2	14267	0	0.00%
	Wild type	145319	53	0.00%
gAAGGGCTgTGGgTCAGAGgAGG	*lpa2* #1	129094	63	0.00%
	lpa2 #2	22739	0	0.00%
	Wild type	274203	2190	0.80%
CgAGGGCTTTGGTgCcGgGATGG	*lpa2* #1	255326	1996	0.80%
	lpa2 #2	6752	16	0.24%
	Wild type	165055	747	0.00%
CgAGGGCTTTGGTgCcGgGATGG	*lpa2* #1	155692	622	0.00%
	lpa2 #2	8237	4	0.00%
	Wild type	45015	5	0.00%
CAAGGGCTTcGGTgCAGccAAGG	*lpa2* #1	41168	10	0.00%
	lpa2 #2	25300	2	0.00%
	Wild type	30798	0	0.00%
CAAGcGCTTTGcaTCAGAGgTGG	*lpa2* #1	29474	2	0.00%
	lpa2 #2	20140	2	0.00%

4 IDENTIFICATION OF DISTINCT PH- AND ZEAXANTHIN-DEPENDENT QUENCHING IN LHCSR3 FROM *CHLAMYDOMONAS REINHARDTII*

Julianne M. Troiano[1], Federico Perozeni[2], Raymundo Moya[1], Luca Zuliani[2], Kwangryul Baek[3], EonSeon Jin[3], Stefano Cazzaniga[2], Matteo Ballottari[2], Gabriela S. Schlau-Cohen[1]

1 Department of Chemistry, Massachusetts Institute of Technology, Cambridge MA 02139 USA; 2 Department of Biotechnology, University of Verona, 37134 Verona, Italy; 3 Department of Life Science, Hanyang University, Seoul, Korea.

Published on eLife, 2021 (https://doi.org/10.7554/eLife.60383)

4.1 ABSTRACT

Under high light, oxygenic photosynthetic organisms avoid photodamage by thermally dissipating absorbed energy, which is called non-photochemical quenching. In green algae, a chlorophyll and carotenoid-binding protein, light-harvesting complex stress-related (LHCSR3), detects excess energy via a pH drop and serves as a quenching site. Using a combined *in vivo* and *in vitro* approach, we investigated quenching within LHCSR3 from *Chlamydomonas reinhardtii*. *in vitro* two distinct quenching processes, individually controlled by pH and zeaxanthin, were identified within LHCSR3. The pH-dependent quenching was removed within a mutant LHCSR3 that lacks the residues that are protonated to sense the pH drop. Observation of quenching in zeaxanthin-enriched LHCSR3 even at neutral pH demonstrated zeaxanthin-dependent quenching, which also occurs in other light-harvesting complexes. Either pH- or zeaxanthin-dependent quenching prevented the formation of damaging reactive oxygen species, and thus the two quenching processes may together provide different induction and recovery kinetics for photoprotection in a changing environment.

4.2 INTRODUCTION

Sunlight is the essential source of energy for most photosynthetic organisms, yet sunlight in excess of the organism's photosynthetic capacity can generate reactive oxygen species (ROS) that lead to cellular damage. To avoid damage, plants respond to high light by activating photophysical pathways that safely convert excess energy to heat, which is known as nonphotochemical quenching (NPQ) (Rochaix, 2014). While NPQ allows for healthy growth, it also limits the overall photosynthetic efficiency under many conditions. If NPQ were optimized for biomass, yields would improve dramatically, potentially by up to 30% (Zhu, Long and Ort, 2010; Kromdijk *et al.*, 2016). However, critical information to guide optimization is still lacking, including the molecular origin of NPQ and the mechanism of regulation.

Green algae are a sustainable alternative for biofuels and livestock feed (Wijffels and Barbosa, 2010; Lum, Kim and Lei, 2013). In *Chlamydomonas* (*C.*) *reinhardtii*, the model organism for green algae, light-harvesting complex stress-related (LHCSR) is the key gene product for NPQ. LHCSR contains chlorophyll (*Chl*) and carotenoid (*Car*) held within its protein scaffold. Two isoforms of LHCSR, LHCSR1 and LHCSR3, are active in NPQ, although LHCSR3 is accumulated at higher levels and so has the major role (Peers *et al.*, 2009; Tokutsu and Minagawa, 2013; Maruyama, Tokutsu and Minagawa, 2014; Dinc *et al.*, 2016). While the photophysical mechanism of quenching in light-harvesting complexes has not been determined, the primary proposals involve *Chl-Car* interactions (Ma *et al.*, 2003; Ruban *et al.*, 2007; Liao *et al.*, 2010; De La Cruz Valbuena *et al.*, 2019; Son, Pinnola and Schlau-Cohen, 2020).

NPQ is triggered by a proton gradient across the thylakoid membrane that forms through a drop in luminal pH (Horton, Ruban and Walters, 1996). Lumen acidification generally occurs when the light available causes an imbalance between the proton generation and the capacity of the photosynthetic apparatus to use protons for ATP production (Joliot and Finazzi, 2010). The C-terminus of LHCSR3 contains a number of luminal residues that are protonated upon the pH drop to trigger quenching (Liguori *et al.*, 2013; Ballottari *et al.*, 2016). The pH drop also activates the enzymatic conversion of the *Car* violaxanthin (*Vio*) to zeaxanthin (*Zea*) (Eskling, Arvidsson and Akerlund, 1997). Along with LHCSR, other

homologous light-harvesting complexes are likely involved in quenching (Nicol, Nawrocki and Croce, 2019). In *C. reinhardtii* , the CP26 and CP29 subunits, which are minor antenna complexes of Photosystem II (PSII), have been implicated in NPQ (Cazzaniga *et al.*, 2020). In higher plants, *Zea* has been reported to be involved in NPQ induction by driving light-harvesting complexes into a quenched state and/or by mediating interaction between light-harvesting complexes and PsbS, non-pigment binding subunits essential for NPQ induction in vascular plants (Ahn *et al.*, 2008; Jahns and Holzwarth, 2012; Sacharz *et al.*, 2017). Similarly, *Zea* binding to LHCSR1 in the moss *Physcomitrella patens* and LHCX1 (a LHCSR homolog) in the microalga *Nannochloropsis oceanica* has been shown to be essential for NPQ (Pinnola *et al.*, 2013; Park *et al.*, 2019). Finally, in *C. reinhardtii*, a reduction of NPQ in the absence of *Zea* has been reported (Niyogi, Björkman and Grossman, 1997b). In contrast, recent work has shown *Zea* to be unnecessary for NPQ induction or related to highly specific growth conditions (Bonente, Ballottari, *et al.*, 2011; Tian *et al.*, 2019; Vidal-Meireles *et al.*, 2019). Thus, the contribution of *Zea* to quenching in green algae remains under debate.

Because of the complexity of NPQ and the large number of homologous light-harvesting complexes, the individual contributions and mechanisms associated with LHCSR3, pH, and *Zea* have been challenging to disentangle, including whether they activate quenching separately or collectively. With the power of mutagenesis, the contribution of LHCSR3, and the dependence of this contribution on pH and *Zea*, can be determined. However, *in vivo* experiments leave the molecular mechanisms of LHCSR3 and its activation obscured. *in vitro* experiments, and particularly single-molecule fluorescence spectroscopy, are a powerful complement to identify protein conformational states (Krüger *et al.*, 2010; Schlau-Cohen *et al.*, 2014, 2015; Gwizdala *et al.*, 2016; Kondo *et al.*, 2017). A recent method to analyze single-molecule data, 2D fluorescence correlation analysis (2D-FLC) (Ishii and Tahara, 2013a; Kondo *et al.*, 2017) quantifies the number of conformational states and their dynamics, including simultaneous, distinct processes. Thus, the conformational changes associated with NPQ can be resolved.

Here, we apply a combined *in vivo* and *in vitro* approach to investigate NPQ in *C. reinhardtii*. We use mutagenesis, NPQ induction experiments, and fluorescence lifetime measurements on whole cells and single LHCSR3 complexes to show that pH and *Zea*

function in parallel and that either parameter can activate full quenching and prevent ROS accumulation. The pH-dependent quenching in LHCSR3 is controlled by the protonation of residues in the C-terminus as shown by mutagenesis to remove these residues. The *Zea*-dependent quenching is activated even at neutral pH both *in vitro* and *in vivo*. Based on the *in vitro* results, we find two likely quenching sites, i.e., *Chl-Car* pairs within LHCSR3, one regulated by pH and the other by *Zea*. The two quenching processes act in combination to provide different time scales of activation and deactivation of photoprotection, allowing survival under variable light conditions.

4.3 RESULTS

4.3.1 Roles of pH and *Zea* in fluorescence intensity *in vivo* and *in vitro*

To disentangle the contributions of LHCSR, pH, and *Zea*, both *in vivo* and *in vitro* measurements were performed on different *C. reinhardtii* genotypes. Wild type (WT) strains (4A+ and CC4349), a strain depleted of LHCSR3 and LHCSR1 subunits (npq4 lhcsr1; Figure 1—figure supplements 1 and 2) (Ballottari *et al.*, 2016), a strain unable to accumulate *Zea* due to knock out of the enzyme responsible for xanthophyll cycle activation (npq1; Figure 1—figure supplement 3) (Li *et al.*, 2016), and a mutant constitutively accumulating *Zea* due to knock out of the zeaxanthin epoxidase enzyme (zep; Figure 1—figure supplement 3) (Niyogi, Björkman and Grossman, 1997a; Baek *et al.*, 2016) were characterized *in vivo*. A mutant depleted of both LHCSR subunits (npq4 lhcsr1) was chosen rather than a mutant missing only LHCSR3 (npq4) due to the partial ability of LHCSR1 to substitute for LHCSR3 in its absence (Girolomoni *et al.*, 2019).

To assess the ability of these phenotypes to undergo quenching of *Chl* fluorescence, the NPQ levels were measured *in vivo* after cells were acclimated to high light (HL, 500 μmol m-2s-1) for several generations to induce LHCSR expression (WT, npq1, and zep strains) and then exposed to strong light treatment (1500 μmol m-2s-1) for 60 minutes to induce maximum drop in luminal pH and *Zea* accumulation (WT, npq1, zep, and npq4 lhcsr1 strains; data for xanthophyll cycle activation shown in Figure 1—figure supplement 3). The NPQ induction kinetics are shown in Figure 1. In the WT strains, the maximum NPQ level was reached after 10 minutes of illumination and fully recovered in the dark (Figure 1A, black), despite a strong accumulation of *Zea* (Figure 1—figure supplement 3). The

recovery of the NPQ traces to similar levels for all mutants acclimated to HL demonstrated that the photodamage, known as photoinhibition, was limited, if any, for these cells during the 60 minutes of illumination. *Zea*-dependent quenching and the reduction in fluorescence emission due photoinhibition have a similar relaxing time. The low level of these two processes observed in our NPQ measurements also suggests that the major component of NPQ in C.reinhardtii is *Zea*-independent, in agreement with previous results (Bonente, Ballottari, *et al.*, 2011). In contrast, in the case of LL acclimated samples, the NPQ induced by WT and npq1 was much lower compared to the HL acclimated cells, with a significant fraction of NPQ that did not recover in the dark (Figure 1 – figure supplement 4). This suggests the possible induction of photoinhibition in LL acclimated cells exposed to strong light treatment for 60 minutes. In the npq4 lhcsr1 strain, which lacks LHCSR subunits, a null NPQ phenotype was observed in both HL and LL acclimated cells (Figure 1A, purple). These results confirm that LHCSR subunits are responsible for light dependent NPQ in *C. reinhardtii* as previously reported (Peers *et al.*, 2009; Ballottari *et al.*, 2016). Consistent with this conclusion, LHCSR accumulation in LL acclimated samples, which exhibit less NPQ, was strongly reduced compared to the corresponding HL samples (Figure 1 – figure supplement 2).

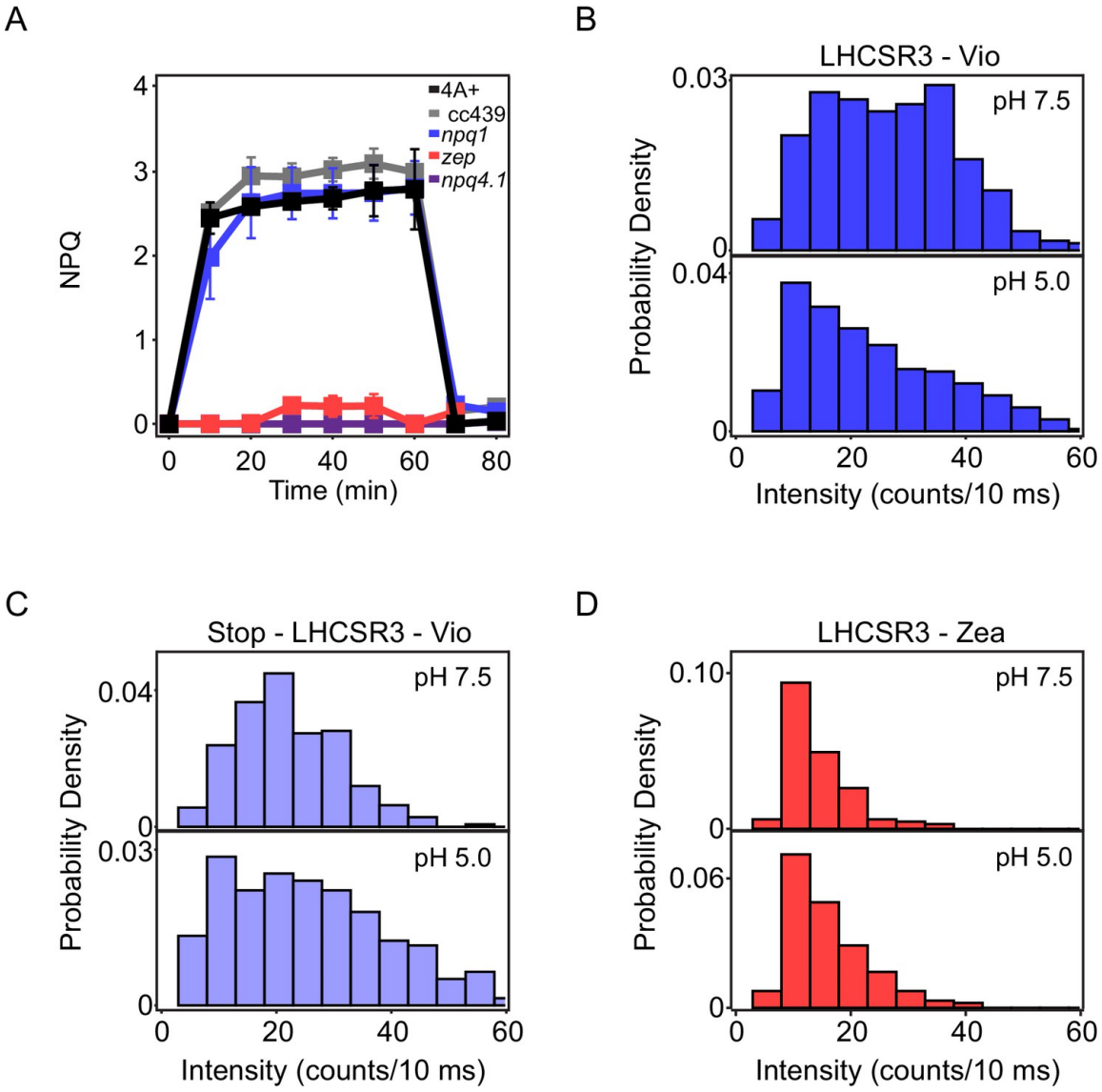

Figure 1. with 10 supplements (in supporting information). Fluorescence measurements of quenching in vivo and in vitro. *(A) In vivo nonphotochemical quenching (NPQ) induction kinetics for high-light acclimated samples measured upon 60 min of high light (1500 µmol m -2 s -1) in vivo. The results are reported as the mean of three independent biological replicates (N=3). Error bars are reported as standard deviation. Kinetics for low-light acclimated samples are shown in Figure 1—figure supplement 4. In vitro single-molecule fluorescence spectroscopy was performed on LHCSR3 (Figure 1—figure supplement 5). The fluorescence intensities measured from ~100 single complexes were used to construct the histograms shown for (B) LHCSR3- Vio, (C) stop-LHCSR3-Vio, and (D) LHCSR3-Zea at pH 7.5 (top) and pH 5.0 (bottom). Statistical parameters are provided in Figure 1—source data 1.*

In the npq1 strain, which lacks *Zea*, no reduction of the maximum level of NPQ was observed compared to its background, the 4A+ WT strain in HL (Figure 1A, blue, black). The similar level and timescales of onset and recovery for NPQ in these two strains suggest a minor role, if any, for *Zea* in light-activated quenching. In the zep strain, which

constitutively accumulates *Zea*, a strong reduction of the NPQ level was observed compared to both WT strains (Figure 1A, red). To understand why, first accumulation of the LHCSR subunits was measured (Figure 1—figure supplements 1 and 2). However, similar LHCSR3 content was found in the WT strains, npq1 and zep mutants. In the case of LHCSR1, similar accumulation was observed in the 4A+ WT strain and zep mutant, while no trace of this subunit was detectable in the CC4349 WT strain. Second, the extent of proton motive force as compared to WT was measured through the electrochromic shift (Bailleul *et al.*, 2010). However, although proton transport into the lumen was reduced in the zep strain at low actinic light, it was similar at the higher irradiance used for measurement of NPQ (Figure 1—figure supplement 6). Therefore, neither differences in LHCSR accumulation nor in proton transport are the cause of the reduced NPQ phenotype in the zep mutant. The PSII maximum quantum yield measured though the photosynthetic parameter Fv/Fm was significantly reduced in the zep mutant compared to the WT case (Figure 1—figure supplement 7), suggesting quenching may be occurring even in dark adapted samples.

In order to investigate the effect of pH and *Zea* at the level of the LHCSR3 subunit, single-molecule fluorescence spectroscopy was used to measure individual complexes *in vitro*. As an initial comparison, we determined the fluorescence intensity from single LHCSR3. Each period of constant intensity was identified (representative intensity traces in Figure 1—figure supplement 5) and the average intensity for each period was calculated. The fluorescence intensities for each period were used to construct histograms as shown in Figure 1B-D. Histograms were constructed for LHCSR3 with *Vio* (LHCSR3-Vio) at high and low pH, which mimic the cellular environment under low and high light conditions, respectively (statistical parameters in Figure 1 — source data 1). The fluorescence intensity decreases, generally along with the fluorescence lifetime, as quenching increases. As shown in Figure 1B, upon a decrease in pH from 7.5 to 5.0, the median fluorescence intensity of LHCSR3-Vio decreased by ~5 counts/10 ms due to an increase in the quenched population, reflecting additional quenching of the excitation energy absorbed. This is consistent with the conclusion from the *in vivo* NPQ experiments that quenching can occur without *Zea* under high light conditions.

Activation of quenching in LHCSR3 was previously suggested to be related to protonation of putative pH-sensing residues present at the C-terminus (Liguori *et al.*, 2013; Ballottari *et al.*, 2016). To assess the role of these pH-sensing residues in pH-dependent quenching, a mutant of LHCSR3 lacking this protein portion (stop-LHCSR3) was produced (Figure 1––figure supplement 8). Stop-LHCSR3 was also measured using single-molecule spectroscopy (Figure 1—figure supplements 9 and 10). Upon the same pH decrease that induced quenching in LHCSR3-Vio, stop-LHCSR3 with *Vio* (stop-LHCSR3-Vio) exhibited similar fluorescence intensity where the median intensity even increases, primarily due to increased heterogeneity in the fluorescence emission at low pH as seen through the standard deviation of the two distributions (Figure 1C, Figure 1—source data 1). The data show that the mutants have lost the ability to activate quenching channels upon a pH drop, highlighting the sensing role of the residues of the C-terminus of LHCSR3.

Single-molecule measurements were also performed on LHCSR3 with *Zea* (LHCSR3-Zea) at high and low pH. Under both conditions, as shown in Figure 1D, LHCSR3-Zea *in vitro* showed a decrease in median fluorescence intensity by ~10-12 counts/10 ms compared to LHCSR3-Vio. The pH-independence of these histograms is consistent with the *in vivo* NPQ measurements in the zep mutants where high light, and the associated pH drop in the lumen, does not change quenching levels (Figure 1A). However, the lower intensity points to the existence of a quenching process that requires only *Zea*, consistent with *in vivo* fluorescence lifetime measurements discussed below.

4.3.2 Roles of pH and *Zea* in fluorescence lifetime *in vitro*

The single-molecule fluorescence intensities are time averages, and so we also analyzed the fluorescence emission from single LHCSR3 through a photon-by-photon method, 2D fluorescence lifetime correlation (2D-FLC) analysis. This method uses the associated lifetime data and is more appropriate to analyze this data as the lifetime decays exhibit complex kinetics (De La Cruz Valbuena *et al.*, 2019). Applying the 2D-FLC analysis to single-molecule data identifies fluorescence lifetime states, which correspond to protein conformations with different extents of quenching, and rates of transitions between states, which correspond to switches between the protein conformations (Kondo *et al.*, 2019).

To determine the number of lifetime states, the distributions of lifetime values were constructed (Figure 2A-D). In a lifetime distribution, lifetime states appear as peaks with varying profiles. Traditional lifetime fitting requires an a priori assumption of the number of exponential terms required to fit a decay curve. In contrast, construction of a lifetime distribution does not require prior assignment of the number of decay timescales, which is particularly important when there are multiple different lifetimes as is the case for LHCSR3 (De La Cruz Valbuena *et al.*, 2019). The lifetime distribution also allows analysis of multi-exponential lifetimes, even for the low signal-to-background regime of single-molecule data. The initial lifetime distribution for each sample was calculated by first performing an inverse Laplace transform of all the lifetime data (time between excitation and emission), which was recorded on a photon-by-photon basis (Figure 2—figure supplement 1). Photon pairs separated by a series of delay times were identified, and a 2D inverse Laplace transform was performed for the photon pairs associated with each delay time (see Methods for details). The final lifetime distributions (Figure 2A-D) were determined by fitting the data in order to optimize the lifetime distributions and to generate the correlation functions, which are discussed in more detail below. For each of the LHCSR3 samples, two lifetime states were observed in the distributions, an unquenched state (~2.5 ns) and a quenched state (~0.5 ns).

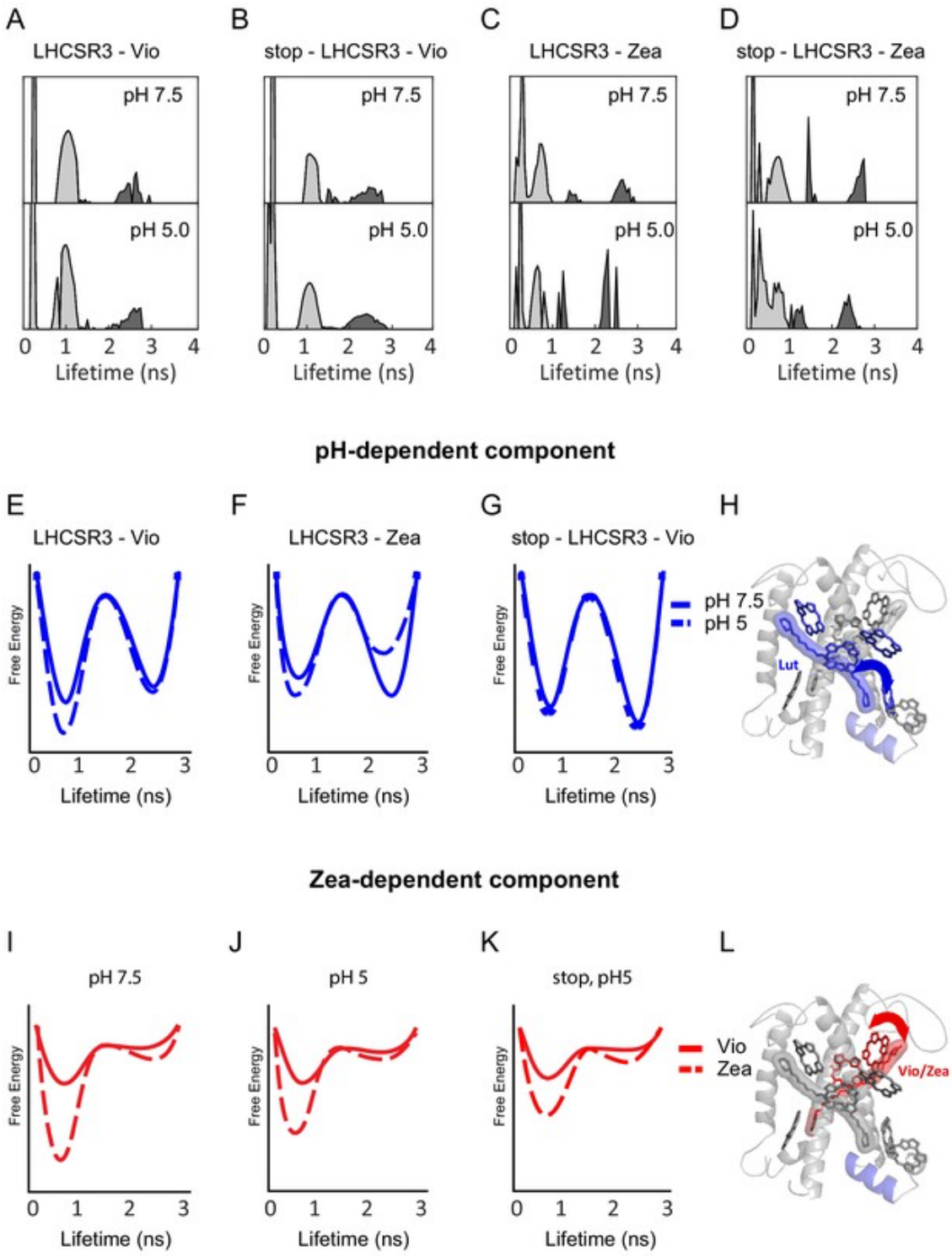

***Figure 2 with 2 supplements (in supporting information)**. pH- and Zea-dependent quenching in LHCSR3. (A-D) Fluorescence lifetime distributions from the global fit in the 2D-FLC analysis for each LHCSR3 sample at pH 7.5 and 5.0 estimated using the maximum entropy method (MEM) to perform an inverse Laplace Transform on the single-molecule emission times. States 1 and 2 are shown in light gray and dark gray, respectively. Free-energy diagrams constructed from the populations and transition rates (Figure 2—source data 1) extracted from the 2D-FLC analysis (E-G and I-K). Structural model with likely quenching sites (H and L) for the effects of pH (top) and Zea (bottom) on protein dynamics.*

The dynamics of the lifetime states were investigated through the auto- and cross-correlation functions for the lifetime states of each sample (Figure 2—figure supplement 2). The correlation function is a normalized measure of how similar the photon emission time, i.e., the lifetime, is as time increases (Nitzan, 2006). Therefore, an auto-correlation function for a given lifetime state contains the timescales for transitions out of the state and a cross-correlation function contains the timescales for transitions between the states (anti-correlation) and similar behavior of the states (correlation) due to processes throughout LHCSR3, such as photobleaching. The auto- and cross-correlations were globally fit to estimate the parameters in the correlation model function given by Eq. 1 in the Methods, which includes the number of lifetime states, the brightness of each state, the population of each state, the rates of transitions between states, and the number of separate processes that transition between states, referred to as dynamic components. The parameters extracted from the fits are given in Figure 2—source data 1 for all samples.

The best fits to the data included three dynamic components, where each component arises from distinct emissive states with separate conformational dynamics within single LHCSR3 (Figure 2—figure supplement 2, Figure 2—source data 1). Correlation-based analysis of the photon fluctuations is a well-established tool to identify the number of independent emissive processes (Mets, 2001; Haustein and Schwille, 2007), and was adapted to determine the number of dynamic components (Kondo *et al.*, 2019). The cross-correlation for all LHCSR3 samples begins above zero (Figure 2—figure supplement 2), which appears in the presence of multiple dynamic components (Kondo *et al.*, 2019). The *Chl* a have the lowest energy levels, and, due to their significantly lower energy than the *Chl* b energy levels, primarily give rise to the emissive states. Because three components were observed within single LHCSR3, they indicate multiple *Chl* a emissive site within each LHCSR3, consistent with previous models of LHCs (Krüger *et al.*, 2010, 2011; Mascoli *et al.*, 2019, 2020). Thus, the dynamic components reflect conformational dynamics that switch between unquenched and quenched lifetime states at different places within LHCSR3.

The rate constants for the transitions between the lifetime states within each component were also extracted from the fit, primarily based on the dynamics of the cross-correlation functions (Figure 2—source data 1). Two of the components exhibit rapid dynamics, which

arise from conformational changes that vary the extent of quenching of the *Chl* a emitters. The timescales of the transitions for one component are tens of microseconds and those for the other are hundreds of microseconds, which are both timescales that would be hidden in traditional single-molecule analyses. The third dynamic component is static at <0.01 s. Due to the lack of dynamics, we assigned the component to emitters far from, and thus unaffected by, quenchers for the unquenched state and partially photobleached complexes for the quenched state.

Finally, the relative populations of the lifetime states for each component were also determined within the model. Assuming a Boltzmann distribution (see Methods), the relative rate constants were used to determine the equilibrium free energy difference between the states for each component (Figure 2—source data 1). The free energy barrier for a transition between states is related to the rate of the transition, which was used to approximate the barrier height (Kondo *et al.*, 2019). These free energy differences and barrier heights were then combined to construct illustrative free energy landscapes, which are shown in Figure 2 for the two dynamic components.

We examined the dependence of the two dynamic components on pH, *Zea* and the C-terminal tail, which contains the pH-sensing residues. Figure 2E and 2F show the pH-dependence of the free energy landscapes for the slower (hundreds of microseconds) dynamic component in LHCSR3-Vio and LHCSR3-Zea, respectively. In both cases, a decrease in pH from 7.5 to 5.0 stabilizes the quenched state. In LHCSR3-Vio, the quenched state is stabilized by a decrease in the transition rate from the quenched to the unquenched state, corresponding to a higher barrier in the free energy landscape. In LHCSR3-Zea, the decrease in the transition rate from the quenched to the unquenched state is also accompanied by an increase in the transition rate from the unquenched to the quenched state, further stabilizing the quenched state relative to the unquenched one. In stop-LHCSR3-Vio, however, no change in the population of the quenched state is observed upon a decrease in pH (Figure 2G), reflecting the expected pH-independence of the sample.

Figure 2I and J show the *Zea*-dependence of the free energy landscapes of LHCSR3 for the faster (tens of microseconds) dynamic component at pH 7.5 and pH 5.0, respectively. At

both pH levels, conversion from *Vio* to *Zea* stabilizes the quenched state via a decrease in the transition rate from the quenched to unquenched state. At pH 5.0, the transition rate to the quenched state increases as illustrated by the lower barrier, which would enable rapid equilibration of population into the quenched state. The *Zea*-dependent behavior is maintained for stop-LHCSR3 (Figure 2K), where the quenched state is still stabilized in the presence of *Zea*.

4.3.3 Roles of pH and *Zea* in fluorescence lifetime *in vivo*

Quenching mechanisms were further investigated *in vivo* by measuring fluorescence emission lifetimes at 77K of whole cells acclimated to low or high light, as traditional NPQ measurements can be affected by artifacts (Tietz *et al.*, 2017). Under these conditions, the photochemical activity is blocked and by following the emission at 680 nm it is possible to specifically investigate the kinetics of PSII, the main target of NPQ. Cells were either grown in low or high light, which determines the level of LHCSR protein (Figure 1—figure supplement 1 and 2) and the fluorescence lifetime was recorded before and after exposure to 60 minutes of high light, which induces ΔpH and determines the level of *Zea*. These light conditions, combined with the genotypes generated, enabled studies that partially or fully separated the contributions of the different components of NPQ.

Whole cell fluorescence lifetime traces show that LHCSR is necessary for the primary light-dependent component of NPQ in *C. reinhardtii* trigged by lumen acidification, in agreement with previous findings (Peers *et al.*, 2009; Ballottari *et al.*, 2016). WT cells and npq1 cells, which lack *Zea*, acclimated to high light show a faster fluorescence decay, or an increase in quenching, after exposure to 60 minutes of high light (Figure 3A, gray bars, fluorescence decays and fits to data shown in SI). For npq4 lhcsr1 cells, which lack LHCSR, similar fluorescence decay kinetics were measured regardless of light treatment (Figure 3A, purple), which is comparable to the unquenched kinetics of WT cells. WT and npq1 cells grown in control light (low LHCSR content) remain unquenched, even after exposure to 60 minutes of high light (Figure 3—figure supplement 1 and 2). These results are consistent with the NPQ measurements shown in Figure 1A. Similar to WT, npq1 cells grown in high light show a faster fluorescence decay after exposure to 60 minutes of high light (Figure 3A, blue bars). While the results from WT show a role for pH and/or *Zea* in

light-induced quenching in LHCSR3, the results from the npq1 strain show that quenching can occur without *Zea*, i.e., induced by the pH drop alone.

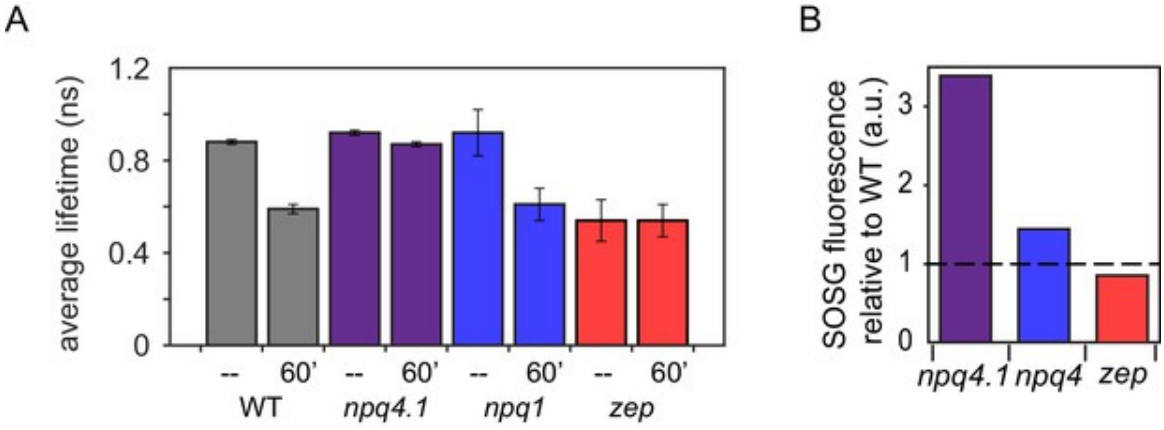

Figure 3 with 6 supplements (in supporting information). Fluorescence lifetime decay of Chlamydomonas reinhardtii whole cells at 77K and singlet oxygen formation*. (A) Fluorescence lifetimes were measured on high light (HL; 500 µmol m -2 s -1) acclimated samples. Each genotype was measured at a dark-adapted state (--) or after 60 min of HL treatment (1500 µmol m -2 s -1 , 60'). WT samples shown here are 4A + strain. Similar results were obtained in the case of CC4349 strain. The npq4 lhcsr1 mutant is indicated here as npq4.1. Fluorescence lifetime values for all genotypes and light conditions are shown in Figure 3—figure supplements 1 and 2. The fluorescence data are provided in Figure 3—source data 1 with fit values in Figure 3—source data 2. (B) Singlet Oxygen Sensor Green (SOSG) fluorescence emission measured for HL acclimated samples relative to WT (4A+ for npq1 and npq4 lhcsr1, CC4349 for zep). Dotted line represents WT level at 1. The results reported are representative of three independent biological replicates for each genotype in low light (LL) or HL. SOSG kinetics are shown in Figure 3—figure supplement 3. LL acclimated samples are shown in Figure 3—figure supplement 4. SOSG emission data is provided in Figure 3—figure supplement 5—source data 1.*

The zep mutant, which constitutively accumulates *Zea*, presented a similar decay among all samples, regardless of high or low light acclimation or light treatment, that was much faster, or more quenched, compared to the decay of dark-adapted WT (Figure 3A, red, Figure 3—figure supplement 1 and 2). These results indicate quenching upon *Zea* accumulation alone, consistent with the reduced Fv/Fm observed in this mutant (Figure 1—supplemental figure 7). This result is also consistent with the pH-independent quenching observed through the single-molecule fluorescence shown in Figure 1D and Figure 2E and 2F. However, the quenching observed in the zep mutant was essentially unchanged in low vs. high light acclimated zep cells suggesting that the *Zea*-dependent quenching observed in zep mutants is a more general process as opposed to one that

occurs solely in LHCSR3 as quenching is observed even in the cells acclimated to low light that lack LHCSR3.

To investigate the generality of this quenching, monomeric or trimeric light-harvesting complexes were isolated from the zep mutant after exposure to 60 minutes of high light, which induces maximum *Zea* accumulation. These complexes had a two-fold higher content of *Zea* compared to the same fraction isolated from WT (CC4349) under the same conditions (Figure 3—supplemental figure 5). The light-harvesting complexes isolated from the zep mutant also showed a 10% decrease in the fluorescence lifetime, suggesting that *Zea*-dependent quenching is at least somewhat shared with other light-harvesting complexes (Figure 3—supplemental figure 6, Figure 3—source data 3, and Figure 3—source data 4). In contrast, no major differences in quenching properties were found in monomeric and trimeric LHC complexes isolated from WT cells before or after exposure to 60 minutes of high light, consistent with previous findings from higher plants and other green algae (Xu *et al.*, 2015; Girolomoni *et al.*, 2020).

4.3.4 Role of *Zea* and NPQ in photoprotection.

The main function of quenching the *Chl* singlet excited states is to thermally dissipate the fraction of absorbed excitation energy in excess of the capacity of the photosynthetic apparatus. Unquenched *Chl* singlet excited states may cause ROS formation and subsequent photoinhibition of their primary target, PSII (Niyogi, 1999). Singlet oxygen is the main ROS species formed at the level of PSII. In order to correlate the NPQ levels and quenching measured with ROS formation, singlet oxygen production was followed in the different genotypes herein investigated by using the fluorescent probe Singlet Oxygen Sensor Green (SOSG) (Flors *et al.*, 2006) (Figure 3B, Figure 3—figure supplements 3 and 4). SOSG fluorescence can be used as a probe to follow singlet oxygen formation, although measuring the true production rates would require a different analytic method. Moreover, SOSG has been reported to produce singlet oxygen itself upon prolonged illumination, and thus requires the use of light filters in order to avoid direct excitation of the dye during high light treatment (Kim, Fujitsuka and Majima, 2013). As expected from the low level of NPQ induction, npq4 lhcsr1, which lacks LHCSR, demonstrated the highest level of singlet oxygen production, regardless of light treatment. Interestingly, the effect of *Zea* was almost negligible in high light acclimated samples (with a very high NPQ induction).

Notably, the amount of singlet oxygen production was correlated with average lifetime (Figure 3A), i.e., inversely correlated with quenching, confirming that the quenching of *Chl* singlet excited states investigated here plays a role in photoprotection.

4.4 DISCUSSION

This work leverages *in vivo* and *in vitro* experimental approaches to investigate NPQ mechanisms in *C. reinhardtii* and the molecular parameters responsible for their activation. In higher plants, both lumen acidification and *Zea* accumulation have been long understood to play a role in the induction of NPQ. While lumen acidification was thought to play a similar role in *C. reinhardtii*, here we characterize the impact of *Zea* accumulation, which had previously been elusive. We also identify the likely conformational dynamics associated with both pH and *Car* composition.

4.4.1 Structural assignment of quenching sites in LHCSR3

Two dynamic components were identified through the 2D-FLC analysis that suggest two distinct photoprotective processes, one pH-dependent and one *Zea*-dependent, operating simultaneously within LHCSR3. Each component likely arises from a *Chl*-*Car* pair, where the *Car* can quench the emissive *Chl*. The two components both have greater population in the quenched state than in the unquenched state (Figure 2—source data 1), consistent with previous work where a quenching component was found to be present in LHCSR3, even at pH 7.5 (De La Cruz Valbuena *et al.*, 2019). By considering the single-molecule results along with previous structural, spectroscopic and theoretical work, we speculate as to the likely sites associated with each component. Although no high-resolution structure of LHCSR3 has been determined, we illustrate possible quenching sites (Figure 2H and L) within a working structural model of LHCSR3 (Bonente et al. 2011). As shown in Figure 2—source data 2, LHCSR3 purified from *C. reinhardtii* contains eight *Chl* molecules (7-8 *Chl* a and 0-1 *Chl* b molecules) and two *Cars* (one lutein (*Lut*) and one *Vio* or *Zea*). Based on sequence comparison with LHCII and CP29, the conserved *Chl* a binding sites are the following: *Chls* a 602, 603, 609, 610, 612 and 613, with *Chls* a604, 608 and 611 proposed as well (Bonente, Ballottari, *et al.*, 2011; Liguori *et al.*, 2016). Previous spectroscopic analysis of LHCSR3 from *C. reinhardtii* has identified the likely binding sites of *Lut* and *Vio*/*Zea* within the structural model (Bonente, Ballottari, *et al.*, 2011).

Given that there are two *Car* bound at the internal sites of LHCSR3, it is likely that each *Car* and its neighboring *Chl* is the major contributor for one of the two dynamic components. The pH-dependent component (Figure 2E-H) likely involves *Lut* and the neighboring *Chl* a 613. Both *Chl* a 612 (coupled to *Chl* as 610 and 611) and *Chl* a 613 have previously been proposed as quenching sites given their physical proximity to the *Lut* (Ruban *et al.*, 2007; Liguori *et al.*, 2016). The *Chl* a 610-612 site contains the lowest energy *Chl* a, which has been shown to be a major energy sink and thus the primary emitter (Schlau-Cohen *et al.*, 2009; Müh, Madjet and Renger, 2010; Novoderezhkin, Marin and Van Grondelle, 2011). Additionally, computational results have shown that the interaction between the *Lut* site and *Chl* a 612 has large fluctuations (Liguori *et al.*, 2015). This agrees with the slower dynamics found for this component. However, recent *in vivo* and *in vitro* analyses found that the removal of *Chl* a 613 results in a reduction in LHCSR specific quenching, while removal of *Chl* a 612 only affected which *Chl* was the final emitter of the complex (Perozeni, Cazzaniga and Ballottari, 2019). While either of these sites are potential quenching sites, it is likely that *Chl* a 613 plays the major role in pH-dependent quenching in LHCSR3 in *C. reinhardtii*.

With a decrease in pH from 7.5 to 5.0, the equilibrium free energy differences for the pH-dependent component, which were calculated using the relative rate constants from the global fit, were shifted toward the quenched state by over 200 cm-1 in LHCSR3-Vio and over 500 cm-1 in LHCSR3-Zea (Figure 2—source data 1). The specific conformational change upon protonation that leads to this stabilization remains undetermined. However, proposals in the literature include reduced electrostatic repulsion in the lumen-exposed domain causes a change in the distance and/or orientation between the helices (Ballottari *et al.*, 2016) and an increase in protein-protein interactions (De La Cruz Valbuena *et al.*, 2019). These conformational changes could produce a displacement of *Lut* towards *Chl* a 613.

Analysis of stop-LHCSR3, which lacks the pH-sensing residues in the C terminus, showed that the C terminus controls quenching activity by pH-induced stabilization of the quenched conformation of LHCSR3. The negligible (<30 cm-1) change in the equilibrium free energy difference for this mutant (Figure 2G, Figure 2—source data 1) upon a pH drop

demonstrates the functional role of the C-terminal tail in the conformational change into the quenched state.

The *Zea*-dependent component (Figure 2J-K) likely involves *Vio*/*Zea* and the neighboring *Chl* as 602-603 (Bonente et al. 2011, Di Valentin et al. 2009, Lampoura et al. 2002). With conversion from *Vio* to *Zea*, the free energy landscape changes significantly, and thus is likely to involve the region of LHCSR3 that surrounds *Vio*/*Zea*. In addition, MD simulations have shown this *Car* site to be highly flexible, sampling many configurations (Liguori *et al.*, 2017), which is consistent with the faster dynamics observed here. Upon substitution of *Zea* for *Vio*, the equilibrium free energy difference becomes further biased towards the quenched state by over 550 cm-1 at pH 7.5 and over 300 cm-1 at pH 5.0, where the difference was calculated from the populations of the lifetime states determined within the model. This result is consistent with a role of *Zea* in quenching of LHCSR3 that does not require a decrease in pH and therefore is distinct from the major pH-dependent component of NPQ observed *in vivo* in npq1, which almost completely recovered in the dark (Figure 1A).

In the stop-LHCSR3, the equilibrium free energy differences for the *Zea*-dependent component is similar to the wild type samples (Figure 2K). This is consistent with the *Vio*/*Zea*-*Chl* a 602-603 site as the major contributor for this component. Although qualitatively similar, there is a small decrease (<200 cm-1) in the stabilization of the quenched state upon *Zea* incorporation. Thus, the C-terminal tail affects the states associated with both dynamic components, which arise from different emissive sites within LHCSR3, and so likely has an allosteric effect throughout the protein.

The static component, which is assigned to emitters far from the quenching site in the unquenched state, has a large contribution to the correlation profiles (Figure 2—source data 1). The large amplitude is consistent with the low number of *Cars* available to interact with the *Chls* and thus the presence of several unquenched emissive *Chl* a. Given the structural arrangement of the *Cars* and *Chls*, the unquenched state within the static component is likely due to *Chls* 604, 608 and 609, which sit far from the Cars. The quenched state within the static component is likely due to partial photobleaching, which can lower the fluorescence intensity (Kondo *et al.*, 2019).

4.4.2 Zea-dependent quenching

Zea-dependent quenching is observed both *in vivo* and *in vitro* even at neutral pH. While the mechanism is described at the molecular level in the case of LHCSR3, it is likely shared with other light-harvesting complexes. A strong reduction of fluorescence lifetime was observed in whole cells in the case of zep mutant, even in low light acclimated cells where the amount of LHCSR3 is minimal (Figure 3—figure supplements 1 and 2). This indicated that LHCSR subunits are not the sole quenching site where *Zea*-dependent quenching occurs, as seen in previous work implicating the minor antenna complexes (Cazzaniga *et al.*, 2020). Consistently, *Zea*-dependent quenching was measured in other light-harvesting complexes isolated from the zep mutant, but it was not sufficient to fully explain the strong quenching observed in whole cells.

In the case of the zep mutant, not only does *Zea* completely substitute *Vio* (de-epoxidation index is 1, Figure 1—figure supplement 3), but also the *Zea*/*Chl* ratio is much higher (~10-fold) compared to the ratio observed in WT or npq4 lhcsr1. This suggests an alternative possibility where the strong quenching observed in the zep mutant could be related to accumulation of *Zea* in the thylakoid membrane changing the environment where the photosystems and light-harvesting complexes are embedded, inducing the latter to a strong quenched state. Indeed, *Zea* has been previously reported to influence the assembly and organization of light-harvesting complexes in the thylakoid membranes of higher plants, affecting their quenching properties (Sacharz *et al.*, 2017). While both possibilities allow for quenching in the presence of *Zea* even at neutral pH, it is the pH-independent quenching itself that is potentially the origin of the seemingly conflicting results in the literature, where *Zea* has been found to both reduce NPQ (Niyogi, Björkman and Grossman, 1997b) and be unnecessary for its induction (Bonente, Ballottari, *et al.*, 2011; Baek *et al.*, 2016).

4.4.3 Quenching processes *in vivo* and *in vitro*

Our *in vitro* results point to pH and *Zea* controlling separate quenching processes within LHCSR3 and that either parameter can provide efficient induction of LHCSR3 to a quenched state for photoprotection. The 2D-FLC analysis on single LHCSR3 quantified two parallel dynamic components, or distinct quenching processes, one of which is pH-dependent and the other *Zea*-dependent. Likewise, *in vivo* full light-induced quenching

upon lumen acidification was observed in the npq1 strain, which lacks *Zea*, and full quenching even at neutral pH was observed in the zep strain, which is *Zea*-enriched, suggesting two quenching and induction processes. The 2D-FLC analysis of the stop-LHCSR3 mutant shows that removal of the C-terminal tail removes pH-dependent quenching, while leaving *Zea*-dependent quenching nearly unaffected. Analogously, the WT low light grown strains, with reduced LHCSR accumulation, also present a significantly lower NPQ induction, supporting the critical role of the protonation of the C terminus residues unique to LHCSR in activating quenching in *C. reinhardtii*.

Taken together, the *in vivo* and *in vitro* results indicated that either pH- or *Zea*-dependent quenching provides efficient photoprotection. While *in vivo* measurements suggest that pH-dependent quenching is often dominant over *Zea*-dependent quenching, and correspondingly more efficient in photoprotection, the conformational states and pigment pairs likely responsible exhibit spectroscopic signatures that suggest both quenching processes have similar conformational dynamics. *in vivo* measurements can be influenced by multiple variables, which are, in some cases, unpredictable, such as pleiotropic effects and acclimation responses. Thus, pH- and *Zea*-dependent quenching may both contribute to all quenching in the WT, while being alternatively triggered in the mutants through a compensatory effect. Under natural conditions, these processes combine to protect the system and there is likely interplay between them through compensatory acclimation or changes to the protein organization within the thylakoid. However, the timescales and induction associated with each quenching process are distinct; responsive pH-dependent quenching works in combination with the guaranteed safety valve of *Zea*-dependent quenching, potentially to protect against a rapid return to high light conditions.

4.5 Materials and Methods

4.5.1 Strains and culture conditions

C. reinhardtii WT (4A+and CC4349) and mutant strains npq1 (Niyogi, Björkman and Grossman, 1997b) and npq4 lhcsr1(Ballottari *et al.*, 2016) in the 4A+ background and zep (Baek *et al.*, 2016) in the CC4349 background were grown at 24°C under continuous illumination with white LED light at 80 μmol photons m−2 s−1 (low light, LL) in high salts (HS) medium (Harris, 2013) on a rotary shaker in Erlenmeyer flasks. 4A+ and CC4349

strains were obtained from the *Chlamydomonas* Resource Center (https://www.chlamycollection.org/) and the npq1 strain (Niyogi, Björkman and Grossman, 1997b) was kindly donated by Prof. Giovanni Finazzi (CEA-Grenoble). High light (HL) acclimation was induced by growing cells for 2 weeks at 500 μmol photons m^{-2} s^{-1} in HS. As acclimation may result in complex single adaptation processes, we do not investigate these processes but instead focus our studies on the effect of acclimation on photoprotective mechanisms.

4.5.2 SDS-PAGE Electrophoresis and Immunoblotting

SDS–PAGE analysis was performed using the Tris-Tricine buffer system (Schägger and von Jagow, 1987). Immunoblotting analysis was performed using αCP43 (AS11 1787), αPSAA (AS06 172), αLHCBM5 (AS09 408), and αLHCSR3 (AS14 2766) antibodies purchased from Agrisera (Sweden). The antibody αLHCBM5 was previously reported to also recognize LHCBM1-9 subunits and was thus used as αLHCII antibody (Girolomoni *et al.*, 2017).

Violaxanthin de-epoxidation kinetics and pigment analysis. Violaxanthin de-epoxidation kinetics were performed by illuminating the different genotypes with red light at 1500 μmol photons m^{-2} s^{-1} up to 60 minutes. Pigments were extracted 80% acetone and analyzed by HPLC as described in (Lagarde, Beuf and Vermaas, 2000).

4.5.3 NPQ and electrochromic shift measurements

NPQ induction curves were measured on 60 minutes dark-adapted intact cells with a DUAL-PAM-100 fluorimeter (Heinz-Walz) at room temperature in a 1x1 cm cuvette mixed by magnetic stirring. Dark adaptation was performed in flasks under strong agitation with a shaker in order to avoid the onset of anaerobic conditions. Red saturating light of 4000 μmol photons m^{-2} s^{-1} and red actinic light of 1500 μmol photons m−2 s−1 were respectively used to measure Fm and Fm' at the different time points. Samples were exposed for 60 minutes to actinic light followed by 20 minutes of dark recovery. Fm was measured on dark adapted cells, while Fm' was measured at 10 minutes intervals. NPQ was then calculated as Fm/Fm'-1. Proton motive force upon exposure to different light intensities was measured by Electrochromic Shift (ECS) with MultispeQ v2.0 (PhotosynQ) according

to Kuhlgert, S. et al. MultispeQ Beta: A tool for large-scale plant phenotyping connected to the open photosynQ network (Kuhlgert *et al.*, 2016).

4.5.4 LHCSR3 WT and stop-LHCSR3 proteins refolding for *in vitro* analysis

pETmHis containing LHCSR3 CDS previously cloned as reported in Perozeni et al. 2019 served as template to produce stop-LHCSR3 using Agilent QuikChange Lightning Site-Directed Mutagenesis Kit. Primer TGGCTCTGCGCTTCTAGAAGGAGGCCATTCT and primer GAATGGCCTCCTTCTAGAAGCGCAGAGCCA were used to insert a premature stop codon to replace residue E231, generating a protein lacking 13 c-terminal residues (stop-LHCSR3). LHCSR3 WT and stop-LHCSR3 protein were overexpressed in BL21 E. coli and refolded *in vitro* in presence of pigments as previously reported (Bonente, Ballottari, *et al.*, 2011). Pigments used for refolding were extracted from spinach thylakoids. Vio or *Zea*-binding versions of LHCSR3 were obtained using *Vio* or *Zea* containing pigment extracts in the refolding procedure. *Zea*-containing pigments were obtained by *in vitro* de-epoxidation (Pinnola *et al.*, 2017; De La Cruz Valbuena *et al.*, 2019). Fluorescence emission at 300K with excitation at 440 nm, 475 nm and 500 nm was used to evaluate correct folding as previously reported (Ballottari *et al.*, 2010).

4.5.5 Isolation of monomeric and trimeric light-harvesting complexes of PSII

Monomeric and trimeric light-harvesting complexes were isolated from solubilized thylakoids by ultracentrifugation in sucrose gradient as described in (Tokutsu *et al.*, 2012).

4.5.6 Singlet oxygen production

Singlet oxygen production were estimated by using the fluorescent probe Singlet Oxygen Sensor Green (SOSG) (Flors *et al.*, 2006). SOSG fluorescence was measured in samples treated with red strong light (2,000 μmol photons m−2 s−1) as described in (Perozeni, Stella and Ballottari, 2018). While singlet oxygen estimation by SOSG is widely used, prolonged irradiation can lead to the formation of singlet oxygen by photodegradation of the fluorescent probe (Kim, Fujitsuka and Majima, 2013). To prevent this artefact, direct excitation of the probe was prevented by insertion of a red filter (>630 nm).

4.5.7 Single-molecule fluorescence spectroscopy

12 μM solutions of purified LHCSR3 complexes were stored at -80°C. Immediately prior to experiments, LHCSR3 samples were thawed over ice and diluted to 50 pM using buffer

containing 0.05% n-dodecyl-α-D-maltoside and either 20 mM HEPES-KOH (pH 7.5) or 40 mM MES-NaOH (pH 5.0). The following enzymatic oxygen-scavenging systems were also used: (1) 25 nM protocatechuate-3,4-dioxygenase and 2.5 mM protocatechuic acid for pH 7.5 and (2) 50 nM pyranose oxidase, 100 nM catalase and 5 mM glucose for pH 5.0.(Aitken et al. 2008, Swoboda et al. 2012) Diluted solutions were incubated for 15 minutes on Ni-NTA coated coverslips (Ni_01, Microsurfaces) fitted with a Viton spacer to allow LHCSR3 complexes to attach to the surface via their His-tag. The sample was rinsed several times to remove unbound complexes and sealed with another coverslip.

Single-molecule fluorescence measurements were performed in a home-built confocal microscope. A fiber laser (FemtoFiber pro, Toptica; 130 fs pulse duration, 80 MHz repetition rate) was tuned to 610 nm and set to an excitation power of 350 nW (2560 nJ/cm2 at the sample plane, assuming a Gaussian beam). Sample excitation and fluorescence collection were accomplished by the same oil-immersion objective (UPLSAPO100XO, Olympus, NA 1.4). The fluorescence signal was isolated using two bandpass filters (ET690/120x and ET700/75m, Chroma). The signal was detected using an avalanche photodiode (SPCM-AQRH-15, Excelitas) and photon arrival times were recorded using a time-correlated single photon counting module (Picoharp 300, Picoquant). The instrument response function was measured from scattered light to be 380 ps (full width at half maximum). Fluorescence intensity was analyzed as described previously using a change-point-finding algorithm (Watkins and Yang, 2005). Fluorescence emission was recorded until photobleaching for the following number of LHCSR3 in each sample: 132 LHCSR3-Vio at pH 7.5 (1.6·107 photons); 173 LHCSR3-Vio at pH 5.5 (1.3·107 photons); 95 LHCSR3-Zea at pH 7.5 (1.4·107 photons); 216 LHCSR3-Zea at pH 5.5 (9.0·106 photons); 125 stop-LHCSR3-Vio at pH 7.5 (2.5·107 photons); 130 stop-LHCSR3-Vio at pH 5.5 (7.9·106 photons); 148 stop-LHCSR3-Zea at pH 7.5 (1.3·107 photons); 116 stop-LHCSR3-Zea at pH 5.5 (9.9·106 photons). Experiments were performed at room temperature. Each data set was collected over two or three days for technical replicates and the distribution generated each day was evaluated for consistency.

4.5.8 2D Fluorescence lifetime correlation analysis

2D fluorescence lifetime correlation analysis was performed as detailed previously (Kondo *et al.*, 2019). Briefly, we performed the following analysis. First, the total number

of states exhibiting distinct fluorescence lifetimes was estimated from the 1D lifetime distribution. The lifetime distribution is determined using the maximum entropy method (MEM) to perform a 1D inverse Laplace transform (1D-ILT) of the 1D fluorescence lifetime decay (Ishii et al. 2013a). Next, a 2D fluorescence decay (2D-FD) matrix was constructed by plotting pairs of photons separated by ΔT values ranging from 10-4 to 10 seconds. The 2D-FD matrix was transformed from t-space to the 2D fluorescence lifetime correlation (2D-FLC) matrix in ◎-space using a 2D-ILT by MEM fitting (Ishii and Tahara, 2012, 2013a, 2013b). The 2D-FLC matrix is made up of two functions: the fluorescence lifetime distribution, A, and the correlation function, G. In practice, the initial fluorescence lifetime distribution, A0, was estimated from the 2D-MEM fitting of the 2D-FD at the shortest ΔT (10-4 s). Then the correlation matrix, G0, was estimated at all ΔT values with A0 as a constant. A0 and G0, along with the state lifetime values determined from the 1D analysis, were used as initial parameters for the global fitting of the 2D-FDs at all ΔT values. A was treated as a global variable and G was treated as a local variable at each ΔT (now G(ΔT)). The resulting fit provides the correlation function, G(ΔT). The correlation function was normalized with respect to the total photon number in each state. Each set of correlation curves (auto- and cross-correlation for one sample) were globally fit using the following model function:

$$G_{ij}^{s}(\Delta T) = q^2 J^2 I \cdot \sum_x \left(\left[\sum_{y \neq x} \left\{ E_y \cdot \Phi_y \cdot R_y(\infty) \right\} + E_x \cdot \Phi_y \cdot R_x(\Delta T) \right] \cdot \left[E_x \cdot \Phi_x \cdot C_x \right] \right) \quad [1]$$

This equation accounts for multiple, independent emitters within one protein (multiple components). Here, x and y indicate the component number, i and j indicate the state (auto correlation for i=j, cross correlation for i≠j), q accounts for experimental factors such as the detection efficiency, filter transmittance, gain of the detector, etc., J is the laser power, and I is the total photon number proportional to the total measurement time. E, Φ, and C are diagonal matrices composed of the optical extinction coefficient, fluorescence quantum yield, and state population, respectively. R is a matrix element that is related to the rate matrix.

The rate constants determined from the 2D-FLC analysis were used to calculate the free energies for each protein state shown in Figure 2E-F and 2H-J. The rate constants for

transitions between the quenched and unquenched states are related to the free energies associated with both states through the Arrhenius equation:

$$k_{Q\to U} = A \exp\left(-\frac{E^*_{Q\to U}}{k_B T}\right) \text{[2]}$$

$$k_{U\to Q} = A \exp\left(-\frac{E^*_{U\to Q}}{k_B T}\right) \text{[3]}$$

Here, $k_{Q\to U}$ and $E^*_{Q\to U}$ ($k_{U\to Q}$ and $E^*_{U\to Q}$) are the rate constant and activation energy, respectively, for the transition from the quenched (Q) to the unquenched (U) state. A is a constant, k_B is the Boltzmann constant, and T is the temperature. Upon equilibration of the Q and A states, the free-energy difference, ΔE^*, is given by the following equation:

$$\frac{k_{Q\to U}}{k_{U\to Q}} = \exp\left(-\frac{\Delta E^*}{k_B T}\right) \text{[4]}$$

Using the dynamic rates determined from the fits to the correlation function, we calculated ΔE^* at T = 300 K. The free-energy differences between the quenched and unquenched states are shown as the energetic differences between the minima in the energy landscapes shown in Figure 2. The potential barriers were scaled by assuming the constant A in Equations [1] and [2] to be 1000, which was shown previously to be a reasonable estimate for LHCSR1 (Kondo *et al.*, 2019).

4.5.9 77K fluorescence

Low temperature quenching measures were performed according to Perozeni, et. al (Perozeni, Cazzaniga and Ballottari, 2019). Cells were frozen in liquid nitrogen after being dark adapted or after 60 minutes of illumination at 1500 μmol photons m−2 s−1 of red light. Fluorescence decay kinetics were then recorded by using Chronos BH ISS Photon Counting instrument with picosecond laser excitation at 447 nm operating at 50 MHz. Fluorescence emissions were recorded at 680 nm in with 4 nm bandwidth. Laser power was kept below 0.1μW.

4.6 SUPPORTING INFORMATION

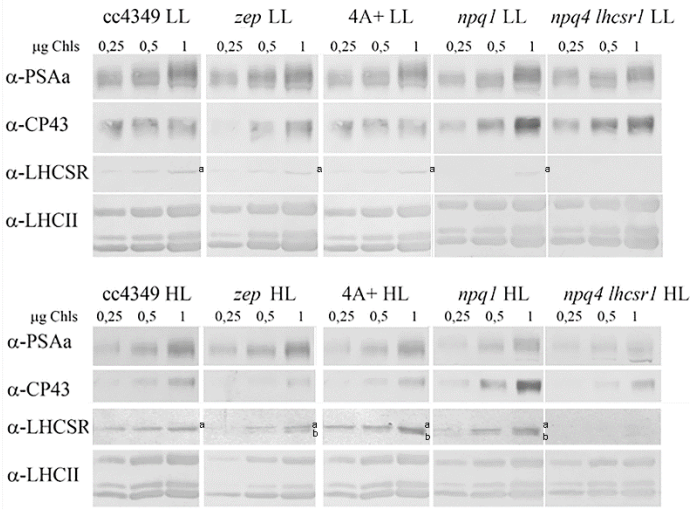

Figure 1—figure supplement 1. *Immunoblot analysis of LHCSR accumulation* in vivo. *Total protein extracts from low Light (LL) or high light (HL) acclimated cells were loaded on a chlorophyll basis (µg of chlorophylls loaded are reported in the figure). Immunoblot analysis was performed using specific antibodies recognizing PsaA, CP43, LHCSR3 (a) and LHCII subunits. The filter used for LHCSR3 detection was then used for LHCSR1 (b) detection using specific antibody. The results reported are representative of two independent experiments with different biological replicates and three technical replicates for each genotype in low light (LL) or high light (HL).*

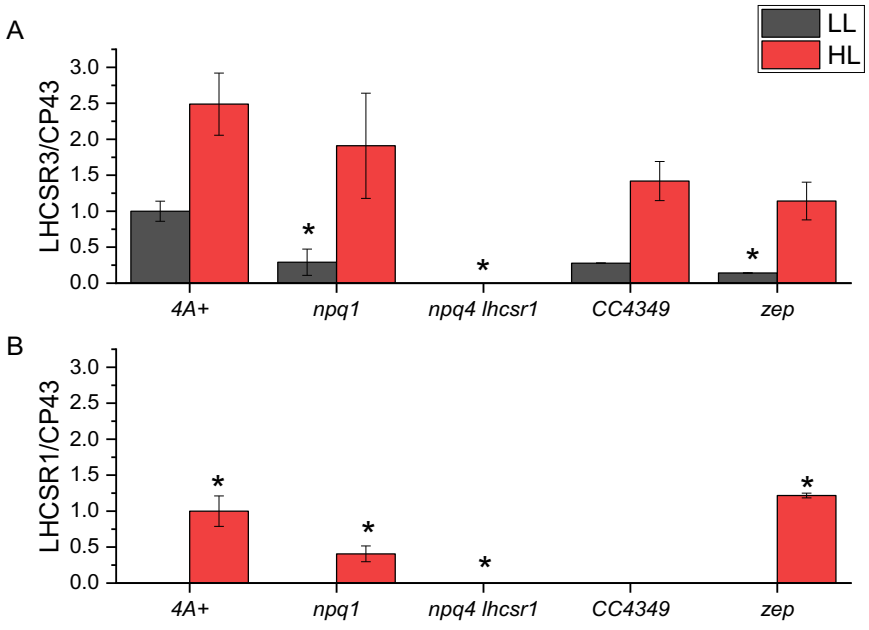

Figure 1—figure supplement 2. *Quantification of LHCSR3 and LHCSR1 accumulation per PSII. Immunoblotting results were analyzed by densitometry. LHCSR3 (A) and LHCSR1 (B) content was then normalized to the amount of CP43 as a reference for PSII. The results obtained were then normalized to the 4A+ low light (LL) case in the case of LHCSR3 and 4A+ high light (HL) case in the case of LHCSR1. The results reported are representative of two independent experiments with different biological replicates and three technical replicates for each genotype in LL or HL. Error bars are reported as standard deviation. The statistical significance of differences compared to WT (4A+ for npq1 and npq1 lhcsr1 mutants, CC4349 for zep mutant) is indicated as * ($p<0.05$), as determined by unpaired two sample t-test (N=3).*

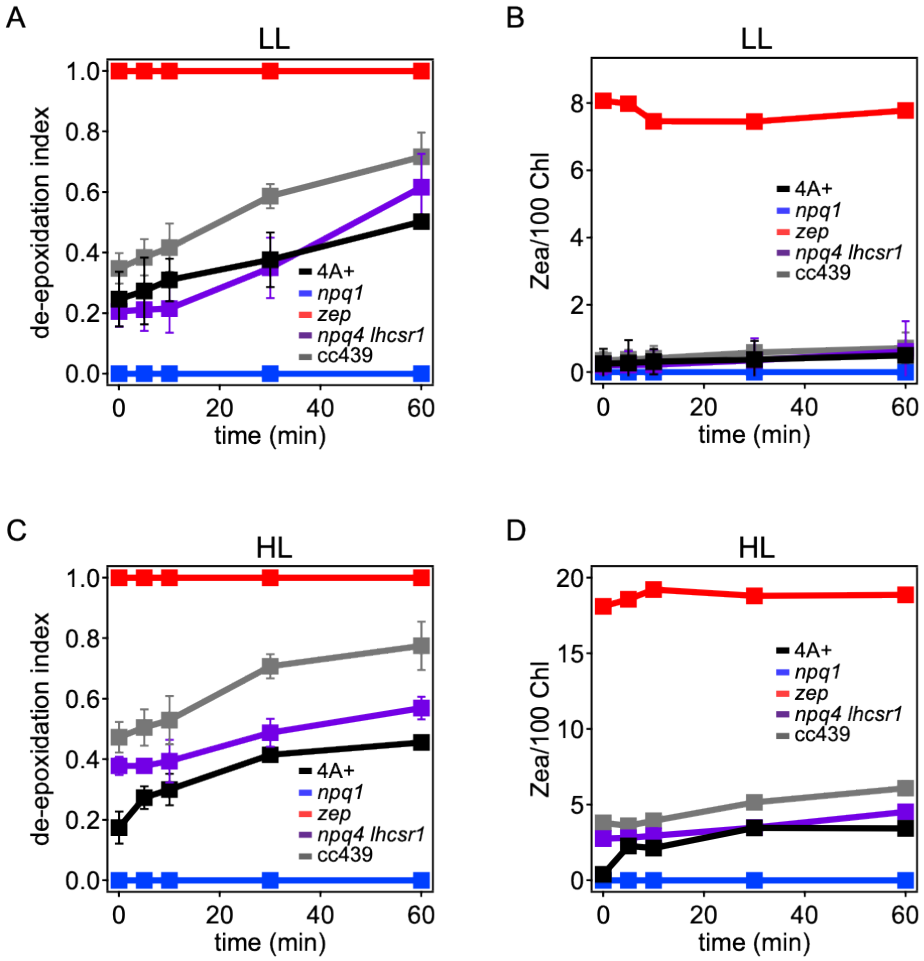

Figure 1—figure supplement 3. *Violaxanthin de-epoxidation kinetics in Chlamydomonas reinhardtii WT and mutant strains. Violaxanthin de-epoxidation kinetics were measured upon 60 minutes of strong light treatment (red light 1500 µmol $m^{-2}s^{-1}$) of low light (LL) or high light (HL) acclimated cells. Panel A, C: de-epoxidation indexes at different time points. Panel B, D: zeaxanthin content per 100 chlorophylls. De-epoxidation index was calculated from the molar concentration of zeaxanthin, anteraxanthin and violaxanthin as ([zeaxanthin]+ [anteraxanthin]/2)/([zeaxanthin]+ [anteraxanthin]+ [violaxanthin]). The results reported are representative of three independent biological replicates for each genotype in LL or HL. Error bars are reported as standard deviation (N=3).*

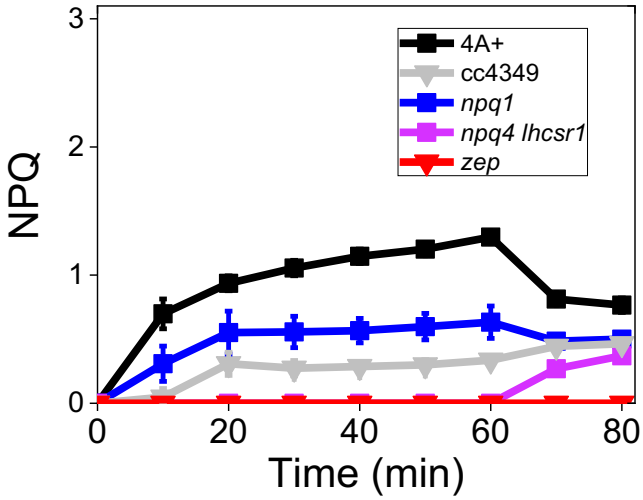

Figure 1—figure supplement 4. *NPQ induction in low light acclimated Chlamydomonas reinhardtii cells. NPQ induction kinetics measured upon 60 minutes of high light (1500 µmol $m^{-2}s^{-1}$) followed by 20 minutes of dark recovery. The results reported are representative of three independent biological replicates for each genotype in LL or HL. Error bars are reported as standard deviation (n=3).*

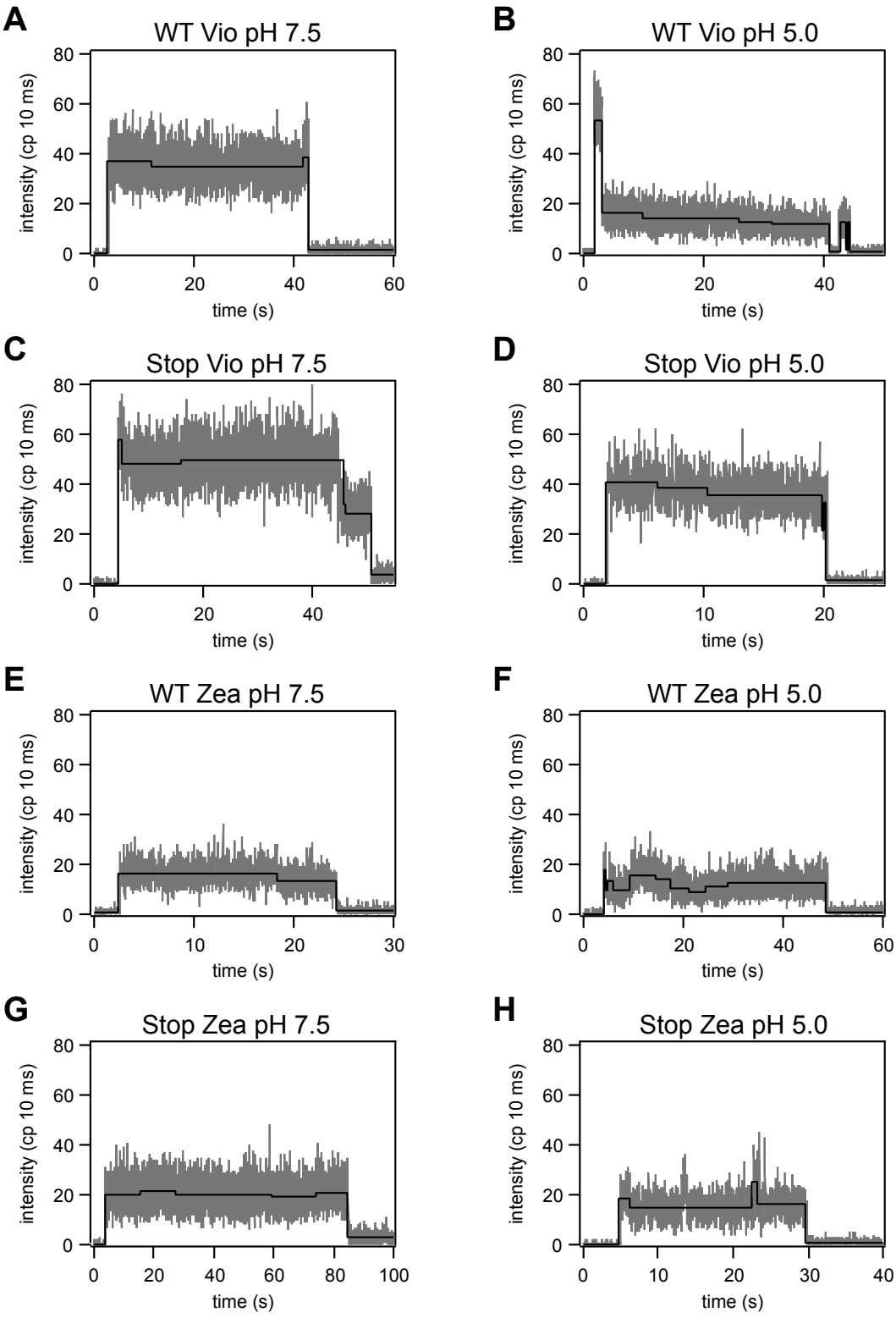

Figure 1—figure supplement 5. Representative fluorescence intensity traces. *Fluorescence intensity traces for LHCSR3 complexes at pH 7.5 and 5.0. The intensity levels determined by the change-point-finding algorithm are shown in black.*

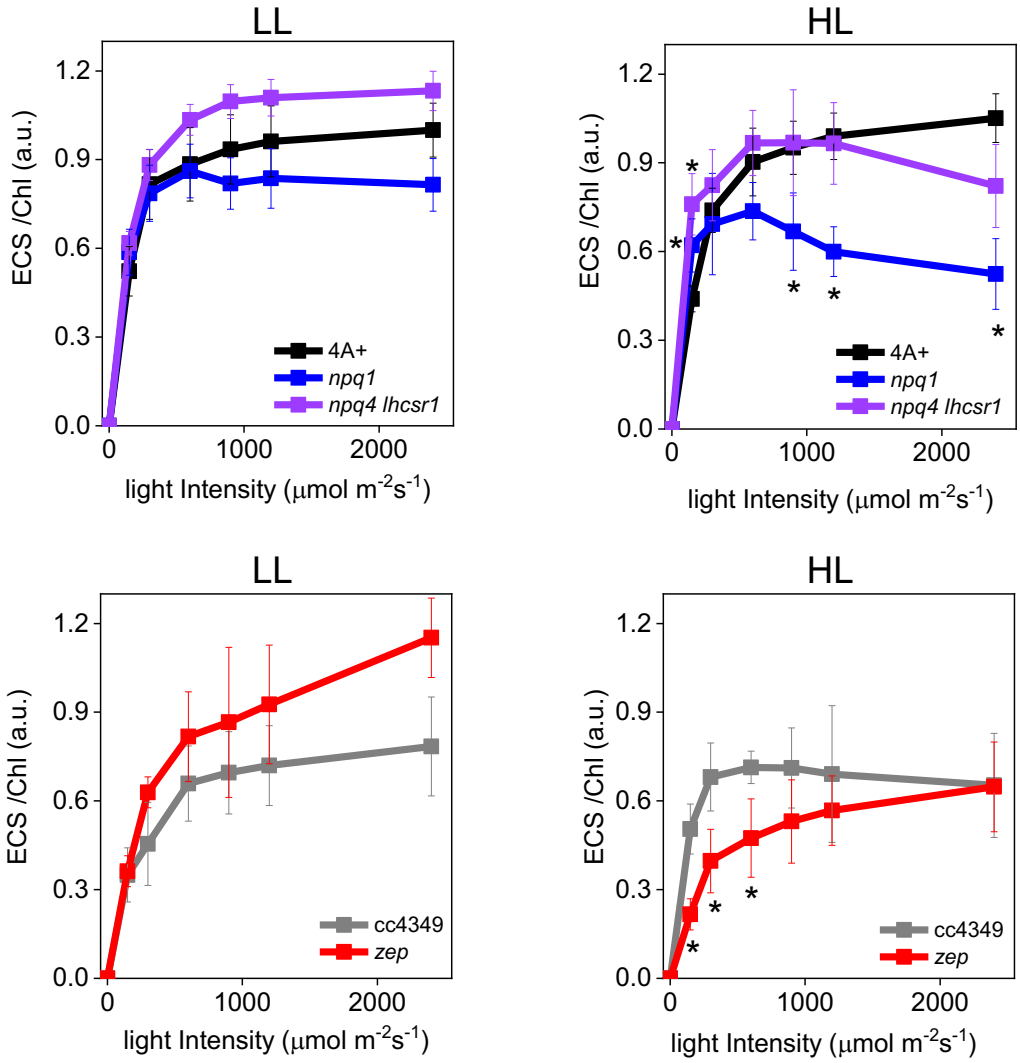

Figure 1—figure supplement 6. *Electrochromic shift measurements at different light intensities in low light and high light acclimated Chlamydomonas reinhardtii cells. Electrochromic shift (ECS) measurements were performed in WT (4A+ and cc4349) and mutant strains (npq4 lhcsr1, npq1 and zep) acclimated to low (Panel A and B) or high (Panel C, D) light. Genotypes having the same background are shown in the same Panel. The results reported are representative of three independent biological replicates for each genotype in LL or HL. Error bars are reported as standard deviation. The statistical significance of differences compared to WT (4A+ for npq1 and npq1 lhcsr1 mutants, CC4349 for zep mutant) is indicated as * (p<0.05), as determined by unpaired two sample t-test (N=3).*

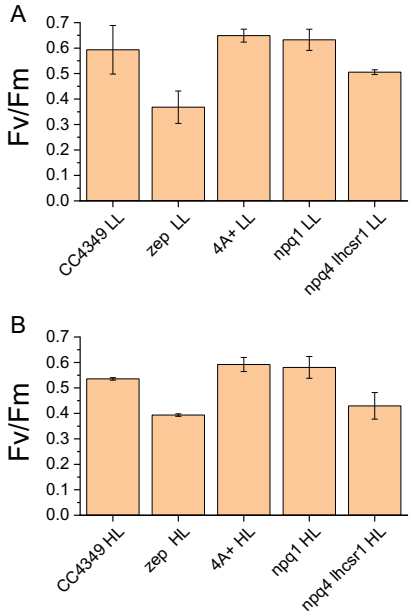

Figure 1-supplemental figure 7. *Maximum quantum yield of Photosystem II in WT (CC4349 and 4A+) and mutant (zep, npq1, npq4 lhcsr1) strains acclimated to low light (LL, Panel A) and high light (HL, Panel B).*

```
                                                ▼
C. reinhardtii LHCSR3  KELNNGRLAMIAIAAFVAQELVEQTEIFEHLALRFEKEAILELDDIERDLGLPVTPLPDNLKSL  259
C. reinhardtii LHCSR1  KELNNGRLAMIAIAAFVAQELVEQTEIFEHLVLRFEKEVILELEDVERDLGLPLTPLPDNLKAI  253
Chlamydomonas sp ICE   KELNNGRLAMIAIAGFTVQELVDGQEIFEHLFVGAADEVVKELDDIERDLGISETPVPFPGF--  257
C. variabilis          KELNNGRLAMIGVAGFVLQELAVKRGIFEHLALYLEREAILEIEDLDPALNIALPTIP------  169
V. carteri                    KELNNGRLAMIAIAAFVAQELVEQTEIFEHLFLRFEKEAILELDDIERDVGLPVTPLPSNLANL
      254
B. natans              KELNNGRLAMLALAGFVAQELVNGKPILG-----------------------------------  185
B. prasinos            KELSHGRLAMVATAFFVAKELVTGNKIFPQFDLYPYQ----------------------------  251
C. cryptica            KELQNGRLAMLAAAGFLAQEAVDGKGILEHFSS--------------------------------  199
P. Tricornutum         KELQNGRLAMLAAAGFMAQELVDGKGILEHLL---------------------------------  210
D. baltica             KELQNGRLAMLAAAGFLAQELVDGKGILEHLQA--------------------------------  209
U. linza                      KELNNGRLAMIAVAGFVAQELVNKQGIIENLKASS-----------------------------
      231
U. prolifera           KELNNGRLAMIAVAGFVAQELVNKQGIIENLKASS------------------------------  230
P. Patens              KELNNGRLAMIAIAAFVAQELVSGEEIFVHLFKRLGL----------------------------  244
A. ubliquus            KELNNGRLAMIAIAAFTVEELVSHQEIFEHPGAAL------------------------------  227
                       ***.:*****:. * *  :* .    *:
```

Figure 1—figure supplement 8*. Alignment of LHCSR-like proteins: protonatable residues are red written while insertion site for TAA mutation to generate the stop-LHCSR3 mutant is indicated by black arrow. Protein number for LHCSR-like proteins used for alignment are listed below: XP_001696064.1 Chlamydomonas reinhardtii LHCSR3, XP_001696125.1 Chlamydomonas reinhardtii LHCSR1, XP_002948670.1 Volvox carteri f. nagariensis, ADP89594.1 Chlamydomonas sp. ICE-L LHCSR2, XP_001768071.1 Physcomitrella patens LHCSR2, ABD58893.1 Acutodesmus obliquus, ADY38581.1 Ulva linza, ADU04518.1 Ulva prolifera, XP_005848576.1 Chlorella variabilis, XP_002178699.1 Phaeodactylum tricornutum, AHH80644.1 Durinskia baltica, AA05890.1 Bigelowiella natans, CCO66741.1 Bathycoccus prasinos.*

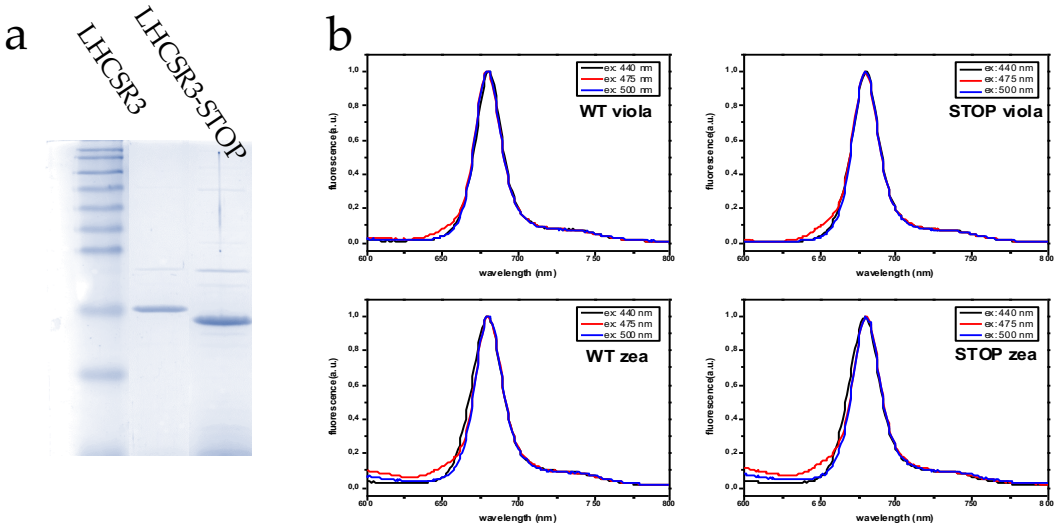

Figure 1—figure supplement 9. *(a) Coomassie brilliant blue stained SDS-page of LHCSR3 apo-protein separated on Tris-Glycine 12%. LHCSR3 STOP protein shows high mobility conferred by its shorter C-terminal with respect to LHCSR3 WT; (b) Fluorescence spectra of LHCSR3 complexes measured at room temperature at different excitation wavelengths (reported in each panel). The results reported are representative of two independent experiments.*

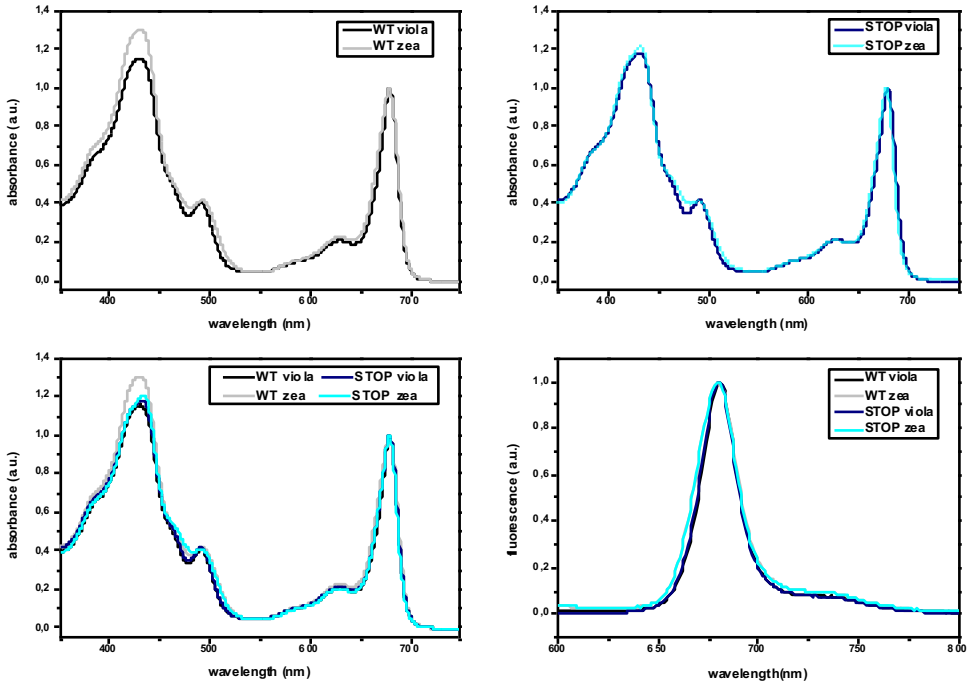

Figure 1—figure supplement 10. *Absorption and fluorescence emission spectra of LHCSR3 WT and STOP. (a-c) Absorption spectra of WT (a) or STOP (b) refolded with violaxanthin or zeaxanthin. (d) Fluorescence emission spectra of LHCSR3 WT and STOP mutant upon excitation at 440 nm with both violaxanthin and zeaxanthin pigments composition. The results reported are representative of two independent experiments.*

	med. intensity (cp 10 ms)	std. intensity (cp 10 ms)
WT Vio pH 7.5	23.2 ± 1.6	12.8 ± 0.8
WT Vio pH 5	18.1 ± 1.4	14.3 ± 0.7
Stop Vio pH 7.5	18.5 ± 0.8	11.1 ± 0.8
Stop Vio pH 5	23.1 ± 1.6	18.4 ± 2.7
WT Zea pH 7.5	9.9 ± 0.5	9.5 ± 2.8
WT Zea pH 5	11.6 ± 0.8	9.3 ± 1.1
Stop Zea pH 7.5	12.4 ± 1.0	11.3 ± 0.9
Stop Zea pH 5	13.6 ± 0.8	13.2 ± 1.7

Figure 1—table supplement 1. *Statistical parameters for the fluorescence intensity of individual complexes are listed. The median (med) and standard deviation (std) are given for each sample. The 95% confidence intervals were determined by bootstrapping the samples 10,000 times.*

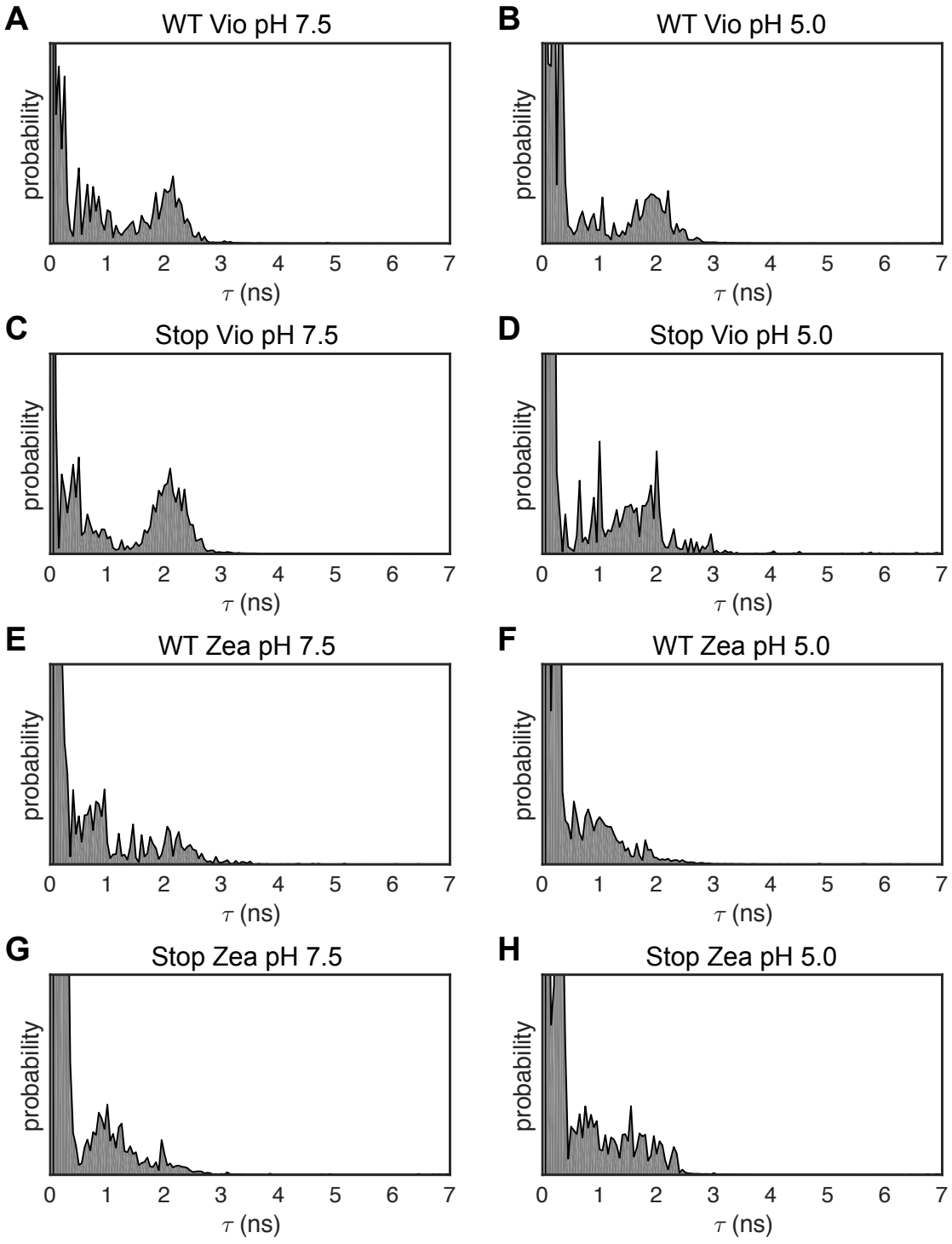

Figure 2—figure supplement 1. 1D Lifetime distributions. *Lifetime distributions from the single-molecule fluorescence from all LHCSR3 samples determined using a one-dimensional inverse Laplace transform (1D-ILT) of the 1D fluorescence lifetime decay. Lifetime states identified from the 1D distribution were used as initial parameters in the fit to the 2D distributions in the 2D-FLC analysis.*

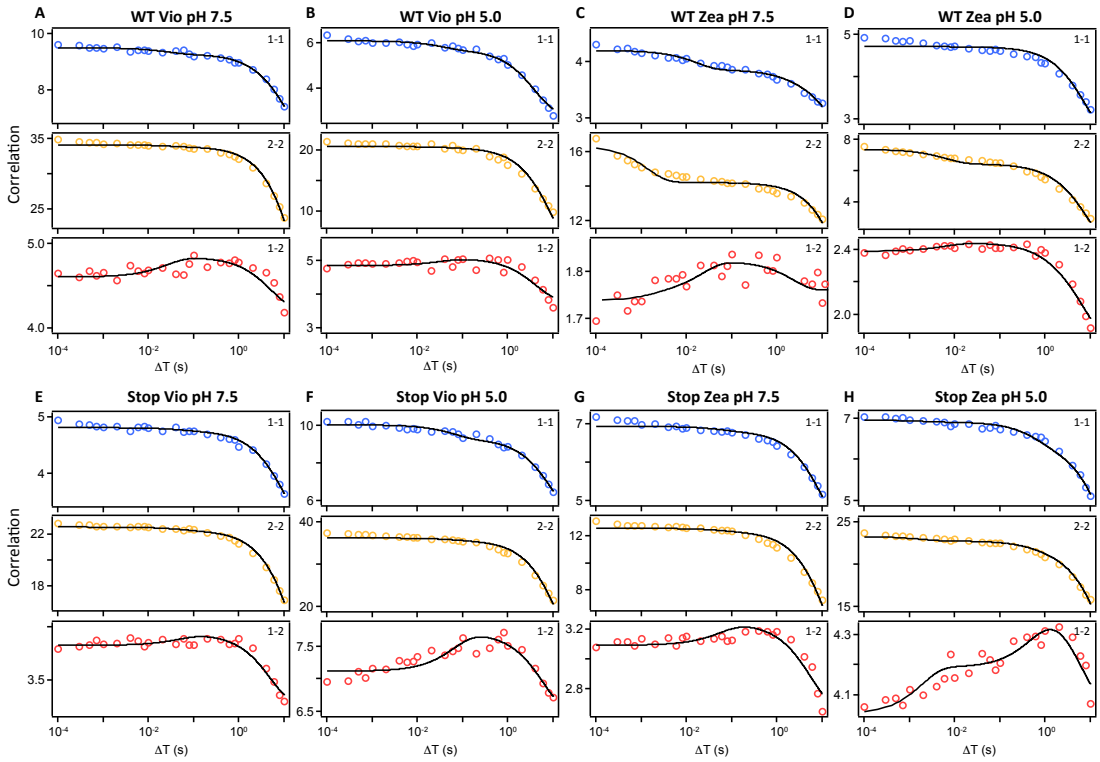

Figure 2—figure supplement 2. Correlation functions used in the 2D-FLC analysis of LHCSR3 complexes. *The auto-correlation and cross-correlation functions of the lifetime states were determined from the single-molecule photon emission for each sample. The auto-correlation is shown in blue for the quenched state and in yellow for the unquenched state. The cross-correlation of the two states is shown in red. The black lines shows the global fitting curves calculated using the model function given by the 2D-FLC analysis using equation (1) and the lifetime distribution as described in the Methods. The correlation functions are shown for single LHCSR3 complexes with Vio at pH 7.5 (A) and pH 5.0 (B), Zea at pH 7.5 (C) and 5.0 (D), stop-LHCSR3 with Vio at pH 7.5 (E) and pH 5.0 (F) and stop-LHCSR3 with Zea at pH 7.5 (G) and pH 5.0 (H).*

WT Vio

pH 7.5

Component	1		2		3	
	Fluorescence					
Lifetime state	1	2	1	2	1	2
Lifetime	0.71	2.45	0.71	2.45	0.71	2.45
Intensity	0.10	0.10	0.080	0.32	0.18	0.13
	Transition rates					
Lifetime state Final \ Initial	1	2	1	2	1	2
1	0.25	23	0.14	850	0.045	0.0017
2	15	0.25	230	0.23	< 0.001	0.039
Population	0.61	0.39	0.79	0.21	0.94	0.060
Free energy difference	90.0		278		587	

pH 5.0

Component	1		2		3	
	Fluorescence					
Lifetime state	1	2	1	2	1	2
Lifetime	0.68	2.43	0.68	2.43	0.68	2.43
Intensity	0.083	0.049	0.074	0.21	0.0013	0.046
	Transition rates					
Lifetime state Final \ Initial	1	2	1	2	1	2
1	0.27	23	0.22	780	0.49	0.0022
2	5.1	0.32	250	0.28	< 0.001	0.10
Population	0.83	0.17	0.72	0.28	0.95	0.050
Free energy difference	314		238		585	

Stop Vio

pH 7.5

Component	1		2		3	
	Fluorescence					
Lifetime state	1	2	1	2	1	2
Lifetime	0.49	2.27	0.49	2.27	0.49	2.27
Intensity	0.052	0.11	0.098	0.47	0.14	0.085
	Transition rates					
Lifetime state Final \ Initial	1	2	1	2	1	2
1	0.28	6.0	0.17	1500	0.047	0.0014
2	13	0.26	320	0.25	< 0.001	0.027
Population	0.32	0.68	0.82	0.18	0.96	0.040
Free energy difference	-156		315		695	

pH 5.0

Component	1		2		3	
	Fluorescence					
Lifetime state	1	2	1	2	1	2
Lifetime	0.53	2.20	0.53	2.45	0.53	2.20
Intensity	0.12	0.096	0.048	0.33	0.12	0.071
	Transition rates					
Lifetime state Final \ Initial	1	2	1	2	1	2
1	0.23	5.2	0.12	870	0.10	0.0010
2	9.7	0.20	280	0.16	< 0.001	0.069
Population	0.35	0.65	0.75	0.25	0.95	0.050
Free energy difference	-129		233		649	

WT Zea

pH 7.5

Component	1		2		3	
	Fluorescence					
Lifetime state	1	2	1	2	1	2
Lifetime	0.47	2.35	0.47	2.35	0.47	2.35
Intensity	0.11	0.022	0.0076	1.0	0.091	0.23
	Transition rates					
Lifetime state Final \ Initial	1	2	1	2	1	2
1	0.56	18	0.038	730	0.021	< 0.001
2	41	0.56	12	0.038	< 0.001	0.021
Population	0.31	0.69	0.98	0.020	0.42	0.58
Free energy difference	-166		857		-66	

pH 5.0

Component	1		2		3	
	Fluorescence					
Lifetime state	1	2	1	2	1	2
Lifetime	0.44	1.97	0.44	1.97	0.44	1.97
Intensity	0.0073	0.13	0.060	0.41	0.046	0.020
	Transition rates					
Lifetime state Final \ Initial	1	2	1	2	1	2
1	1.2	130	0.14	860	0.11	0.0031
2	25	0.33	53	0.23	< 0.001	0.11
Population	0.97	0.030	0.84	0.16	0.94	0.060
Free energy difference	342		581		712	

Stop Zea

pH 7.5

Component	1		2		3	
	Fluorescence					
Lifetime state	1	2	1	2	1	2
Lifetime	0.46	2.17	0.46	2.17	0.46	2.17
Intensity	0.051	0.066	0.078	0.28	0.11	0.037
	Transition rates					
Lifetime state Final \ Initial	1	2	1	2	1	2
1	0.29	6.7	0.15	1900	0.068	0.0017
2	9.9	0.29	270	0.15	< 0.001	0.066
Population	0.40	0.60	0.87	0.13	0.97	0.030
Free energy difference	-82		400		768	

pH 5.0

Component	1		2		3	
	Fluorescence					
Lifetime state	1	2	1	2	1	2
Lifetime	0.46	1.90	0.46	1.90	0.46	1.90
Intensity	0.060	0.11	0.043	0.14	0.11	0.083
	Transition rates					
Lifetime state Final \ Initial	1	2	1	2	1	2
1	< 0.001	0.56	1.7	470	0.050	0.0011
2	0.97	0.25	67	1.2	< 0.001	0.041
Population	0.37	0.63	0.88	0.12	0.90	0.010
Free energy difference	-114		406		466	

Figure 2—table supplement 1. Summary of parameters estimated from the global fit to the correlation functions using the 2D-FLC analysis. The number of dynamic components, fluorescence lifetime states, intensity of each lifetime state,

population of each state, and transition rates between states were estimated by global fitting of the correlation functions shown in Figure 2 – figure supplement 3 using the model function described in the Methods and the fluorescence lifetime distribution. The fluorescence intensity is a relative intensity that is normalized by the total measurement time for each sample and scaled to set the maximum intensity to 1. The free-energy differences were calculated as described in the Methods.

	Total Chlorophylls	Chlorophyll a	Chlorophyll b	Chla/Chlb	Neoxanthin	Violaxanthin	Anteraxanthin	Lutein	Zeaxanthin	Total Carotenoids	Chl/Car
WT VIOLA	7	6,59 ± 0,00	0,41 ± 0,00	16,16 ± 0,16	0,00 ± 0,00	0,98 ± 0,00	0,09 ± 0,03	1,02 ± 0,02	0,08 ± 0,01	2,17 ± 0,02	3,22 ± 0,02
STOP VIOLA	7	6,38 ± 0,01	0,62 ± 0,01	10,33 ± 0,12	0,00 ± 0,00	0,99 ± 0,07	0,07 ± 0,02	0,95 ± 0,08	0,03 ± 0,04	2,04 ± 0,05	3,43 ± 0,08
WT ZEA	7	6,82 ± 0,01	0,18 ± 0,01	37,58 ± 2,82	0,00 ± 0,00	0,27 ± 0,00	0,00 ± 0,00	0,31 ± 0,04	1,41 ± 0,02	1,99 ± 0,03	3,51 ± 0,05
STOP ZEA	7	6,81 ± 0,00	0,19 ± 0,00	36,56 ± 0,35	0,00 ± 0,00	0,22 ± 0,00	0,00 ± 0,00	0,44 ± 0,47	1,09 ± 0,02	1,75 ± 0,00	3,99 ± 0,00

Figure 2—table supplement 2. *Pigment binding properties of recombinant LHCSR3 WT and STOP refolded in vitro. Binding pigments are reported referred to 7 Chlorophyll. The results reported are representative of two independent experiments. Errors are reported as standard deviation.*

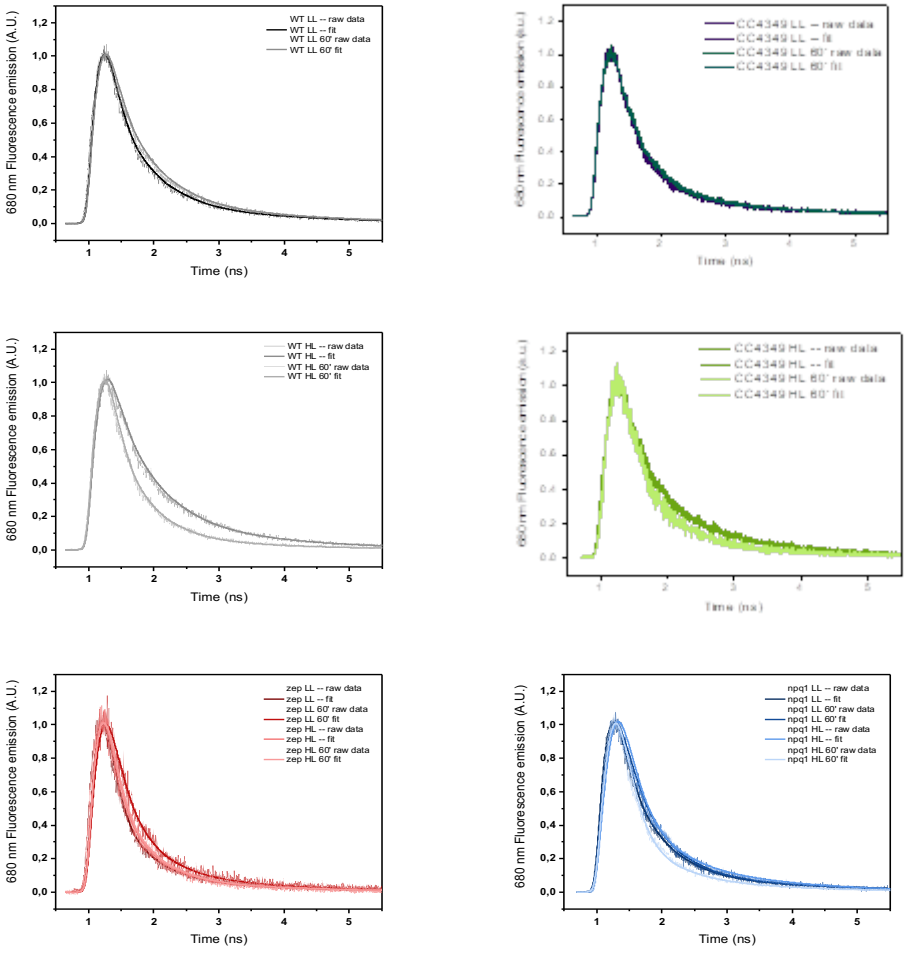

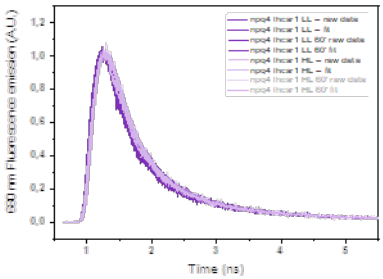

Figure 3—figure supplement 1. *77K raw and fitted traces acquired by TCSPC of Chlamydomonas reinhardtii WT (4a+) and mutant strains. The results reported are representative of two independent experiments with two independent biologic replicates.*

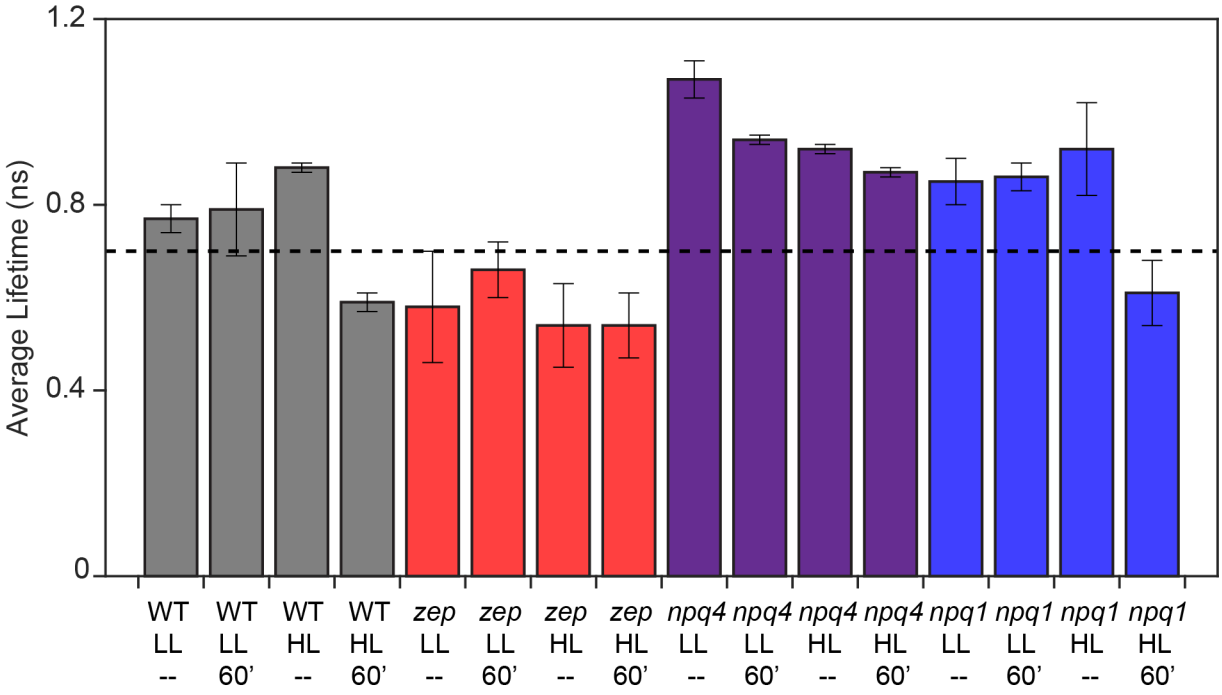

Figure 3—figure supplement 2. *Average fluorescence lifetime for WT (4A+) and mutant strains under all light conditions. The other WT strain (cc4349) has similar values. Above dotted line at 0.75 ns is referred to as unquenched and below the dotted line is referred to as quenched. The results reported are representative of two independent experiments with two independent biologic replicates.*

	t1	f1	t2	f2	t3	f3	avg lifetime	t1	f1	t2	f2	t3	f3	avg lifetime	mean avg lifetime	dev.st.
4A+ LL --	0.04	0.27	0.45	0.40	1.77	0.34	0.78	0.04	0.28	0.38	0.40	1.79	0.33	0.75	0.77	0.03
4A+LL 60'	0.04	0.21	0.47	0.43	1.78	0.36	0.85	0.04	0.21	0.43	0.48	1.60	0.32	0.72	0.79	0.10
4A+HL --	0.04	0.16	0.48	0.41	1.61	0.43	0.89	0.04	0.16	0.52	0.53	1.88	0.31	0.87	0.88	0.01
4A+HL 60'	0.04	0.29	0.37	0.46	1.57	0.25	0.58	0.04	0.33	0.40	0.41	1.64	0.26	0.61	0.59	0.02
npq4 lhcsr1 LL --	0.04	0.19	0.54	0.41	2.00	0.41	1.04	0.04	0.17	0.56	0.39	2.00	0.44	1.10	1.07	0.04
npq4 lhcsr1 LL 60'	0.04	0.19	0.47	0.46	2.06	0.35	0.95	0.04	0.19	0.44	0.45	2.03	0.36	0.94	0.94	0.01
npq4 lhcsr1 HL --	0.04	0.18	0.42	0.46	2.02	0.36	0.93	0.04	0.19	0.42	0.47	2.09	0.34	0.91	0.92	0.01
npq4 lhcsr1 HL 60'	0.04	0.15	0.40	0.49	1.90	0.36	0.88	0.04	0.20	0.41	0.46	1.94	0.34	0.86	0.87	0.01
npq1 LL --	0.04	0.22	0.43	0.46	2.12	0.32	0.88	0.04	0.31	0.42	0.42	2.33	0.27	0.81	0.85	0.05
npq1 LL 60'	0.04	0.15	0.40	0.52	1.89	0.33	0.84	0.04	0.28	0.46	0.44	2.34	0.29	0.88	0.86	0.03
npq1 HL --	0.04	0.25	0.53	0.44	1.92	0.32	0.85	0.04	0.24	0.52	0.44	2.37	0.32	0.99	0.92	0.10
npq1 HL 60'	0.04	0.35	0.34	0.35	1.46	0.30	0.57	0.04	0.32	0.46	0.42	1.75	0.26	0.66	0.61	0.07
cc4349 LL --	0.04	0.27	0.39	0.43	2.24	0.30	0.86	0.04	0.33	0.44	0.39	2.10	0.29	0.79	0.82	0.05
cc4349 LL 60'	0.04	0.24	0.42	0.45	2.37	0.31	0.94	0.04	0.26	0.41	0.45	1.87	0.29	0.75	0.84	0.14
cc4349 HL --	0.04	0.19	0.42	0.38	1.70	0.42	0.89	0.04	0.21	0.40	0.41	1.66	0.38	0.81	0.85	0.06
cc4349 HL 60'	0.04	0.26	0.34	0.42	1.37	0.31	0.59	0.04	0.25	0.35	0.48	1.76	0.27	0.66	0.62	0.05
zep LL --	0.04	0.41	0.40	0.32	1.93	0.27	0.67	0.04	0.46	0.34	0.33	1.72	0.21	0.49	0.58	0.12
zep LL 60'	0.04	0.21	0.33	0.45	1.58	0.34	0.70	0.04	0.38	0.39	0.37	1.82	0.25	0.61	0.66	0.06
zep HL --	0.04	0.36	0.38	0.39	1.79	0.25	0.61	0.04	0.32	0.27	0.39	1.23	0.30	0.48	0.54	0.09
zep HL 60'	0.04	0.34	0.36	0.39	1.59	0.27	0.59	0.04	0.38	0.31	0.37	1.49	0.24	0.49	0.54	0.07

Figure 3—table supplement 1. *77K time resolved fluorescence analysis and average fluorescence decay lifetimes of whole cells. Kinetics were fitted with a three-exponential decay function using Vinci 2 software from ISS. Fractions (fi) and time constants (τi) are reported. Average fluorescence lifetimes were calculated as Σfiτi. The results reported are two independent experiments with two independent biologic replicates.*

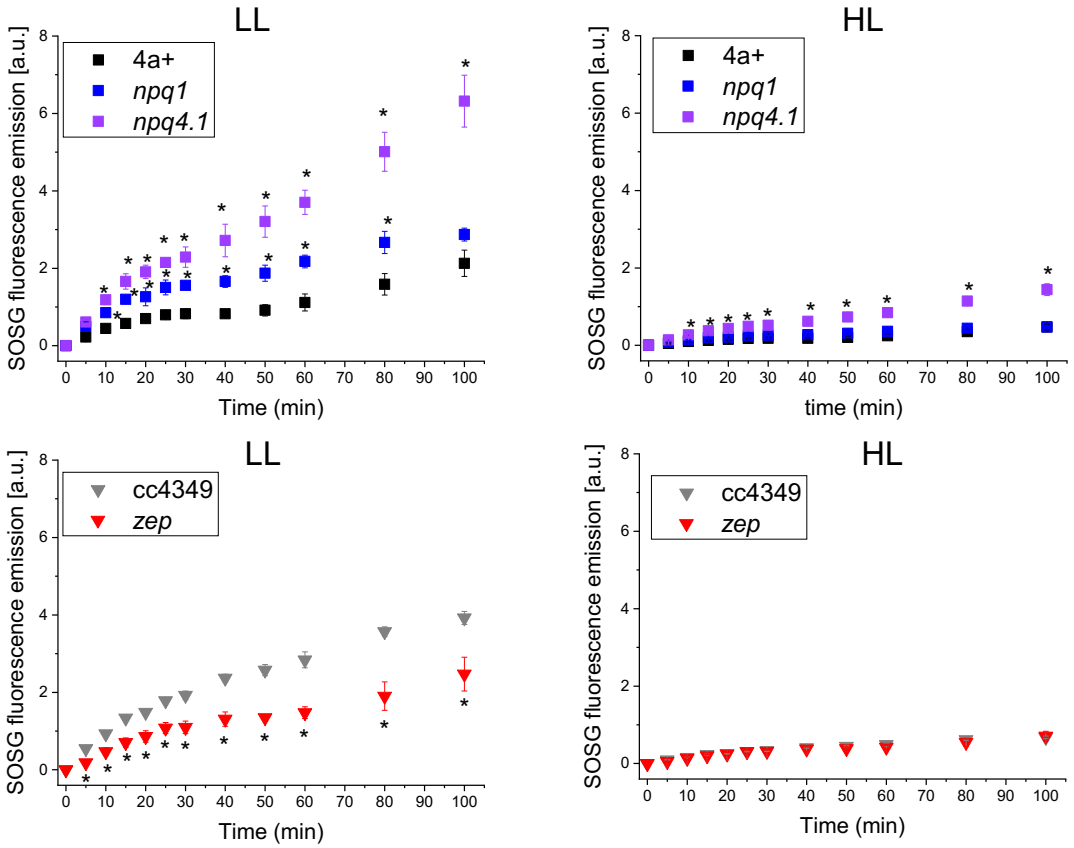

Figure 3—figure supplement 3. *SOSG fluorescence emission kinetics in WT and mutant strains. Singlet oxygen production was measured via the singlet oxygen sensor green (SOSG) fluorescence probe. Low light (LL) or high light (HL) acclimated samples were exposed to strong red light (2000 µmol $m^{-2} s^{-1}$) and singlet oxygen production rate was probed at the different time points by following SOSG fluorescence at 530 nm. Genotypes having the same background are shown in the same Panel. The results reported are representative of three independent biological replicates for each genotype in LL or HL. Error bars are reported as standard deviation (N=3). The statistical significance of differences compared to WT (4A+ for npq1 and npq1 lhcsr1 mutants, CC4349 for zep mutant) is indicated as * (p<0.05), as determined by unpaired two sample t-test (N=3).*

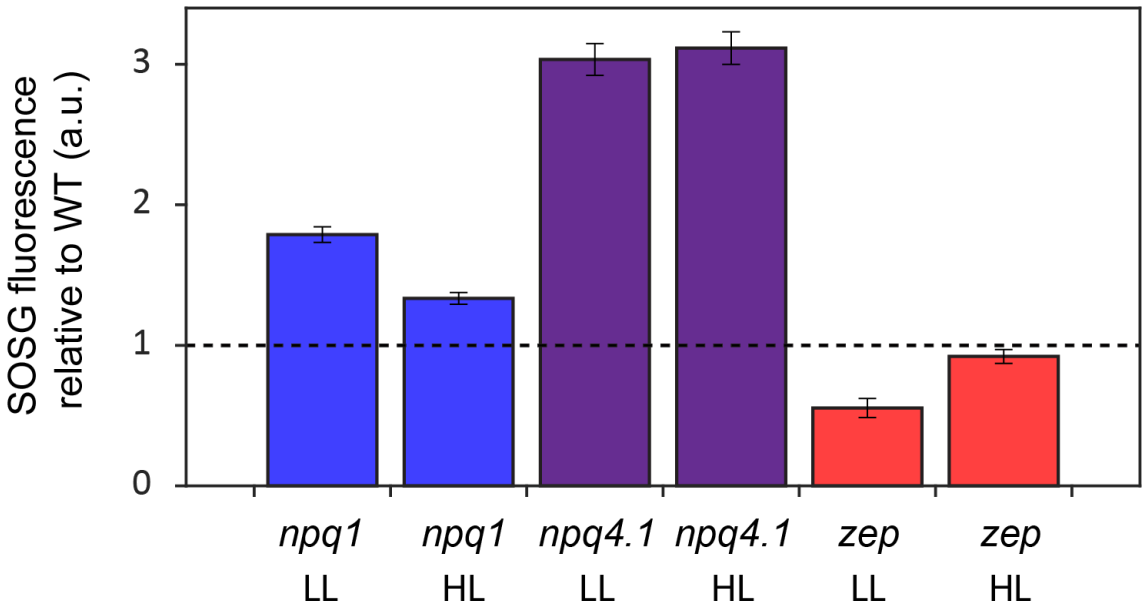

Figure 3—figure supplement 4. *Singlet oxygen sensor green (SOSG) fluorescence emission in WT and mutant strains. Singlet oxygen production rate was measured by SOSG as a fluorescence probe. Low light (LL), left, or high light (HL), right, acclimated samples were exposed to strong red light (2000 µmol $m^{-2} s^{-1}$), right. SOSG emission relative to WT (4A+ for npq1 and npq4 lhcsr1, cc4349 for zep). The results reported are representative of three independent biological replicates for each genotype in LL or HL. Unnormalized data are reported in figure supplement 3.*

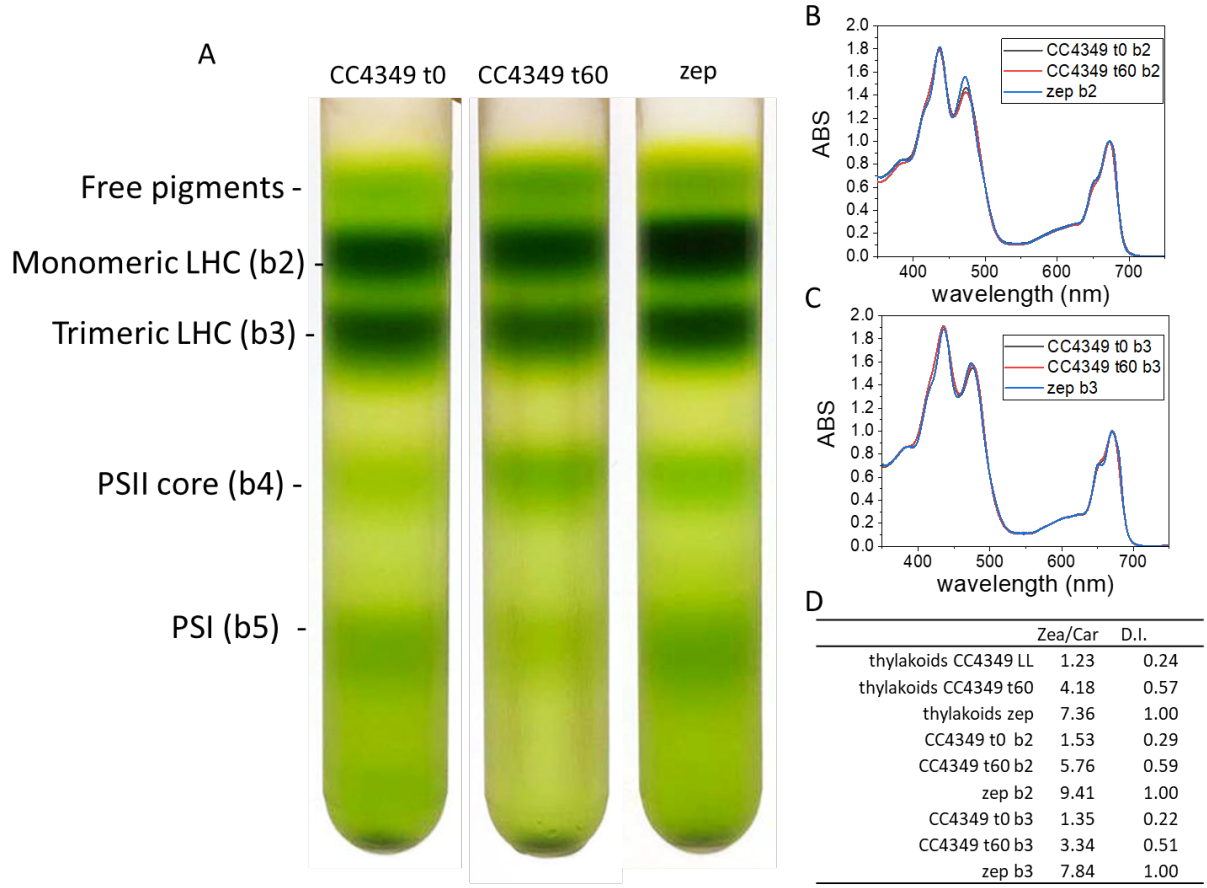

D

	Zea/Car	D.I.
thylakoids CC4349 LL	1.23	0.24
thylakoids CC4349 t60	4.18	0.57
thylakoids zep	7.36	1.00
CC4349 t0 b2	1.53	0.29
CC4349 t60 b2	5.76	0.59
zep b2	9.41	1.00
CC4349 t0 b3	1.35	0.22
CC4349 t60 b3	3.34	0.51
zep b3	7.84	1.00

Figure 3-supplemental figure 5. Isolation and characterization of monomeric and trimeric light-harvesting complexes (LHC). *(A) CC4349 cells acclimated to low light (LL) after 60 minutes of dark adaptation (t0) were exposed for 60 minutes to high light at 1500 µmol $m^{-2} s^{-1}$ (t60). Thylakoid membranes were purified, solubilized in 0.8% n-dodecyl-α-D-maltoside and the different pigment binding complexes were separated by ultracentrifugation in 0.1-1M sucrose gradient. A similar procedure was conducted in the case of dark-adapted zep cells acclimated to LL. Absorption spectra of fractions corresponding to monomeric (b2) and trimeric (b3) complexes are reported in (B) and (C), respectively. (D) The* Zea *fraction of total carotenoids (Zea/Car) and the de-epoxidation index (D.I.) where standard deviation is below 15% (n=2).*

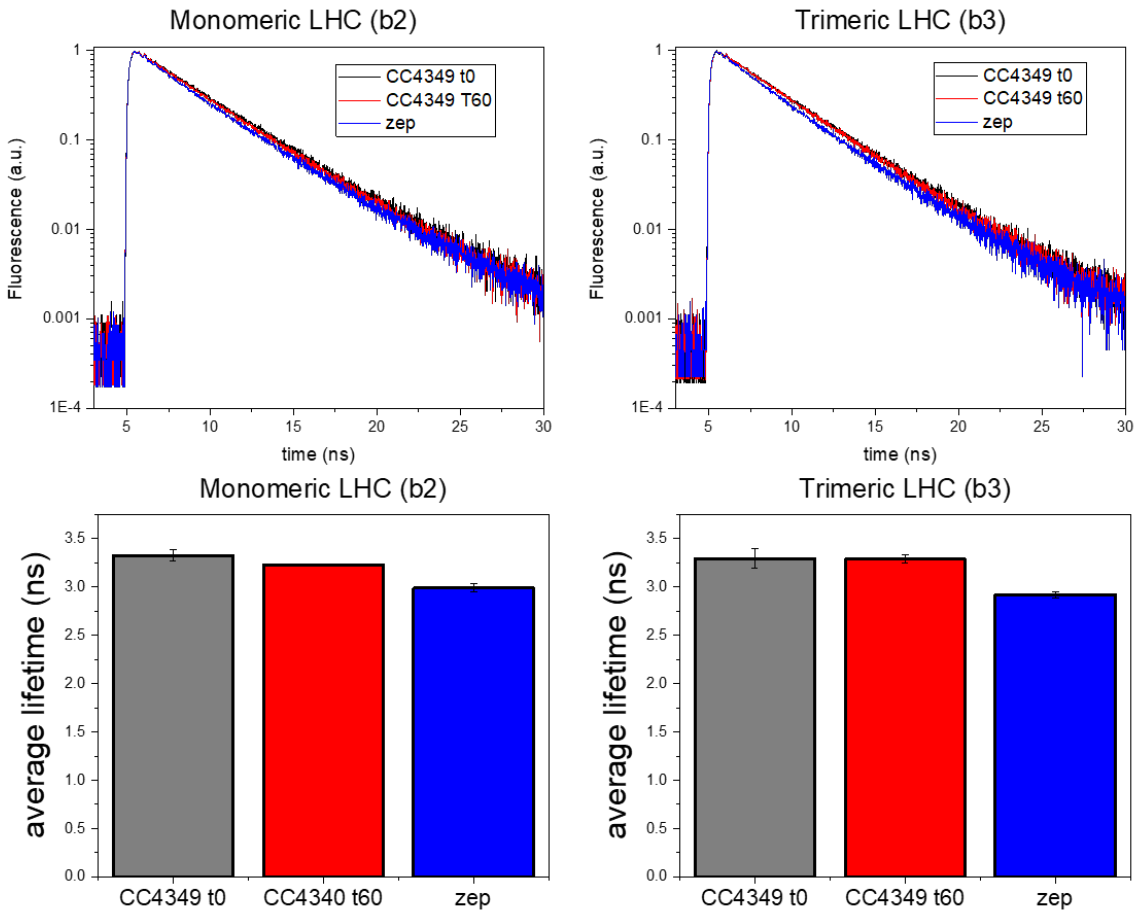

Figure 3-supplemental figure 6. *Time-resolved fluorescence emission decays were measured by time-correlated single-photon counting on isolated monomeric (b2) and trimeric (b3) light-harvesting complexes (LHC) as reported in Figure 3 – supplemental figure 5. Average fluorescence lifetimes for each sample are reported as an average of two independent experiments.*

	τ1 (ns)	f1	τ2 (ns)	f2	τavg (ns)
CC4349 t0 b2	3.560 ± 0.014	0.926 ± 0.013	0.438 ± 0.049	0.074 ± 0.013	3.327 ± 0.058
CC4349 t60 b2	3.505 ± 0.021	0.904 ± 0.006	0.629 ± 0.091	0.096 ± 0.006	3.230 ± 0.012
zep B2	3.475 ± 0.021	0.811 ± 0.007	0.920 ± 0.057	0.189 ± 0.007	2.992 ± 0.045
CC4349 t0 b3	3.410 ± 0.099	0.961 ± 0.000	0.506 ± 0.107	0.039 ± 0.000	3.296 ± 0.100
CC4349 t60 b3	3.345 ± 0.049	0.963 ± 0.003	1.825 ± 0.049	0.037 ± 0.003	3.289 ± 0.041
zep B3	3.280 ± 0.000	0.843 ± 0.012	1.000 ± 0.028	0.157 ± 0.012	2.921 ± 0.032

Figure 3-supplemental table 2. *Time resolved fluorescence analysis and average fluorescence decay lifetimes of isolated monomeric (b2) and trimeric (b3) light-harvesting complexes. Kinetics were fitted with a two-exponential decay function using Vinci 2 software from ISS. Fractions (fi) and time constants (τi) are reported. Average fluorescence lifetimes were calculated as Σfiτi. Errors are reported as standard deviation (n=2).*

5 THE ROLE OF ACIDIC RESIDUES IN THE C-TERMINAL TAIL OF THE LHCSR3 PROTEIN OF *CHLAMYDOMONAS REINHARDTII* IN NON-PHOTOCHEMICAL QUENCHING

Franco V. A. Camargo[1], Federico Perozeni[2], Gabriel de la Cruz Valbuena[1], Luca Zuliani[2], Giulio Cerullo[1], Cosimo D'Andrea[1,3], and Matteo Ballottari[2]

1 IFN-CNR, Dipartimento di Fisica, Politecnico di Milano, Piazza L. da Vinci 32, 20133 Milano, Italy; 2 Dipartimento di Bio-tecnologie, Università di Verona, Strada Le Grazie 15, 37134 Verona, Italy; 3 Istituto Italiano di Tecnologia, Center for Nano Science and Technology, via Pascoli 70/3, 20133 Milano, Italy

Published on J. Phys. Chem. Lett. 2021, 12, 29, 6895–6900 (https://doi.org/10.1021/acs.jpclett.1c01382)

5.1 ABSTRACT

Light Harvesting Complex-stress related (LHCSR) proteins in green algae are essential for photoprotection via non-photochemical quenching (NPQ), playing the dual role of pH sensing and dissipation of chlorophylls excited state energy. pH sensing occurs via protonation of acidic residues located mainly on its lumen-exposed C-terminus. Here, we combine in vivo and in vitro studies to ascertain the role in NPQ of these protonatable C-terminal residues in LHCSR3 from Chlamydomonas reinhardtii. In vivo studies show that four of the residues, D239, D240, E242 and D244, are not involved in NPQ. In vitro experiments on a LHCSR3 chimeric protein, obtained substituting the C terminal with that of another LHC protein lacking acidic residues, show a reduction of NPQ compared to the wild type, but preserving the quenching mechanism involving charge transfer from carotenoids to chlorophylls. NPQ in LHCSR3 is thus a complex mechanism, composed of multiple contributions triggered by different acidic residues.

5.2 INTRODUCTION

Photosynthetic organisms rely on the photochemical conversion of the absorbed light energy for their survival. However, excessive illumination can be harmful for them as it can lead to the formation of reactive oxygen species (ROS) that induce photodamage and, in extreme cases, even cell death (Barber and Andersson, 1992; Tardy and Havaux, 1996; Murata *et al.*, 2007; Takahashi and Murata, 2008). When the absorbed light power exceeds the capacity to re-generate NADP+ and ADP, precursors of NADPH and ATP, the photosynthetic apparatus undergoes overexcitation. From this point, production of increasing amounts of ROS can lead to cellular damage (Niyogi, 1999).

A series of photoprotective mechanisms has been evolved to mitigate photodamage, whose onset depends on the exposure time to the incident light. The most rapidly activated mechanism is called Non-Photochemical Quenching (NPQ) and leads to dissipation of the absorbed light energy into heat by non-radiative relaxation of the photoexcited chlorophylls (*Chls*), in parallel to the usual photochemical quenching pathway which involves excitation energy transfer (EET) to the reaction center (Demmig-Adams *et al.*, 1996; Niyogi, 1999). NPQ is a multi-component phenomenon which consists of several processes occurring over a variety of timescales: energy-dependent feedback deexcitation quenching (qE) (Müller, Li and Niyogi, 2001), state transition dependent quenching (qT) (Minagawa, 2011), and a slowly relaxing quenching component (qI) which could be partially related to photodamage and chlorophyll degradation (Niyogi, 2000). Among NPQ mechanisms, qE has the fastest response which is triggered by the acidification which occurs within the lumen of the thylakoids upon saturation of the photosynthetic apparatus caused by intense illumination.

In *Chlamydomonas* (*C.*) *reinhardtii*, a model organism for green algae, two light-harvesting complexes (LHCs), the LHCSR1 and LHCSR3 proteins, have been reported to be essential for qE induction (Peers *et al.*, 2009; Ballottari *et al.*, 2016; Kim *et al.*, 2017). These LHC subunits are differently expressed in *C. reinhardtii*: both are upregulated in high light conditions, while high CO2 availability downregulates LHCSR3 expression and triggers LHCSR1 (Yamano, Miura and Fukuzawa, 2008; Maruyama, Tokutsu and Minagawa, 2014). Both proteins are located inside the thylakoid membrane and possess protonatable

residues exposed to the luminal side that are able to sense pH acidification and trigger heat dissipation (Liguori *et al.*, 2013; Ballottari *et al.*, 2016). LHCSRs thus perform both the sensing and quenching roles in the qE process. Between LHCSR1 and LHCSR3 the latter has been reported to have the main role in qE induction (Peers *et al.*, 2009; Perozeni *et al.*, 2020).

The detailed molecular mechanisms of qE are still under debate and several non-mutually exclusive models have been proposed. Mainly, these mechanisms involve the interaction of *Chls* with carotenoids (*Cars*), either through an EET from the *Chl* singlet excited state to dark *Car* excited states (Ruban *et al.*, 2007; Staleva *et al.*, 2015; Niedzwiedzki *et al.*, 2016; Liguori *et al.*, 2017), or through a charge transfer (CT) from *Cars* to *Chls*, forming a *Car* radical cation in the process (Holt *et al.*, 2005; Ahn *et al.*, 2008; Avenson *et al.*, 2008; Li *et al.*, 2009). Other studies pointed out the effect of *Chl-Chl* interactions in the presence of protein aggregation (Müller *et al.*, 2010; Wahadoszamen *et al.*, 2014). Recently we reported the identification of multiple quenching mechanisms in the in vitro refolded LHCSR3 using a combination of picosecond time-resolved photoluminescence (TRPL) and femtosecond transient absorption (TA) spectroscopy. We observed a pH triggered electron transfer from *Chl* to *Car* which was however unable to fully account for the NPQ process, suggesting the presence of an aggregation dependent quenching due to protein-protein interactions (De La Cruz Valbuena *et al.*, 2019).

pH sensing in LHCSR3 occurs via protonation of acidic residues (aspartic and glutamic acids) located on the lumen-exposed side of the protein, mostly concentrated in the C-terminal portion, or in between the α-helices (Liguori *et al.*, 2013; Ballottari *et al.*, 2016). Unlike most of other LHCSR subunits from different microalgae species, the LHCSR's C-terminal of C. reinhardtii is especially rich in protonatable residues, hinting at a probable pH-sensing role of this protein fragment (Liguori *et al.*, 2013; Ballottari *et al.*, 2016). The importance of protonation as a trigger for quenching is well known and previous works showed the involvement of specific residues in the activation of NPQ (Liguori *et al.*, 2013; Ballottari *et al.*, 2016; Troiano *et al.*, 2021). Still, the detailed role of these protonatable residues in triggering the LHCSR3 quenching mechanisms is not understood.

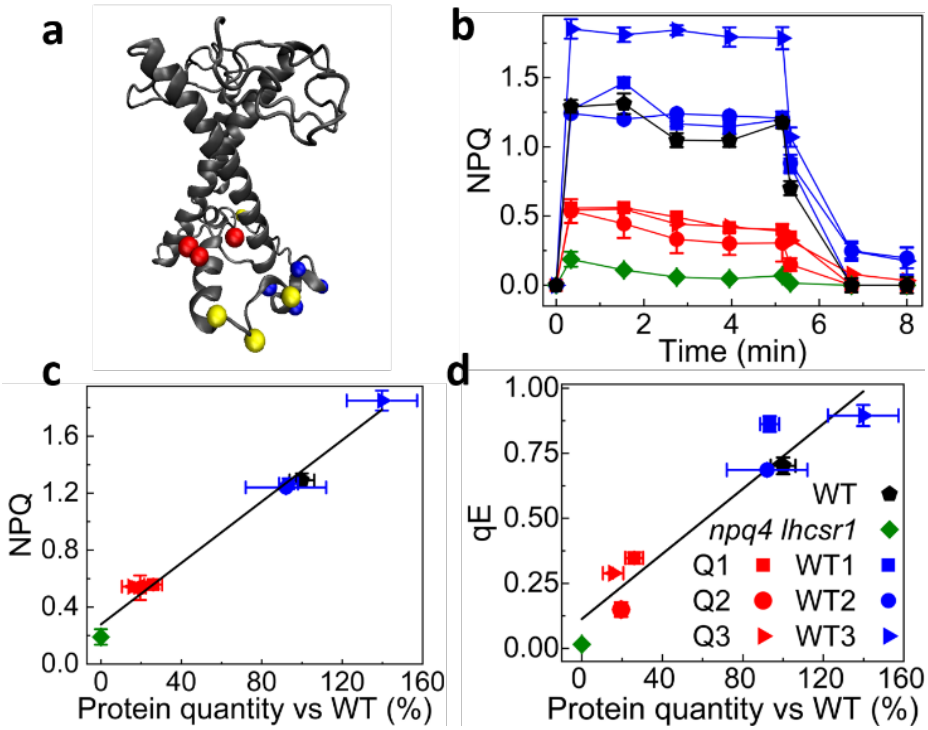

***Figure 1**. (a) Structural model of LHCSR3 obtained by sequence alignment with CP29 (PDB n. 3PL9); protonatable residues are highlighted as yellow, red and blue beads. Red beads (D117, E221, E224) are the protonatable residues described in Ref. 10; blue beads are the protonatable residues (D239-D240-E242-D244) substituted in the Q mutant, yellow beads (E231, E233, E237 and D254) are the remaining acidic residues. (b) NPQ traces for WT, npq4 lhcsr1 complemented with LHCSR3 WT (WT1, WT2, WT3) or with the Q mutant (Q1, Q2, Q3). Light was turned on from 0 to 5 minutes and then turned off. (c) Linear regression of NPQ versus LHCSR3 content per PSII. (d) Linear regression of qE versus LHCSR3 content per PSII. In Panel b, c and d error bars are reported as standard deviations (n=3).*

Here we combine *in vivo* and *in vitro* studies to ascertain the role of the protonatable C-terminal residues of LHCSR3 from *C. reinhardtii* in the NPQ process. *In vivo* experiments are performed on the npq4lhcsr1 mutant, which is depleted of all LHCSRs proteins, complemented with a mutant of LHCSR3 lacking 4 protonatable residues. *In vitro* experiments are performed with a chimeric fusion protein in which the C terminus of LHCSR3 is substituted with that of another LHC protein, LHCBM6, which completely lacks protonatable residues. Our results indicate that protonatable residues at the C-terminal loop of LHCSR3 are specifically involved in the pH dependent activation of a LHCSR3 quenching mechanism, which is however not based on *Chl* to *Car* CT.

5.3 RESULTS

5.3.1 The C-terminal of *C. reinhardtii* LHCSR3

LHCSR3 from *C. reinhardtii* presents a peculiar C-terminal containing 10 acidic residues (the 4 aspartates D239, D240, D244 and D254 and the 6 glutamates E221, E224, E231, E232, E237 and E242), as shown in Figure S1 in the Supporting Information (SI). A phylogenetic analysis of LHCSR-like protein sequences, reported in Figure S2, shows that sequences with a >50% conservation of protonatable residues can be found in evolutionarily related species. Among the different acidic residues, the highest residue conservation was found in the case of E221 and E224, which indeed have been already reported to have a role in LHCSR3 pH sensing (Ballottari *et al.*, 2016). In the case of the other protonatable amino acids, a cluster of four residues, D239, D240, E242 and D244, was characterized by high solvent accessibility but low conservation among the different LHCSR-like subunits, which can indicate a possible role in quenching mechanisms peculiar to *C. reinhardtii* (Figure S3).

5.3.2 Investigation of some LHCSR3 C-terminal's acidic residues role

To investigate the potential role of D239-D240-E242-D244 in LHCSR3 qE activity, we generated a site-specific mutant of the lhcsr3.2 gene (Perozeni, Cazzaniga and Ballottari, 2019), which was used to complement the *npq4 lhcsr1* mutant. Wild type (WT) lhcsr3.2 gene was also used for *npq4 lhcsr1* complementation as a control. LHCSR3 accumulation per Photosystem II (PSII) was then evaluated by western blot (Perozeni, Cazzaniga and Ballottari, 2019) Both for WT and D239N-D240N-E242Q-D244N (hereafter named Q mutant, for quadruple) LHCSR3 variants, complemented lines with different levels of protein accumulation were obtained upon high light adaptation, likely due to a position effect. In fact, the point in which the exogenous sequence is integrated in the host genome is random and can positively or negatively affect the gene expression capabilities. NPQ induction of the complemented lines was then measured by pulse amplitude modulation fluorescence in whole cells (Figure 1b), obtaining as a result a NPQ effect proportional to the LHCSR3 protein content (Peers *et al.*, 2009; Bonente *et al.*, 2012). Indeed, by plotting the maximum of the NPQ (Figure 1c) and of the qE (Figure 1d) component as a function of the ratio between LHCSR and PSII,29 a linear correlation is observed for both WT and Q lines.

These results demonstrate that the substitution of the acidic residues D239-D240-E242-D244 with non-protonatable residues does not lead to a measurable perturbation of the overall pH sensing and NPQ activity of LHCSR3.

In vivo results suggest either the absence of a specific role for these 4 residues or the presence of a redundant mechanism in which the lack of specific protonatable sites can be compensated by the others. These results motivated us to generate a new LHCSR3 mutant in which 8 acidic residues at the C-terminus were substituted by neutral ones. In addition to the above mentioned D239N, D240N, E242Q and D244N mutations, other mutations were introduced in the same coding sequence inducing E231Q, E233Q, E237Q and D254N substitution. This new mutant sequence, carrying 8 mutations at the C-terminus, was again used to complement the *npq4 lhcsr1* mutant and test, after high light exposure of colonies, NPQ and LHCSR3 protein accumulation. 192 resistant colonies were screened by immunoblotting after high light exposure, but none of them was found to accumulate a detectable amount of protein. We conclude that the mutations introduced on the eight acidic residues at the C-terminus destabilize the LHCSR3 protein, preventing its accumulation *in vivo*.

5.3.3 Switching of LHCSR3's C-terminal with LHBM6's

For this reason, a new LHCSR3 mutant was generated substituting the C-terminus of LHCSR3 with the C-terminus of another LHC protein found in the same host organism, the LHCBM6 subunit of *C. reinhardtii* (Figure S4). We chose LHCBM6 as candidate considering that it does not contain acidic residues in the C-terminal region (Girolomoni *et al.*, 2017). This chimeric version of LHCSR3 (called hereafter LHCSR3-BM6) was used to complement the *npq4 lhcsr1* mutant but once again, among the 288 screened colonies, none was found to accumulate the mutated protein.

The inability to characterize *in vivo* the mutant lacking 8 protonatable residues at the C-terminus motivated us to proceed with an *in vitro* characterization. LHCSR3 WT and LHCSR3-BM6 were thus over-expressed in *Escherichia coli*, purified and refolded *in vitro*, as previously described (Bonente, Ballottari, *et al.*, 2011). It is worth to mention that in the LHCSR3-BM6 chimeric protein the acidic residues D119, E221 and E224, previously reported to be involved in the LHCSR3 pH sensing activity *in vivo* are still present

(Ballottari *et al.*, 2016), while the 8 acidic residues at the C-terminus, proposed to act as a pH-sensing switch in LHCSR3, are absent (Liguori *et al.*, 2013).

In steady state, both the LHCSR3 WT and the LHCSR3-BM6 mutant showed an absorption peak at 679.2 nm and a photoluminescence (PL) peak at 683.5 nm, in agreement with previous findings (Figure S5) (Bonente, Ballottari, *et al.*, 2011; De La Cruz Valbuena *et al.*, 2019). Pigment binding properties of both refolded proteins, reported in Table S1 in the SI, show no significant differences between the WT and the mutant. This, along with the overall similarity of absorption and PL spectra, suggests that no dramatic changes occur in the overall structure and pigment binding properties of LHCSR3 upon substitution of the C-terminal region with that of LHCBM6. It is worth to note that these conclusions are based on results obtained with recombinant proteins refolded *in vitro*, thus not including possible effects of the thylakoid environment.

5.3.4 Study of the chimeric protein through TRPL and TA spectroscopies

To investigate the possible effects on the quenching activity of LHCSR3 induced by the substitution of its C-terminus, we compared the transient optical response of WT LHCSR3 and LHCSR3-BM6 after selective excitation of *Chls*, using both TRPL and TA spectroscopies. The combination of these techniques is particularly powerful, since TRPL measures the lifetime of the emitting excited states, such as the *Chl* singlet excited state (*1Chl**), while TA also allows the identification of non-emitting states, such as the *Chl* and *Car* triplet states (*3Chl**, *3Car**), the *Car* dark state S1 as well as *Car* radical cations. It is well known that aggregation has an important effect on the fluorescence lifetime in LHCSR (Ballottari *et al.*, 2016; De La Cruz Valbuena *et al.*, 2019). Indeed, proteins in low detergent concentration undergo clustering that favors protein-protein interactions and potential nonlinear annihilation of the excitations. Here, to avoid effects ascribable to small detergent differences, all measurements were performed maintaining a detergent concentration of 0.03% of alpha-dodecyl maltoside. The aggregation state of refolded LHCSR3 proteins at pH 7.5 and pH 5 were monitored by fluorescence emission at 77K, where the possible formation of aggregates is detectable by the appearance of new red shifted fluorescence bands above 700 nm (Miloslavina *et al.*, 2008). That was not the case for any of our samples, as reported in Figure S6.

Figure 2a displays the TRPL maps of LHCSR3-BM6 at pH 5 while Figure 2c compares the normalized TRPL kinetics, integrated over the 650-750 nm range, for LHCSR3 WT and LHCSR3-BM6 at pH 7.5 and pH 5, respectively. TRPL maps, PL spectra integrated over the full experimental time window and the results of the bi-exponential fits are shown in Figures S7 and S8 and in Table S2 in the SI, respectively. LHCSR3 WT at pH 5 shows a faster decay than at pH 7.5, in agreement with previous studies that revealed a pH-dependent quenching mechanism in the same protein (Troiano *et al.*, 2021), or in a related one, LHCSR1 (Pinnola *et al.*, 2016). Interestingly, the same pH dependence is also present in the LHCSR3-BM6 samples but with a clearly reduced quenching with respect to the WT. Hence, we conclude that pH-induced quenching is reduced, but not completely suppressed, in the LHCSR3-BM6 mutant. When TRPL analysis was performed comparing LHCSR3 WT and LHCSR3-Q, the fluorescence kinetics were similar between the WT and mutant (Figure S9), consistently with the similar LHCSR3 quenching activity evinced by in vivo analysis (Figure 1).

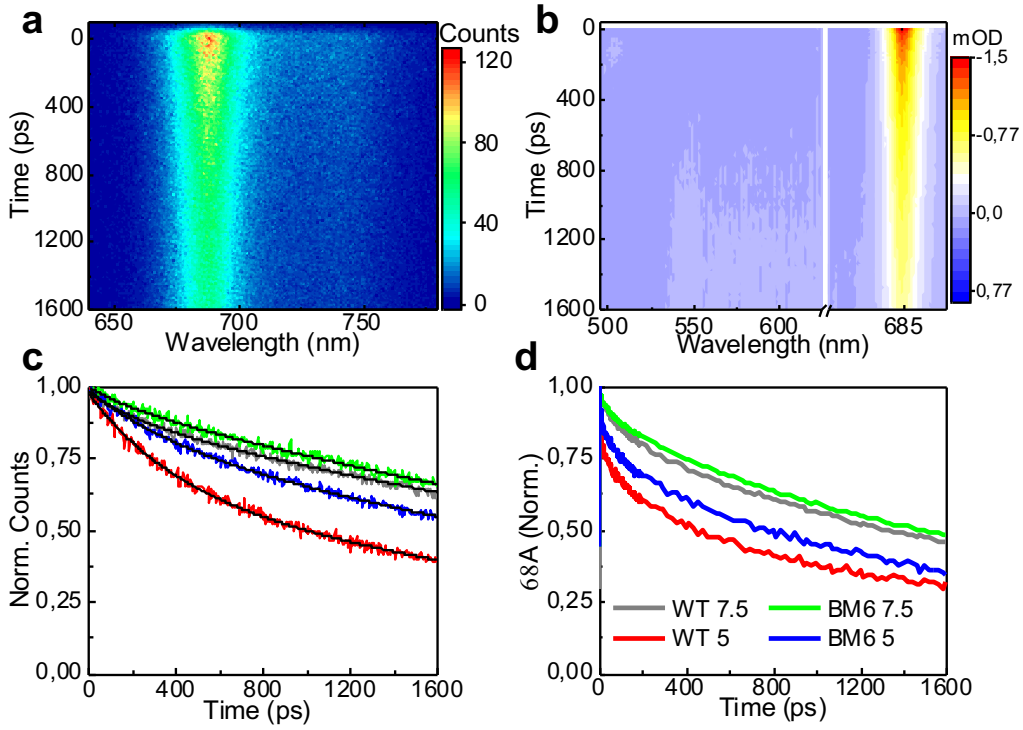

***Figure 2**. (a) TRPL and (b) TA maps of the LHCSR3-BM6 mutant at pH 5. (c) TRPL time traces for WT and mutant samples at pH 5 and pH 7.5. The TRPL data was integrated between 650 and 750 nm and the black lines are multi-exponential fits to the data. (d) TA kinetic traces at 685 nm following 630 nm photoexcitation.*

To shed further light on the mechanisms presiding over quenching in LHCSR3-BM6, we performed TA spectroscopy. Figure 2b shows the TA maps of LHCSR3-BM6 at pH 5 after selective *Chl* excitation at 630 nm, while Figure 2d compares pH-dependent normalized TA kinetics of WT and mutant samples at 680 nm. TA maps and TA spectra at selected time delays are reported in Figures S10 and S11, respectively. To avoid kinetic distortions due to singlet-singlet annihilation (Van Oort *et al.*, 2018), we carried out fluence dependent measurements (see Figure S12 in the SI) and selected fluences for which annihilation effects are negligible (7 μJ/cm2 for the pH 7.5 WT sample and 2 μJ/cm2 for the other samples). TA spectra at early times (see Figure S11) show the same features for all samples: a strong negative peak around 680 nm due to *1Chl** ground state bleaching (GSB) and stimulated emission (SE), and a broad positive band extending from 450 to 600 nm corresponding to a *1Chl** photoinduced absorption (PA). *Chl* GSB/SE kinetics (Figure 2d) agree with TRPL decays (Figure 2c), showing a faster GSB decay at lower pH in LHCSR3 WT and LHCSR3-BM6, with the latter exhibiting a reduced quenching. The TRPL and TA data thus consistently indicate that LHCSR3-BM6, due to the absence of 8 protonatable residues in the C-terminal region, displays a reduced pH dependent qE activity.

Since most proposed mechanisms for qE are associated with *Chl-Car* interactions, we then focused on the spectral region of *Car* activity (450-600 nm), which overlaps with the broad *1Chl** PA. Since the 630-nm pump pulses do not directly excite the *Cars*, any observed signal from the *Cars* must be assigned to interaction of *1Chl** with them. Figure S11 reports TA spectra in the 450-600 nm wavelength range at different delays. The broad positive band is assigned to PA from *1Chl**. On top of this band, we observe the formation of a narrower negative band peaking at ⊚490 nm over tens of picoseconds. We assign the signal to *Car* GSB, in agreement with previous results (Polívka and Sundström, 2004; Polívka and Frank, 2010; Pinnola *et al.*, 2016). Figure 3a compares the normalized TA time traces of all samples at 500 nm in the first 250 ps. We observe a positive signal that partially decays on the tens of picoseconds timescale. This decay, which is assigned to the formation the *Car* GSB overlapping with the *1Chl** PA, is more pronounced for pH 5 than for pH 7.5. This result confirms the involvement of *Cars* in the pH dependent qE process in LHCSR3. Nevertheless, the similarities between the kinetics of the WT sample and the LHCSR3-BM6 mutant at the same pH values are remarkable.

On the nanosecond timescale, we also see a rising PA signal around 510 nm (Figure 3b) which can be attributed to the build-up of the *Car* triplet state, *3Car** (Mozzo *et al.*, 2008). This state is formed by triplet-triplet energy transfer from *3Chl** to *3Car**, following intersystem crossing (ISC) in *Chl*, according to the scheme *1Chl**-> *3Chl**-> *3Car**. We observe that the Car triplet formation is more pronounced at pH 7.5 as opposed to pH 5 and in the mutant with respect to WT. This is consistent with a longer *1Chl** lifetime due to a reduced qE, which makes the ISC process more likely. These results show a correlation between the *1Chl** lifetime quenching observed in TRPL and TA experiments and the build-up of the *Car* GSB.

A possible *1Chl** quenching mechanism is the EET from the *1Chl** state to a *Car* dark state, such as S1 or the recently proposed S* (Ruban *et al.*, 2007; Niedzwiedzki *et al.*, 2016). Population of a *Car* dark state can be measured indirectly by observing the S1→Sn PA which, depending on the *Car* involved, peaks in the 530-580 nm range (Pinnola *et al.*, 2016). Due to the short *Car* S1 lifetime, this transition can only be detected when the state is highly populated. The TA dynamics at 570 nm (Figure S13) do not show a formation, thus indicating that the qE mechanism involving EET to a *Car* dark state is either inactive or of minor importance.

An alternative *1Chl** quenching mechanism is CT from the *Cars*, which results in *Car* radical cation formation. To probe this process, we extended our TA detection window to the near infrared (NIR) region (850-1050 nm), where *Car* radical cations absorb (Holt *et al.*, 2005). TA spectra in the NIR at different time delays are shown in Figure S14. At early times (500 fs) we observe a broad positive band, which we assign to *1Chl** PA (Holt *et al.*, 2005). On the 20 ps timescale this band remains substantially constant for the pH 7.5 samples, while it displays a clear build-up at pH 5 for both the WT and the mutant samples. The TA dynamics at 880 nm, reported in Figure 3c, show a signal growth by ⌾40% for the pH 5 samples.

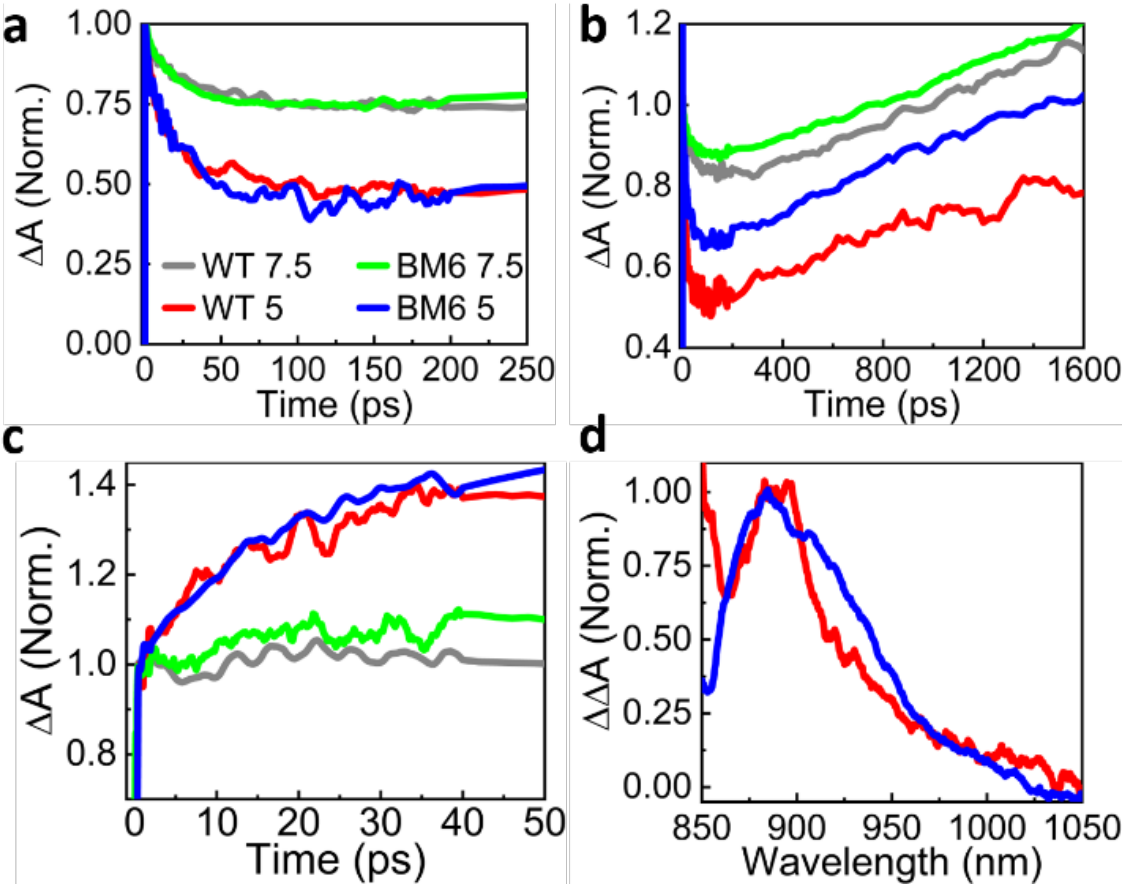

***Figure 3**. LHCSR3 WT and LHCSR-BM6 TA kinetics after 630 nm excitation of (a) Car GSB at 500 nm, (b) Car triplet formation at 510 nm and (c) Car radical cation formation at 880 nm. (d) Double difference ΔΔA spectra of the pH 5 sample showing lutein radical cation formation at ≈880 nm.*

We assign the NIR TA build-up in the pH5 samples to the formation of a Car radical cation. To determine which Car is involved in the process, we subtract the TA spectra at 500 fs from those at 20 ps, generating double difference spectra ΔΔA. Normalized ΔΔA spectra at pH 5 are shown in Figure 3d for both WT and mutant samples. The peaks at around 880 nm are in good agreement with the PA spectrum of the lutein radical cation (Amarie *et al.*, 2007; De La Cruz Valbuena *et al.*, 2019). Taken together, the visible and NIR TA data indicate quenching of *1Chl** via CT from the *Car*, which results in the simultaneous build-up of the *Car* GSB (Figure 3a) and of the PA of the *Car* radical cation (Figure 3c). Notably, the data in Figure 3a and Figure 3c do not highlight significant differences between the WT and the LHCSR3-BM6 mutant, demonstrating that the qE mechanism related to CT from the *Cars* is not triggered by the protonatable residues on the C-terminus.

5.3.5 Conclusion

In conclusion, our work sheds new light on the molecular mechanisms underlying the pH dependent quenching activity of LHCSR3. First, using *in vivo* measurements, we found that four of the acidic residues at the C-terminus previously reported to be involved in pH sensing, namely D239, D240, E242 and D244, are not essential, since the LHCSR3 quenching activity is similar when they are substituted with neutral ones. The pH sensing property of LHCSR3 is thus likely based on a redundant role of the different acidic residues. When the whole C-terminus of LHCSR3 was substituted with the C-terminus of a LHC protein with no pH sensing properties, *in vitro* experiments showed that the pH dependent protein activation as a quencher was reduced, consistently with previous results (Liguori *et al.*, 2013; Troiano *et al.*, 2021), but not fully impaired. In particular, the quenching mechanism based on *Chl-Car* interaction and lutein radical cation formation was found to be unaltered even in the LHCSR3-BM6 mutant and could be likely attributed to the pH sensing of the remaining protonatable residues E221, E224 and D117, whose role in LHCSR3 quenching activity has been demonstrated by *in vivo* mutagenesis and complementation (Ballottari *et al.*, 2016). The possible involvement of E221, E224 and D117 protonatable residues on *Car-Chl* charge transfer quenching needs to be proven by future work on recombinant LHCSR3 protein variants.

pH dependent activation of LHCSR3 quenching mechanisms is thus composed of multiple contributions: protonatable residues E221, E224 and D117, are involved in pH dependent activation of qE via lutein radical cation formation (Ballottari *et al.*, 2016), while acidic residues at the C-terminal loop, E231, E233, E237, D239, D240, E242, D244 and D254, are involved in the pH dependent activation of other LHCSR3 quenching mechanisms, which do not involve interactions between *Chls* and *Cars*, and can be putatively assigned to *Chl-Chl* interactions.

5.4 SUPPORTING INFORMATION

5.4.1 Structural model and bioinformatics analysis

A model of the LHCSR3 structure was obtained as described in reference (Ballottari *et al.*, 2016) by using the structure of CP29 (PDB 3PL9) as a reference (Pan *et al.*, 2011). The protein structure was then visualized by Chimera 1.13 software. Solvent accessibility for

C-terminal region (residues 220-259) of *C. reinhardtii* LHCSR3 (XP_001696064.1) was predicted using I-TASSER software (Roy, Kucukural and Zhang, 2010). All alignments and phylogenetic tree were done using Clustal Omega, BLAST or NCBI tree viewer software with parameters listed in each figure.

5.4.2 LHCSR3 *in vitro* reconstitution and sample preparation

LHCSR3 in vitro refolding was obtained as previously reported in (Bonente, Ballottari, *et al.*, 2011). In particular, lhcsr3 cDNA was cloned in pET28-His vector for overexpression in *E.coli* removing the coding sequence for the first 14 residues, being the predicted transit peptide for chloroplast localization (Bonente, Ballottari, *et al.*, 2011; Perozeni, Cazzaniga and Ballottari, 2019). For LHCSR3-Q mutant the aspartate and glutamate residues D239-D240-E242-D244 were substituted respectively by asparagine or glutamine by using QuikChange® Site-Directed Mutagenesis Kit according to the manufacturer's instructions (Ballottari *et al.*, 2016). For LHCSR3-BM6 mutant the C-term region of LHCSR3 was substituted by PCR with the 60bp region of LHCSBM6. LHCSR3 apoproteins were purified from *E. coli* as reported by (Liguori *et al.*, 2013) and refolded *in vitro* in presence of pigments as previously described (Ballottari *et al.*, 2016). Samples, both for time resolved fluorescence and transient absorption, were prepared as reported in (De La Cruz Valbuena *et al.*, 2019).

5.4.3 Steady state absorption and fluorescence

Absorption measurements were performed with a Cary 4000, Varian spectrophotometer. Steady state fluo-rescence measurements were performed with a BeamBio custom device equipped with an USB2000+ Ocean Optics spectrometer and custom LED light sources for excitation.

5.4.4 Pigment analysis

Pigment analyses were performed by HPLC as described (Lagarde, Beuf and Vermaas, 2000). HPLC analysis was performed with a Jasco LC-4000 Extrema HPLC system (Jasco, Italy) equipped with a C18 column (Synergi 4u Hydro-RP 80A, Phenomenex, USA) and 350–750 nm diode array detector.

5.4.5 *In vivo* complementation of npq4 lhcsr1 *C. reinhardtii* mutant

In vivo complementation of *npq4 lhcsr1* mutant was performed as described in (Perozeni, Cazzaniga and Ballottari, 2019). The LHCSR3.2 gene (Cre08.g367400) was amplified from *C. reinhardtii* genomic DNA as previously described (Ballottari *et al.*, 2016). In particular, the DNA region amplified was from –1000bp upstream the 5′ untranslated region (UTR) to 300bp downstream the 3′ UTR (Perozeni, Cazzaniga and Ballottari, 2019). Amplified DNA was then inserted in pBC1 vector as described by (Ballottari *et al.*, 2016). Site-specific mutagenesis was performed on identified protonatable residues using QuikChange® Site-Directed Mutagenesis Kit according to the manufacturer's instructions (Ballottari *et al.*, 2016). Cells transformation and transformant selection was performed as described in (Ballottari *et al.*, 2016; Perozeni, Cazzaniga and Ballottari, 2019). Paromomycin was used as selective marker. Resistant colonies were then transferred in TAP medium at 25 °C in flasks with white light (70 μE m−2 s−1, 16h light/8h dark photoperiod). High light acclimation was induced in WT (4A+ strain), *npq4 lhcsr1* mutant and transformant lines by growing cells in HS medium at 400 μE m−2 s−1 (Ballottari *et al.*, 2016). LHCSR3 protein content in the WT and complemented lines was analyzed by immunoblotting by using a specific antibody α-LHCSR3 (AS14 2766, Agrisera, Sweden). In order to retrieve the LHCSR3 content per PSII, the accumulation of PSII core subunits CP43 was monitored as a proxy of PSII by immunoblot-ting by using α-CP43 antibody (AS11 1787) (Ballottari *et al.*, 2016; Perozeni, Cazzaniga and Ballottari, 2019).

5.4.6 NPQ analysis

NPQ induction curves were measured on *C. reinhardtii* strains by using a Dual-PAM 100 instrument (WALZ, Germany). NPQ analyses were performed on *C. reinhardtii* cultures in exponential phase acclimated to high light for 4 days. Measuring, saturating and actinic light was respectively 7, 5000 and 1200 μmol m-2 s-1.

5.4.7 Time-Resolved photoluminescence

Time-resolved photoluminescence measurements were carried out using a Ti:sapphire laser (Chameleon Ultra II, Coherent) with a repetition rate of 80 MHz and pulse width of about 100 fs at FWHM. The laser output was set at 860 nm and then frequency doubled by a β-barium borate (BBO) crystal to generate the 430 nm excitation. The detection system consists in a spectrometer coupled with a streak camera (C5680, Hamamatsu)

which provides spectral-temporal matrices with spectral and temporal resolutions of ~1 nm and ~20 ps, respectively. TRPL and TA measurements were carried out in cuvettes with optical path-length of 3 and 1 mm, respectively. The sample temperature has been maintained at 10 degrees Celsius to avoid protein unfolding.

5.4.8 Transient absorption

Transient absorption measurements were carried out using a home-made setup, based on a regeneratively amplified Ti:Sapphire laser (Libra, Coherent) at 800 nm wavelength with 100 fs pulse duration and 1 kHz repetition rate. A fraction of the fundamental wavelength was used to seed a non-collinear optical parametric amplifier (NOPA) delivering ~80 fs pulses at a central wavelength of 630 nm. The pump fluence was adjusted to minimize bimolecular recombination. The broadband probe beam was obtained through white light continuum generation by focusing the fundamental pulses either in a 2-mm-thick sapphire plate or in a 4-mm-thick YAG crystal, in combination with appropriate filters to reject the remaining light at 800 nm. The spectrum generated covered respectively the visible (470-700 nm) or the infrared (850-1050 nm) range. After the sample, the transmitted probe was sent to a spectrometer (SP2150 Acton, Princeton Instruments) and detected using a linear image sensor driven and read out by a custom-built board (Stresing Entwicklungsburo). For each probe wavelength, the differential absorption (ΔA) was measured as a function of the pump-probe delay. All measurements were acquired at magic angle (54.7°) polarization. Before each measurement, the beam profile of pump and probe beams was imaged at the overlap position using a camera, and the cross-sections obtained were used to calculate the fluence. The sample was kept at 12°C during all TA experiments. The signal levels of different TA scans were compared to check for possible sample degradation during each measurement, and that was never the case under these measurement conditions.

XP_001696064.1	Chlamydomonas reinhardtii
XP_001696125.1	Chlamydomonas reinhardtii
KXZ50176.1	Gonium pectorale
XP_002948670.1	Volvox carteri f. nagariensis
KXZ42803.1	Gonium pectorale
PNH03463.1	Tetrabaena socialis
ADP89594.1	Chlamydomonas sp. ICE-L
AUI41106.1	Haematococcus lacustris
XP_013900766.1	Monoraphidium neglectum
ADU04495.1	Chlamydomonas sp. ICE-L
GBP96674.1	Raphidocelis subcapitata
XP_013902010.1	Monoraphidium neglectum
GAX82638.1	Chlamydomonas eustigma
PSC68059.1	Micractinium conductrix
GAX82637.1	Chlamydomonas eustigma
XP_024397313.1	Physcomitrella patens
XP_024384898.1	Physcomitrella patens
ABD58893.1	Tetradesmus obliquus
GAQ89003.1	Klebsormidium nitens
XP_005647960.1	Coccomyxa subellipsoidea C-169
ADY38581.1	Ulva linza
ADU04518.1	Ulva prolifera
KAA6421517.1	Trebouxia sp. A1-2
XP_005848576.1	Chlorella variabilis
ABD37894.1	Mesostigma viride
OEU14205.1	Fragilariopsis cylindrus CCMP1102
XP_002178699.1	Phaeodactylum tricornutum CCAP 1055/1
XP_002295258.1	Thalassiosira pseudonana CCMP1335
OEU07230.1	Fragilariopsis cylindrus CCMP1102
VEU36249.1	Pseudo-nitzschia multistriata
CAA04404.1	Cyclotella cryptica
XP_002179760.1	Phaeodactylum tricornutum CCAP 1055/1
EJK49165.1	Thalassiosira oceanica
AHH80644.1	Durinskia baltica
XP_002176987.1	Phaeodactylum tricornutum CCAP 1055/1
EJK66358.1	Thalassiosira oceanica
GAX14211.1	Fistulifera solaris
CEM23154.1	Vitrella brassicaformis CCMP3155
OEU11939.1	Fragilariopsis cylindrus CCMP1102
EJK48687.1	Thalassiosira oceanica
AAP79202.1	Bigelowiella natans
AAP79203.1	Bigelowiella natans
XP_007511181.1	Bathycoccus prasinos
KOO27643.1	Chrysochromulina tobinii
EJK65083.1	Thalassiosira oceanica
XP_002287075.1	Thalassiosira pseudonana CCMP1335
XP_005756200.1	Emiliania huxleyi CCMP1516
KOO21812.1	Chrysochromulina tobinii
GAX18433.1	Fistulifera solaris
OEU11878.1	Fragilariopsis cylindrus CCMP1102
ABV22207.1	Karlodinium veneficum
CBJ27803.1	Ectocarpus siliculosus
ABA55558.1	Karlodinium veneficum
OEU10866.1	Fragilariopsis cylindrus CCMP1102
XP_002182760.1	Phaeodactylum tricornutum CCAP 1055/1
CBJ27804.1	Ectocarpus siliculosus
KOO26795.1	Chrysochromulina tobinii
ABA55525.1	Isochrysis galbana
CBJ27807.1	Ectocarpus siliculosus
DAA05894.1	Bigelowiella natans
ABV22205.1	Karlodinium veneficum
CBJ27806.1	Ectocarpus siliculosus
ABA55557.1	Karlodinium veneficum
CBJ27788.1	Ectocarpus siliculosus
ABA55555.1	Karlodinium veneficum
CBJ27790.1	Ectocarpus siliculosus
VEU39636.1	Pseudo-nitzschia multistriata
CBJ27787.1	Ectocarpus siliculosus
CBJ27268.1	Ectocarpus siliculosus
XP_005788307.1	Emiliania huxleyi CCMP1516
CEL96922.1	Vitrella brassicaformis CCMP3155
OEU15317.1	Fragilariopsis cylindrus CCMP1102
KOO33027.1	Chrysochromulina tobinii

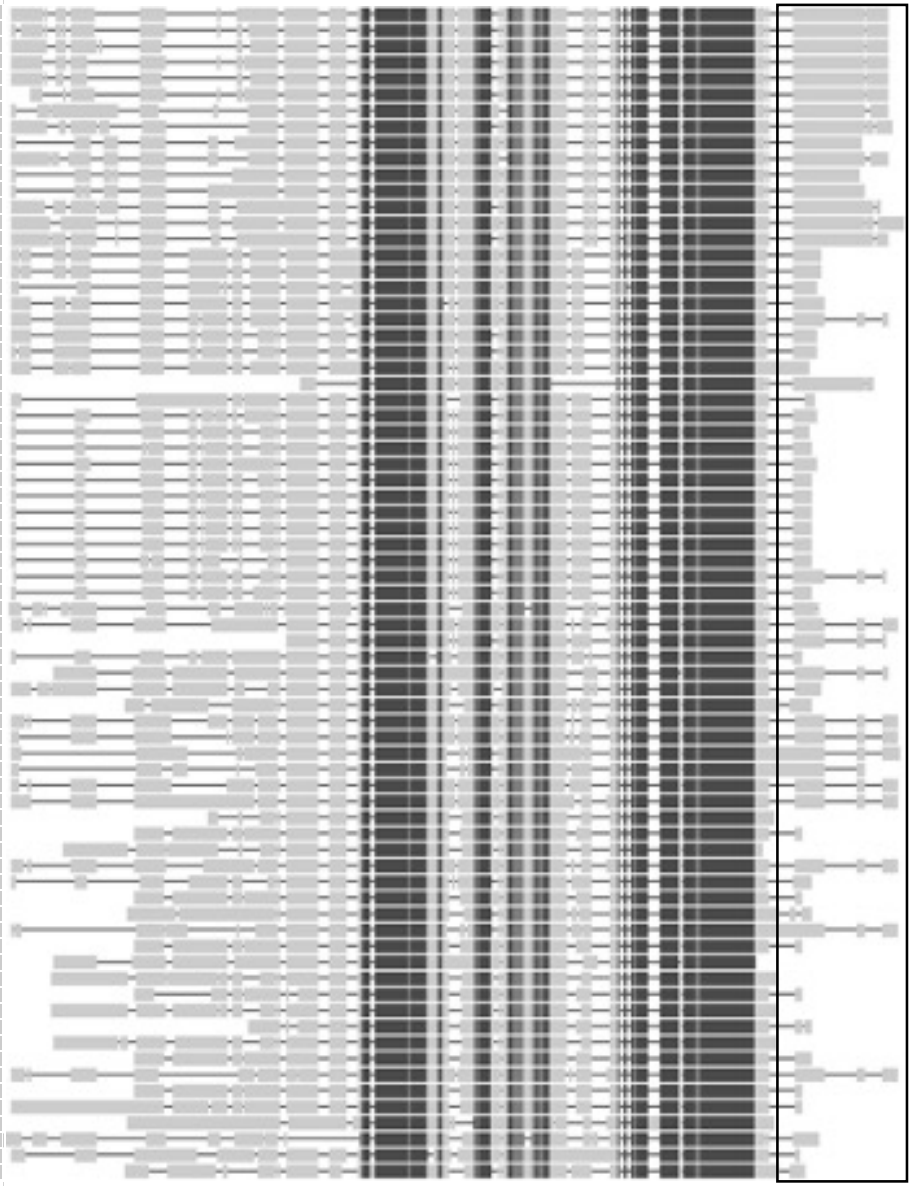

```
220 T----------EIFEHLALRFEKEAILELDDIERDLGLPVT-PLPDNLKSL-------  259
214 T----------EIFEHLVLRFEKEVILELEDVERDLGLPLT-PLPDNLKAI-------  253
216 T----------EIFEHLFLRFEKEAILELDDIERDIGLPVT-PLPDNLKAL-------  255
215 T----------EIFEHLFLRFEKEAILELDDIERDVGLPVT-PLPSNLANL-------  254
209 T----------EIFEHLFLRFEKEAILELDDIERDIGLPVT-PLPENLKAI-------  248
207 T----------EIFEHLFLRFEKEAILELDDLEVDLGLPVT-PLPDALKAI-------  246
220 Q----------EIFEHLFVGAADEVVKELDDIERDLGISET---PVPFPGF-------  257
219 V----------EIFEHLFYDIEKEVVLELDDIERDLGLPET-PIP-VLRTRGA-----  259
213 R----------EIFEHLFIGVENEVIAEATLVEKEIGLIQ-----------------  242
224 Q----------GIFEHLAATVADDVVREVDVLEKAAGLPET---PIPFPGF-------  261
209 R----------EIFEHLFIGIEKEILAEEVTVEKEVGIL-----------------  237
219 R----------EIFEHLFVSIGKEIEAEEVLVEREVGILPK---------------  249
240 V----------EIFEHLFFNVEKEVIEEIDEIEAELGLPPSIPIP-TL---------  276
234 R----------EIFEHLALYAERELILEIEDLDPALNIPVP-DIP--PAGIGAAFYNK  278
235 V----------EIFEHLFFDVEKLAIEEIDEIEVELGLPPSIPIP-TIPLK------  274
233 ----------EIFEHLFKRLGL-----------------------------------  244
233 ----------EIFVHLFKRLGL-----------------------------------  244
218 ----------EIFEHPGAAL-------------------------------------  227
232 ----------GIFEHLFKRLGLD----------------------------------  244
231 ----------EIFYQVGDTVKGS-------------SSP--------PL-------  248
222 ----------GIIENLKASS-------------------------------------  231
221 ----------GIIENLKASS-------------------------------------  230
233 PIFNSLGGRVLGTVEKTN---------------------------------------  250
136 R----------GIFEHLALYLEREAILEIEDLDPALNIALP-TIP-----------  169
222 P--------------IFGQ-------------------------------------  226
211 ----------GIIQHFTASS-------------------------------------  220
204 ----------GILEHLL----------------------------------------  210
202 ----------GILEHFSS---------------------------------------  209
215 ----------GIIQHFTASS-------------------------------------  224
206 ----------GIIEHFTA---------------------------------------  213
203 ----------GILEHFSS---------------------------------------  210
202 ----------GILENLQG---------------------------------------  209
203 ----------GILETLLN---------------------------------------  210
202 ----------GILEHLQA---------------------------------------  209
196 ----------GILENLGL---------------------------------------  203
203 ----------GIVQHFQVGMIEK-------------AVQ--------L--------  219
208 ----------GIIEHFLG----------------------------------------  215
213 Q----------KILDHLGIT-G----------------------------------  223
224 E----------IFVHLGLAPDTF-------------DPT--------SLPVTF---  245
164 ----------GIVQHFQVGMIEK-------------AVQ--------L--------  180
214 ----------PILG----------------------------------------  217
242 T----------MYEALNLDKLVP-------------PHG--------PI-------  259
240 K----------IFPQFDLYPYQ-----------------------------------  251
210 TWGAY-----FGVASNPFQ-------------------------------------  223
224 E----------ILVHAGLAPDDF-------------DPS--------SLPVQF---  245
215 E----------IFVNLGLATDRF-------------DPS--------TLPVQF---  236
202 TWSQQDVNFEGLLLGGYFSQEAAE-------------VAR--------DAAASAL--  235
189 TWASTDSTEEGILLGGWFAQRAAD-------------LAQ----------------  215
219 E----------IFVNLGLAQDRF-------------DPS--------VLPIQF---  240
246 E----------IFVNLGLAPDTF-------------DPS--------SLPVKF---  267
170 KLF----------------------------------------------------  172
217 D----------ILG----------------------------------------  220
                ----------------------------------------
225 E----------IFVNFGLAPDTF-------------DPT--------SLPVTF---  246
205 ----------GILENLFG----------------------------------------  212
217 D----------ILG----------------------------------------  220
220 TWGTY-----FG---RPDL-----------------------------------  230
192 TWSQQDTGFEGLLLGGYFNQEAAE-------------LAR--------DAATGL---  224
217 D----------ILG----------------------------------------  220
                ----------------------------------------
237 KLFA----------------------------------------------------  240
193 D----------ILG----------------------------------------  196
235 KLFA----------------------------------------------------  238
172 N----------ILD-FLH----------------------------------------  178
233 KLFQ----------------------------------------------------  236
217 D----------ILPNFFF----------------------------------------  224
210 E----------IFVNAGLAEDRF-------------DPS--------KLPIQF---  231
217 D----------ILG----------------------------------------  220
268 P----------IFG----------------------------------------  271
232 KLF----------------------------------------------------  234
194 Q----------EILEHLGVTTG----------------------------------  205
238 T----------LF----------------------------------------  240
200 TWGAY-----WGDASF----------------------------------------  210
```

***Figure S1**. Alignment of LHCSR-like protein sequences. BLAST of LHCSR-like proteins using LHCSR3 from Chlamydomonas reinhardtii (XP_001696064.1). Sequences with e-value and score higher than 3e-39 and 144 respectively are listed with accession number and organisms and a graphic overview is presented. On right, focus on C-terminal region; conserved protonatable residues are written in red. Accession numbers highlighted in yellow represent proteins with protonatable residues conservation higher than 50%.*

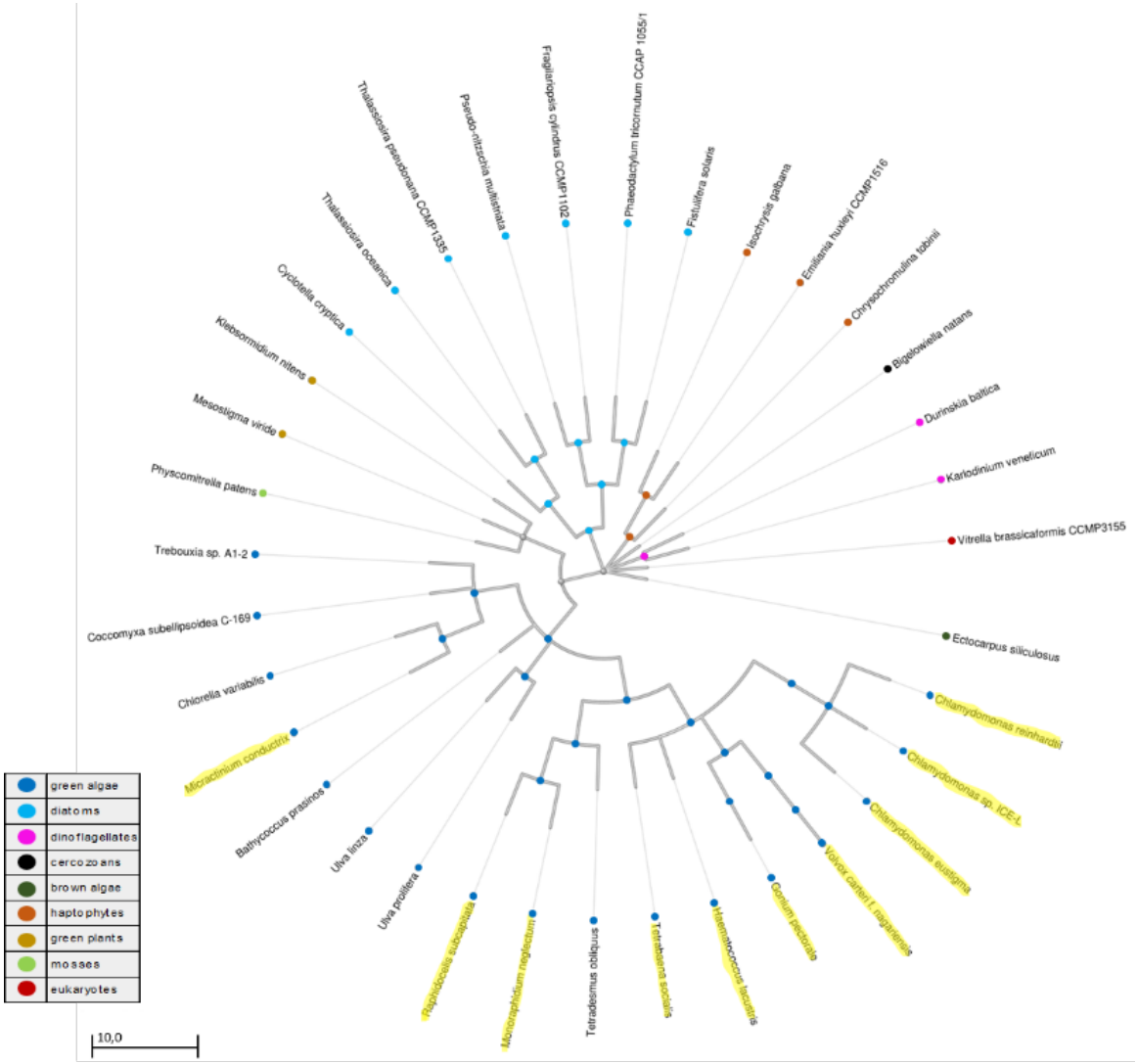

***Figure S2**. Phylogenetic tree of the organisms possessing LHCSR-like proteins. Organism listed in Figure S1 were subjected to a phylogenetic tree building using NCBI taxonomy database. Yellow highlighted organisms are those presenting protein with protonatable residues conservation higher than 50%, which are the same highlighted in Figure S1.*

		E221			E224							E231		E233				E237		D239	D240		E242		D244												D254					
Sequence	T	E	I	F	E	H	L	A	L	R	F	E	K	E	A	I	L	E	L	D	D	I	E	R	D	L	G	L	P	V	T	P	L	P	D	N	L	K	S	L
Solvent accessibility	4	2	1	0	3	1	0	2	4	1	0	4	4	1	1	1	2	2	0	3	4	0	4	5	4	2	2	1	3	3	0	3	1	3	6	4	0	4	7	5
Protonatable residues solvent accessibility		2			3							4		1				2		3	4		4		4										6					
Residue conservation (all sequences)		3			5							2		2				2		2	1		2		1										1					
conservation >50%)		9			10							8		9				10		7	6		9		5										3					
TOTAL SCORE		3			0							6		4				4		6	7		6		8										10					

***Figure S3**. Solvent accessibility and residues conservation. Solvent accessibility for C-terminal region (residues 220-259) of C. reinhardtii LHCSR3 (XP_001696064.1) was predicted using I-TASSER software which attributes to each residue a 0-9 score indicating the probability for solvent exposure (high score indicates higher probability). Residues*

*conservation between all the sequences used for alignment and between 15 sequences showing protonatable residues conservation higher than 50% (same highlighted in figure S1 and S2). Conservation is expressed by a 0-10 score with 10 meaning conservation in all sequences and 0 in none. Total score calculated as [(3*ResiduesConservation)-SolventAccessibility] is expressed as 0-10 score; high score means higher probability to be peculiar sites in C. reinhardtii based on residues conservation and solvent accessibility.*

```
LHCSR3_WT       MLANVVSRKASGLRQTPARATVAVKSVSGRRTTAAEPQTAAPVAAEDVFAYTKNLPGVTA      60
LHCSR3_BM6      MLANVVSRKASGLRQTPARATVAVKSVSGRRTTAAEPQTAAPVAAEDVFAYTKNLPGVTA      60
                ************************************************************
LHCSR3_WT       PFEGVFDPAGFLATASIKDVRRWRESEITHGRVAMLAALGFVVGEQLQDFPLFFNWDGRV      120
LHCSR3_BM6      PFEGVFDPAGFLATASIKDVRRWRESEITHGRVAMLAALGFVVGEQLQDFPLFFNWDGRV      120
                ************************************************************
LHCSR3_WT       SGPAIYHFQQIGQGFWEPLLIAIGVAESYRVAVGWATPTGTGFNSLKDDYEPGDLGFDPL      180
LHCSR3_BM6      SGPAIYHFQQIGQGFWEPLLIAIGVAESYRVAVGWATPTGTGFNSLKDDYEPGDLGFDPL      180
                ************************************************************
LHCSR3_WT       GLKPTDPEELKVMQTKELNNGRLAMIAIAAFVAQELVEQTEIFEHLALRFEKEAILELDD      240
LHCSR3_BM6      GLKPTDPEELKVMQTKELNNGRLAMIAIAAFVAQELVEQTEIFEHLALRFANPTVNNAFA      240
                ********************************************** : :: :
LHCSR3_WT       IERDLGLPVTPLPDNLKSL   259
LHCSR3_BM6      FATKFT----PSA------   249
                :  .:     *
```

***Figure S4**. Alignment of LHCSR3 and LHCSR3-BM6 protein sequences. LHCSR3 and LHCSR3 peptide sequences. "*" indicates perfect alignment; ":" indicates a site belonging to group exhibiting strong similarity while "." indicates a site belonging to a group exhibiting weak similarity. Putative transit peptide and substitute LHCBM6 C-terminal region are orange and blue respectively highlighted. Protonatable residues, exposed to the lumen, according to* (Ballottari *et al.*, 2016) *are red written.*

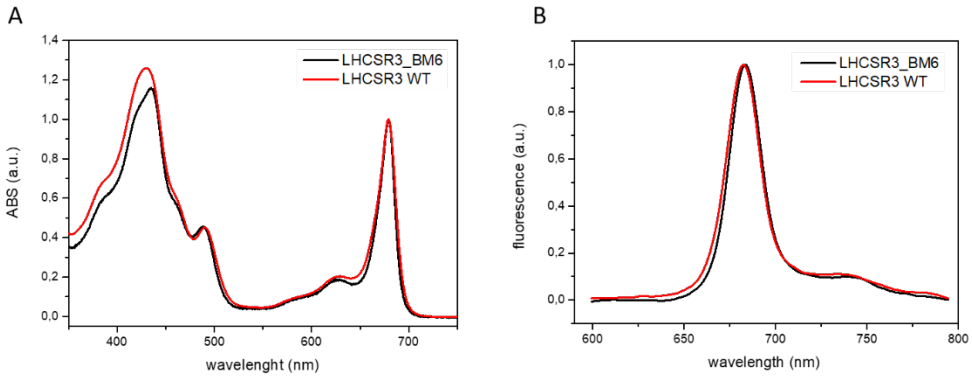

*Figure **S5**. Absorption and fluorescence of LHCSR recombinant proteins. Absorption (A) and room temperature fluorescence (excitation at 440nm) (B) of LHCSR3 WT and LHCSR3-BM6.*

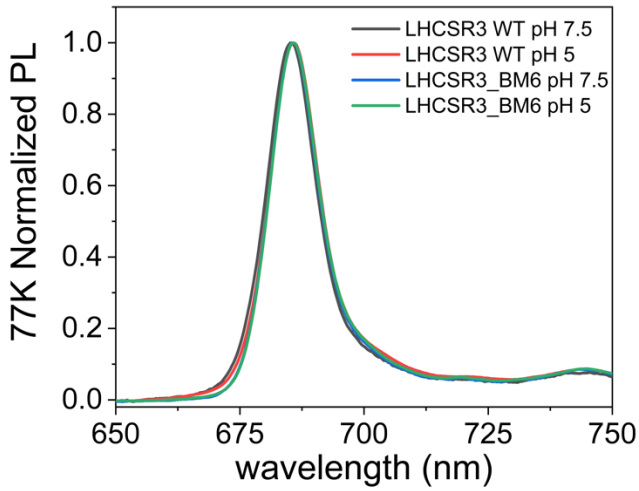

***Figure S6**. 77K fluorescence emission of LHCSR3 recombinant proteins. Fluorescence emission spectra at 77K (excitation at 440 nm) of LHCSR3 WT and LHCSR3-BM6.*

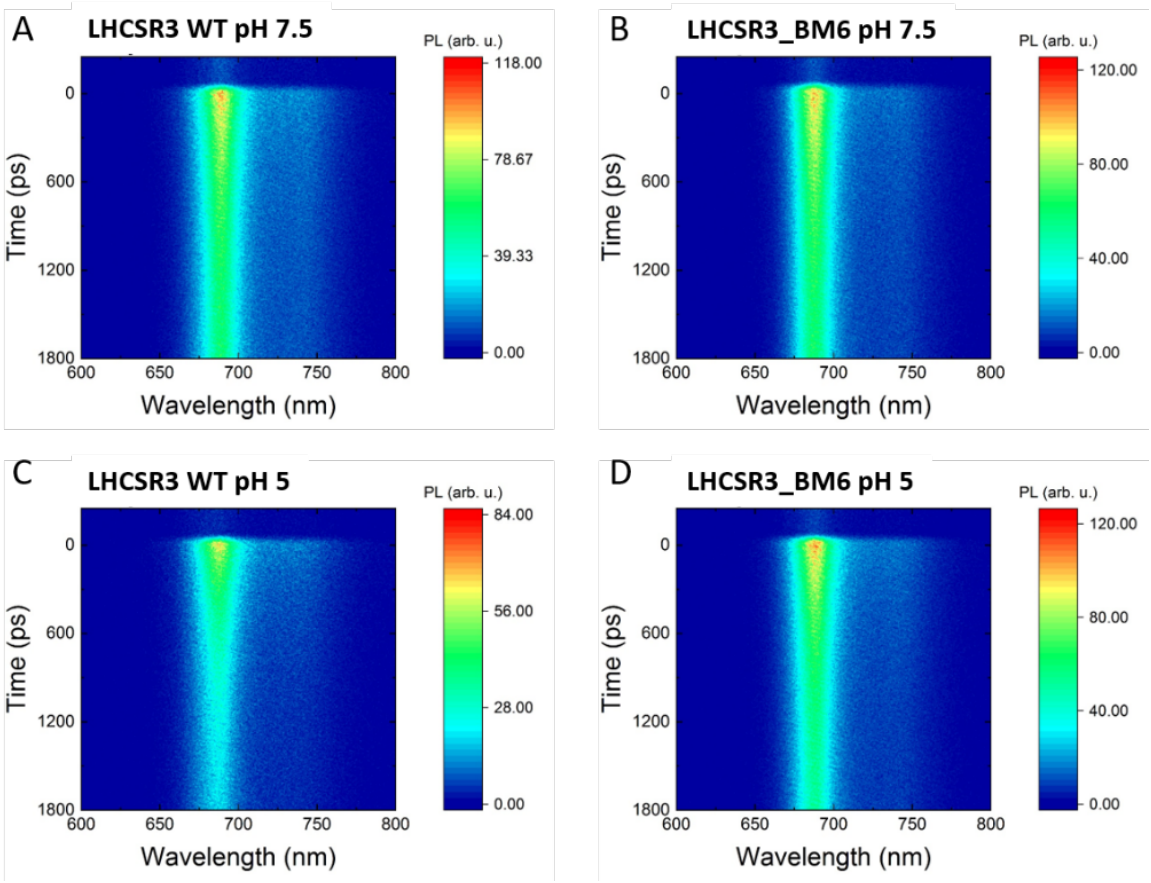

***Figure S7**. TRPL maps. TRPL maps (pump at 430nm) of LHCSR3 WT pH 7.5 (A) and pH 5 (C); LHCSR3-BM6 pH 7.5 (B) and 5 (D).*

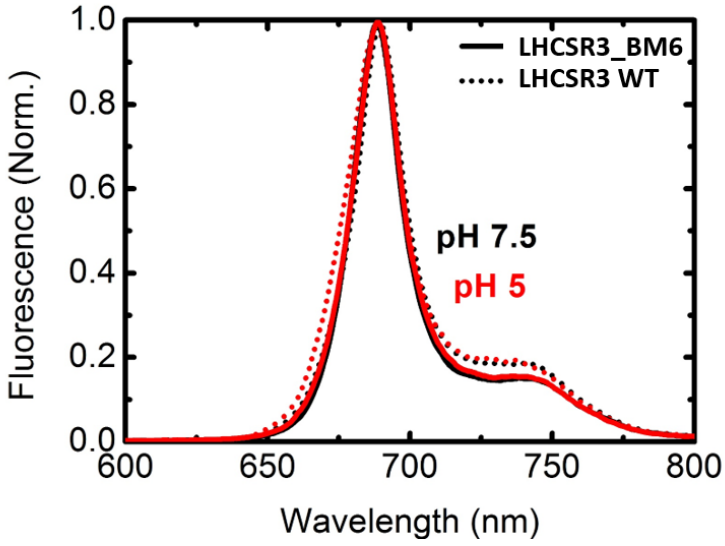

***Figure S8**. Time integrated TRPL spectra. Integrated TRPL spectra of LHCSR3 WT and LHCSR3-BM6 (pump at 430 nm, integration up to 1.8 ns).*

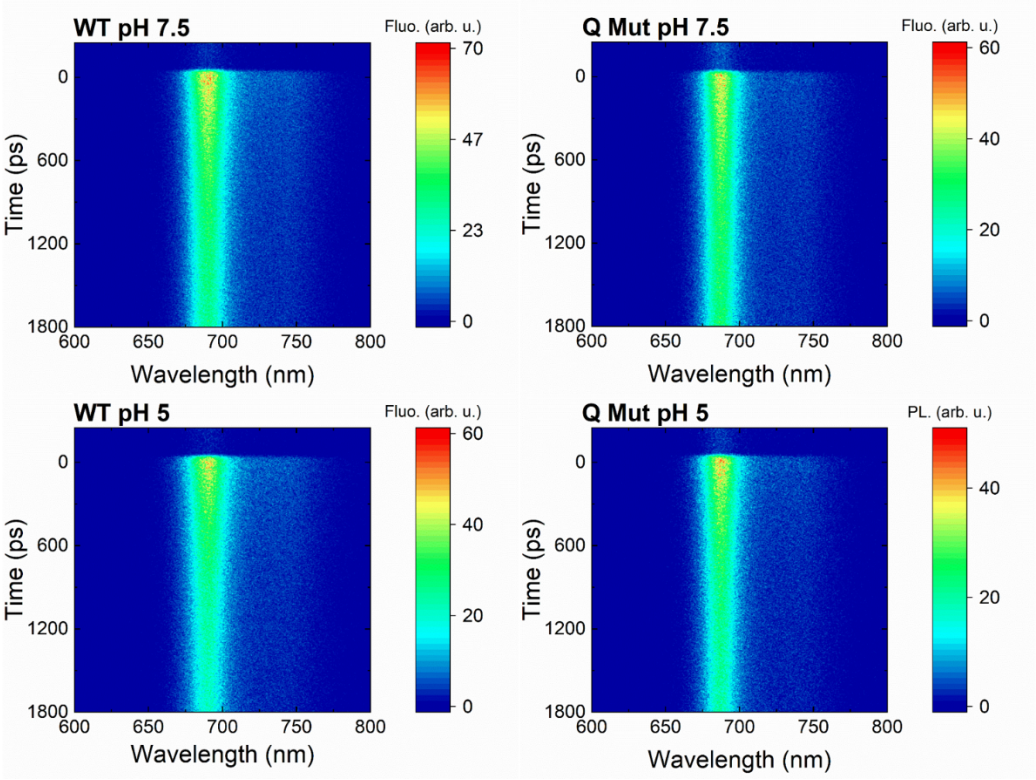

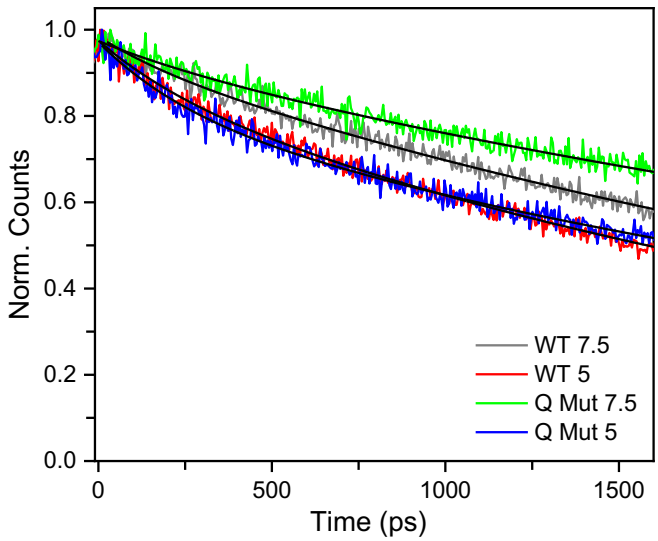

***Figure S9**. TRPL maps and time traces for LHCSR3 WT and LHCSR3-Q mutant at pH 5 and pH 7.5. The mutant and the WT, which acts as control sample, were prepared at the same time and with the same pigment mix. TRPL time traces for LHCSR-WT and LHCSR3-Q mutant samples at pH 5 and pH 7.5 were retrieved from TRPL maps upon spectral integration. We attribute the slightly longer TRPL kinetics of the Q Mutant with respect to the LHCSR3-WT at pH 7.5 to a slightly higher concentration of loosely bound Chls which are not fully energetically connected to the other pigments within the protein.*

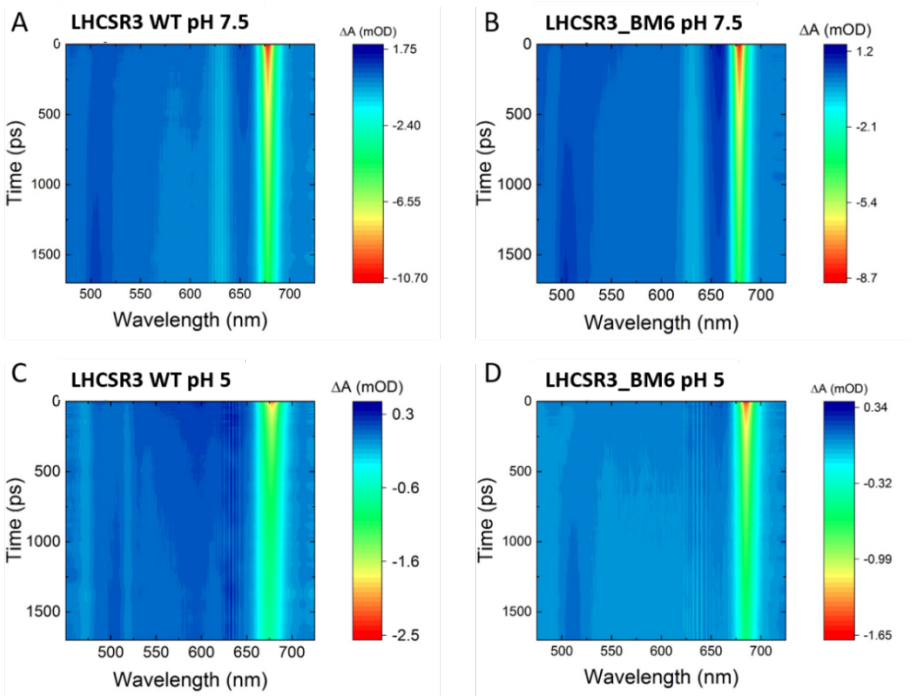

***Figure S10**. Visible TA maps. Visible TA maps (pump at 630 nm) of LHCSR3 WT pH 7.5 (A) and pH 5 (C); LHCSR3-BM6 pH 7.5 (B) and 5 (D).*

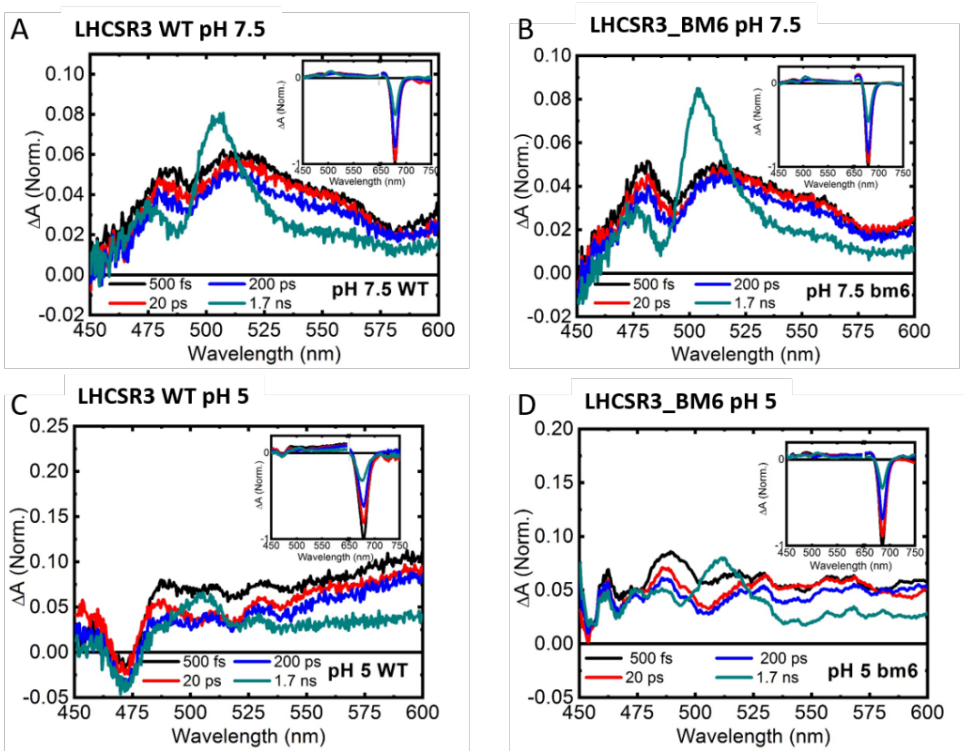

***Figure S11**. Visible TA spectra. Visible TA spectra of LHCSR3 WT pH 7.5 (A) and pH 5 (C); LHCSR3-BM6 pH 7.5 (B) and 5 (D). 500 fs, 20 ps, 200 ps and 1.7 ns after excitation are plotted. Whole TA spectra are plotted in each inset while the main graph represents a zoom into carotenoids region.*

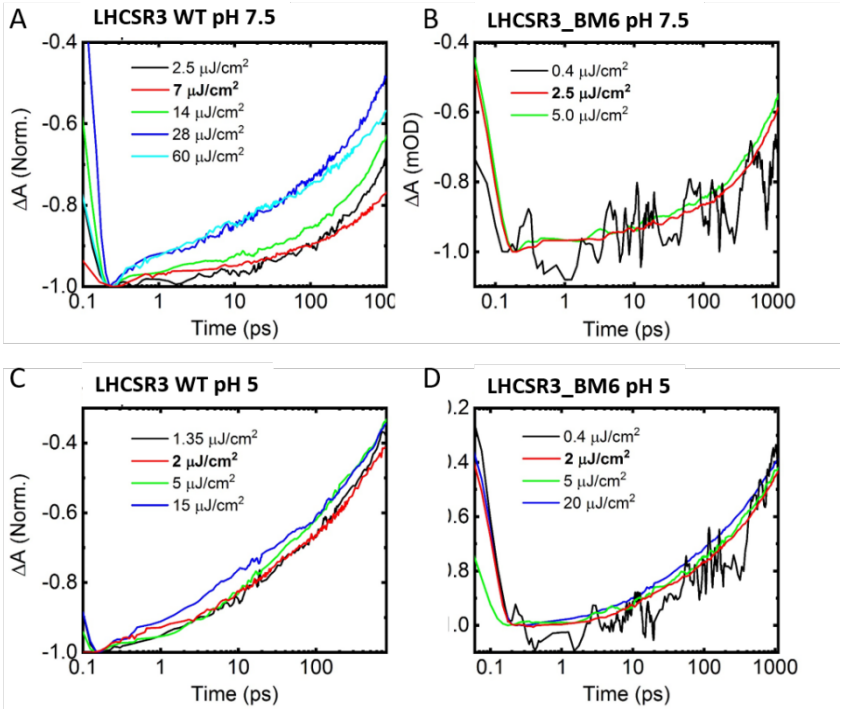

***Figure S12**. Fluence dependent TA dynamics. Fluence dependence for LHCSR3 WT and LHCSR3-BM6 at 680 nm. At the excitation fluence of 7 µJ/cm2 for LHCSR3 WT pH 7.5 and 2 µJ/cm2 for other samples used in the experiments, no singlet-singlet annihilation is detected.*

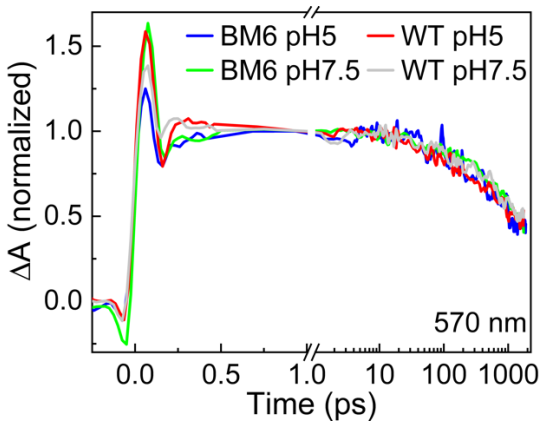

***Figure S13**. TA kinetic traces at 570 nm normalized at 1 ps.*

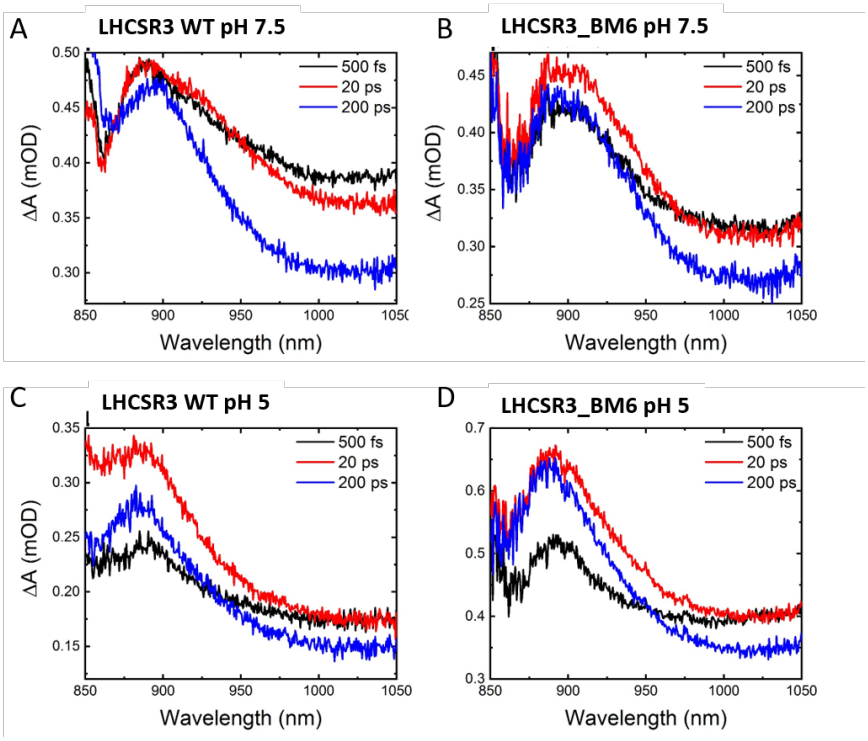

***Figure S14**. NIR TA spectra. NIR TA spectra of LHCSR3 WT pH 7.5 (A) and pH 5 (C); LHCSR3-BM6 pH 7.5 (B) and 5 (D). 500fs, 20ps and 200ps after excitation are plotted.*

	Chl	Chla	Chlb	Chl/Car	Car	violaxanthin	anteraxanthin	lutein	β-carotene
LHCSR3 WT	7.00	6.42 ±0.37	0.57 ±0.37	1.79	3.92	2.10 ±0.23	0.07 ±0.07	1.72 ±0.13	0.04 ±0.04
LHCSR3_BM6	7.00	6.20 ±0.12	0.71 ±0.12	2.06	3.40	1.94 ±0.17	0.07 ±0.02	1.37 ±0.17	0.03 ±0.02

***Table S1**. Pigment profiles. Pigment analysis of refolded LHCSR3 WT and LHCSR3-BM6 complexes. Chls: total number of chlorophylls; Cars: total number of carotenoids.*

	A_1 (%)	t_1 (ps)	A_2 (%)	t_2 (ps)	t_{avg} (ps)
pH 7,5 LHCSR3 WT	37	498	63	9762	6437
pH 5 LHCSR3 WT	49	386	51	3297	1871
pH 7,5 LHCSR3_BM6	37	582	63	9996	6513
pH 5 LHCSR3_BM6	44	478	56	6197	3681

***Table S2**. Time constants. Time constant of LHCSR3 WT and LHCSR3-BM6 obtained by bi-exponential fits of TRPL maps in the whole spectral range.*

6 CONCLUSION

Profitability of a sustainable implementation of microalgae on a large scale can be reached if relevant strains domestication is achieved. One main goal in this matter is to improve biomass accumulation efficiency in the conditions of industrial applications. Unlike natural environment, large-scale cultivation may translate to the use of photobioreactors at high cellular concentration, in which light penetration could be limited and stressing, considering a continuous illumination regime. Moreover, growth medium composition may be suboptimal, even presenting pollutant compounds and/or high-CO_2 flue gasses. With the long-run aim of meeting these requirements, this thesis focused in its first chapters on the understanding of the mechanisms behind microalgae adaptation to a high-CO_2 growth regime, photoprotection and on the process of PSII assembly. In the first study we observed that CO_2 is indeed a limiting factor for microalgae growth, as for plants in general. We assessed that supplying excess carbon results in faster replication rates which in turn are translated into higher biomass yields. The increased carbon fixation rate impacted photosynthesis as well as the overall energetic flow of the cell. In fact, we assisted to an altered mitochondrial respiration in response of the increased energetic sink that the chloroplast represents in such conditions. The quality of the biomass itself resulted altered towards TAGs accumulation, which in some industrial applications (e.g., biofuels and food/feed production), is desirable. Moreover, starch and protein content are lowered, probably as a response to a decreased C/N ratio and to a shift in the spatial ATP synthesis site either towards the chloroplast or cytosol.

As abovementioned, contrary to the natural environment, growth conditions in mass cultures requires high-cell concentration, therefore, due to the absorption of pigments bound to the antenna systems, light penetration within the culture is insufficient to sustain a profitable algal growth. Strains carrying truncated antennae are already known to perform better than the WT in small- and large-scale photobioreactors. The study of the mechanisms behind PSII assembly, herein presented in the third chapter, could enable us in the future to tune such complex process to achieve new mutants with reduced light harvesting capabilities through lower levels of PSII accumulation. On a related note, stoichiometry changes between PSII and PSI in favor of a reduced PSII content are

preferable for prolonged H_2 production in microalgae as presented by (Krishna, Styring and Mamedov, 2019). In the case of our study, we generated target-specific lpa2 knockout mutants by using the RNP complex–mediated CRISPR-Cas9 technique. We determined that the LPA2 protein has a role in PSII assembly and that its deletion caused an almost complete impairment of PSII function and accumulation, as evidenced by the blot analysis. As a consequence, chlorophyll content per cell, PSII quantum yield and photosynthetic oxygen evolution were strongly reduced, making the mutant limited in photoautotrophic growth.

In the last two chapters are presented our efforts into shedding light on the molecular mechanism behind the activation of thermal dissipation on behalf of the LHCSR3 protein of *C. reinhardtii*. NPQ is a multi-level mechanism evolved by photosynthetic organisms to withstand conditions of excessive light. *C. reinhardtii* relies on the activity of LHCSR3 as both sensor of such threatening circumstances and main actor of the quenching activity itself. Deepening the knowledge about the triggering of dissipative mechanisms could enable us to tune the extent of activation of photoprotection and adapt it to the finely controlled conditions of industrial mass culture, in which a conservation-oriented growth strategy typical of the natural environment results in an inadequate light-to-biomass conversion yield. We proceeded with a double approach, combining *in vivo* and *in vitro* studies to disentangle the components that concur in LHCSR3 quenching behavior. In chapter four, we contributed to the understanding of the long-debated and elusive role of zeaxanthin in the energy quenching of *C. reinhardtii*. Two distinct quenching mechanisms were identified within LHCSR3: a minor one dependent on the presence of zeaxanthin in the protein and a pH-dependent one as main mechanism. We also evidenced that constitutive zeaxanthin accumulation *in vivo* establishes a basal energy dissipation mechanism which is not specifically located within LHCSRs subunits, but rather delocalized among LHCs proteins. In the last chapter, we further analyzed the pH dependent LHCSR3 activation mechanism, generating a chimeric version of LHCSR3 which C-terminal portion has been substituted with the one of another LHC subunit unable to sense pH changes in the luminal space, therefore its activation as a quencher was reduced. From a spectroscopic point of view, we were able to determine that *Chl-Car*

interactions within the mutant protein were unchanged, compared to the WT, and that the resulted lowered quenching activation could be assigned to *Chl-Chl* interactions.

BIBLIOGRAPHY

Ahn, T. K. *et al.* (2008) 'Architecture of a charge-transfer state regulating light harvesting in a plant antenna protein', *Science*, 320(5877), pp. 794–797. doi: 10.1126/science.1154800.

Akerele, O. A. and Cheema, S. K. (2016) 'A balance of omega-3 and omega-6 polyunsaturated fatty acids is important in pregnancy', *Journal of Nutrition and Intermediary Metabolism*. Elsevier Inc, pp. 23–33. doi: 10.1016/j.jnim.2016.04.008.

Al-Dhabi, N. A. and Valan Arasu, M. (2016) 'Quantification of Phytochemicals from Commercial Spirulina Products and Their Antioxidant Activities', *Evidence-based Complementary and Alternative Medicine*, 2016. doi: 10.1155/2016/7631864.

Alboresia, A. *et al.* (2010) 'Physcomitrella patens mutants affected on heat dissipation clarify the evolution of photoprotection mechanisms upon land colonization', *Proceedings of the National Academy of Sciences of the United States of America*, 107(24), pp. 11128–11133. doi: 10.1073/pnas.1002873107.

Allen, J. F. (1992) 'Protein phosphorylation in regulation of photosynthesis.', *Biochimica et biophysica acta*, 1098(3), pp. 275–335. doi: 10.1016/s0005-2728(09)91014-3.

Allen, M. M. and Stanier, R. Y. (1968) 'Growth and division of some unicellular blue-green algae.', *Journal of general microbiology*, 51(2), pp. 199–202. doi: 10.1099/00221287-51-2-199.

Allorent, G. *et al.* (2013) 'Dual strategy to cope with high light in Chlamydomonas reinhardtii', *Plant Cell*, 25(2), pp. 545–557. doi: 10.1105/tpc.112.108274.

Amarie, S. *et al.* (2007) 'Carotenoid radical cations as a probe for the molecular mechanism of nonphotochemical quenching in oxygenic photosynthesis', *Journal of Physical Chemistry B*, 111(13), pp. 3481–3487. doi: 10.1021/jp066458q.

Amunts, A. *et al.* (2010) 'Structure determination and improved model of plant photosystem I', *Journal of Biological Chemistry*, 285(5), pp. 3478–3486. doi: 10.1074/jbc.M109.072645.

Amunts, A. and Nelson, N. (2009) 'Plant Photosystem I Design in the Light of Evolution', *Structure*. Cell Press, pp. 637–650. doi: 10.1016/j.str.2009.03.006.

Armbruster, U. *et al.* (2010) 'The Arabidopsis thylakoid protein PAM68 is required for

efficient D1 biogenesis and photosystem II assembly', *Plant Cell*, 22(10), pp. 3439–3460. doi: 10.1105/tpc.110.077453.

Aro, E. M. *et al.* (2005) 'Dynamics of photosystem II: A proteomic approach to thylakoid protein complexes', in *Journal of Experimental Botany*. Oxford Academic, pp. 347–356. doi: 10.1093/jxb/eri041.

Aro, E. M., Virgin, I. and Andersson, B. (1993) 'Photoinhibition of Photosystem II. Inactivation, protein damage and turnover', *BBA - Bioenergetics*. Elsevier, pp. 113–134. doi: 10.1016/0005-2728(93)90134-2.

Avenson, T. J. *et al.* (2008) 'Zeaxanthin radical cation formation in minor light-harvesting complexes of higher plant antenna', *Journal of Biological Chemistry*, 283(6), pp. 3550–3558. doi: 10.1074/jbc.M705645200.

Bae, S., Park, J. and Kim, J. S. (2014) 'Cas-OFFinder: A fast and versatile algorithm that searches for potential off-target sites of Cas9 RNA-guided endonucleases', *Bioinformatics*, 30(10), pp. 1473–1475. doi: 10.1093/bioinformatics/btu048.

Baek, K. *et al.* (2016) 'DNA-free two-gene knockout in Chlamydomonas reinhardtii via CRISPR-Cas9 ribonucleoproteins', *Scientific Reports*, 6(1), p. 30620. doi: 10.1038/srep30620.

Bailleul, B. *et al.* (2010) 'Electrochromism: A useful probe to study algal photosynthesis', *Photosynthesis Research*, 106(1), pp. 179–189. doi: 10.1007/s11120-010-9579-z.

Bailleul, B. *et al.* (2015) 'Energetic coupling between plastids and mitochondria drives CO 2 assimilation in diatoms', *Nature*, 524(7565), pp. 366–369. doi: 10.1038/nature14599.

Ballottari, M. *et al.* (2007) 'Contrasting behavior of higher plant photosystem I and II antenna systems during acclimation', *Journal of Biological Chemistry*, 282(12), pp. 8947–8958. doi: 10.1074/jbc.M606417200.

Ballottari, M. *et al.* (2010) 'Identification of the chromophores involved in aggregation-dependent energy quenching of the monomeric photosystem II antenna protein Lhcb5', *Journal of Biological Chemistry*, 285(36), pp. 28309–28321. doi: 10.1074/jbc.M110.124115.

Ballottari, M. *et al.* (2016) 'Identification of ph-sensing sites in the light harvesting complex stress-related 3 protein essential for triggering non-photochemical quenching in

chlamydomonas reinhardtii', *Journal of Biological Chemistry*, 291(14), pp. 7334–7346. doi: 10.1074/jbc.M115.704601.

Barber, J. and Andersson, B. (1992) 'Too much of a good thing: light can be bad for photosynthesis', *Trends in Biochemical Sciences*, 17(2), pp. 61–66. doi: 10.1016/0968-0004(92)90503-2.

BASSI, R. *et al.* (1993) 'Carotenoid-binding proteins of photosystem II', *European Journal of Biochemistry*, 212(2), pp. 297–303. doi: 10.1111/j.1432-1033.1993.tb17662.x.

Beckmann, J. *et al.* (2009) 'Improvement of light to biomass conversion by de-regulation of light-harvesting protein translation in Chlamydomonas reinhardtii', *Journal of Biotechnology*, pp. 70–77. doi: 10.1016/j.jbiotec.2009.02.015.

Bennoun, P. (1982) 'Evidence for a respiratory chain in the chloroplast', *Proceedings of the National Academy of Sciences*, 79(14), pp. 4352–4356. doi: 10.1073/pnas.79.14.4352.

Benvenuti, G. *et al.* (2017) 'Towards microalgal triglycerides in the commodity markets', *Biotechnology for Biofuels*, 10(1), p. 188. doi: 10.1186/s13068-017-0873-2.

Berger, H. *et al.* (2014) 'Integration of carbon assimilation modes with photosynthetic light capture in the green alga Chlamydomonas reinhardtii', *Molecular Plant*, 7(10), pp. 1545–1559. doi: 10.1093/mp/ssu083.

Bhosale, P. and Bernstein, P. S. (2005) 'Microbial xanthophylls', *Applied Microbiology and Biotechnology*. Appl Microbiol Biotechnol, pp. 445–455. doi: 10.1007/s00253-005-0032-8.

Blankenship, R. E. (2010) 'Early Evolution of Photosynthesis', *Plant Physiology*, 154(2), pp. 434–438. doi: 10.1104/pp.110.161687.

Blifernez-Klassen, O. *et al.* (2021) ' A gene regulatory network for antenna size control in carbon dioxide-deprived Chlamydomonas reinhardtii cells ', *The Plant Cell*. doi: 10.1093/plcell/koab012.

Boehm, M. *et al.* (2011) 'Investigating the early stages of photosystem II assembly in Synechocystis sp. PCC 6803: Isolation of CP47 and CP43 complexes', *Journal of Biological Chemistry*, 286(17), pp. 14812–14819. doi: 10.1074/jbc.M110.207944.

Boekema, E. J. and Braun, H. P. (2007) 'Supramolecular structure of the mitochondrial

oxidative phosphorylation system', *Journal of Biological Chemistry*. J Biol Chem, pp. 1–4. doi: 10.1074/jbc.R600031200.

Böhme, H. (1976) 'Photoreactions of Cytochrome b6and Cytochrome f in Chloroplast Photosystem I Fragments', *Zeitschrift fur Naturforschung - Section C Journal of Biosciences*, 31(1–2), pp. 68–77. doi: 10.1515/znc-1976-1-215.

Bonente, G. *et al.* (2008) 'Interactions between the photosystem II subunit PsbS and xanthophylls studied in vivo and in vitro', *Journal of Biological Chemistry*, 283(13), pp. 8434–8445. doi: 10.1074/jbc.M708291200.

Bonente, G., Ballottari, M., *et al.* (2011) 'Analysis of LHcSR3, a protein essential for feedback de-excitation in the green alga Chlamydomonas reinhardtii', *PLoS Biology*. Edited by T. Shikanai, 9(1), p. e1000577. doi: 10.1371/journal.pbio.1000577.

Bonente, G., Formighieri, C., *et al.* (2011) 'Mutagenesis and phenotypic selection as a strategy toward domestication of Chlamydomonas reinhardtii strains for improved performance in photobioreactors', *Photosynthesis Research*, pp. 107–120. doi: 10.1007/s11120-011-9660-2.

Bonente, G. *et al.* (2012) 'Acclimation of Chlamydomonas reinhardtii to different growth irradiances', *Journal of Biological Chemistry*, 287(8), pp. 5833–5847. doi: 10.1074/jbc.M111.304279.

Bricker, T. M. *et al.* (2012) 'The extrinsic proteins of Photosystem II', *Biochimica et Biophysica Acta - Bioenergetics*, 1817(1), pp. 121–142. doi: 10.1016/j.bbabio.2011.07.006.

Brinkert, K. *et al.* (2016) 'Photocurrents from photosystem II in a metal oxide hybrid system: Electron transfer pathways', *Biochimica et Biophysica Acta - Bioenergetics*, 1857(9), pp. 1497–1505. doi: 10.1016/j.bbabio.2016.03.004.

Brown, M. R. and Blackburn, S. I. (2014) 'Biofuels from microalgae', *Sustainable Energy Solutions in Agriculture*, 0(0), pp. 277–321. doi: 10.1201/b16643.

Buchanan BB, G. W. and (eds.), J. R. L. (2015) 'Biochemistry and Molecular Biology of Plants (second edition)', *Wiley, Blackwell (Chichester, UK)*, pp. 568–628. Available at: https://books.google.be/books?id=F4AZCgAAQBAJ&printsec=frontcover&dq=Biochemistry+and+Molecular+Biology+of+Plants,+2nd+Edition&hl=nl&sa=X&ved=2ahUKEwiXtrnS

1NTtAhXEi1wKHcITAEcQ6AEwAHoECAUQAg#v=onepage&q=Biochemistry and Molecular Biology of Plants%2C 2nd E.

Buick, R. (2008) 'When did oxygenic photosynthesis evolve?', *Philosophical Transactions of the Royal Society B: Biological Sciences*, 363(1504), pp. 2731–2743. doi: 10.1098/rstb.2008.0041.

Burlacot, A., Peltier, G. and Li-Beisson, Y. (2019) 'Subcellular Energetics and Carbon Storage in Chlamydomonas', *Cells*. NLM (Medline). doi: 10.3390/cells8101154.

Caffarri, S. *et al.* (2001) 'The Major Antenna Complex of Photosystem II Has a Xanthophyll Binding Site Not Involved in Light Harvesting', *Journal of Biological Chemistry*, 276(38), pp. 35924–35933. doi: 10.1074/jbc.M105199200.

Caffarri, S. *et al.* (2014) 'A Comparison Between Plant Photosystem I and Photosystem II Architecture and Functioning', *Current Protein & Peptide Science*, 15(4), pp. 296–331. doi: 10.2174/1389203715666140327102218.

Cai, W. *et al.* (2010) 'Cooperation of LPA3 and LPA2 is essential for photosystem II assembly in Arabidopsis', *Plant Physiology*, 154(1), pp. 109–120. doi: 10.1104/pp.110.159558.

Cazzaniga, S. *et al.* (2020) 'Photosystem II antenna complexes CP26 and CP29 are essential for nonphotochemical quenching in Chlamydomonas reinhardtii', *Plant Cell and Environment*, 43(2), pp. 496–509. doi: 10.1111/pce.13680.

Cazzonelli, C. I. (2011) 'Carotenoids in nature: Insights from plants and beyond', *Functional Plant Biology*, pp. 833–847. doi: 10.1071/FP11192.

Cecchin, M. *et al.* (2019) 'Chlorella vulgaris genome assembly and annotation reveals the molecular basis for metabolic acclimation to high light conditions', *Plant Journal*, 100(6), pp. 1289–1305. doi: 10.1111/tpj.14508.

Cheah, W. Y. *et al.* (2015) 'Biosequestration of atmospheric CO2 and flue gas-containing CO2 by microalgae', *Bioresource Technology*, 184, pp. 190–201. doi: 10.1016/j.biortech.2014.11.026.

Chi, W., Ma, J. and Zhang, L. (2012) 'Regulatory factors for the assembly of thylakoid membrane protein complexes', *Philosophical Transactions of the Royal Society B: Biological Sciences*, 367(1608), pp. 3420–3429. doi: 10.1098/rstb.2012.0065.

Chisti, Y. (2007) 'Biodiesel from microalgae', *Biotechnology Advances*, 25(3), pp. 294–306. doi: 10.1016/j.biotechadv.2007.02.001.

Croce, R. and Van Amerongen, H. (2013) 'Light-harvesting in photosystem i', *Photosynthesis Research*. Springer, pp. 153–166. doi: 10.1007/s11120-013-9838-x.

Dall'Osto, L., Caffarri, S. and Bassi, R. (2005) 'A mechanism of nonphotochemical energy dissipation, independent from PsbS, revealed by a conformational change in the antenna protein CP26', *Plant Cell*, 17(4), pp. 1217–1232. doi: 10.1105/tpc.104.030601.

Dang, K. Van *et al.* (2014) 'Combined increases in mitochondrial cooperation and oxygen photoreduction compensate for deficiency in cyclic electron flow in Chlamydomonas reinhardtii', *Plant Cell*, 26(7), pp. 3036–3050. doi: 10.1105/tpc.114.126375.

Dau, H. (1994) 'Molecular Mechanisms and Quantitative Models of Variable Photosystem Ii Fluorescence', *Photochemistry and Photobiology*. John Wiley & Sons, Ltd, pp. 1–23. doi: 10.1111/j.1751-1097.1994.tb03937.x.

Dekker, J. P. and Boekema, E. J. (2005) 'Supramolecular organization of thylakoid membrane proteins in green plants', *Biochimica et Biophysica Acta - Bioenergetics*. Elsevier, pp. 12–39. doi: 10.1016/j.bbabio.2004.09.009.

Demmig-Adams, B. *et al.* (1996) 'Using chlorophyll fluorescence to assess the fraction of absorbed light allocated to thermal dissipation of excess excitation', *Physiologia Plantarum*, 98(2), pp. 253–264. doi: 10.1034/j.1399-3054.1996.980206.x.

Depège, N., Bellafiore, S. and Rochaix, J. D. (2003) 'Role of chloroplast protein kinase Stt7 in LHCII phosphorylation and state transition in Chlamydomonas', *Science*, 299(5612), pp. 1572–1575. doi: 10.1126/science.1081397.

Dinc, E. *et al.* (2016) 'LHCSR1 induces a fast and reversible pH-dependent fluorescence quenching in LHCII in Chlamydomonas reinhardtii cells', *Proceedings of the National Academy of Sciences of the United States of America*, 113(27), pp. 7673–7678. doi: 10.1073/pnas.1605380113.

Dobáková, M., Tichý, M. and Komenda, J. (2007) 'Role of the PsbI protein in photosystem II assembly and repair in the cyanobacterium Synechocystis sp. PCC 6803', *Plant Physiology*, 145(4), pp. 1681–1691. doi: 10.1104/pp.107.107805.

Drop, B. *et al.* (2011) 'Photosystem I of Chlamydomonas reinhardtii contains nine light-harvesting complexes (Lhca) located on one side of the core', *Journal of Biological Chemistry*, 286(52), pp. 44878–44887. doi: 10.1074/jbc.M111.301101.

Dubini, A. and Ghirardi, M. L. (2015) 'Engineering photosynthetic organisms for the production of biohydrogen', *Photosynthesis Research*, pp. 241–253. doi: 10.1007/s11120-014-9991-x.

Dufossé, L. *et al.* (2005) 'Microorganisms and microalgae as sources of pigments for food use: A scientific oddity or an industrial reality?', in *Trends in Food Science and Technology*, pp. 389–406. doi: 10.1016/j.tifs.2005.02.006.

Elrad, D., Niyogi, K. K. and Grossman, A. R. (2002) 'A major light-harvesting polypeptide of photosystem II functions in thermal dissipation', *Plant Cell*, 14(8), pp. 1801–1816. doi: 10.1105/tpc.002154.

Erickson, E., Wakao, S. and Niyogi, K. K. (2015) 'Light stress and photoprotection in Chlamydomonas reinhardtii', *Plant Journal*, 82(3), pp. 449–465. doi: 10.1111/tpj.12825.

Escoubas, J. M. *et al.* (1995) 'Light intensity regulation of cab gene transcription is signaled by the redox state of the plastoquinone pool', *Proceedings of the National Academy of Sciences of the United States of America*, 92(22), pp. 10237–10241. doi: 10.1073/pnas.92.22.10237.

Eskling, M., Arvidsson, P.-O. and Akerlund, H.-E. (1997) 'The xanthophyll cycle, its regulation and components', *Physiologia Plantarum*, 100(4), pp. 806–816. doi: 10.1111/j.1399-3054.1997.tb00007.x.

Falkowski, P. G., Fenchel, T. and Delong, E. F. (2008) 'The microbial engines that drive earth's biogeochemical cycles', *Science*. American Association for the Advancement of Science, pp. 1034–1039. doi: 10.1126/science.1153213.

Fan, M. *et al.* (2015) 'Crystal structures of the PsbS protein essential for photoprotection in plants', *Nature Structural and Molecular Biology*, 22(9), pp. 729–735. doi: 10.1038/nsmb.3068.

Fang, W. *et al.* (2012) 'Transcriptome-wide changes in Chlamydomonas reinhardtii gene expression regulated by carbon dioxide and the CO2-concentrating mechanism regulator CIA5/CCM1', *Plant Cell*, 24(5), pp. 1876–1893. doi: 10.1105/tpc.112.097949.

Ferrante, P. *et al.* (2012) 'LHCBM1 and LHCBM2/7 polypeptides, components of major LHCII complex, have distinct functional roles in photosynthetic antenna system of Chlamydomonas reinhardtii', *Journal of Biological Chemistry*, 287(20), pp. 16276–16288. doi: 10.1074/jbc.M111.316729.

Field, C. B. *et al.* (1998) 'Primary production of the biosphere: Integrating terrestrial and oceanic components', *Science*, 281(5374), pp. 237–240. doi: 10.1126/science.281.5374.237.

Finazzi, G. (2005) 'The central role of the green alga Chlamydomonas reinhardtii in revealing the mechanism of state transitions', *Journal of Experimental Botany*, 56(411), pp. 383–388. doi: 10.1093/jxb/erh230.

Fleischmann, M. M. *et al.* (1999) 'Isolation and characterization of photoautotrophic mutants of Chlamydomonas reinhardtii deficient in state transition', *Journal of Biological Chemistry*, 274(43), pp. 30987–30994. doi: 10.1074/jbc.274.43.30987.

Flors, C. *et al.* (2006) 'Imaging the production of singlet oxygen in vivo using a new fluorescent sensor, Singlet Oxygen Sensor Green®', *Journal of Experimental Botany*, 57(8), pp. 1725–1734. doi: 10.1093/jxb/erj181.

FOYER, C. H., DESCOURVIÈRES, P. and KUNERT, K. J. (1994) 'Protection against oxygen radicals: an important defence mechanism studied in transgenic plants', *Plant, Cell & Environment*, 17(5), pp. 507–523. doi: 10.1111/j.1365-3040.1994.tb00146.x.

Frank, H. A. *et al.* (2000) 'Mechanism of nonphotochemical quenching in green plants: Energies of the lowest excited singlet states of violaxanthin and zeaxanthin', *Biochemistry*, 39(11), pp. 2831–2837. doi: 10.1021/bi9924664.

Fu, A. *et al.* (2007) 'A chloroplast cyclophilin functions in the assembly and maintenance of photosystem II in Arabidopsis thaliana', *Proceedings of the National Academy of Sciences of the United States of America*, 104(40), pp. 15947–15952. doi: 10.1073/pnas.0707851104.

Galka, P. *et al.* (2012) 'Functional analyses of the plant photosystem I-light-harvesting complex II supercomplex reveal that light-harvesting complex II loosely bound to photosystem ii is a very efficient antenna for photosystem I in state II', *Plant Cell*, 24(7), pp. 2963–2978. doi: 10.1105/tpc.112.100339.

García, J. L., de Vicente, M. and Galán, B. (2017) 'Microalgae, old sustainable food and

fashion nutraceuticals', *Microbial Biotechnology*. John Wiley and Sons Ltd, pp. 1017–1024. doi: 10.1111/1751-7915.12800.

Genty, B., Briantais, J. M. and Baker, N. R. (1989) 'The relationship between the quantum yield of photosynthetic electron transport and quenching of chlorophyll fluorescence', *Biochimica et Biophysica Acta - General Subjects*, 990(1), pp. 87–92. doi: 10.1016/S0304-4165(89)80016-9.

Girolomoni, L. *et al.* (2017) 'The function of LHCBM4/6/8 antenna proteins in Chlamydomonas reinhardtii', *Journal of Experimental Botany*, 68(3), pp. 627–641. doi: 10.1093/jxb/erw462.

Girolomoni, L. *et al.* (2019) 'LHCSR3 is a nonphotochemical quencher of both photosystems in Chlamydomonas reinhardtii', *Proceedings of the National Academy of Sciences of the United States of America*, 116(10), pp. 4212–4217. doi: 10.1073/pnas.1809812116.

Girolomoni, L. *et al.* (2020) 'Evolutionary divergence of photoprotection in the green algal lineage: a plant-like violaxanthin de-epoxidase enzyme activates the xanthophyll cycle in the green alga Chlorella vulgaris modulating photoprotection', *New Phytologist*, 228(1), pp. 136–150. doi: 10.1111/nph.16674.

Gokhale, Z. and Sayre, R. T. (2009) 'Photosystem II, a Structural Perspective', in Harris, E. H., Stern, D. B., and Witman, G. B. (eds) *The Chlamydomonas Sourcebook 3-Vol set*. Second Edi. London: Academic Press, pp. 573–602. doi: 10.1016/B978-0-12-370873-1.00024-1.

Gradinaru, C. C. *et al.* (2000) 'Identifying the pathways of energy transfer between carotenoids and chlorophylls in LHCII and CP29. A multicolor, femtosecond pump-probe study', *Journal of Physical Chemistry B*, 104(39), pp. 9330–9342. doi: 10.1021/jp001752i.

Guindon, S. *et al.* (2010) 'New algorithms and methods to estimate maximum-likelihood phylogenies: Assessing the performance of PhyML 3.0', *Systematic Biology*, 59(3), pp. 307–321. doi: 10.1093/sysbio/syq010.

Gwizdala, M. *et al.* (2016) 'Controlling Light Harvesting with Light', *Journal of the American Chemical Society*, 138(36), pp. 11616–11622. doi: 10.1021/jacs.6b04811.

Hakeem, K. R. (2015) 'Crop production and global environmental issues', *Crop Production*

and Global Environmental Issues, (September), pp. 1–598. doi: 10.1007/978-3-319-23162-4.

Harbinson, J. and Foyer, C. H. (1991) 'Relationships between the efficiencies of photosystems I and II and stromal redox state in CO2-free air - Evidence for cyclic electron flow in vivo', *Plant Physiology*, 97(1), pp. 41–49. doi: 10.1104/pp.97.1.41.

Harris, E. H. (2013) *The Chlamydomonas Sourcebook Volume1: Introduction to Chlamydomonas and Its Laboratory Use*, *Journal of Chemical Information and Modeling*.

Haustein, E. and Schwille, P. (2007) 'Fluorescence correlation spectroscopy: Novel variations of an established technique', *Annual Review of Biophysics and Biomolecular Structure*. Annu Rev Biophys Biomol Struct, pp. 151–169. doi: 10.1146/annurev.biophys.36.040306.132612.

Havaux, M., Dall'Osto, L. and Bassi, R. (2007) 'Zeaxanthin has enhanced antioxidant capacity with respect to all other xanthophylls in arabidopsis leaves and functions independent of binding to PSII antennae', *Plant Physiology*, 145(4), pp. 1506–1520. doi: 10.1104/pp.107.108480.

Havaux, M. and Niyogi, K. K. (1999) 'The violaxanthin cycle protects plants from photooxidative damage by more than one mechanism', *Proceedings of the National Academy of Sciences of the United States of America*, 96(15), pp. 8762–8767. doi: 10.1073/pnas.96.15.8762.

Hill, R. and Bendall, F. (1960) 'Function of the two cytochrome components in chloroplasts: A working hypothesis', *Nature*, 186(4719), pp. 136–137. doi: 10.1038/186136a0.

Hoefnagel, M. H. N., Atkin, O. K. and Wiskich, J. T. (1998) 'Interdependence between chloroplasts and mitochondria in the light and the dark', *Biochimica et Biophysica Acta - Bioenergetics*, pp. 235–255. doi: 10.1016/S0005-2728(98)00126-1.

Holt, N. E. *et al.* (2005) 'Carotenoid cation formation and the regulation of photosynthetic light harvesting', *Science*, 307(5708), pp. 433–436. doi: 10.1126/science.1105833.

Holt, N. E., Fleming, G. R. and Niyogi, K. K. (2004) 'Toward an understanding of the mechanism of nonphotochemical quenching in green plants', *Biochemistry*, pp. 8281–8289. doi: 10.1021/bi0494020.

Horton, P. and Hague, A. (1988) 'Studies on the induction of chlorophyll fluorescence in isolated barley protoplasts. IV. Resolution of non-photochemical quenching', *BBA - Bioenergetics*, 932(C), pp. 107–115. doi: 10.1016/0005-2728(88)90144-2.

Horton, P., Ruban, A. V. and Walters, R. G. (1996) 'Regulation of light harvesting in green plants', *Annual Review of Plant Physiology and Plant Molecular Biology*, 47(1), pp. 655–684. doi: 10.1146/annurev.arplant.47.1.655.

Huang, C. W. *et al.* (2016) 'Role of n-3 polyunsaturated fatty acids in ameliorating the obesity-induced metabolic syndrome in animal models and humans', *International Journal of Molecular Sciences*. MDPI AG. doi: 10.3390/ijms17101689.

Hynstova, V. *et al.* (2018) 'Separation, identification and quantification of carotenoids and chlorophylls in dietary supplements containing Chlorella vulgaris and Spirulina platensis using High Performance Thin Layer Chromatography', *Journal of Pharmaceutical and Biomedical Analysis*, 148, pp. 108–118. doi: 10.1016/j.jpba.2017.09.018.

Ishii, K. and Tahara, T. (2012) 'Extracting decay curves of the correlated fluorescence photons measured in fluorescence correlation spectroscopy', *Chemical Physics Letters*, 519–520(519-20:130-133), pp. 130–133. doi: 10.1016/j.cplett.2011.11.024.

Ishii, K. and Tahara, T. (2013a) 'Two-dimensional fluorescence lifetime correlation spectroscopy. 1. Principle', *Journal of Physical Chemistry B*, 117(39), pp. 11414–11422. doi: 10.1021/jp406861u.

Ishii, K. and Tahara, T. (2013b) 'Two-dimensional fluorescence lifetime correlation spectroscopy. 2. Application', *Journal of Physical Chemistry B*, 117(39), pp. 11423–11432. doi: 10.1021/jp406864e.

Jahns, P. and Holzwarth, A. R. (2012) 'The role of the xanthophyll cycle and of lutein in photoprotection of photosystem II', *Biochimica et Biophysica Acta - Bioenergetics*, 1817(1), pp. 182–193. doi: 10.1016/j.bbabio.2011.04.012.

Jans, F. *et al.* (2008) 'A type II NAD(P)H dehydrogenase mediates light-independent plastoquinone reduction in the chloroplast of Chlamydomonas', *Proceedings of the National Academy of Sciences of the United States of America*, 105(51), pp. 20546–20551. doi: 10.1073/pnas.0806896105.

Jansson, S. (1999) 'A guide to the Lhc genes and their relatives in Arabidopsis', *Trends in Plant Science*. Elsevier Ltd, pp. 236–240. doi: 10.1016/S1360-1385(99)01419-3.

Järvi, S., Suorsa, M. and Aro, E. M. (2015) 'Photosystem II repair in plant chloroplasts - Regulation, assisting proteins and shared components with photosystem II biogenesis', *Biochimica et Biophysica Acta - Bioenergetics*, 1847(9), pp. 900–909. doi: 10.1016/j.bbabio.2015.01.006.

Jensen, P. E. *et al.* (2007) 'Structure, function and regulation of plant photosystem I', *Biochimica et Biophysica Acta - Bioenergetics*. Elsevier, pp. 335–352. doi: 10.1016/j.bbabio.2007.03.004.

Jeong, J. *et al.* (2017) 'Loss of CpSRP54 function leads to a truncated light-harvesting antenna size in Chlamydomonas reinhardtii', *Biochimica et Biophysica Acta - Bioenergetics*, 1858(1), pp. 45–55. doi: 10.1016/j.bbabio.2016.10.007.

Jeong, J. *et al.* (2018) 'Deletion of the chloroplast LTD protein impedes LHCI import and PSI-LHCI assembly in Chlamydomonas reinhardtii', *Journal of Experimental Botany*, 69(5), pp. 1147–1158. doi: 10.1093/jxb/erx457.

Jin, E. S. *et al.* (2003) 'Role of the reversible xanthophyll cycle in the photosystem II damage and repair cycle in Dunaliella salina', *Plant Physiology*, 132(1), pp. 352–364. doi: 10.1104/pp.102.019620.

Johnson, M. P. (2016) 'Photosynthesis', *Essays in Biochemistry*, 60(3), pp. 255–273. doi: 10.1042/EBC20160016.

Joliot, P. A. and Finazzi, G. (2010) 'Proton equilibration in the chloroplast modulates multiphasic kinetics of nonphotochemical quenching of fluorescence in plants', *Proceedings of the National Academy of Sciences of the United States of America*, 107(28), pp. 12728–12733. doi: 10.1073/pnas.1006399107.

Jordan, P. *et al.* (2001) 'Three-dimensional structure of cyanobaoterial photosystem I at 2.5 Å resolution', *Nature*, 411(6840), pp. 909–917. doi: 10.1038/35082000.

Khan, S. A. *et al.* (2009) 'Prospects of biodiesel production from microalgae in India', *Renewable and Sustainable Energy Reviews*. Pergamon, pp. 2361–2372. doi: 10.1016/j.rser.2009.04.005.

Khush, G. S. (2001) 'Green revolution: The way forward', *Nature Reviews Genetics*. Nature Publishing Group, pp. 815–822. doi: 10.1038/35093585.

Kim, E. *et al.* (2017) 'Fluorescence lifetime analyses reveal how the high light-responsive protein LHCSR3 transforms PSII light-harvesting complexes into an energy-dissipative state', *Journal of Biological Chemistry*, 292(46), pp. 18951–18960. doi: 10.1074/jbc.M117.805192.

Kim, S., Fujitsuka, M. and Majima, T. (2013) 'Photochemistry of singlet oxygen sensor green', *Journal of Physical Chemistry B*, 117(45), pp. 13985–13992. doi: 10.1021/jp406638g.

Kirst, H. and Melis, A. (2014) 'The chloroplast signal recognition particle (CpSRP) pathway as a tool to minimize chlorophyll antenna size and maximize photosynthetic productivity', *Biotechnology Advances*, 32(1), pp. 66–72. doi: 10.1016/j.biotechadv.2013.08.018.

Komenda, J. *et al.* (2007) 'The exposed N-terminal tail of the D1 subunit is required for rapid D1 degradation during photosystem II repair in Synechocystis sp PCC 6803', *Plant Cell*, 19(9), pp. 2839–2854. doi: 10.1105/tpc.107.053868.

Komenda, J. *et al.* (2008) 'The cyanobacterial homologue of HCF136/YCF48 is a component of an early photosystem II assembly complex and is important for both the efficient assembly and repair of photosystem II in Synechocystis sp. PCC 6803', *Journal of Biological Chemistry*, 283(33), pp. 22390–22399. doi: 10.1074/jbc.M801917200.

Komenda, J. *et al.* (2012) 'The Psb27 assembly factor binds to the CP43 complex of photosystem II in the cyanobacterium Synechocystis sp. PCC 6803', *Plant Physiology*, 158(1), pp. 476–486. doi: 10.1104/pp.111.184184.

Komenda, J. and Barber, J. (1995) 'Comparison of psbO and psbH Deletion Mutants of Synechocystis PCC 6803 Indicates that Degradation of D1 Protein Is Regulated by the QB Site and Dependent on Protein Synthesis', *Biochemistry*, 34(29), pp. 9625–9631. doi: 10.1021/bi00029a040.

Kondo, T. *et al.* (2017) 'Single-molecule spectroscopy of LHCSR1 protein dynamics identifies two distinct states responsible for multi-timescale photosynthetic photoprotection', *Nature Chemistry*, 9(8), pp. 772–778. doi: 10.1038/NCHEM.2818.

Kondo, T. *et al.* (2019) 'Microsecond and millisecond dynamics in the photosynthetic

protein LHCSR1 observed by single-molecule correlation spectroscopy', *Proceedings of the National Academy of Sciences of the United States of America*, 166(23), pp. 11247–11252. doi: 10.1073/pnas.1821207116.

Kosuge, K. *et al.* (2018) *LHCSR1-dependent fluorescence quenching is mediated by excitation energy transfer from LHCII to photosystem I in Chlamydomonas reinhardtii*, *Proceedings of the National Academy of Sciences of the United States of America*. Proc Natl Acad Sci U S A. doi: 10.1073/pnas.1720574115.

Krishna, P. S., Styring, S. and Mamedov, F. (2019) 'Photosystem ratio imbalance promotes direct sustainable H2 production in: Chlamydomonas reinhardtii', *Green Chemistry*, 21(17), pp. 4683–4690. doi: 10.1039/c9gc01416k.

Kromdijk, J. *et al.* (2016) 'Improving photosynthesis and crop productivity by accelerating recovery from photoprotection', *Science*, 354(6314), pp. 857–861. doi: 10.1126/science.aai8878.

Krüger, T. P. J. *et al.* (2010) 'Fluorescence spectral dynamics of single LHCII trimers', *Biophysical Journal*, 98(12), pp. 3093–3101. doi: 10.1016/j.bpj.2010.03.028.

Krüger, T. P. J. *et al.* (2011) 'Conformational switching explains the intrinsic multifunctionality of plant light-harvesting complexes', *Proceedings of the National Academy of Sciences of the United States of America*, 108(33), pp. 13516–13521. doi: 10.1073/pnas.1105411108.

Kuhlgert, S. *et al.* (2016) 'MultispeQ Beta: A tool for large-scale plant phenotyping connected to the open photosynQ network', *Royal Society Open Science*, 3(10). doi: 10.1098/rsos.160592.

De La Cruz Valbuena, G. *et al.* (2019) 'Molecular Mechanisms of Nonphotochemical Quenching in the LHCSR3 Protein of Chlamydomonas reinhardtii', *Journal of Physical Chemistry Letters*, 10(10), pp. 2500–2505. doi: 10.1021/acs.jpclett.9b01184.

Laemmli, U. K. (1970) 'Cleavage of structural proteins during the assembly of the head of bacteriophage T4', *Nature*, 227(5259), pp. 680–685. doi: 10.1038/227680a0.

Lagarde, D., Beuf, L. and Vermaas, W. (2000) 'Increased production of zeaxanthin and other pigments by application of genetic engineering techniques to Synechocystis sp.

strain PCC 6803', *Applied and Environmental Microbiology*, 66(1), pp. 64–72. doi: 10.1128/AEM.66.1.64-72.2000.

Lefort, V., Longueville, J.-E. and Gascuel, O. (2017) 'SMS: Smart Model Selection in PhyML.', *Molecular biology and evolution*, 34(9), pp. 2422–2424. doi: 10.1093/molbev/msx149.

Lemeille, S. *et al.* (2009) 'Analysis of the Chloroplast Protein Kinase Stt7 during State Transitions', *PLoS Biology*. Edited by A. R. Grossman, 7(3), p. e1000045. doi: 10.1371/journal.pbio.1000045.

Lepot, K. *et al.* (2008) 'Microbially-influenced formation of 2,724 million-years old stromatolites', *Nature Geoscience*, 1, pp. 118–121.

Li-Beisson, Y. *et al.* (2019) 'The lipid biochemistry of eukaryotic algae', *Progress in Lipid Research*. Elsevier Ltd, pp. 31–68. doi: 10.1016/j.plipres.2019.01.003.

Li, T. *et al.* (2015) 'Regulation of starch and lipid accumulation in a microalga Chlorella sorokiniana', *Bioresource Technology*, 180, pp. 250–257. doi: 10.1016/j.biortech.2015.01.005.

Li, X. P. *et al.* (2000) 'A pigment-binding protein essential for regulation of photosynthetic light harvesting', *Nature*, 403(6768), pp. 391–395. doi: 10.1038/35000131.

Li, X. P. *et al.* (2004) 'Regulation of photosynthetic light harvesting involves intrathylakoid lumen pH sensing by the PsbS protein', *Journal of Biological Chemistry*, 279(22), pp. 22866–22874. doi: 10.1074/jbc.M402461200.

Li, Z. *et al.* (2009) 'Lutein accumulation in the absence of zeaxanthin restores nonphotochemical quenching in the arabidopsis thaliana npq1 mutant', *Plant Cell*, 21(6), pp. 1798–1812. doi: 10.1105/tpc.109.066571.

Li, Z. *et al.* (2016) 'Evolution of an atypical de-epoxidase for photoprotection in the green lineage', *Nature Plants*, 2(10). doi: 10.1038/nplants.2016.140.

Liao, P. N. *et al.* (2010) 'Correlation of car S1 → Chl with Chl → Car S 1 energy transfer supports the excitonic model in quenched light harvesting complex II', *Journal of Physical Chemistry B*, 114(47), pp. 15650–15655. doi: 10.1021/jp1034163.

Liguori, N. *et al.* (2013) 'Regulation of light harvesting in the green alga chlamydomonas

reinhardtii: The c-terminus of lhcsr is the knob of a dimmer switch', *Journal of the American Chemical Society*, 135(49), pp. 18339–18342. doi: 10.1021/ja4107463.

Liguori, N. *et al.* (2015) 'From light-harvesting to photoprotection: Structural basis of the dynamic switch of the major antenna complex of plants (LHCII)', *Scientific Reports*, 5(1), p. 15661. doi: 10.1038/srep15661.

Liguori, N. *et al.* (2016) 'Excitation dynamics and structural implication of the stress-related complex LHCSR3 from the green alga Chlamydomonas reinhardtii', *Biochimica et Biophysica Acta - Bioenergetics*, 1857(9), pp. 1514–1523. doi: 10.1016/j.bbabio.2016.04.285.

Liguori, N. *et al.* (2017) 'Different carotenoid conformations have distinct functions in light-harvesting regulation in plants', *Nature Communications*, 8(1), pp. 1–9. doi: 10.1038/s41467-017-02239-z.

Lindsey, R. (2020) *Climate Change: Atmospheric Carbon Dioxide | NOAA Climate.gov*, *Climate.gov*. Available at: https://www.climate.gov/news-features/understanding-climate/climate-change-atmospheric-carbon-dioxide (Accessed: 26 April 2021).

Linke, K. and Ho, F. M. (2014) 'Water in Photosystem II: Structural functional and mechanistic considerations', *Biochimica et Biophysica Acta - Bioenergetics*. Elsevier, pp. 14–32. doi: 10.1016/j.bbabio.2013.08.003.

Loera-Quezada, M. M. *et al.* (2016) 'A novel genetic engineering platform for the effective management of biological contaminants for the production of microalgae', *Plant Biotechnology Journal*, 14(10), pp. 2066–2076. doi: 10.1111/pbi.12564.

Lu, Y. (2016) 'Identification and roles of photosystem II assembly, stability, and repair factors in Arabidopsis', *Frontiers in Plant Science*, 7(FEB2016), p. 168. doi: 10.3389/fpls.2016.00168.

Lum, K. K., Kim, J. and Lei, X. G. (2013) 'Dual potential of microalgae as a sustainable biofuel feedstock and animal feed', *Journal of Animal Science and Biotechnology*, 4(1). doi: 10.1186/2049-1891-4-53.

Lupatini, A. L. *et al.* (2017) 'Potential application of microalga Spirulina platensis as a protein source', *Journal of the Science of Food and Agriculture*. John Wiley and Sons Ltd, pp. 724–732. doi: 10.1002/jsfa.7987.

Ma, J. *et al.* (2007) 'LPA2 is required for efficient assembly of photosystem II in Arabidopsis thaliana', *Plant Cell*. 2007/06/29, 19(6), pp. 1980–1993. doi: 10.1105/tpc.107.050526.

Ma, Y. Z. *et al.* (2003) 'Evidence for direct carotenoid involvement in the regulation of photosynthetic light harvesting', *Proceedings of the National Academy of Sciences of the United States of America*, 100(8), pp. 4377–4382. doi: 10.1073/pnas.0736959100.

Magdaong, N. C. M. and Blankenship, R. E. (2018) 'Photoprotective, excited-state quenching mechanisms in diverse photosynthetic organisms', *Journal of Biological Chemistry*. American Society for Biochemistry and Molecular Biology Inc., pp. 5018–5025. doi: 10.1074/jbc.TM117.000233.

Malkin, S. *et al.* (1981) 'Photosystem II Photosynthetic Unit Sizes from Fluorescence Induction in Leaves', *Plant Physiology*, 67(3), pp. 570–579. doi: 10.1104/pp.67.3.570.

Manayi, A. *et al.* (2016) 'Lutein and cataract: from bench to bedside', *Critical Reviews in Biotechnology*. Taylor and Francis Ltd, pp. 829–839. doi: 10.3109/07388551.2015.1049510.

De Marchis, F. *et al.* (2018) 'Expression of CLAVATA3 fusions indicates rapid intracellular processing and a role of ERAD', *Plant Science*, 271(February), pp. 67–80. doi: 10.1016/j.plantsci.2018.03.020.

Marín-Navarro, J. *et al.* (2007) 'Chloroplast translation regulation', *Photosynthesis Research*, 94(2–3), pp. 359–374. doi: 10.1007/s11120-007-9183-z.

Maruyama, S., Tokutsu, R. and Minagawa, J. (2014) 'Transcriptional regulation of the stress-responsive light harvesting complex genes in Chlamydomonas reinhardtii', *Plant and Cell Physiology*, 55(7), pp. 1304–1310. doi: 10.1093/pcp/pcu068.

Mascoli, V. *et al.* (2019) 'Capturing the Quenching Mechanism of Light-Harvesting Complexes of Plants by Zooming in on the Ensemble', *Chem*, 5(11), pp. 2900–2912. doi: 10.1016/j.chempr.2019.08.002.

Mascoli, V. *et al.* (2020) 'Design principles of solar light harvesting in plants: Functional architecture of the monomeric antenna CP29', *Biochimica et Biophysica Acta - Bioenergetics*, 1861(3). doi: 10.1016/j.bbabio.2020.148156.

Mayfield, S. P. and Franklin, S. E. (2005) 'Expression of human antibodies in eukaryotic

micro-algae', in *Vaccine*. Elsevier BV, pp. 1828–1832. doi: 10.1016/j.vaccine.2004.11.013.

Mellis, A. (1999) 'Photosystem-II damage and repair cycle in chloroplasts: What modulates the rate of photodamage in vivo?', *Trends in Plant Science*, 4(4), pp. 130–135. doi: 10.1016/S1360-1385(99)01387-4.

Merchant, S. S. *et al.* (2007) 'The Chlamydomonas genome reveals the evolution of key animal and plant functions', *Science*, 318(5848), pp. 245–251. doi: 10.1126/science.1143609.

Mets, Ü. (2001) 'Antibunching and rotational diffusion in FCS', in *Springer Series in Chemical Physics*. Springer, pp. 346–359. doi: 10.1007/978-3-642-59542-4_16.

Metz, J. G. *et al.* (1989) 'Directed Alteration of the D1 Polypeptide of Photosystem II: Evidence That Tyrosine-161 Is the Redox Component, Z, Connecting the Oxygen-Evolving Complex to the Primary Electron Donor, P680', *Biochemistry*, 28(17), pp. 6960–6969. doi: 10.1021/bi00443a028.

Meurer, J. *et al.* (1998) 'A nuclear-encoded protein of prokaryotic origin is essential for the stability of photosystem II in Arabidopsis thaliana', *EMBO Journal*, 17(18), pp. 5286–5297. doi: 10.1093/emboj/17.18.5286.

Miloslavina, Y. *et al.* (2008) 'Far-red fluorescence: A direct spectroscopic marker for LHCII oligomer formation in non-photochemical quenching', *FEBS Letters*, 582(25–26), pp. 3625–3631. doi: 10.1016/j.febslet.2008.09.044.

Mimuro, M. and Katoh, T. (1991) 'Carotenoids in photosynthesis: Absorption, transfer and dissipation of light energy', *Pure and Applied Chemistry*, 63(1), pp. 123–130. doi: 10.1351/pac199163010123.

Minagawa, J. (2011) 'State transitions-the molecular remodeling of photosynthetic supercomplexes that controls energy flow in the chloroplast', *Biochimica et Biophysica Acta - Bioenergetics*, 1807(8), pp. 897–905. doi: 10.1016/j.bbabio.2010.11.005.

Montingelli, M. E., Tedesco, S. and Olabi, A. G. (2015) 'Biogas production from algal biomass: A review', *Renewable and Sustainable Energy Reviews*, pp. 961–972. doi: 10.1016/j.rser.2014.11.052.

Moore, A. L. *et al.* (1982) 'Photoprotection by carotenoids during photosynthesis: Motional

dependence of intramolecular energy transfer', *Science*, 216(4549), pp. 982–984. doi: 10.1126/science.216.4549.982.

Morosinotto, T. *et al.* (2003) 'The nature of a chlorophyll ligand in Lhca proteins determines the far red fluorescence emission typical of photosystem I.', *The Journal of biological chemistry*, 278(49), pp. 49223–49229. doi: 10.1074/jbc.M309203200.

Mozzo, M. *et al.* (2008) 'Photoprotection in the antenna complexes of photosystem II: Role of individual xanthophylls in chlorophyll triplet quenching', *Journal of Biological Chemistry*, 283(10), pp. 6184–6192. doi: 10.1074/jbc.M708961200.

Mozzo, M. *et al.* (2010) 'Functional analysis of Photosystem I light-harvesting complexes (Lhca) gene products of Chlamydomonas reinhardtii', *Biochimica et Biophysica Acta - Bioenergetics*, 1797(2), pp. 212–221. doi: 10.1016/j.bbabio.2009.10.005.

Müh, F., Madjet, M. E. A. and Renger, T. (2010) 'Structure-based identification of energy sinks in plant light-harvesting complex II', *Journal of Physical Chemistry B*, 114(42), pp. 13517–13535. doi: 10.1021/jp106323e.

Müller-Moulé, P., Havaux, M. and Niyogi, K. K. (2003) 'Zeaxanthin Deficiency Enhances the High Light Sensitivity of an Ascorbate-Deficient Mutant of Arabidopsis', *Plant Physiology*, 133(2), pp. 748–760. doi: 10.1104/pp.103.026252.

Müller, M. G. *et al.* (2010) 'Singlet energy dissipation in the photosystem II light-harvesting complex does not involve energy transfer to carotenoids', *ChemPhysChem*, 11(6), pp. 1289–1296. doi: 10.1002/cphc.200900852.

Müller, P., Li, X. P. and Niyogi, K. K. (2001) 'Non-photochemical quenching. A response to excess light energy', *Plant Physiology*, 125(4), pp. 1558–1566. doi: 10.1104/pp.125.4.1558.

Murata, N. *et al.* (2007) 'Photoinhibition of photosystem II under environmental stress', *Biochimica et Biophysica Acta - Bioenergetics*, 1767(6), pp. 414–421. doi: 10.1016/j.bbabio.2006.11.019.

Mussgnug, J. H. *et al.* (2005) 'NAB1 is an RNA binding protein involved in the light-regulated differential expression of the light-harvesting antenna of Chlamydomonas reinhardtii', *Plant Cell*, 17(12), pp. 3409–3421. doi: 10.1105/tpc.105.035774.

Naguib, Y. M. A. (2000) 'Antioxidant activities of astaxanthin and related carotenoids', *Journal of Agricultural and Food Chemistry*, 48(4), pp. 1150–1154. doi: 10.1021/jf991106k.

Nelson, N. and Junge, W. (2015) 'Structure and energy transfer in photosystems of oxygenic photosynthesis', *Annual Review of Biochemistry*, 84, pp. 659–683. doi: 10.1146/annurev-biochem-092914-041942.

Nelson, N. and Yocum, C. F. (2006) 'Structure and function of photosystems I and II', *Annual Review of Plant Biology*, 57(1), pp. 521–565. doi: 10.1146/annurev.arplant.57.032905.105350.

Nickelsen, J. and Rengstl, B. (2013) 'Photosystem II assembly: From cyanobacteria to plants', *Annual Review of Plant Biology*, 64, pp. 609–635. doi: 10.1146/annurev-arplant-050312-120124.

Nicol, L., Nawrocki, W. J. and Croce, R. (2019) 'Disentangling the sites of non-photochemical quenching in vascular plants', *Nature Plants*, 5(11), pp. 1177–1183. doi: 10.1038/s41477-019-0526-5.

Niedzwiedzki, D. M. *et al.* (2016) 'Carotenoid-induced non-photochemical quenching in the cyanobacterial chlorophyll synthase-HliC/D complex', *Biochimica et Biophysica Acta - Bioenergetics*, 1857(9), pp. 1430–1439. doi: 10.1016/j.bbabio.2016.04.280.

Nield, J. and Barber, J. (2006) 'Refinement of the structural model for the Photosystem II supercomplex of higher plants', *Biochimica et Biophysica Acta - Bioenergetics*, 1757(5–6), pp. 353–361. doi: 10.1016/j.bbabio.2006.03.019.

Nilkens, M. *et al.* (2010) 'Identification of a slowly inducible zeaxanthin-dependent component of non-photochemical quenching of chlorophyll fluorescence generated under steady-state conditions in Arabidopsis', *Biochimica et Biophysica Acta - Bioenergetics*, 1797(4), pp. 466–475. doi: 10.1016/j.bbabio.2010.01.001.

Nitzan, A. (2006) *Chemical Dynamics in Condensed Phases*, *Chemical Dynamics in Condensed Phases*. Oxford University Press. doi: 10.1093/oso/9780198529798.001.0001.

Nixon, P. J. *et al.* (2010) 'Recent advances in understanding the assembly and repair of photosystem II', *Annals of Botany*. Oxford University Press, pp. 1–16. doi: 10.1093/aob/mcq059.

Niyogi, K. K. (1999) 'Photoprotection revisited: Genetic and molecular approaches', *Annual Review of Plant Biology*, 50(1), pp. 333–359. doi: 10.1146/annurev.arplant.50.1.333.

Niyogi, K. K. (2000) 'Safety valves for photosynthesis', *Current Opinion in Plant Biology*, 3(6), pp. 455–460. doi: 10.1016/S1369-5266(00)00113-8.

Niyogi, K. K., Björkman, O. and Grossman, A. R. (1997a) 'Chlamydomonas xanthophyll cycle mutants identified by video imaging of chlorophyll fluorescence quenching', *Plant Cell*, 9(8), pp. 1369–1380. doi: 10.1105/tpc.9.8.1369.

Niyogi, K. K., Björkman, O. and Grossman, A. R. (1997b) 'The roles of specific xanthophylls in photoprotection', *Proceedings of the National Academy of Sciences of the United States of America*, 94(25), pp. 14162–14167. doi: 10.1073/pnas.94.25.14162.

Novoderezhkin, V., Marin, A. and Van Grondelle, R. (2011) 'Intra- and inter-monomeric transfers in the light harvesting LHCII complex: The Redfield-Förster picture', *Physical Chemistry Chemical Physics*, 13(38), pp. 17093–17103. doi: 10.1039/c1cp21079c.

Van Oort, B. *et al.* (2018) 'Revisiting the Role of Xanthophylls in Nonphotochemical Quenching', *Journal of Physical Chemistry Letters*, 9(2), pp. 346–352. doi: 10.1021/acs.jpclett.7b03049.

Oreb, M., Tews, I. and Schleiff, E. (2008) 'Policing Tic "n" Toc, the doorway to chloroplasts', *Trends in Cell Biology*, 18(1), pp. 19–27. doi: 10.1016/j.tcb.2007.10.002.

Oswald, W. J. and Golueke, C. G. (1960) *Biological Transformation of Solar Energy*, *Advances in Applied Microbiology*. Elsevier (Advances in Applied Microbiology). doi: 10.1016/S0065-2164(08)70127-8.

Pan, X. *et al.* (2011) 'Structural insights into energy regulation of light-harvesting complex CP29 from spinach', *Nature Structural and Molecular Biology*, 18(3), pp. 309–315. doi: 10.1038/nsmb.2008.

Park, J. *et al.* (2017) 'Cas-analyzer: An online tool for assessing genome editing results using NGS data', *Bioinformatics*, 33(2), pp. 286–288. doi: 10.1093/bioinformatics/btw561.

Park, S. *et al.* (2019) 'Chlorophyll–carotenoid excitation energy transfer and charge transfer in Nannochloropsis oceanica for the regulation of photosynthesis', *Proceedings of the*

National Academy of Sciences of the United States of America, 116(9), pp. 3385–3390. doi: 10.1073/pnas.1819011116.

PAULSEN, H., FINKENZELLER, B. and KÜHLEIN, N. (1993) 'Pigments induce folding of light-harvesting chlorophyll a/b-binding protein', *European Journal of Biochemistry*, 215(3), pp. 809–816. doi: 10.1111/j.1432-1033.1993.tb18096.x.

Peers, G. *et al.* (2009) 'An ancient light-harvesting protein is critical for the regulation of algal photosynthesis', *Nature*, 462(7272), pp. 518–521. doi: 10.1038/nature08587.

Peers, G. (2011) *Enhancement of biomass production by disruption of light energy dissipation pathways*. Available at: https://patents.google.com/patent/US8940508 (Accessed: 29 April 2021).

Perin, G. *et al.* (2015) 'Generation of random mutants to improve light-use efficiency of Nannochloropsis gaditana cultures for biofuel production', *Biotechnology for Biofuels*, 8(1), p. 161. doi: 10.1186/s13068-015-0337-5.

Perozeni, F. *et al.* (2020) 'Chlamydomonas reinhardtii LHCSR1 and LHCSR3 proteins involved in photoprotective non-photochemical quenching have different quenching efficiency and different carotenoid affinity', *Scientific Reports*, 10(1), p. 21957. doi: 10.1038/s41598-020-78985-w.

Perozeni, F., Cazzaniga, S. and Ballottari, M. (2019) 'In vitro and in vivo investigation of chlorophyll binding sites involved in non-photochemical quenching in Chlamydomonas reinhardtii', *Plant Cell and Environment*, 42(8), pp. 2522–2535. doi: 10.1111/pce.13566.

Perozeni, F., Stella, G. R. and Ballottari, M. (2018) 'LHCSR expression under HSP70/RBCS2 promoter as a strategy to increase productivity in microalgae', *International Journal of Molecular Sciences*, 19(1). doi: 10.3390/ijms19010155.

Petroutsos, D. *et al.* (2011) 'The chloroplast calcium sensor CAS is required for photoacclimation in Chlamydomonas reinhardtii', *Plant Cell*, 23(8), pp. 2950–2963. doi: 10.1105/tpc.111.087973.

Pinnola, A. *et al.* (2013) 'Zeaxanthin binds to light-harvesting complex stress-related protein to enhance nonphotochemical quenching in Physcomitrella patens', *Plant Cell*, 25(9), pp. 3519–3534. doi: 10.1105/tpc.113.114538.

Pinnola, A. *et al.* (2016) 'Electron transfer between carotenoid and chlorophyll contributes to quenching in the LHCSR1 protein from Physcomitrella patens', *Biochimica et Biophysica Acta - Bioenergetics*, 1857(12), pp. 1870–1878. doi: 10.1016/j.bbabio.2016.09.001.

Pinnola, A. *et al.* (2017) 'Functional modulation of LHCSR1 protein from Physcomitrella patens by zeaxanthin binding and low pH', *Scientific Reports*, 7(1), pp. 1–14. doi: 10.1038/s41598-017-11101-7.

Plumley, F. G. and Schmidt, G. W. (1987) 'Reconstitution of chlorophyll a/b light-harvesting complexes: Xanthophyll-dependent assembly and energy transfer', *Proceedings of the National Academy of Sciences*, 84(1), pp. 146–150. doi: 10.1073/pnas.84.1.146.

Polívka, T. and Frank, H. A. (2010) 'Light Harvesting by Carotenoids', *Accounts of Chemical Research*, 43(8), pp. 1125–1134.

Polívka, T. and Sundström, V. (2004) 'Ultrafast dynamics of carotenoid excited states-from solution to natural and artificial systems', *Chemical Reviews*, 104(4), pp. 2021–2071. doi: 10.1021/cr020674n.

Polukhina, I. *et al.* (2016) 'Carbon supply and photoacclimation cross talk in the green alga Chlamydomonas reinhardtii', *Plant Physiology*, 172(3), pp. 1494–1505. doi: 10.1104/pp.16.01310.

Potter, S. C. *et al.* (2018) 'HMMER web server: 2018 update', *Nucleic Acids Research*, 46(W1), pp. W200–W204. doi: 10.1093/nar/gky448.

Quaas, T. *et al.* (2015) 'Non-photochemical quenching and xanthophyll cycle activities in six green algal species suggest mechanistic differences in the process of excess energy dissipation', *Journal of Plant Physiology*, 172, pp. 92–103. doi: 10.1016/j.jplph.2014.07.023.

Raymond, J. and Blankenship, R. E. (2004) 'Biosynthetic pathways, gene replacement and the antiquity of life', *Geobiology*, 2(4), pp. 199–203. doi: 10.1111/j.1472-4677.2004.00037.x.

Renberg, L. *et al.* (2010) 'A metabolomic approach to study major metabolite changes during acclimation to limiting CO2 in Chlamydomonas reinhardtii', *Plant Physiology*, 154(1), pp. 187–196. doi: 10.1104/pp.110.157651.

Rochaix, J. D. (2014) 'Regulation and dynamics of the light-harvesting system', *Annual*

Review of Plant Biology, 65(65:287-309), pp. 287–309. doi: 10.1146/annurev-arplant-050213-040226.

Rokka, A. *et al.* (2005) 'Synthesis and assembly of thylakoid protein complexes: Multiple assembly steps of photosystem II', *Biochemical Journal*, 388(1), pp. 159–166. doi: 10.1042/BJ20042098.

Rosenberg, J. N. *et al.* (2011) 'Microalgal biomass production and carbon dioxide sequestration from an integrated ethanol biorefinery in Iowa: A technical appraisal and economic feasibility evaluation', *Biomass and Bioenergy*, 35(9), pp. 3865–3876. doi: 10.1016/j.biombioe.2011.05.014.

Roy, A., Kucukural, A. and Zhang, Y. (2010) 'I-TASSER: A unified platform for automated protein structure and function prediction', *Nature Protocols*, 5(4), pp. 725–738. doi: 10.1038/nprot.2010.5.

Ruban, A. V. *et al.* (1999) 'Determination of the stoichiometry and strength of binding of xanthophylls to the photosystem II light harvesting complexes', *Journal of Biological Chemistry*, 274(15), pp. 10458–10465. doi: 10.1074/jbc.274.15.10458.

Ruban, A. V. *et al.* (2007) 'Identification of a mechanism of photoprotective energy dissipation in higher plants', *Nature*, 450(7169), pp. 575–578. doi: 10.1038/nature06262.

Sacharz, J. *et al.* (2017) 'The xanthophyll cycle affects reversible interactions between PsbS and light-harvesting complex II to control non-photochemical quenching', *Nature Plants*, 3(2). doi: 10.1038/nplants.2016.225.

Salomé, P. A. and Merchant, S. S. (2019) 'A series of fortunate events: Introducing chlamydomonas as a reference organism', *Plant Cell*. American Society of Plant Biologists, pp. 1682–1707. doi: 10.1105/tpc.18.00952.

Schägger, H. and von Jagow, G. (1987) 'Tricine-sodium dodecyl sulfate-polyacrylamide gel electrophoresis for the separation of proteins in the range from 1 to 100 kDa', *Analytical Biochemistry*, 166(2), pp. 368–379. doi: 10.1016/0003-2697(87)90587-2.

Schlau-Cohen, G. S. *et al.* (2009) 'Pathways of energy flow in LHCII from two-dimensional electronic spectroscopy', *Journal of Physical Chemistry B*, 113(46), pp. 15352–15363. doi: 10.1021/jp9066586.

Schlau-Cohen, G. S. *et al.* (2014) 'Single-molecule spectroscopy of photosynthetic proteins in solution: Exploration of structure-function relationships', *Chemical Science*, 5(8), pp. 2933–2939. doi: 10.1039/c4sc00582a.

Schlau-Cohen, G. S. *et al.* (2015) 'Single-molecule identification of quenched and unquenched states of LHCII', *Journal of Physical Chemistry Letters*, 6(5), pp. 860–867. doi: 10.1021/acs.jpclett.5b00034.

Schneider, A. *et al.* (2014) 'The Arabidopsis Tellurite resistance C protein together with ALB3 is involved in photosystem II protein synthesis', *Plant Journal*, 78(2), pp. 344–356. doi: 10.1111/tpj.12474.

Schreiber, U. and Klughammer, C. (2009) 'New NADPH / 9-AA module for the DUAL-PAM-100 : Description , operation and examples of application .', *PAM application Notes*, 2, pp. 1–13.

Shapira, M. *et al.* (1997) 'Differential regulation of chloroplast gene expression in Chlamydomonas reinhardtii during photoacclimation: Light stress transiently suppresses synthesis of the Rubisco LSU protein while enhancing synthesis of the PS II D1 protein', *Plant Molecular Biology*, 33(6), p. 1001. doi: 10.1023/A:1005814800641.

Shen, J. R. (2015) 'The structure of photosystem II and the mechanism of water oxidation in photosynthesis', *Annual Review of Plant Biology*, 66(1), pp. 23–48. doi: 10.1146/annurev-arplant-050312-120129.

Shen, L. *et al.* (2019) 'Structure of a C2S2M2N2-type PSII–LHCII supercomplex from the green alga Chlamydomonas reinhardtii', *Proceedings of the National Academy of Sciences of the United States of America*, 116(42), pp. 21246–21255. doi: 10.1073/pnas.1912462116.

Shikanai, T. *et al.* (1999) 'Identification and characterization of Arabidopsis mutants with reduced quenching of chlorophyll fluorescence', *Plant and Cell Physiology*, 40(11), pp. 1134–1142. doi: 10.1093/oxfordjournals.pcp.a029498.

Shikanai, T. and Yamamoto, H. (2017) 'Contribution of Cyclic and Pseudo-cyclic Electron Transport to the Formation of Proton Motive Force in Chloroplasts', *Molecular Plant*. Cell Press, pp. 20–29. doi: 10.1016/j.molp.2016.08.004.

Shinozaki, K. *et al.* (1986) 'The complete nucleotide sequence of the tobacco chloroplast

genome: Its gene organization and expression', *EMBO Journal*, 5(9), pp. 2043–2049. doi: 10.1002/j.1460-2075.1986.tb04464.x.

Shokrkar, H., Ebrahimi, S. and Zamani, M. (2017) 'Bioethanol production from acidic and enzymatic hydrolysates of mixed microalgae culture', *Fuel*, 200, pp. 380–386. doi: 10.1016/j.fuel.2017.03.090.

Shuba, E. S. and Kifle, D. (2018) 'Microalgae to biofuels: "Promising" alternative and renewable energy, review', *Renewable and Sustainable Energy Reviews*, pp. 743–755. doi: 10.1016/j.rser.2017.08.042.

Simionato, D. *et al.* (2013) 'The response of Nannochloropsis gaditana to nitrogen starvation includes de novo biosynthesis of triacylglycerols, a decrease of chloroplast galactolipids, and reorganization of the photosynthetic apparatus', *Eukaryotic Cell*, 12(5), pp. 665–676. doi: 10.1128/EC.00363-12.

Snellenburg, J. J. *et al.* (2017) 'A model for the 77 K excited state dynamics in Chlamydomonas reinhardtii in state 1 and state 2', *Biochimica et Biophysica Acta - Bioenergetics*, 1858(1), pp. 64–72. doi: 10.1016/j.bbabio.2016.10.001.

Son, M., Pinnola, A. and Schlau-Cohen, G. S. (2020) 'Zeaxanthin independence of photophysics in light-harvesting complex II in a membrane environment', *Biochimica et Biophysica Acta - Bioenergetics*, 1861(5–6), p. 148115. doi: 10.1016/j.bbabio.2019.148115.

Soo, R. M. *et al.* (2017) 'On the origins of oxygenic photosynthesis and aerobic respiration in Cyanobacteria', *Science*, 355(6332), pp. 1436–1440. doi: 10.1126/science.aal3794.

Spaniol, B. *et al.* (2021) 'Complexome profiling on the lpa2 mutant reveals insights into PSII biogenesis and new PSII associated proteins', *bioRxiv*. doi: 10.1101/2021.01.04.425283.

Staleva, H. *et al.* (2015) 'Mechanism of photoprotection in the cyanobacterial ancestor of plant antenna proteins', *Nature Chemical Biology*, 11(4), pp. 287–291. doi: 10.1038/nchembio.1755.

Sueoka, N. (1960) 'Mitotic Replication of Deoxyribonucleic Acid in Chlamydomonas Reinhardi', *Proceedings of the National Academy of Sciences*, 46(1), pp. 83–91. doi: 10.1073/pnas.46.1.83.

Takahashi, S. and Murata, N. (2008) 'How do environmental stresses accelerate photoinhibition?', *Trends in Plant Science*, pp. 178–182. doi: 10.1016/j.tplants.2008.01.005.

Tang, J. X. *et al.* (2018) 'CRISPR/Cas9-mediated genome editing induces gene knockdown by altering the pre-mRNA splicing in mice', *BMC Biotechnology*, 18(1), pp. 1–9. doi: 10.1186/s12896-018-0472-8.

Tardy, F. and Havaux, M. (1996) 'Photosynthesis, chlorophyll fluorescence, light-harvesting system and photoinhibition resistance of a zeaxanthin-accumulating mutant of Arabidopsis thaliana', *Journal of Photochemistry and Photobiology B: Biology*, 34(1), pp. 87–94. doi: 10.1016/1011-1344(95)07272-1.

Tian, L. *et al.* (2019) 'PH dependence, kinetics and light-harvesting regulation of nonphotochemical quenching in Chlamydomonas', *Proceedings of the National Academy of Sciences of the United States of America*, 116(17), pp. 8320–8325. doi: 10.1073/pnas.1817796116.

Tibiletti, T. *et al.* (2016) 'Chlamydomonas reinhardtii PsbS protein is functional and accumulates rapidly and transiently under high light', *Plant Physiology*, 171(4), pp. 2717–2730. doi: 10.1104/pp.16.00572.

Tietz, S. *et al.* (2017) 'NPQ(T): a chlorophyll fluorescence parameter for rapid estimation and imaging of non-photochemical quenching of excitons in photosystem-II-associated antenna complexes', *Plant Cell and Environment*, 40(8), pp. 1243–1255. doi: 10.1111/pce.12924.

Tokutsu, R. *et al.* (2012) 'Revisiting the supramolecular organization of photosystem II in Chlamydomonas reinhardtii', *Journal of Biological Chemistry*, 287(37), pp. 31574–31581. doi: 10.1074/jbc.M111.331991.

Tokutsu, R. and Minagawa, J. (2013) 'Energy-dissipative supercomplex of photosystem II associated with LHCSR3 in Chlamydomonas reinhardtii', *Proceedings of the National Academy of Sciences of the United States of America*, 110(24), pp. 10016–10021. doi: 10.1073/pnas.1222606110.

Troiano, J. M. *et al.* (2021) 'Identification of 1 distinct pH- and zeaxanthin-dependent quenching in LHCSR3 from chlamydomonas reinhardtii', *eLife*, 10, pp. 1–59. doi:

10.7554/eLife.60383.

Tuladhar, R. *et al.* (2019) 'CRISPR-Cas9-based mutagenesis frequently provokes on-target mRNA misregulation', *Nature Communications*, 10(1), pp. 1–10. doi: 10.1038/s41467-019-12028-5.

Uniacke, J. and Zerges, W. (2007) 'Photosystem II assembly and repair are differentially localized in Chlamydomonas', *Plant Cell*, 19(11), pp. 3640–3654. doi: 10.1105/tpc.107.054882.

Valente, L. M. P. *et al.* (2021) 'Microalgae as feed ingredients for livestock production and aquaculture', in *Microalgae*. Elsevier, pp. 239–312. doi: 10.1016/b978-0-12-821218-9.00009-8.

Vanlerberghe, G. C. (2013) 'Alternative oxidase: A mitochondrial respiratory pathway to maintain metabolic and signaling homeostasis during abiotic and biotic stress in plants', *International Journal of Molecular Sciences*. Int J Mol Sci, pp. 6805–6847. doi: 10.3390/ijms14046805.

Venkata Mohan, S. *et al.* (2015) 'Heterotrophic microalgae cultivation to synergize biodiesel production with waste remediation: Progress and perspectives', *Bioresource Technology*, 184, pp. 169–178. doi: 10.1016/j.biortech.2014.10.056.

Vidal-Meireles, A. *et al.* (2019) 'Ascorbate deficiency does not limit non-photochemical quenching in Chlamydomonas reinhardtii', *bioRxiv*, 182(1), pp. 597–611. doi: 10.1101/813766.

Vílchez, C. *et al.* (2011) 'Marine carotenoids: Biological functions and commercial applications', *Marine Drugs*. MDPI AG, pp. 319–333. doi: 10.3390/md9030319.

Wahadoszamen, M. *et al.* (2014) 'The role of charge-transfer states in energy transfer and dissipation within natural and artificial bacteriochlorophyll proteins', *Nature Communications*, 5, p. 5287. doi: 10.1038/ncomms6287.

Wang, P. *et al.* (2013) 'Evidence for a role of chloroplastic m-type thioredoxins in the biogenesis of photosystem II in arabidopsis', *Plant Physiology*, 163(4), pp. 1710–1728. doi: 10.1104/pp.113.228353.

Wang, Y., Stessman, D. J. and Spalding, M. H. (2015) 'The CO2 concentrating mechanism and photosynthetic carbon assimilation in limiting CO2: How Chlamydomonas works against the gradient', *Plant Journal*, 82(3), pp. 429–448. doi: 10.1111/tpj.12829.

Watkins, L. P. and Yang, H. (2005) 'Detection of intensity change points in time-resolved single-molecule measurements', *Journal of Physical Chemistry B*, 109(1), pp. 617–628. doi: 10.1021/jp0467548.

Wei, L. *et al.* (2010) 'LPA19, a Psb27 homolog in Arabidopsis thaliana, facilitates D1 protein precursor processing during PSII biogenesis', *Journal of Biological Chemistry*, 285(28), pp. 21391–21398. doi: 10.1074/jbc.M110.105064.

Von Wettstein, D., Gough, S. and Kannangara, C. G. (1995) 'Chlorophyll biosynthesis', *Plant Cell*. American Society of Plant Physiologists, pp. 1039–1057. doi: 10.1105/tpc.7.7.1039.

Whelan, S. and Goldman, N. (2001) 'A General Empirical Model of Protein Evolution Derived from Multiple Protein Families Using a Maximum-Likelihood Approach', *Molecular Biology and Evolution*, 18(5), pp. 691–699. doi: 10.1093/oxfordjournals.molbev.a003851.

Wientjes, E., Van Amerongen, H. and Croce, R. (2013) 'LHCII is an antenna of both photosystems after long-term acclimation', *Biochimica et Biophysica Acta - Bioenergetics*, 1827(3), pp. 420–426. doi: 10.1016/j.bbabio.2012.12.009.

Wijffels, R. H. and Barbosa, M. J. (2010) 'An outlook on microalgal biofuels', *Science*, 329(5993), pp. 796–799. doi: 10.1126/science.1189003.

Wilson, A. *et al.* (2006) 'A soluble carotenoid protein involved in phycobilisome-related energy dissipation in cyanobacteria', *Plant Cell*, 18(4), pp. 992–1007. doi: 10.1105/tpc.105.040121.

Wu, Q. *et al.* (2016) 'The antioxidant, immunomodulatory, and anti-inflammatory activities of Spirulina: an overview', *Archives of Toxicology*. Springer Verlag, pp. 1817–1840. doi: 10.1007/s00204-016-1744-5.

Xiang, Y., Zhang, J. and Weeks, D. P. (2001) 'The Cia5 gene controls formation of the carbon concentrating mechanism in Chlamydomonas reinhardtii', *Proceedings of the*

National Academy of Sciences of the United States of America, 98(9), pp. 5341–5346. doi: 10.1073/pnas.101534498.

Xu, P. *et al.* (2015) 'Molecular insights into Zeaxanthin-dependent quenching in higher plants', *Scientific Reports*, 5(1), pp. 1–10. doi: 10.1038/srep13679.

Yamamoto, H. Y. and Kamite, L. (1972) 'The effects of dithiothreitol on violaxanthin de-epoxidation and absorbance changes in the 500-nm region', *BBA - Bioenergetics*, 267(3), pp. 538–543. doi: 10.1016/0005-2728(72)90182-X.

Yamamoto, H. Y., Nakayama, T. O. M. and Chichester, C. O. (1962) 'Studies on the light and dark interconversions of leaf xanthophylls', *Archives of Biochemistry and Biophysics*, 97(1), pp. 168–173. doi: 10.1016/0003-9861(62)90060-7.

Yamano, T., Miura, K. and Fukuzawa, H. (2008) 'Expression analysis of genes associated with the induction of the carbon-concentrating mechanism in Chlamydomonas reinhardtii', *Plant Physiology*, 147(1), pp. 340–354. doi: 10.1104/pp.107.114652.

Yang, W. *et al.* (2015) 'Algae after dark: Mechanisms to cope with anoxic/hypoxic conditions', *Plant Journal*, 82(3), pp. 481–503. doi: 10.1111/tpj.12823.

Young, A. J. and Lowe, G. L. (2018) 'Carotenoids—antioxidant properties', *Antioxidants*. MDPI AG. doi: 10.3390/antiox7020028.

Zerges, W., Auchincloss, A. H. and Rochaix, J. D. (2003) 'Multiple translational control sequences in the 5′ leader of the chloroplast psbC mRNA interact with nuclear gene products in Chlamydomonas reinhardtii', *Genetics*, 163(3), pp. 895–904. doi: 10.1093/genetics/163.3.895.

Zhang, D. *et al.* (2011) 'HCF243 encodes a chloroplast-localized protein involved in the D1 protein stability of the Arabidopsis Photosystem II complex', *Plant Physiology*, 157(2), pp. 608–619. doi: 10.1104/pp.111.183301.

Zhang, J. *et al.* (2014) 'Microalgal carotenoids: Beneficial effects and potential in human health', *Food and Function*. Royal Society of Chemistry, pp. 413–425. doi: 10.1039/c3fo60607d.

Zhang, S., Frankel, L. K. and Bricker, T. M. (2010) 'The Sll0606 protein is required for

photosystem II assembly/stability in the cyanobacterium Synechocystis sp. PCC 6803', *Journal of Biological Chemistry*, 285(42), pp. 32047–32054. doi: 10.1074/jbc.M110.166983.

Zhu, X. G., Long, S. P. and Ort, D. R. (2010) 'Improving photosynthetic efficiency for greater yield', *Annual Review of Plant Biology*, 61(61:235-261), pp. 235–261. doi: 10.1146/annurev-arplant-042809-112206.

Ziehe, D., Dünschede, B. and Schünemann, D. (2017) 'From bacteria to chloroplasts: Evolution of the chloroplast SRP system', *Biological Chemistry*, 398(5–6), pp. 653–661. doi: 10.1515/hsz-2016-0292.

Zuliani, L. *et al.* (2016) 'Microalgae cultivation on anaerobic digestate of municipalwastewater, sewage sludge and agro-waste', *International Journal of Molecular Sciences*, 17(10). doi: 10.3390/ijms17101692.